MASSEY UNIVERSITY

TE KUNENGA KI PŪREHUROA

UNIVERSITY OF NEW ZEALAND

Theoretical Study of Weakly Interacting Systems: Noble Gas Compounds

by

Edison Florez

A thesis presented in partial fulfillment of the

requirements for the degree of

Doctor of Philosophy

in

Physics

at

Massey University, Albany

New Zealand

2023

Abstract

The dispersion bonds—also known as London or Van der Waals interactions—are usually considered the weakest and the least important of the several types of chemical bonding models known. However, dispersion interactions play a crucial role in chemistry; particularly, defining functions and structural stability of proteins and Watson-Crick pairs in biochemical systems, to name just a few.

Through the Periodic Table, noble gas aggregates are one of the prime examples of systems strongly influenced by dispersion interactions. In addition, from helium—the smallest and most unreactive—to radon, periodic trends emerge; the atomic mass/radius and the dispersion interactions increase, resulting in increasing melting points, boiling points, enthalpies of vaporization, etc. However, Oganesson (Og, Z = 118)— the heaviest noble gas and element synthesized at the limit of nuclear mass and charge—may behave differently from what would be predicted by simple extrapolations in the Periodic Table. This is due to relativistic effects. Those effects are more pronounced in heavier elements (high nuclear charge Z) and significantly influence both chemical and physical properties.

The research presented here is divided into three parts. First, we explore the behavior of neon clusters under high magnetic fields in the range of $B = 0 - 0.3$ a.u. $(0 - 7.5 \times 10^5$ Tesla). Under these extreme conditions, atoms and molecules reveal exotic chemical characteristics such as squeezed and twisted structures as dispersion interactions are affected by the so-called perpendicular paramagnetic bonding giving rise to molecules and materials that do not exist on Earth (but in environments of white dwarfs and magnetic stars). Our results show that, regarding the field-free case, there is an energetic stabilization for the neon

interaction in a magnetic field, leading to enhanced melting temperatures of more than 70% and reducing the entropy of the system, squeezing the structures perpendicular to the applied magnetic field.

Second, we analyzed the chemical nature of Flerovium clusters and their noble gas-like behavior upon melting. Here, we studied closed-shell flerovium in detail to predict solid-state properties including the melting point from a decomposition of the total energy into many-body forces derived from relativistic coupled-cluster and density functional theory. Our results show that the noble gas behavior of flerovium enhances resistance to bond formation. Flerovium atoms are only weakly bound, less compared to mercury, but more than in xenon. This makes the accurate prediction of phase transitions very difficult. Nevertheless, we made the first prediction by Monte-Carlo simulation estimates the melting point at 284 ± 50 K.

Finally, we studied the structure, stability, and chemical bonding of fluorides noble gas compounds, NgF_n ($n = 2, 4, 6$), where Ng comes from Argon, Krypton, Xenon, Radon, and Oganesson. The heaviest element, Oganesson, unlike all other noble gas compounds, is enhancing the tendency to adopt a tetrahedral local environment. These results indicate that there may be a partial role reversal of the elements Fl and Og important in the future of atom-at-a-time chemistry. Oganesson di- and tetra-fluorides are stable with and without relativistic effects, whereas hexafluoride is unstable. This creates such a radical departure from periodic group trends that the rules of the periodic table appear to be broken by relativity, suggesting an end to periodicity.

Acknowledgements

I express my gratitude to my supervisor, Peter Schwerdtfeger, for his continuous support (academic and personal), expert advice, encouraging words, and fruitful discussions. It was a pleasure to work with him and I am grateful for the many opportunities that were created. I also thank Elke Pahl for her help in the development of the Fortran code and the insightful discussions on computation and physical properties. I would also like to thank my colleagues Odile, Morten, Antony, Ray, Paul, Peter, and Jan for their cooperation and support.

I am grateful to my parents, Juan Carlos and Lilia, for their endless support and encouragement throughout my professional journey. You both have encouraged me to have big dreams. Thank you for your love and unconditional support. And last but not least, I would like to thank my wife and my daughter. I could not have completed this huge endeavor without their unwavering love, patience, and understanding. My wife, Paola, has been my greatest strength, offering unwavering love, patience, and understanding. She has made numerous sacrifices along the way and I am truly grateful for everything she has done for me. My daughter, Mariana, has brought so much joy and happiness to my life, even during the most challenging times. She has been a constant source of motivation and inspiration for me. Her playful nature has always lifted my spirits and kept me going. I hope I have made you all proud and that this achievement inspires my daughter to pursue her dreams as well.

Contents

List of Figures

List of Tables

Chapter 1

Theoretical background

Computer simulations are a crucial tool for understanding the properties of molecular systems, providing insights into chemical bonding that are difficult to obtain through other means. Accurate theoretical models are essential for ensuring the realism and predictive power of these simulations. Theoretical models must accurately represent the potential energy of the system and incorporate proper quantum mechanical treatment of nuclear dynamics. The Schrödinger and Dirac equations provide a framework for understanding the behavior of atoms, electrons, and the interactions between them. In quantum chemistry, various methods have been developed to study the properties of molecules and materials, including Hartree-Fock (HF) theory, density functional theory (DFT), second-order perturbation theory (MP2), and coupled-cluster (CC) methods for electron correlation. Furthermore, Monte Carlo simulations can be used to compute phase transitions and other important physical properties of systems at the quantum level. This chapter provides the theoretical background to study molecular interactions and dynamics in atomic and molecular systems. The theoretical foundations of these methods will be discussed with an emphasis on their practical applications for simulating molecular systems. Technical terms and equations will be explained in detail to make the material more accessible.

1.1 Introduction

An accurate first ansatz to describe molecular interactions at the nonrelativistic level is given by the Schrödinger equation

$$i\hbar\frac{\partial}{\partial t}\Psi(\mathbf{r},t) = \mathscr{H}\Psi(\mathbf{r},t) \tag{1.1}$$

where all the information about the system is contained in the *wave function* (Ψ) and the Hamiltonian $\mathscr{H}$ operator describes the simultaneous movement of the nuclei and electrons and their interactions. For a system of M nuclei and N electrons, we assume for the moment the nuclei and electrons to be point masses and neglect spin-orbit and other relativistic and quantum electrodynamic contributions. The Hamiltonian operator is then given as (in atomic units)

$$\begin{aligned}\mathscr{H} = -\frac{1}{2}\sum_{i}^{N}\nabla_i^2 - \frac{1}{2}\sum_{\alpha}^{M}\frac{1}{m_\alpha}\nabla_\alpha^2 + \sum_{\alpha}^{M}\sum_{\beta>\alpha}^{M}\frac{Z_\alpha Z_\beta}{|\mathbf{R}_\alpha - \mathbf{R}_\beta|} \\ - \sum_{\alpha}^{M}\sum_{i}^{N}\frac{Z_\alpha}{|\mathbf{r}_i - \mathbf{R}_\alpha|} + \sum_{i}^{N}\sum_{j>i}^{N}\frac{1}{|\mathbf{r}_i - \mathbf{r}_j|}\end{aligned} \tag{1.2}$$

where the indices i and j refer to electrons and α and β refer to nuclei. The first term in Equation (1.2) is the operator for the kinetic energy of the electrons. The second term is the operator for the kinetic energy of the nuclei with mass m_α. The third term is the potential energy of the repulsions between the nuclei, where $\mathbf{R}_\alpha$, $\mathbf{R}_\beta$ are the coordinates of nuclei with atomic numbers Z_α and Z_β, respectively. The fourth term is the potential energy of the attractions between the electrons and the nuclei, where $\mathbf{r}_j$, $\mathbf{R}_\alpha$ are the coordinates of the i-th electron and α-th nucleus, respectively. The last term is the potential energy of the repulsions between the electrons, where $\mathbf{r}_i$, $\mathbf{r}_j$ are the coordinates of electrons. In Equation (1.2), the Hamiltonian operator could be restated by

$$\mathscr{H} \equiv \mathcal{T}_i + \mathcal{T}_\alpha + \mathcal{V}_{\alpha\beta} + \mathcal{V}_{\alpha i} + \mathcal{V}_{ij} \tag{1.3}$$

where each operator represents the electronic and nuclear kinetic energy operators ($\mathcal{T}$), the nuclear-nuclear, electron-nuclear, and electron-electron interaction potential operators ($\mathcal{V}$), respectively.

1.2 The Born-Oppenheimer Approximation

The time-dependent Schrödinger equation is formidable looking, Equation (1.1), and only for a few quantum systems are analytical solutions available. For many applications of quantum mechanics, including those in this work, the simpler **time-independent** or stationary form is used, and the wave functions and energies of an atomic/molecular system are obtained after solving

$$\mathscr{H}\ \Psi(\mathbf{R}_\alpha, \mathbf{r}_i) = \mathscr{E}\ \Psi(\mathbf{R}_\alpha, \mathbf{r}_i) \tag{1.4}$$

where $\mathscr{H}$ is the Hamiltonian operator in Equation (1.2) and $\mathscr{E}$ is the total energy of the system. It is important to note that neither the Hamiltonian nor the energy has a time dependence. The molecular wave function is $\Psi(\mathbf{R}_\alpha, \mathbf{r}_i)$ and $\mathbf{R}_\alpha$, $\mathbf{r}_j$ are the coordinates of the α-th nucleus and i-th electron, respectively.

Since nuclei are much heavier than electrons ($m_\alpha \gg m_i$), the electrons travel faster than the nuclei. From the point of view of an electron, we can define nuclei as fixed points while the electrons are moving. Therefore, the approximation of separating electronic and nuclear motions is known as the **Born-Oppenheimer** approximation (BOA), which allows us to write the molecular wave function (Ψ) as a product of nuclear (φ) and electronic (ψ) terms,

$$\Psi(\mathbf{R}_\alpha, \mathbf{r}_i) = \varphi(\mathbf{R}_\alpha)\psi(\mathbf{R}_\alpha; \mathbf{r}_i) \tag{1.5}$$

The BOA is based on the fact that the nuclei are far more massive than the electrons, which allows us to say that the nuclei are nearly fixed according to electronic motion. As a result, from Equation (1.3), the nuclear kinetic energy term ($\mathcal{T}_\alpha$) can be neglected, and the repulsion between nuclei ($\mathcal{V}_{\alpha\beta}$) can be considered as a constant. However, the $\mathcal{V}_{\alpha i}$ term prevents us from completely separating the Hamiltonian operator into nuclear and electronic parts; this term is significant and cannot be neglected. The later and remaining terms in Equation (1.3) compose the electronic Hamiltonian ($\mathcal{H}_{electronic}$ or simply $\mathcal{H}$) describing the motions of the electrons in the field of M nuclei (point charges), so

$$\mathcal{H} \equiv \mathcal{T}_i + \mathcal{V}_{\alpha i} + \mathcal{V}_{ij} \tag{1.6}$$

and the electronic Schrödinger equation is

$$\mathcal{H}\psi(\mathbf{R}_\alpha; \mathbf{r}_i) = \mathcal{E}(\mathbf{R}_\alpha)\psi(\mathbf{R}_\alpha; \mathbf{r}_i). \tag{1.7}$$

Here, the electronic wave function (ψ) and the electronic energy ($\mathcal{E}$) explicitly depend on the electronic coordinates $\mathbf{r}_i$ and parametrically on nuclear coordinates $\mathbf{R}_\alpha$. By parametric dependence, we mean that for different nuclei arrangements ($\mathbf{R}_\alpha$) we have a different electronic energy ($\mathcal{E}$) and wave function (ψ).

To solve the electronic problem, Equation (1.7), we fix the nuclear configuration $\mathbf{R}_\alpha$ at some value, so we can obtain a set of electronic wave functions ψ and corresponding electronic energies $\mathcal{E}$. Of course, there is an infinite number of possible nuclear configurations. If we do this for a range of different nuclei arrangement $\mathbf{R}_\alpha$, we obtain the potential energy surface along which the nuclei move. The sum of the electronic energy $\mathcal{E}$ does not include any electronic degrees of freedom. The electronic energy $\mathcal{E}(\mathbf{R}_\alpha)$ is also known as the interatomic potential as a function of the nuclear coordinates.

1.3 Interatomic Potentials

The laws of quantum mechanics control the dynamics of atoms and molecules and electrons define the bonding. The interatomic potential, $\mathcal{E}(\mathbf{R})$ in Equation (1.7), of a system of M atoms can be expanded in a many-body expansion

$$\mathcal{E}(\mathbf{R}) = \sum_a \mathcal{E}^{(1)}(\mathbf{R}_a) + \sum_{a<b} \mathcal{E}^{(2)}(\mathbf{R}_{ab}) + \sum_{a<b<c} \mathcal{E}^{(3)}(\mathbf{R}_{ab}, \mathbf{R}_{bc}, \mathbf{R}_{ac}) + \cdots \tag{1.8}$$

where

- $\mathcal{E}^{(1)}$ is the one-body term and (besides the atomic total energies which we can set

arbitrarily to zero) only arises in the case of an external field or boundary conditions (wall of a container). For simplicity, we will use the notation $\mathcal{E}(a)$.

- $\mathcal{E}^{(2)}$ is the two-body term or **pair potential**. The interaction of any pair of atoms depends only on their spacing and is not affected by the presence of other atoms. For simplicity, we will use the notation $\mathcal{E}(ab)$.

- $\mathcal{E}^{(3)}$ is the three-body term that arises when the presence of a third atom modifies the interaction of a pair of atoms. For simplicity, we will use the notation $\mathcal{E}(abc)$.

The expansion is formally exact but may be slowly converging. However, for a few systems, in particular, the ones regarded in this work, the many-body expansion converges rapidly. Therefore, four-body and higher-order terms are small in comparison with two- and three-body terms and can be neglected.[9] Two- and three-body terms can either be calculated with high accuracy via ab initio methods or they can be described by empirical potentials with parameters derived from experiments. However, for metallic systems, for example, it is well known that this many-body decomposition is not converging smoothly.[10]

The Lennard–Jones potential (LJ) is one of the most straightforward and idealized interatomic potentials commonly used in computer simulations.[11] The LJ potential describes the interactions between two neutral atoms using a relatively simple mathematical model; describing both the attractive and repulsive forces between the two atoms:

$$\mathcal{E}^{\mathrm{LJ}}(ab) = 4\varepsilon \left[\left(\frac{\sigma}{|\mathbf{R}_a - \mathbf{R}_b|} \right)^{12} - \left(\frac{\sigma}{|\mathbf{R}_a - \mathbf{R}_b|} \right)^{6} \right]. \tag{1.9}$$

Here ε is the potential well depth, and σ is the distance where the potential is equal to zero (Figure 1.1). The relationship between σ and the distance where the potential reaches a minimum; i.e., the equilibrium position of the two particles is $r_{min} = \sqrt[6]{2} \cdot \sigma$.

The short-range part of the LJ potential is repulsive when two atoms come close to each other, Equation (1.9). This repulsion follows from a polynomial distribution where the $1/r^{12}$ repulsive term was found to describe molecular

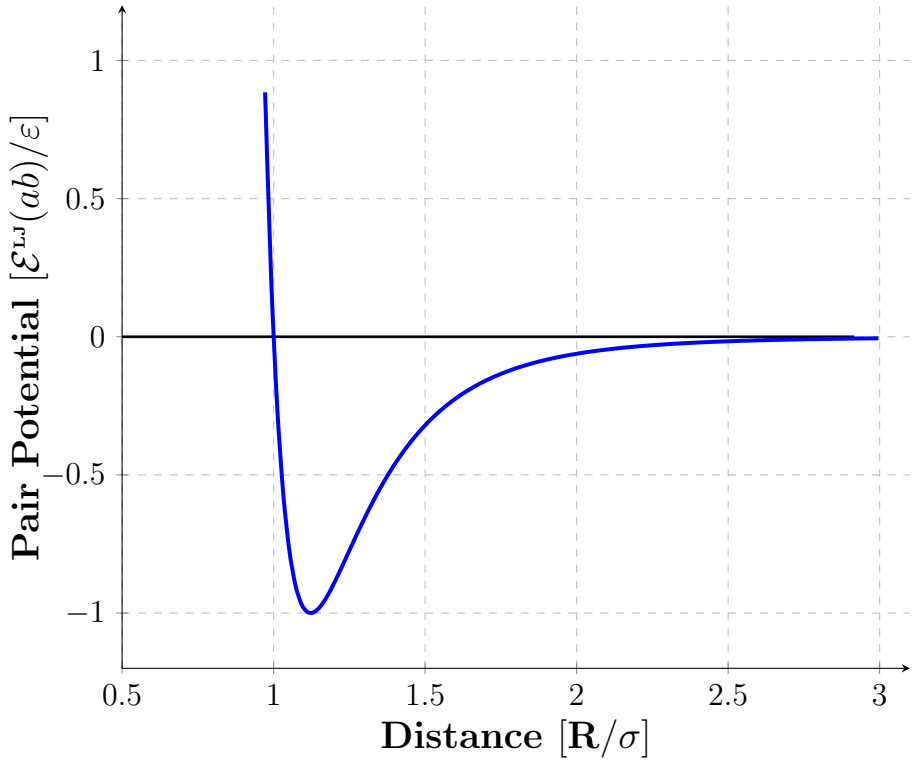

Figure 1.1: The Lennard–Jones potential approximates the intermolecular interactions between two atoms. The potential is defined in terms of the well-depth (ε) and the intercept (σ) where the potential is zero. Other formulations use the radius where the minimum occurs, i.e. the equilibrium distance.

interactions relatively accurately. This term shows that the repulsive contribution to the potential energy drops off fast as particles separate. In contrast, the long-range part is attractive and dominated by the London dispersive type $-1/r^6$ term; which correctly describes the interaction between neutral atoms at large separations.

Additionally, an extended version of the Lennard-Jones potential in terms of an inverse power expansion is known as the Extended Lennard-Jones (ELJ) potential[8,9]

$$\mathcal{E}^{\text{ELJ}}(ab) = \sum_{k=1}^{n} \frac{C_{k+5}}{|\mathbf{R}_a - \mathbf{R}_b|^{k+5}} \tag{1.10}$$

with coefficients C_{k+5} as shown Table A.1. These coefficients can be determined by fits to accurate ab initio two-body potentials computed with highly accurate quantum-chemical methods such as the relativistic coupled-cluster theory.

As simple as the Lennard-Jones potential is, unlike Hooke's law potential (harmonic oscillator), analytical solutions for the Schrödinger equation are not available. As an inverse power expansion, it has the advantage, however, of leading to analytical expressions for solid-state properties[12].

For the three-body term, the repulsive Axilrod-Teller (AT) potential is a mathematical model used to describe the interaction between three atoms. It follows from the classical triple-dipole Drude model, but can also be derived more rigorously from a quantum theoretical treatment of a dispersive type of interactions. This three-body potential takes into account the effect three atoms have on each other, rather than just the interaction between two atoms. The AT potential[13,14] is

$$\mathcal{E}^{(3)}(abc) = \varepsilon_{abc}\left[\frac{1+3\cos\theta_a\cos\theta_b\cos\theta_c}{(|\mathbf{R}_a-\mathbf{R}_b||\mathbf{R}_b-\mathbf{R}_c||\mathbf{R}_a-\mathbf{R}_c|)^3}\right] \tag{1.11}$$

where θ_a, θ_b, and θ_c are the inner angles of the triangle formed between the three atoms. Higher-order contributions like the attractive quadruple dipole term or quadrupolar terms are usually neglected for the treatment of weakly interacting systems. For three identical atoms, we have $\varepsilon_{abc} = (9/16)I\alpha^3$, where I and α are the first ionization potential and polarizability of the atom, respectively.

The LJ, ELJ, and AT models have been widely used to describe interatomic interactions for many different problems, from pure physical-mathematical applications to biochemical systems and solid-state physics. For example, the LJ potential in noble gas systems has been used to compute many physical-chemical properties, such as phase transition temperatures,[15] density,[16] pressure,[17] viscosity,[18] radial distributions,[19] etc.

1.4 The Hartree-Fock Method

The term with r_{ij} in Equation (1.7) has non-separable variables that relate to the position of pairs of electrons in the system. One can, however, for the moment

consider the simple solution for a single electron Schrödinger equation. Therefore, we define a one-electron operator $h(i)$ as follows

$$h(i) = -\frac{1}{2}\nabla_i^2 - \sum_A^M \frac{Z_A}{|\mathbf{r}_i - \mathbf{R}_A|} = \mathcal{T}_i + \mathcal{V}_i \tag{1.12}$$

The Schrödinger equation for a single electron in an external Coulomb potential can be solved analytically by the method of separation of variables

$$h(i)\phi_i(\mathbf{r}_i) = \epsilon_i\phi_i(\mathbf{r}_i) \tag{1.13}$$

where, for the i-th electron, ϕ is the one-electron wave function (orbital) and ϵ is the one-electron energy. In general, we can write the electronic Hamiltonian, Equation (1.6), as

$$\mathcal{H} = \sum_i^N h(i) + \sum_i^N \sum_{j>i}^N \frac{1}{|\mathbf{r}_i - \mathbf{r}_j|} = h + V_{\text{ee}} \tag{1.14}$$

The wave function $\psi(\mathbf{r}_1, \mathbf{r}_2, \ldots, \mathbf{r}_N)$ in Equation (1.7) of a system of N electrons can be approximated as a product of one-electron wave functions ϕ.

$$\psi^{HP}(\mathbf{r}_1, \mathbf{r}_2, \ldots, \mathbf{r}_N) = \phi(\mathbf{r}_1)\phi(\mathbf{r}_2)\ldots\phi(\mathbf{r}_N) \tag{1.15}$$

which is known as a Hartree Product (HP) and solving the Schrödinger equation for this wave function

$$\mathcal{H}\psi^{HP} = \mathcal{E}\psi^{HP} \tag{1.16}$$

gives the total energy as the sum of the one-electron energies, $\mathcal{E} = \epsilon_1 + \epsilon_2 + \cdots + \epsilon_N$. However, electronic wave functions have to be antisymmetric and the Hartree product needs to be anti-symmetrized, i.e. $\mathcal{A}\{\phi(\mathbf{r}_1)\phi(\mathbf{r}_2)\ldots\phi(\mathbf{r}_N)\}$, leading to the well known Slater determinant of one-particle functions.

In Equation (1.15), $\phi(\mathbf{r}_k)$ is the k-th space-spin wave function (*aka* orbital) of the k-th electron and the set of space-spin coordinates $\mathbf{r} = \{\mathbf{x}, \omega\}$. According to the antisymmetry principle, a wave function describing fermions should be

antisymmetric regarding the interchange of any electronic coordinates. Fermions are described using spin coordinates in addition to their three degrees of spatial freedom. Therefore, an orbital is composed of a space function $\chi(\mathbf{x})$ and a spin function, up $\alpha(\omega)$ or down $\beta(\omega)$.

$$\phi(\mathbf{x}) = \begin{cases} \chi(\mathbf{x})\alpha(\omega), & \text{up}(\uparrow) \\ \chi(\mathbf{x})\beta(\omega), & \text{down}(\downarrow) \end{cases} \tag{1.17}$$

the spatial function $\chi(\mathbf{x})$ depends only on the electron coordinates and can be written as the **Linear Combination of Atomic Orbitals** (*aka* expansion on a basis set), as

$$\chi_i(\mathbf{r}) = \sum_j^k C_{ij} g_j(\mathbf{r}) \tag{1.18}$$

where k is the number of basis functions, C_{ij} are the expansion coefficients and $g_j(\mathbf{r})$ are the j-th (atom-centered) basis (or trial) functions for the i-th electron, respectively. On the other hand, the spin orbitals $\alpha(\omega)$ and $\beta(\omega)$ satisfy the orthonormality relation

$$\begin{aligned} \int \alpha^*(\omega)\alpha(\omega)d\omega = \int \beta^*(\omega)\beta(\omega)d\omega = 1 \qquad \text{and} \\ \int \alpha^*(\omega)\beta(\omega)d\omega = \int \beta^*(\omega)\alpha(\omega)d\omega = 0 \end{aligned} \tag{1.19}$$

or using the Dirac notation,

$$\int \alpha^*(\omega)\beta(\omega)d\omega = \langle\alpha|\beta\rangle = \delta_{\alpha\beta} \qquad \text{where} \qquad \delta_{\alpha\beta} = \begin{cases} 0, & \alpha \neq \beta \\ 1, & \alpha = \beta \end{cases} \tag{1.20}$$

where $\delta_{\alpha\beta}$ is the Kronecker delta function. The spin functions are independently integrated and are orthonormal. As a result, the energy from Equation (1.16) can be written in terms of the special functions $\chi_i(\mathbf{x_j})$, or simply χ_i, as (using Dirac notation)

$$\begin{aligned}\mathcal{E} &= \langle \mathcal{A}\{\chi_1\chi_2\dots\chi_N\}|\mathcal{H}|\mathcal{A}\{\chi_1\chi_2\dots\chi_N\rangle\} \\ &= \langle \mathcal{A}\{\chi_1\chi_2\dots\chi_N\}|h + V_{\text{ee}}|\mathcal{A}\{\chi_1\chi_2\dots\chi_N\}\rangle\end{aligned} \tag{1.21}$$

where $\mathcal{A}$ indicated that we take the antisymmetrized product (Slater determinant). Although not proven here, using the variational principle one can optimize the above expression for the energy by varying the orbitals or the coefficients C_{ij} of the basis set. The resulting expression is known as the Hartree-Fock equation

$$\mathcal{F}_i|\chi_a(\mathbf{r}_i)\rangle = \epsilon_a|\chi_a(\mathbf{r}_i)\rangle \tag{1.22}$$

where $\mathcal{F}$ is the Fock operator defined as

$$\mathcal{F}_i|\chi_a(\mathbf{r}_i)\rangle = \left(h(i) + \sum_{b\neq a}^{N}\left[J_b(i) - K_b(i)\right]\right)|\chi_a(\mathbf{r}_i)\rangle \tag{1.23}$$

where $h(i)$ is the one-electron Hamiltonian, Equation (1.14), $J_b(i)$ is the Coulomb operator and $K_b(i)$ is the exchange operator. The Coulomb operator is defined as

$$J_b(i)|\chi_a(\mathbf{r}_i)\rangle = \int \frac{\chi_b^*(\mathbf{r}_j)\chi_b(\mathbf{r}_j)}{|\mathbf{r}_i - \mathbf{r}_j|}d\mathbf{r}_j|\chi_a(\mathbf{r}_i)\rangle = \langle\chi_b(\mathbf{r}_j)|\frac{1}{|\mathbf{r}_i - \mathbf{r}_j|}|\chi_b(\mathbf{r}_j)\rangle|\chi_a(\mathbf{r}_i)\rangle \tag{1.24}$$

and the exchange operator is defined as

$$K_b(i)|\chi_a(\mathbf{r}_i)\rangle = \int \frac{\chi_b^*(\mathbf{r}_j)\chi_a(\mathbf{r}_j)}{|\mathbf{r}_i - \mathbf{r}_j|}d\mathbf{r}_j|\chi_b(\mathbf{r}_i)\rangle = \langle\chi_b(\mathbf{r}_j)|\frac{1}{|\mathbf{r}_i - \mathbf{r}_j|}|\chi_a(\mathbf{r}_j)\rangle|\chi_b(\mathbf{r}_i)\rangle \tag{1.25}$$

There is a clear interpretation of the Coulomb operator. The classic Coulomb interaction within two charge units is described according to $\frac{1}{|\mathbf{r}_i - \mathbf{r}_j|}$. In the same way, electron one in χ_a experiences a one-electron potential from χ_b that is equal to the Coulomb operator in Equation (1.24). Each electron experiences a Coulomb repulsion from every other electron as the summation is over all orbitals. The exchange operator arises from the exchange and the correlation among electrons with parallel spins and lacks a classical interpretation. An exchange operator

suggests that the Hartree-Fock equation takes into account at least the correlation between electrons with parallel spins (Hartree-Fock is identical to first-order Møller-Plesset perturbation theory).

In this approach, the interactions between the electrons are replaced with an effective single-particle potential, known as the mean field, that captures the average effect of all the other electrons (an electronic cloud). This allows the many-particle system to be treated as a collection of non-interacting particles, each moving in this mean-field potential. This can greatly simplify the calculations involved in solving the Hartree-Fock equations providing satisfactory results as an initial approximation to the true behavior of the system in many cases.

However, there are still limitations when, for instance, the fluctuations or quantum mechanical correlations between the particles are not taken into account in systems with strong or weak interactions (specifically at low temperatures). The electron correlation energy ($\mathcal{E}_{corr}$) is defined as

$$\mathcal{E}_{corr} = \mathcal{E}_{exact} - \mathcal{E}_{HF} \tag{1.26}$$

where $\mathcal{E}_{exact}$ is the exact energy and $\mathcal{E}_{HF}$ the Hartree-Fock total energy. Therefore, different post-Hartree-Fock methods have been developed to include a more precise description of the electronic correlation and the electronic exchange, for example, Møller–Plesset Perturbation Theory (MP2), Configuration Interaction (CI), Multi-Reference (MR) or Coupled Cluster (CC) methods. Alternatively, one can try to improve the mean-field theory through Density Functional Theory (DFT), which will be discussed in the next section.

1.5 Density Functional Theory

In recent years, computational methods based on Density Functional Theory (DFT) have become increasingly popular because they can provide more accurate results than the Hartree-Fock approximation while requiring in general less

computational resources. DFT incorporates electron correlation effects through the use of electron density functionals, which contain terms for the kinetic energy, electron-nucleus interaction, Coulombic repulsion, and electronic exchange and correlation. This allows DFT to capture electron correlation effects within a mean-field theory that requires a lower computational cost than the more traditional wave function-based methods such as MP2 or CC methods. It is fair to say that DFT has led to a revolution in quantum chemical applications over the past 20 years for large molecules or extended systems.

From the wave function, Equation (1.17), we derive the one-particle density by integration,

$$\rho(\mathbf{r}) = N \int \cdots \int \psi^*(\mathbf{r}_1, \mathbf{r}_2, ..., \mathbf{r}_N)\psi(\mathbf{r}_1, \mathbf{r}_2, ..., \mathbf{r}_N)d\mathbf{r}_2...d\mathbf{r}_N = |\phi(\mathbf{r})|^2 \tag{1.27}$$

(ψ normalized) where N is the total number of electrons, and the integration of the density over the whole space is

$$\int \rho(\mathbf{r})d\mathbf{r} = \int |\phi(\mathbf{r})|^2 d\mathbf{r} = \langle \phi(\mathbf{r})|\phi(\mathbf{r})\rangle = N \tag{1.28}$$

Now, we can find a functional $F[\rho]$ that operates only on the one-particle density and incorporates both exchange and electron correlation effects by returning the correct total energy of the system (Hohenberg-Kohn approach). Consider briefly the electron-nucleus interaction operator V_{eN}, *aka* external potential, which can be expressed in terms of the electron density as

$$V_{\text{eN}}[\rho] = -\int \sum_A \frac{Z_A}{|\mathbf{r} - \mathbf{r_A}|}\rho(\mathbf{r})d\mathbf{r} \tag{1.29}$$

Similarly, the pure Coulomb term,

$$J[\rho] = \frac{1}{2}\int \frac{\rho(\mathbf{r})\rho(\mathbf{r}')}{|\mathbf{r} - \mathbf{r}'|}d\mathbf{r}d\mathbf{r}' \tag{1.30}$$

However, the kinetic energy and the electron exchange operator cannot be so easily expressed in terms of electron density. Nevertheless, the Hohenberg-Kohn

theorem states that a unique functional of the electron density exists returning the total energy of the system, and the Kohn-Sham approach expresses the (unknown exact) one-particle density in terms of trial functions (the Kohn-Sham orbitals). The total energy is then approximated in terms of the electron density by

$$E_{\mathrm{DFT}}[\rho] = T[\rho] + V_{\mathrm{eN}}[\rho] + J[\rho] + V_{xc}[\rho] \tag{1.31}$$

There are no explicit expressions for the kinetic energy $T[\rho]$ and the exchange-correlation $V_{xc}[\rho]$ functional in terms of the electronic density. As a result, the universal functional $F[\rho]$ is a mathematical construct whose analytical form is unknown.

Kohn and Sham proposed the first approach by constructing the unknown density from one-particle trial functions as mentioned above. As a result, the kinetic energy can be treated in the usual way,

$$E_{\mathrm{DFT}}[\rho] = -\frac{1}{2}\sum_{i}^{N}\int \phi_i(\mathbf{r})\nabla^2\phi_i(\mathbf{r})d^3\mathbf{r} + V_{xc}[\rho] + \sum_{i<j}^{N}\int\int \rho(\mathbf{r_i})\frac{1}{\mathbf{r_{ij}}}\rho(\mathbf{r_j})d\mathbf{r_i}d\mathbf{r_j} \tag{1.32}$$

where

$$\rho(\mathbf{r}) = \sum_{i}^{N}|\phi_i(\mathbf{r})|^2 \tag{1.33}$$

One of the first approximations for the exchange-correlation term was the Local Density Approximation (LDA) where the system is described as a gas of uniform electrons, then the term V_{xc} is

$$V_{xc}^{LDA}[\rho] = \int \rho(\mathbf{r})\epsilon_{xc}\rho(\mathbf{r})d\mathbf{r} \tag{1.34}$$

where ϵ_{xc} is the exchange and correlation energy per particle of an inhomogeneous electron gas of density $\rho(\mathbf{r})$. Another approximation is the General Gradient Approximation (GGA), which relies on the electron density and electron density gradient to account for inhomogeneity in the electron density. According to GGA, the term V_{xc} is

$$V_{xc}^{GGA}[\rho] = \int f\left(\rho(\mathbf{r}), \overrightarrow{\nabla}\rho(\mathbf{r})\right) d\mathbf{r} \tag{1.35}$$

Finally, the term V_{xc} using the hybrid functionals (B3LYP)

$$\begin{aligned} V_{xc}^{B3LYP}[\rho] = E_x^{LDA} + \alpha_o\left(E_x^{HF} - E_x^{LDA}\right) + \alpha_x\left(E_x^{GGA} - E_x^{LDA}\right) \\ + E_c^{LDA} + \alpha_c\left(E_c^{GGA} - E_c^{LDA}\right) \end{aligned} \tag{1.36}$$

where α are a fitting parameters, $\alpha_o = 0.20$, $\alpha_x = 0.72$, and $\alpha_c = 0.81$. Terms E_x and E_c are the exchange and correlation energies for LDA or GGA approximations, Equations (1.34) and (1.35), respectively. For the hybrid functional B3LYP, B3 is the exchange functional developed by Becke, parameterized three times, and LYP corresponds to the correlation functional of Lee, Yang and Parr.

The primary approximation in DFT is the exchange-correlation functional. It is acknowledged that this functional essentially approximates unknown physics, yet it has notably succeeded in practice.[20] DFT's accuracy may be enhanced by formulating exchange-correlation effects that account for additional quantum mechanical phenomena. A wide range of functionals of different rungs has been developed for use in DFT, which differs in the way they treat the kinetic, exchange, and correlation terms.

Perdew and Schmidt[21] proposed a hierarchical classification scheme for DFT functionals based on the rung of a ladder; a so-called "Jacob's ladder" referring to progressive levels of increasing sophistication and consequently the accuracy of the functional's exchange-correlation treatment in DFT functional development.[22–25] This extends from the basic local density approximation up through generalized gradient approximation, meta-GGA, hybrid-functional, double hybrid-functional approaches, and beyond.

Firstly, on the first rung are local exchange and correlation functionals, such as the Local Density Approximation (LDA), which only considers the electron spin

density in the functional. Secondly, gradient-corrected functionals, known as Generalized Gradient Approximations (GGAs), take into account not only the spin density but also its spatial gradients. Thirdly, hybrid functionals, such as the B3LYP functional, combine local exchange terms with the Hartree-Fock exchange. On the next rung, meta-GGAs and meta-hybrids, such as TPSS and TPSSh, include a GGA or Hartree-Fock exchange part in combination with a kinetic energy density term. Finally, the double-hybrid functionals are considered to be on a higher rung of Jacob's ladder. Double-hybrid functionals comprise a category of approximations that combines Hartree-Fock exchange energy, second-order Møller-Plesset correlation energy perturbations (see Section 1.6), and a semi-local exchange-correlation density functional.[26,27]

Corrections to the total energy can also be included to account for long-range interactions (CAM) or dispersion forces such as the Grimme dispersion correction.[28,29] In strongly correlated solid-state systems the Hubbard onsite-repulsion model is often used to improve electron localization and to prevent the incorrect prediction of the metal-to-insulator transition.[30] Furthermore, in systems with heavy atoms (see Section 1.8), the electron density has to be extended to the four-component (spinors) wave function for a correct relativistic treatment of the electrons at the Dirac level of theory.[31]

As a final remark, Density Functional Theory is based on the following fundamentals, the two theorems of Hohenberg and Kohn (sometimes regarded as being trivial):

1. A unique external potential determines a unique ground state electron density. An external potential (v_{ext}) corresponds to the ground state wave function ($\psi_o(\mathbf{r})$) as a result $\rho_o(\mathbf{r})$ refers to the electron density of the ground state. That is, for two different N-electrons systems described by two Hamiltonian operators with different external potentials, they cannot have fundamental states with the same electron density.

2. The variational principle for density functionals

$$E[\rho] = \langle \psi_o(\mathbf{r}) | \mathcal{H} | \psi_o(\mathbf{r}) \rangle \quad \leq \quad \langle \tilde{\psi}_o(\mathbf{r}) | \mathcal{H} | \tilde{\psi}_o(\mathbf{r}) \rangle = E[\tilde{\rho}(r)] \tag{1.37}$$

where $E[\rho]$, $\rho(\mathbf{r})$ and $\psi_o(\mathbf{r})$ are the exact electronic energy, density and wave function of a N-electrons system, respectively, while $E[\tilde{\rho}]$ and $\tilde{\rho}(\mathbf{r})$ correspond to the energy, density of the triad wave function $\tilde{\psi}_o(\mathbf{r})$.

1.6 Møller-Plesset Perturbation Theory

Previously, in the Hartree-Fock approximation, we showed that the electronic wave function is represented as a combination of single-particle wave functions and involves the electron-electron Coulomb repulsion term. However, the Hartree-Fock approximation only accounts for exchange effects, but not for electron correlation effects. On the other hand, Density Functional Theory (DFT) is a more accurate method that accounts for both electronic exchange and correlation effects by using a functional to represent the electron density. However, DFT still has some limitations and may not accurately capture certain types of electron correlation effects, especially for systems with strong electron correlation or for weakly interacting systems.

Møller-Plesset perturbation theory (MP) is a method for improving upon the results obtained from Hartree-Fock theory or perhaps Density Functional Theory (DFT). It is an extension of the HF method that takes into account electron correlation effects by including Rayleigh-Schrödinger perturbation terms in the energy expression. The electronic Hamiltonian in Equation (1.14) for an unperturbed electronic system is renamed as $\mathcal{H}_o$ and the equation is

$$\mathcal{H}_o |\phi_o(\mathbf{r})\rangle = \mathcal{E}_o |\phi_o(\mathbf{r})\rangle \tag{1.38}$$

Next, we introduce a perturbation using the operator $\mathcal{V}$ controlled by the coefficient λ (where $0 \leq \lambda \leq 1$), as a result the new Hamiltonian $\mathcal{H}$ representing the perturbed system is

$$\mathcal{H}|\phi_i(\mathbf{r})\rangle = \mathcal{E}_i|\phi_i(\mathbf{r})\rangle, \qquad \text{where} \qquad \mathcal{H} = \mathcal{H}_o + \lambda\mathcal{V} \tag{1.39}$$

When λ is small enough, the energy ($\mathcal{E}_i$) and wave function (ϕ_i) can be assumed to approximate the solutions of $\mathcal{H}_o$, Equation (1.38). We could use a Taylor series in λ to expand the energy of the perturbed system as

$$\mathcal{E}_i = \epsilon_i^{(0)} + \lambda\epsilon_i^{(1)} + \lambda^2\epsilon_i^{(2)} + ... \tag{1.40}$$

where $\epsilon_i^{(n)}$ corresponds to the correction to the n-order energy of the i-th state. The perturbed wave function as

$$|\phi_i\rangle = |\psi_i^{(0)}\rangle + \lambda|\psi_i^{(1)}\rangle + \lambda^2|\psi_i^{(2)}\rangle + ... \tag{1.41}$$

where $\psi_i^{(n)}$ is the correction to the n-order wave function of the i-th state and the dyadic product is

$$\sum |\psi_j^{(0)}\rangle\langle\psi_j^{(0)}| = \mathbf{1} \tag{1.42}$$

and the orthogonality condition is

$$\langle\psi_i^{(n)}|\psi_j^{(n)}\rangle = \delta_{ij} \tag{1.43}$$

The first term in both equations are the energy $\epsilon_i^{(0)} = \mathcal{E}_o$ and wave function $|\psi_i^{(0)}\rangle = |\phi_o(\mathbf{r})\rangle$ of the unperturbed system, respectively. In general,

$$\epsilon_i^{(n)} = \frac{1}{n!}\frac{\partial^n\mathcal{E}_i}{\partial\lambda^n} \qquad \text{and} \qquad \psi_i^{(n)} = \frac{1}{n!}\frac{\partial^n\psi_i}{\partial\lambda^n} \qquad \text{for} \qquad n = 1, 2, \ldots \tag{1.44}$$

Now, we are going to multiply from the left Equation (1.41) by the complex conjugate $\langle\psi_i^{(0)}|$

$$\langle\psi_i^{(0)}|\phi_i\rangle = \langle\psi_i^{(0)}|\psi_i^{(0)}\rangle + \lambda\langle\psi_i^{(0)}|\psi_i^{(1)}\rangle + \lambda^2\langle\psi_i^{(0)}|\psi_i^{(2)}\rangle + \ldots \tag{1.45}$$

and the intermediate normalization condition is

$$\langle \psi_i^{(0)} | \psi_i^{(n)} \rangle = 0 \qquad \text{for} \quad n = 1, 2, \ldots \tag{1.46}$$

to normalize

$$\langle \psi_i^{(0)} | \phi_i \rangle = 1 \tag{1.47}$$

Now, substituting Equations (1.40) and (1.41) into Equation (1.39), we obtain

$$\begin{aligned}(\mathcal{H}_o + \lambda\mathcal{V})(|\psi_i^{(0)}\rangle + \lambda|\psi_i^{(1)}\rangle + \lambda^2|\psi_i^{(2)}\rangle + \ldots) = \\ (\epsilon_i^{(0)} + \lambda\epsilon_i^{(1)} + \lambda^2\epsilon_i^{(2)} + \ldots)(|\psi_i^{(0)}\rangle + \lambda|\psi_i^{(1)}\rangle + \lambda^2|\psi_i^{(2)}\rangle + \ldots)\end{aligned} \tag{1.48}$$

splitting by each coefficient λ^n,

$$n = 0 \quad \longrightarrow \quad \mathcal{H}_o|\psi_i^{(0)}\rangle = \epsilon_i^{(0)}|\psi_i^{(0)}\rangle \tag{1.49}$$

$$\begin{aligned} n = 1 \quad \longrightarrow \quad \mathcal{H}_o|\psi_i^{(1)}\rangle + \mathcal{V}|\psi_i^{(0)}\rangle = \epsilon_i^{(0)}|\psi_i^{(1)}\rangle + \epsilon_i^{(1)}|\psi_i^{(0)}\rangle \qquad \text{or} \\ (\epsilon_i^{(0)} - \mathcal{H}_o)|\psi_i^{(1)}\rangle = (\mathcal{V} - \epsilon_i^{(1)})|\psi_i^{(0)}\rangle \end{aligned} \tag{1.50}$$

$$n = 2 \quad \longrightarrow \quad \mathcal{H}_o|\psi_i^{(2)}\rangle + \mathcal{V}|\psi_i^{(1)}\rangle = \epsilon_i^{(0)}|\psi_i^{(2)}\rangle + \epsilon_i^{(1)}|\psi_i^{(1)}\rangle + \epsilon_i^{(2)}|\psi_i^{(0)}\rangle \tag{1.51}$$

In the above equations, we multiplied from the left by $\langle \psi_i^{(0)}|$ and after some algebra using the orthogonality relation, Equation (1.46), we obtain the energies of order

$$\epsilon_i^{(0)} = \langle \psi_i^{(0)} | \hat{\mathcal{H}}_o | \psi_i^{(0)} \rangle \tag{1.52}$$

$$\epsilon_i^{(1)} = \langle \psi_i^{(0)} | \mathcal{V} | \psi_i^{(0)} \rangle \tag{1.53}$$

$$\epsilon_i^{(2)} = \langle \psi_i^{(0)} | \mathcal{V} | \psi_i^{(1)} \rangle \tag{1.54}$$

Now, multiplying Equation (1.50) by the wave function of the j-th state, $\langle \psi_j^{(0)}|$, and using the orthogonality condition, Equation (1.43), we obtain

$$(\epsilon_i^{(0)} - \epsilon_j^{(0)}) \langle \psi_j^{(0)} | \psi_i^{(1)} \rangle = \langle \psi_j^{(0)} | \mathcal{V} | \psi_i^{(0)} \rangle, \qquad \text{for } i \neq j \tag{1.55}$$

After setting $\lambda = 1$ and using Equations (1.42) and (1.55) into Equation (1.41), the first order corrected wave function is

$$\begin{aligned} |\phi_i\rangle &= |\psi_i^{(0)}\rangle + \sum_j |\psi_j^{(0)}\rangle \langle \psi_j^{(0)} | \psi_i^{(1)} \rangle \\ &= |\psi_i^{(0)}\rangle + \sum_{j \neq i} \frac{\langle \psi_i^{(0)} | \mathcal{V} | \psi_j^{(0)} \rangle}{\epsilon_i^{(0)} - \epsilon_j^{(0)}} |\psi_j^{(0)}\rangle \end{aligned} \tag{1.56}$$

Similarly, we can use Equations (1.42) and (1.55) to obtain the correction of order two to the energy in Equation (1.54)

$$\begin{aligned} \epsilon_i^{(2)} = \langle \psi_i^{(0)} | \mathcal{V} | \psi_i^{(1)} \rangle &= \sum_j \langle \psi_i^{(0)} | \mathcal{V} | \psi_j^{(0)} \rangle \langle \psi_j^{(0)} | \psi_i^{(1)} \rangle \\ &= \sum_{j \neq i} \frac{\langle \psi_i^{(0)} | \mathcal{V} | \psi_j^{(0)} \rangle \langle \psi_j^{(0)} | \mathcal{V} | \psi_i^{(0)} \rangle}{\epsilon_i^{(0)} - \epsilon_j^{(0)}} \end{aligned} \tag{1.57}$$

Then, the energy corrected to the second order is

$$\mathcal{E}_i = \epsilon_i^{(0)} + \langle \psi_i^{(0)} | \mathcal{V}_o | \psi_i^{(0)} \rangle + \sum_{j \neq i} \frac{\langle \psi_i^{(0)} | \mathcal{V} | \psi_j^{(0)} \rangle \langle \psi_j^{(0)} | \mathcal{V} | \psi_i^{(0)} \rangle}{\epsilon_i^{(0)} - \epsilon_j^{(0)}} \tag{1.58}$$

Finally, to get the second-order Møller–Plesset approximation (MP2) we must get the explicit form of the perturbation term $\mathcal{V}$. We define the unperturbed Hamiltonian, Equation (1.38), as the Hartree–Fock Hamiltonian

$$\mathcal{H}_o = \sum_i \left(h(i) + \sum_b \left[\mathcal{J}_b(i) - \mathcal{K}_b(i) \right] \right) \tag{1.59}$$

From Equation (1.39), when $\lambda = 1$ we know that $\mathcal{V} = \mathcal{H} - \mathcal{H}_o$, where $\mathcal{H}$ is the

Hamiltonian in Equation (1.14). Thus, we can write the perturbation term

$$\mathcal{V} = \mathcal{H} - \mathcal{H}_o = \sum_i \left(\sum_{j>i} \frac{1}{|\mathbf{r}_i - \mathbf{r}_j|} - \sum_{b \neq a} [\mathcal{J}_b(i) - \mathcal{K}_b(i)] \right) \tag{1.60}$$

and we can prove that the first correction to the energy is

$$\epsilon_i^{(1)} = \langle \psi_i^{(0)} | \mathcal{V} | \psi_i^{(0)} \rangle = -\frac{1}{2} \sum_{ij} \langle ij || ij \rangle \tag{1.61}$$

where the double-bar integrals, in Dirac notation, are defined as an anti-symmetrized product of the two-electron integral

$$\langle ab || cd \rangle = \int \int \psi_a^*(i) \psi_b^*(j) \frac{1}{r_{ij}} \left[\psi_r(i) \psi_s(j) - \psi_s(i) \psi_r(j) \right] d\tau_1 d\tau_2 \tag{1.62}$$

where τ denoted integration over the electron's coordinates and spin. Finally, the second-order correction to the energy is

$$\epsilon_i^{(2)} = \sum_{j \neq i} \frac{\langle \psi_i^{(0)} | \mathcal{V} | \psi_j^{(0)} \rangle \langle \psi_j^{(0)} | \mathcal{V} | \psi_i^{(0)} \rangle}{\epsilon_i^{(0)} - \epsilon_j^{(0)}} = \frac{1}{4} \sum_{ij}^{occ} \sum_{rs}^{vir} \frac{\langle ij || rs \rangle \langle rs || ij \rangle}{\epsilon_i + \epsilon_j - \epsilon_r - \epsilon_s} \tag{1.63}$$

Higher-order approximations, like MP3 or MP4, include more terms in the perturbation expansion, leading to increased accuracy at the cost of increased computational complexity. To find higher corrections to the energy and wave function, proceed similarly as illustrated for the second-order energy, Equation (1.57).

One of the main advantages of the MP2 method is that it includes a significant portion of the electron-electron interactions, making it more accurate than the HF method for predicting the electronic energy of a system. This is especially important for systems with strong electron-electron interactions, such as those found in chemistry and materials science. The MP2 method is also relatively computationally efficient compared to more accurate methods such as the coupled cluster (CC) method, making it a popular choice for calculating the electronic

energy of larger systems. Overall, the MP2 method is important because it provides a balance between accuracy and computational efficiency, making it a useful tool for predicting the electronic energy of a wide range of chemical and materials systems.

One note of caution should be added here. The Møller-Plesset expressions are series expansions and as such have a convergence radius, that is the series can even diverge. This can easily be seen from the energy expression above where the denominator in Equation (1.63) can become (close to) zero for (quasi-) degenerate occupied/unoccupied energy levels. In such cases, coupled-cluster, configuration interaction, or multi-reference methods become the preferred treatment for electron correlation.

1.7 Coupled Cluster Theory

In the last two sections, Sections 1.5 and 1.6, we showed how to describe electron correlation going beyond the Hartree-Fock (HF) approximation. Interaction among electrons has a significant impact on the electronic structure and properties of the system and is, therefore, crucial to consider when describing the electronic energy and other properties of a chemical or materials system.

In this section, we will discuss the coupled cluster (CC) method, which is one of the most accurate methods for describing electron correlation. The CC method in its CCSD(T) variant is often referred to as the "gold standard" of quantum chemistry methods. It is widely used to benchmark a wide range of properties in chemical systems, mainly from small molecules, and is a valuable tool for chemists and physicists who want to understand the behavior of highly correlated many-electron systems.

The coupled cluster wave function ψ_{CC} is derived from the Hartree-Fock wave function, Equation (1.15), by adding additional terms that account for electron

correlation effects,

$$\psi_{CC} = \mathrm{e}^{\hat{T}}\psi_{HF} \tag{1.64}$$

where T is the cluster operator given by

$$\hat{T} = \hat{T}_1 + \hat{T}_2 + \hat{T}_3 + \cdots + \hat{T}_n \tag{1.65}$$

where n is the number of electrons in the system. The operator $\mathrm{e}^{\hat{T}}$ is defined by the Taylor series expansion

$$\mathrm{e}^{\hat{T}} = 1 + \hat{T} + \frac{1}{2!}\hat{T}^2 + \frac{1}{3!}\hat{T}^3 + \cdots = \sum_{n=0}^{\infty}\frac{1}{n!}\hat{T}^n \tag{1.66}$$

As a result, from Equations (1.65) and (1.66), the explicit form of the exponential operator is

$$\begin{aligned}\mathrm{e}^{\hat{T}} = 1 + \hat{T}_1 + \left(\hat{T}_2 + \frac{1}{2}\hat{T}_1^2\right) + \left(\hat{T}_3 + \hat{T}_2\hat{T}_1 + \frac{1}{6}\hat{T}_1^3\right) \\ + \left(\hat{T}_4 + \hat{T}_3\hat{T}_1 + \frac{1}{2}\hat{T}_1^2 + \hat{T}_2\hat{T}_1^2 + \frac{1}{24}\hat{T}_1^4\right) + \cdots\end{aligned} \tag{1.67}$$

The first term generates the reference HF energy and the second all the singly excited states. The first parenthesis generates all the doubly excited states, and the second and third parenthesis generate all the triply and the quadruply excited states, respectively.

The one-particle cluster operator $\hat{T}_1$ and the two-particle cluster operator $\hat{T}_2$ are defined as

$$\hat{T}_1|\psi_o\rangle = \sum_{a>n}^{\infty}\sum_{i}^{n} t_i^a|\psi_i^a\rangle \tag{1.68}$$

$$\hat{T}_2|\psi_o\rangle = \sum_{b>a}^{\infty}\sum_{a>n}^{\infty}\sum_{j>i}^{m>n}\sum_{i}^{n} t_{ij}^{ab}|\psi_{ij}^{ab}\rangle \tag{1.69}$$

The limits of the summaries are chosen to include all possible single and double excitations without duplication of any excitation. The numerical coefficients t_i^a and

t_{ij}^{ab} are the cluster amplitudes. The singly excited state $|\psi_i^a\rangle$ with the occupied i-th spin-orbital replaced by the virtual a-th spin-orbital. The doubly excited state $|\psi_{ij}^{ab}\rangle$ with the occupied i,j-th spin-orbitals replaced by the virtual a,b-th spin-orbitals.

Using the coupled cluster wave function in Equation (1.64), the Schrödinger equation can be written as

$$\mathcal{H}\mathrm{e}^{\hat{T}}\psi_o = \mathcal{E}_{CC}\mathrm{e}^{\hat{T}}\psi_o \tag{1.70}$$

and the coupled cluster energy is given by

$$\begin{aligned}\langle\psi_o|\mathcal{H}|\mathrm{e}^{\hat{T}}\psi_o\rangle &= \mathcal{E}_{CC}\langle\psi_o|\mathrm{e}^{\hat{T}}\psi_o\rangle \\ &= \mathcal{E}_{CC}\langle\psi_o|\left(1+\hat{T}_1+\hat{T}_2+\frac{1}{2}\hat{T}_1^2+\ldots\right)\psi_o\rangle\end{aligned} \tag{1.71}$$

if we truncated the series expansion at the second order, the coupled cluster energy is given by

$$\begin{aligned}\mathcal{E}_{CC} &= \langle\psi_o|\mathcal{H}|\mathrm{e}^{\hat{T}}\psi_o\rangle \\ &= \langle\psi_o|\mathcal{H}\left(1+\hat{T}_1+\hat{T}_2+\frac{1}{2}\hat{T}_1^2\right)\psi_o\rangle \\ &= \langle\psi_o|\mathcal{H}|\psi_o\rangle + \langle\psi_o|\mathcal{H}|\hat{T}_1\psi_o\rangle + \langle\psi_o|\mathcal{H}|\hat{T}_2\psi_o\rangle + \frac{1}{2}\langle\psi_o|\mathcal{H}|\hat{T}_1^2\psi_o\rangle \\ &= \mathcal{E}_o + \sum_i^{occ}\sum_a^{vir} t_i^a\langle\psi_o|\mathcal{H}|\psi_i^a\rangle + \sum_{i>j}^{occ}\sum_{a>b}^{vir}\left(t_{ij}^{ab}+t_i^a t_j^b - t_i^b t_j^a\right)\langle\psi_o|\mathcal{H}|\psi_{ij}^{ab}\rangle\end{aligned} \tag{1.72}$$

The coupled cluster correlation of the energy is therefore determined completely by the singles and doubles amplitudes and the two-electron integrals. Similar to MP methods, the CC methods are size extensive—and the energy of the system scales with the number of electrons—[32] but not variational, where the energy of any trial wave function is not an upper bound to the exact ground state energy. As a result, we can not minimize this upper bound to approximate the true ground state energy.[33–35]

The CCSD method is when $\hat{T} = \hat{T}_1 + \hat{T}_2$ including all the single and double excited states or after inclusion of $\hat{T}_3$, the CC singles, doubles, and triples (CCSDT) method is obtained. Several approximate forms of CCSDT have been developed [36,37] where the most widely used approximation is the coupled cluster with the inclusion of single and double excitations and perturbative inclusion of triple excitations, CCSD(T). Here, the triples contribution is calculated using the same perturbation equation presented in MP4 but substitutes the CCSD-derived amplitude for the wave function in place of MP4's perturbation coefficients. Additionally, a fifth-order coupling term between single and triple excitations is incorporated into the calculation. [38]

1.8 Relativistic Effects: Dirac Equation

In previous sections, we outlined the most relevant methodologies to describe the electronic structure of molecules, including the Hartree-Fock (HF) method, the density functional theory (DFT), the second order Møller-Plesset perturbation theory (MP2), and the coupled cluster (CC) method. We also discussed the importance of including electron correlation in the description of the electronic structure of molecules.

In Figure 1.2, we show the hierarchy among three major axes of the levels of theory, including the level of electron correlation on the Hamiltonian, the size of the basis set, and the level of inclusion of the relativistic effects. Increasing the level of accuracy in any of these three axes increases the complexity and computational cost. A complete description of any atomic or molecular system requires the inclusion of all three axes up to the highest level of accuracy, reaching either the exact solution of the Schrödinger equation or the exact solution of the Dirac equation (or its extension to quantum electrodynamics, QED).

In addition to electron correlation, including relativistic effects in the description of electrons in molecular systems can provide a more accurate and

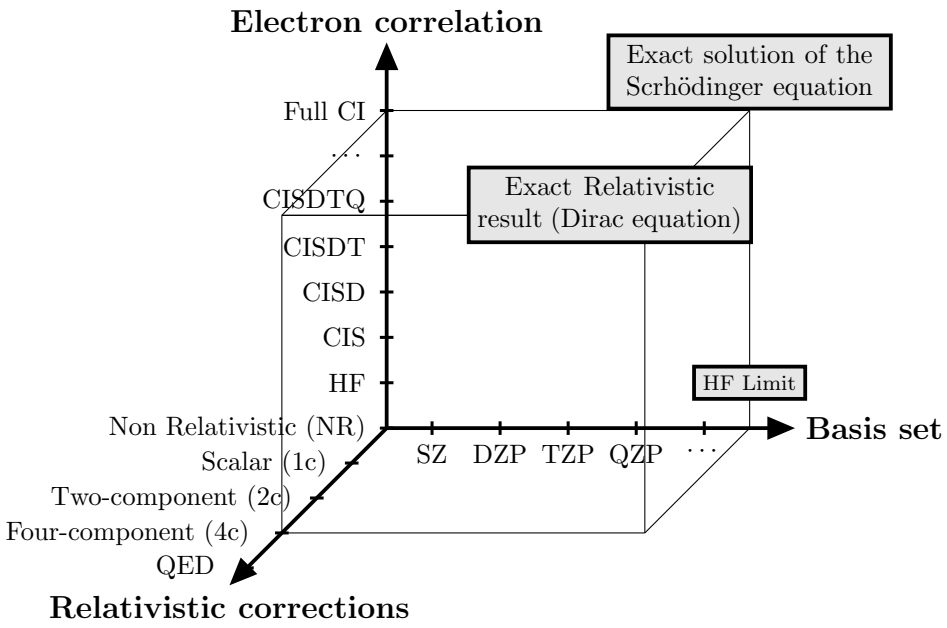

Figure 1.2: Converging the computational results by increasing the basis set, the amount of electron correlation and the description of the relativistic effects.

comprehensive understanding of the physical and chemical properties of these systems, which is important in a variety of fields, including chemistry, physics, and materials science.[39–42] Relativistic effects can alter the strength of chemical bonds, the stability of radicals, the rates of chemical reactions, the bonding and reactivity of molecules, as well as their thermodynamic and kinetic properties, especially in heavy element-containing compounds as relativistic effects scale like $\sim Z^2$.

At the beginning of this chapter, we showed that the Schrödinger equation is a mathematical equation that describes the time evolution of a quantum mechanical system. It is a linear partial differential equation that describes how the wave function of a quantum system changes over time. The Schrödinger equation is central to the study of quantum mechanics and is used to predict the behavior of quantum systems, including energy levels and corresponding wave functions for atoms, molecules, and extended systems such as the solid state. It is named after the Austrian physicist Erwin Schrödinger, who developed the equation in 1926.

The Dirac equation is a relativistic quantum mechanical wave equation that describes the behavior of spin-1/2 particles (fermions), such as electrons. The Dirac equation describes how the wave function of a spin-1/2 particle changes over

time and space, taking into account the effects of the particle's mass, spin, and electric charge. It was developed by the British physicist Paul Dirac in 1928 and can be seen as an extension of the Schrödinger equation to include the effects of special relativity (albeit both differential equations have very different mathematical features).

Similar to the Schrödinger equation, Section 1.2, in the non-relativistic regime

$$\mathcal{H}\psi(\mathbf{r}) = \mathcal{E}\psi(\mathbf{r}) \tag{1.73}$$

and taking into account that the energy-momentum relation of the theory of special relativity

$$\mathcal{E}^2 = (\mathbf{p}c)^2 + (mc^2)^2 \tag{1.74}$$

where c is the speed of light, m is the rest mass of the electron, $\mathbf{p}$ is the electron momentum, one can derive the time-independent one-electron Dirac equation from the conditions that the time derivative is of the first order and so are the space derivatives to ensure Lorentz invariance,

$$\mathcal{H}\psi(\mathbf{r}) = \left(c\sum_{n}^{3} \boldsymbol{\alpha}_n \mathbf{p}_n + \boldsymbol{\beta} mc^2 + \mathcal{V} \right) \psi(\mathbf{r}) = \mathcal{E}\psi(\mathbf{r}) \tag{1.75}$$

where $\mathcal{V}$ is the external potential due to nuclei, Section 1.2, and the operators $\boldsymbol{\alpha}$, $\boldsymbol{\beta}$ are the 4×4 Dirac matrices. It is possible to select a set of Dirac matrices that meet the appropriate anti-commutation requirements. In general, the standard set is given by

$$\boldsymbol{\beta} = \begin{pmatrix} \mathbf{1_2} & \mathbf{0_2} \\ \mathbf{0_2} & -\mathbf{1_2} \end{pmatrix} = \begin{pmatrix} 1 & 0 & 0 & 0 \\ 0 & 1 & 0 & 0 \\ 0 & 0 & -1 & 0 \\ 0 & 0 & 0 & -1 \end{pmatrix} \tag{1.76}$$

and $\boldsymbol{\alpha}_n$ matrices containing the Pauli spin-matrices are given by

$$\boldsymbol{\alpha}_1 = \begin{pmatrix} 0 & 0 & 0 & 1 \\ 0 & 0 & 1 & 0 \\ 0 & 1 & 0 & 0 \\ 1 & 0 & 0 & 0 \end{pmatrix}, \boldsymbol{\alpha}_2 = \begin{pmatrix} 0 & 0 & 0 & -i \\ 0 & 0 & i & 0 \\ 0 & -i & 0 & 0 \\ i & 0 & 0 & 0 \end{pmatrix}, \quad \boldsymbol{\alpha}_3 = \begin{pmatrix} 0 & 0 & 1 & 0 \\ 0 & 0 & 0 & -1 \\ 1 & 0 & 0 & 0 \\ 0 & -1 & 0 & 0 \end{pmatrix} \tag{1.77}$$

The Dirac's $\boldsymbol{\alpha}_n$ could be written in terms of the 2×2 Pauli's spin matrices $\boldsymbol{\sigma}_i$ as coupled differential equations. Using the Dirac equation, Equation (1.75), a peculiar prediction was made that there exists an uncountable infinite set of quantum states (continuum) in which the electron has negative energy. This strange result made it possible to predict the existence of positively charged electrons. In 1932, this prediction was verified with the discovery of the positron.

Similar to the Dirac matrices, the wave function (ψ) in Equation (1.75) must be a 4-component mathematical entity, a 4×1 column matrix

$$\psi(\mathbf{r}) = \begin{pmatrix} \phi_1(\mathbf{r}) \\ \phi_2(\mathbf{r}) \\ \phi_3(\mathbf{r}) \\ \phi_4(\mathbf{r}) \end{pmatrix} \tag{1.78}$$

where ϕ_n are known as spinor states. Analogously to the non-relativistic electronic density, Equation (1.27), the relativistic electron density or four-component (4c) density can therefore be written as

$$\psi^*(\mathbf{r})\psi(\mathbf{r}) = |\psi(\mathbf{r})|^2 = |\phi_1(\mathbf{r})|^2 + |\phi_2(\mathbf{r})|^2 + |\phi_3(\mathbf{r})|^2 + |\phi_4(\mathbf{r})|^2 \tag{1.79}$$

The wave function contains two sets of degrees of freedom, loosely speaking, one associated with positive energy (spinor ϕ_1 and ϕ_2) and one with negative energy (spinor ϕ_3 and ϕ_4). It would be useful to write them in terms of two wave functions of two components each, called large components (ϕ^L) for ϕ_1, ϕ_2 and small components

(ϕ^S) for ϕ_3, ϕ_4 as

$$\psi(\mathbf{r}) = \begin{pmatrix} \phi_1(\mathbf{r}) \\ \phi_2(\mathbf{r}) \\ \phi_3(\mathbf{r}) \\ \phi_4(\mathbf{r}) \end{pmatrix} = \begin{pmatrix} \psi^L(\mathbf{r}) \\ \psi^S(\mathbf{r}) \end{pmatrix} \tag{1.80}$$

Using the Dirac matrices, Equation (1.77) and Equation (1.76), the Dirac equation can be written as in the language of the large and small components (ψ^L and ψ^S) as

$$\begin{pmatrix} \mathcal{V} - \mathcal{E} + mc^2 & c(\boldsymbol{\sigma} \cdot \mathbf{p}) \\ c(\boldsymbol{\sigma} \cdot \mathbf{p}) & \mathcal{V} - \mathcal{E} - mc^2 \end{pmatrix} \begin{pmatrix} \psi^L(\mathbf{r}) \\ \psi^S(\mathbf{r}) \end{pmatrix} = 0 \tag{1.81}$$

The total energy ($\mathcal{E}_{tot}$) can be defined as a sum of the rest energy term (mc^2) and residual energy ($\mathcal{E}$).

$$\mathcal{E}_{tot} = mc^2 + \mathcal{E} \tag{1.82}$$

After introducing the total energy, Equation (1.82), into the Equation (1.81)

$$(\mathcal{V} - \mathcal{E}_{tot})\psi^L + c(\boldsymbol{\sigma} \cdot \mathbf{p})\psi^S = 0 \tag{1.83a}$$

$$c(\boldsymbol{\sigma} \cdot \mathbf{p})\psi^L + (\mathcal{V} - \mathcal{E}_{tot} - 2mc^2)\psi^S = 0 \tag{1.83b}$$

from Equation (1.83b), we can write the small component as

$$\psi^S = \left[2mc^2 + \mathcal{E}_{tot} - \mathcal{V}\right]^{-1} c(\boldsymbol{\sigma} \cdot \mathbf{p})\psi^L \tag{1.84}$$

after introducing this equation into Equation (1.83a) we can obtain

$$\psi^S = \frac{1}{2mc^2}\left[1 - \frac{\mathcal{V} - \mathcal{E}_{tot}}{2mc^2}\right]^{-1} c(\boldsymbol{\sigma} \cdot \mathbf{p})\psi^L \tag{1.85}$$

when the speed of light is large ($c \to \infty$) the small component becomes

$$\psi^S \approx \frac{\boldsymbol{\sigma} \cdot \mathbf{p}}{2mc}\psi^L \tag{1.86}$$

This condition is called the kinetic balance prescription and ensures that the kinetic energy is properly represented in the non-relativistic limit. This relation between the large and small components on the limit of $c \to \infty$ keeps only positive energy states discarding the negative energy states below $-2mc^2$. Equation (1.86) shows that ψ^S is by a factor of $1/c$ smaller than ψ^L, which is the reason why ψ^L is also called the large component and ψ^S the small component.

In the non-relativistic limit when $c \to \infty$ the small components vanishes, $\psi^S = 0$, and we can recover the Schrödinger equation by replacing Equation (1.86) into Equation (1.83a)

$$(\mathcal{V} - \mathcal{E}_{tot})\,\psi^L + \frac{(\boldsymbol{\sigma}\cdot\mathbf{p})(\boldsymbol{\sigma}\cdot\mathbf{p})}{2m}\psi^L = 0 \tag{1.87}$$

Using the commutation properties of the Pauli matrices where

$$(\boldsymbol{\sigma}\cdot\mathbf{u})(\boldsymbol{\sigma}\cdot\mathbf{v}) = \mathbf{u}\cdot\mathbf{v} + i\boldsymbol{\sigma}\cdot(\mathbf{u}\times\mathbf{v}) \tag{1.88}$$

we can rewrite the Equation (1.87) and recover the Schrödinger equation

$$\left(\frac{\mathbf{p}\cdot\mathbf{p}}{2m} + \mathcal{V}\right)\psi^L = \mathcal{E}_{tot}\psi^L \qquad (\mathbf{p}\times\mathbf{p} = 0) \tag{1.89}$$

where the electronic spin is included in ψ^L (two-component spinor). This proves that there is a link between the Dirac equation and the Schrödinger equation using the speed of light. In Figure 1.2, one could module the inclusion of relativistic effects by formally changing the speed of light in the Dirac equation, from a fully relativistic treatment with $c = 137.035999$ (in atomic units) to a non-relativistic treatment with $c \to \infty$.

1.8.1 Approximation to the Dirac Equation

One of the main findings of the Dirac theory is that the wave function is a four-component spinor, Equation (1.78), that represents the quantum state of a relativistic electron. The **large component** —with two spin states ϕ_1, ϕ_2— is directly connected to the probability amplitude for an electron in a state with

positive energy, while the **small component** —with two spin states ϕ_3, ϕ_4— corresponds to the probability amplitude for a positron in a state with negative energy.

In the Equation (1.80), we showed a simple approximation to reduce the Dirac wave function from four-component to large and small components. Using this regular transformation of the small components, Equations (1.84) and (1.85), we can find different approximations of the Dirac equation that are in use within the quantum chemistry community.

First, from the Equation (1.85), we can use the Taylor expansion of the term

$$\left[1 - \frac{\mathcal{V} - \mathcal{E}}{2mc^2}\right]^{-1} \approx 1 + \frac{\mathcal{V} - \mathcal{E}}{2mc^2} + \frac{(\mathcal{V} - \mathcal{E})^2}{4m^2c^4} + \cdots \tag{1.90}$$

where the series is valid for $(\mathcal{E} - \mathcal{V}) < 2mc^2$, for an electronic system where electrons are far enough to the nucleus to avoid that the potential $\mathcal{V}$ decreases exponentially when $r \to 0$.

We can substitute this expansion into the Equation (1.83a)

$$(\mathcal{V} - \mathcal{E})\psi^L + \frac{(\boldsymbol{\sigma} \cdot \mathbf{p})}{2m}\left[1 + \frac{\mathcal{V} - \mathcal{E}}{2mc^2} + \frac{(\mathcal{V} - \mathcal{E})^2}{4m^2c^4} + \cdots\right](\boldsymbol{\sigma} \cdot \mathbf{p})\psi^L + \cdots = 0 \tag{1.91}$$

to obtain

$$(\mathcal{V} - \mathcal{E})\psi^L + \frac{(\boldsymbol{\sigma} \cdot \mathbf{p})(\boldsymbol{\sigma} \cdot \mathbf{p})}{2m}\psi^L + (\boldsymbol{\sigma} \cdot \mathbf{p})\frac{\mathcal{V} - \mathcal{E}}{4m^2c^2}(\boldsymbol{\sigma} \cdot \mathbf{p})\psi^L + \cdots = 0 \tag{1.92}$$

After some algebra* and renormalization of the large components, we can obtain the Pauli Hamiltonian

$$\mathcal{H}^{Pauli} = \frac{\mathbf{p}^2}{2m} + \mathcal{V} + \frac{\mathbf{p}^4}{8m^3c^2} + \frac{\hbar^2}{8m^2c^2}(\nabla^2\mathcal{V}) + \frac{\hbar}{4m^2c^2}\boldsymbol{\sigma} \cdot (\nabla\mathcal{V}) \times \mathbf{p} \tag{1.93}$$

*using the relation $(\boldsymbol{\sigma} \cdot \mathbf{p})(\mathcal{V} - \mathcal{E})(\boldsymbol{\sigma} \cdot \mathbf{p}) = (\mathcal{V} - \mathcal{E})\mathbf{p}^2 + \hbar\left[\boldsymbol{\sigma} \cdot (\Delta\mathcal{V}) \times \mathbf{p} - i(\Delta\mathcal{V}) \cdot \mathbf{p}\right]$

where the new terms are relativistic corrections. The $\mathbf{p}^4$ is called the mass-velocity correction that comes from the variation of the electron mass on the velocity. The second relativistic term is called the Darwin correction and has no classical analog and the only important contributions come from the s functions. The last term is called the spin-orbit correction resulting from the interaction of the spin of the electron with the magnetic field generated by its orbital angular momentum around the nucleus. The spin-orbit effects, where the spin and angular momentum are combined, are classified as two-component (2c) methods, Figure 1.2. On the other hand, mass-velocity and Darwin terms are often called scalar relativistic correction methods since they do not have spin dependence (spin-free). In general, all the relativistic corrections without spin dependence are classified as one-component (1c) methods, Figure 1.2. Although the Pauli Hamiltonian is nice for interpreting relativistic effects, the operator is unbound and singular and is therefore rarely used in the relativistic community.

Additionally, we can get another approximation to the Dirac equation from a modified version of the Equation (1.84),

$$\begin{aligned}\psi^S &= \left[2mc^2 + \mathcal{E} - \mathcal{V}\right]^{-1} c(\boldsymbol{\sigma}\cdot\mathbf{p})\psi^L \\ &= \frac{1}{2mc^2}\left[1 + \frac{\mathcal{E}}{2mc^2 - \mathcal{V}}\right]^{-1} c(\boldsymbol{\sigma}\cdot\mathbf{p})\psi^L\end{aligned} \tag{1.94}$$

We can substitute this modified version into the Equation (1.83a) to obtain

$$(\mathcal{V} - \mathcal{E})\psi^L + \frac{c(\boldsymbol{\sigma}\cdot\mathbf{p})}{2mc^2 - \mathcal{V}}\left[1 + \frac{\mathcal{E}}{2mc^2 - \mathcal{V}}\right]^{-1} c(\boldsymbol{\sigma}\cdot\mathbf{p})\psi^L = 0 \tag{1.95}$$

using a Taylor expansion of the term

$$\left[1 + \frac{\mathcal{E}}{2mc^2 - \mathcal{V}}\right]^{-1} \approx 1 - \frac{\mathcal{E}}{2mc^2 - \mathcal{V}} + \frac{\mathcal{E}^2}{(2mc^2 - \mathcal{V})^2} - \cdots \tag{1.96}$$

The power series expansion now depends on the energy instead of significantly relying on the potential $\mathcal{V}$ for convergence, in contrast to the Pauli approximation, see Equation (1.90). The expansion is valid everywhere, for energies $|\mathcal{E}| < 2mc^2$, including all the electron-bound states, and free (continuum) states up to an

energy of $2mc^2$.

Similar to the Pauli approximation, we can truncate the expansion in Equation (1.96) to the zeroth order and obtain the ZORA Hamiltonian from the Equation (1.95) as

$$\begin{aligned} \mathcal{H}^{ZORA} &= \mathcal{V} + (\boldsymbol{\sigma}\cdot\mathbf{p})\left[\frac{c^2}{2mc^2-\mathcal{V}}\right](\boldsymbol{\sigma}\cdot\mathbf{p}) \\ &= \mathcal{V} + \frac{1}{2m}(\boldsymbol{\sigma}\cdot\mathbf{p})\left[1-\frac{\mathcal{V}}{2mc^2}\right]^{-1}(\boldsymbol{\sigma}\cdot\mathbf{p}) \end{aligned} \tag{1.97}$$

we can expand the inverse term to give

$$\mathcal{H}^{ZORA} = \mathcal{V} + \frac{1}{2m}(\boldsymbol{\sigma}\cdot\mathbf{p})\left[1+\frac{\mathcal{V}}{2mc^2}+\frac{\mathcal{V}^2}{(2mc^2)^2}+\cdots\right](\boldsymbol{\sigma}\cdot\mathbf{p}) \tag{1.98}$$

Note that after comparison with the Pauli equation in the Equations (1.92) and (1.93), ZORA Hamiltonian should reproduce spin-orbit coupling and only some part of the Darwin term but it will be deficient in the mass-velocity correction[†]. Therefore, the ZORA Hamiltonian reproduces partly the spin-free relativistic corrections. These examples show that when series expansions are used one can get many different relativistic equations which all have their advantages and disadvantages. One of the most widely used series expansions in this respect is the Douglas-Kroll Hamiltonian and the reader is referred to the appropriate literature[43–45].

1.8.2 Two-Component Approximation

In the previous section, we have seen that the Pauli and ZORA approximations as approximations to the Dirac equation, reducing the four-component wave function to two-component wave functions. Although these approximations are useful to decouple spin-dependent terms into one- and two-component relativistic corrections, their Hamiltonian representation depends on the energy of the system.

[†]It is because the absence of the term involving the energy, $(\boldsymbol{\sigma}\cdot\mathbf{p})(-\mathcal{E})(\boldsymbol{\sigma}\cdot\mathbf{p})$, in the Equation (1.92), which gives rise to the mass-velocity correction and part of the Darwin term.

The obvious next step is to obtain an energy-independent Hamiltonian.

We can start by defining an energy-independent operator to generalize the connection between the large and small components of the Dirac equation, Equations (1.84) and (1.85). We seek for a transformation $\mathbf{U}$ that changes the four-component into a two-component wave equation, Equation (1.80), so

$$\mathbf{U}\begin{pmatrix}\psi^L(\mathbf{r})\\ \psi^S(\mathbf{r})\end{pmatrix} = \begin{pmatrix}\psi^{2c}(\mathbf{r})\\ 0\end{pmatrix} \tag{1.99}$$

where $\psi^{2c}(\mathbf{r})$ shows that after the transformation only the transformed large components are left. Considering one-electron Dirac Hamiltonian, Equation (1.81),

$$\mathcal{H} = \begin{pmatrix}\mathbf{h}_{LL} & \mathbf{h}_{LS}\\ \mathbf{h}_{SL} & \mathbf{h}_{SS}\end{pmatrix} \tag{1.100}$$

which contain off-diagonal terms that couple the large and the small components of the wave function. We can formally define an energy-independent unitary transformation $\mathbf{U}$ to decouple these terms, so

$$\mathbf{U}\mathcal{H}\mathbf{U}^\dagger = \mathbf{U}\begin{pmatrix}\mathbf{h}_{LL} & \mathbf{h}_{LS}\\ \mathbf{h}_{SL} & \mathbf{h}_{SS}\end{pmatrix}\mathbf{U}^\dagger = \begin{pmatrix}\mathbf{h}_{LL} & 0\\ 0 & \mathbf{h}_{SS}\end{pmatrix} \tag{1.101}$$

where the electronic (positive) and positronic (negative) energy states are described independently by $\mathbf{h}_L$ and $\mathbf{h}_S$, respectively. In other words, the Dirac equation, as a system of coupled equations

$$\begin{aligned}\mathbf{h}_{LL}\psi^L + \mathbf{h}_{LS}\psi^S &= \mathcal{E}\psi^L\\ \mathbf{h}_{SL}\psi^L + \mathbf{h}_{SS}\psi^S &= \mathcal{E}\psi^S\end{aligned} \tag{1.102}$$

To achieve this, we introduce the operator $\mathbf{X}$, a generalization of the connection between large and small components as

$$\psi^S = \mathbf{X}\psi^L \tag{1.103}$$

to eliminate ψ^S and obtain a two-component equation for the large component

only

$$\left(\mathbf{h}_{LL} + \mathbf{h}_{LS}\mathbf{X}\right)\psi^L = \mathbf{E}\psi^L \tag{1.104}$$

The unitary transformation $\mathbf{U}$ is the Foldy-Wouthuysen transformation

$$\mathbf{U} = \begin{pmatrix} \frac{1}{\sqrt{1+\mathbf{X}^\dagger\mathbf{X}}} & \frac{1}{\sqrt{1+\mathbf{X}^\dagger\mathbf{X}}}\mathbf{X}^\dagger \\ -\frac{1}{\sqrt{1+\mathbf{X}^\dagger\mathbf{X}}}\mathbf{X} & \frac{1}{\sqrt{1+\mathbf{X}^\dagger\mathbf{X}}} \end{pmatrix} \tag{1.105}$$

where the square root factors ensure normalization. We define a new operator $\mathbf{\Omega}$ as

$$\mathbf{\Omega} = \frac{1}{\sqrt{1+\mathbf{X}^\dagger\mathbf{X}}}; \qquad \mathbf{\Omega}^\dagger = \frac{1}{\sqrt{1+\mathbf{X}\mathbf{X}^\dagger}}; \tag{1.106}$$

And we can use the unitary transformation $\mathbf{U}$ in the Equation (1.99) as

$$\mathbf{U}\begin{pmatrix} \psi^L(\mathbf{r}) \\ \psi^S(\mathbf{r}) \end{pmatrix} = \begin{pmatrix} \mathbf{\Omega}\left(\psi^L + \mathbf{X}^\dagger\psi^S\right) \\ \mathbf{\Omega}^\dagger\left(\psi^S - \mathbf{X}\psi^L\right) \end{pmatrix} \tag{1.107}$$

here, we want only positive energy solutions, from Equation (1.103) the lower components are zero, $\psi^S - \mathbf{X}\psi^L = 0$ and the two component wave function is

$$\begin{aligned} \psi^{2c} &= \frac{1}{\sqrt{1+\mathbf{X}^\dagger\mathbf{X}}}\left(\psi^L + \mathbf{X}^\dagger\psi^S\right) \\ &= \frac{1}{\sqrt{1+\mathbf{X}^\dagger\mathbf{X}}}\left(\psi^L + \mathbf{X}\mathbf{X}^\dagger\psi^L\right) = \left(\sqrt{1+\mathbf{X}^\dagger\mathbf{X}}\right)\psi^L \end{aligned} \tag{1.108}$$

suggesting that ψ^{2c} can be expanded in the large component only. Similarly, we decouple the Hamiltonian in the Equation (1.100) as

$$\mathbf{h}^{2c} = \sqrt{1+\mathbf{X}^\dagger\mathbf{X}}\left(\mathbf{h}_{LL} + \mathbf{h}_{LS}\mathbf{X}\right)\sqrt{1+\mathbf{X}^\dagger\mathbf{X}} \tag{1.109}$$

In the so-called Exact Two-Component (X2C) methods, the operator $\mathbf{X}$ is constructed from Equation (1.108) as a matrix representation in a finite basis set from the solution of the full four-component wave function, only including the one-electron potential energy operator. Later, one can use this $\mathbf{X}$ to construct the unitary transformation $\mathbf{U}$, Equation (1.105), and the two-component Hamiltonian

$\mathbf{h}^{2c}$, Equation (1.109). In principle, the X2C solutions reproduce exactly the positive-energy spectrum of the parent four-component Dirac Hamiltonian.[46,47]

1.9 Statistical Mechanics for Phase Transitions

The laws of quantum mechanics do not contain thermodynamical concepts such as temperature, heat, or heat capacity, Section 1.2. However, statistical mechanics provides a connection between the microscopic behavior of particles and the macroscopic properties of materials. Macroscopic systems possess an enormous number of particles; for example, one mole consists of 6.022×10^{23} particles. A numerical solution for a system of 10^{23} particles is beyond the available computing resources both today and in the foreseeable future (even with quantum computers).

In statistical mechanics, the macroscopic properties of a system, such as pressure and temperature, are determined by averages of the behavior of its constituent particles, rather than their individual details. The fundamental concept on which this field is based is that of an ensemble, which refers to a group of systems in varying quantum states that share the same macroscopic features. By taking averages over the members of an ensemble, one can determine the thermodynamic properties of the system, such as its melting temperature or pressure. In other words, statistical mechanics considers all possible quantum states and microscopic arrangements to obtain a comprehensive understanding of a system's macroscopic behavior.

In the canonical ensemble, the number of particles (N), temperature (T), and volume (V) is constant; then, it can be shown that the ensemble average of any property ($\mathcal{O}$) is

$$\langle \mathcal{O} \rangle_{\text{NVT}} = \frac{\int d\mathbf{R}\ \mathcal{O}\ e^{-\beta \mathcal{E}(\mathbf{R})}}{\int d\mathbf{R}\ e^{-\beta \mathcal{E}(\mathbf{R})}} \approx \frac{\sum_i \mathcal{O}_i\ e^{-\beta \mathcal{E}_i(\mathbf{R})}}{\sum_i e^{-\beta \mathcal{E}_i(\mathbf{R})}} \tag{1.110}$$

where the integrals are over the configurational space $\mathbf{R} \equiv \{\mathbf{r}_i\}$, $\mathcal{O}_i$ is the value

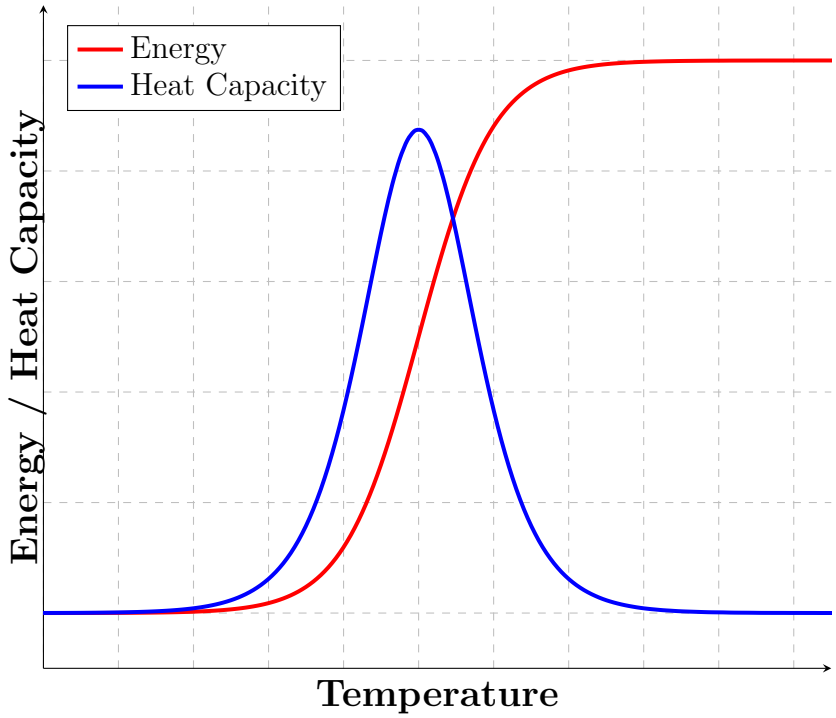

Figure 1.3: Schematic representation of a caloric curve. The heat capacity is the first derivative of the energy with respect to temperature and its maximum is the transition temperature. The height of the heat capacity pick corresponds with the latent heat is the energy absorbed or released during a phase transition.

of the operator $\mathcal{O}$ in the quantum state i, $\mathcal{E}$ is the energy, β is the inverse temperature $1/k_BT$, and the angled brackets denote an ensemble average.

Even with the help of computer simulation, we can not define accurately what a phase is. However, one can describe the thermodynamic changes that a system undergoes during a phase transition. In a macroscopic system, the increase in temperature is proportional to the absorbed energy as long as there is a single phase in the system. Then the temperature remains constant as long as the two phases coexist with each other, and the absorbed energy is only used to transform the low-temperature phase into the high-temperature phase. Once the former has disappeared, the temperature starts increasing again. A schematic plot of the energy as a function of temperature, the caloric curve, is given in Figure 1.3.

Finite-size clusters also display a solid-like phase (ordered) at low temperatures as well as a more disordered liquid-like phase upon heating. A system at thermodynamical equilibrium continually changes its configuration visiting states

of total energy $\mathcal{E}$ with the corresponding Boltzmann probability. The internal energy is precisely equivalent to the average of all these energies, Equation (1.111). It is thus sufficient to compute the temperature dependence of the average potential energy.

In Figure 1.3, when the temperature increases the system absorbs energy and its "jump" corresponds to a peak in the heat capacity. The heat capacity C_V is the derivative of the energy, the caloric curve. This allows us to define more precisely the melting point as the temperature where C_V reaches its maximum (although other criteria can be used as well).

1.10 Monte Carlo Simulations

Monte Carlo methods have been used in numerous contexts, in fields as diverse as finance and insurance, project management, manufacturing, transportation, engineering, the environment, sociology, medicine, research and development, and of course science.[48–52] This method was first used by Stanislaw Ulam, Nicholas Metropolis, and John von Neumann working on the atom bomb; it was named after Monaco resort town renowned for its casinos. A Monte Carlo simulation is a broad class of computational algorithms; it is a stochastic strategy that relies on repeated random sampling to obtain numerical results (probabilities). The essential idea is to use randomness by generating draws from a probability distribution.

The prime purpose of this type of Monte Carlo method is to compute the equilibrium properties of classical many-body systems. To simulate a transition between different states or configurations we: *i*) generate a random trial configuration; *ii*) evaluating an acceptance criterion by calculating the change in energy and other properties in the trial configuration, and *iii*) comparing the acceptance criterion to a random number and either accepting or rejecting the trial configuration.

In order to find an estimate for $\langle \mathcal{O} \rangle$ from the Equation (1.110), we formally replace the integrals by sums and construct a long sequence of randomly sampled states i to estimate the numerator and the denominator by using a sample mean integration method. As a result, in the context of a Monte Carlo simulation in the canonical ensemble, the potential energy average of the ensemble can be obtained from

$$\langle \mathcal{E} \rangle = \frac{1}{\mathcal{N}} \sum_{i}^{\mathcal{N}} \mathcal{E}_i \tag{1.111}$$

where $\mathcal{N}$ is the total number of possible states i of the system; i.e., the total of Monte Carlo cycles. Typically, each energy calculation involves a summation over all distinct pairs of molecules although other many-body interactions can be included as well (Section 1.3).

Furthermore, the method of calculating thermodynamic derivatives is ensemble-dependent. The results are summarized below, and a detailed explanation is available elsewhere.[53,54] The thermodynamic relationship for the heat capacity at constant volume is $C_V = (\partial U/\partial T)_V$, where U is the internal energy. The heat capacity is often used to gauge transition temperatures in molecular systems. Nevertheless, a more conventional approach of estimating C_V, from the average of the configurational potential energy is[55]

$$C_V(T) = \frac{1}{k_B T^2} \left[\frac{1}{\mathcal{N}} \sum_{i}^{\mathcal{N}} (\mathcal{E}_i)^2 - \left(\frac{1}{\mathcal{N}} \sum_{i}^{\mathcal{N}} \mathcal{E}_i \right)^2 \right] = \frac{\langle (\mathcal{E} - \langle \mathcal{E} \rangle)^2 \rangle}{k_B T^2} \tag{1.112}$$

where $\langle \mathcal{O}^2 \rangle - \langle \mathcal{O} \rangle^2 = \langle (\mathcal{O} - \langle \mathcal{O} \rangle)^2 \rangle$ and $\mathcal{E}_i$ is the sequence of energies accepted at temperature T during the Monte Carlo procedure. Also, we calculate its temperature derivative dC_V/dT based on the following equation:

$$\frac{dC_V}{dT} = \frac{\langle (\mathcal{E} - \langle \mathcal{E} \rangle)^3 \rangle}{k_B^2 T^4} - \frac{2 \langle (\mathcal{E} - \langle \mathcal{E} \rangle)^2 \rangle}{k_B T^3} \tag{1.113}$$

Although these equations give good predictions of thermodynamical properties,

we shall see that the histogram-derived values show a substantial reduction in uncertainty[48].

To accurately determine the properties of the system in the finite time available for a simulation, it is crucial to sample those states that make the most significant contributions, not all states will make a significant contribution. This is achieved by generating a Markov chain. A Markov chain is a sequence of trials in which the outcome of successive trials depends only on the immediate predecessor. In a Markov chain, a new state will only be accepted if it is more favorable than the existing state. The following scheme shows a general view of a single Monte Carlo cycle.

1. Select a molecule/atom at random (configuration a)
2. Calculate the total energy ($\mathcal{E}_a$)
3. Give the molecule/atom a random move (configuration b)
4. Calculate the new total energy ($\mathcal{E}_b$)
5. Accept the move from a to b with probability (Metropolis criterion)

$$\mathcal{P}(a \to b) = \min\left[1, e^{-\beta\Delta\mathcal{E}}\right] \tag{1.114}$$

   If rejected, the old configuration (a) is kept.

where min means the minimum value between one and the Boltzmann probability for the energy change $\Delta\mathcal{E} = \mathcal{E}_b - \mathcal{E}_a$.

Chapter 2

Phase transition in Atomic and Molecular Clusters

Monte Carlo simulations are a powerful tool to study the thermodynamic properties of atomic and molecular clusters, including their phase transitions. In this chapter, we present a new Fortran code for simulating phase transitions using the Parallel Tempering Monte Carlo (PTMC) method. The PTMC method is an improvement over previous methods due to its ability to efficiently explore the phase space and accurately compute the interaction energy using many-body expansion techniques such as MP2 and coupled-cluster theory for atomic and molecular clusters. We apply the PTMC method to study the melting transitions of noble gases (Ne, Ar, Kr, and Xe) and water clusters, as well as a novel study of melting transitions of neon clusters in a homogeneous ultra-high magnetic field of up to 70,500 Tesla. Our results show that the PTMC method is effective in accurately computing the inner energies and heat capacities of these clusters, providing valuable insights into their structural and dynamic behavior during melting transitions. Specifically, our novel study of neon clusters in a homogeneous ultra-high magnetic field reveals that these clusters experience elevated melting points and are squeezed in the perpendicular plane. These findings contribute to our understanding of the effects of strong magnetic fields on the melting behavior of atomic and molecular clusters and could have implications for future research in this area. This code is freely available on www.github.com/e-florez/PTMC

2.1 Introduction

In this work, we implemented the Parallel Tempering Monte Carlo code, `mPTMC`. The `mPTMC` code enables Monte Carlo simulations in the canonical ensemble, and we implemented it using Fortran 2003. Over the past 50 years, Fortran has undergone significant improvements and is now an efficient language that is well-suited for operations involving arrays and parallel algorithms. The Auckland group previously developed a Monte Carlo code for atomic systems at Auckland University, and we extended this code to include simulations of melting points for molecules.

Molecular systems, as opposed to atomic ones, pose a unique set of challenges due to their multiple degrees of freedom. While the primary focus of this work lies in investigating the thermodynamic properties of neon clusters in high magnetic fields, the inclusion of other noble gas and water clusters serves as a pivotal benchmark and an avenue for methodological validation. By using our `mPTMC` code to water clusters, we not only validate its accuracy and efficiency in capturing the behavior of molecular clusters with multiple degrees of freedom but also demonstrate its versatility across different cluster types. Water clusters, with their intricate hydrogen bonding networks and diverse structural isomers, present a unique challenge in computational simulations. Understanding the thermodynamic properties of water clusters is pivotal, however, this endeavor is beyond the scope of this work.

In the following section, we detail the development and implementation of `mPTMC` code. Secondly, we present the application and validation of this code to noble gas clusters, unraveling their thermodynamic behaviors and elucidating phase transitions. Thirdly, we pivot our focus to the realm of water clusters, employing the `mPTMC` code to validate its applicability in the landscape of hydrogen bonding and diverse structural configurations. Finally, we analyze the behavior of neon clusters under the influence of ultra-high magnetic fields, an unprecedented exploration that sheds light on the interplay between strong magnetic forces and molecular structures. Our novel study demonstrates the PTMC method's efficacy

in calculating inner energies and heat capacities, yielding crucial insights into the structural and dynamic changes during cluster melting.

2.2 Parallel Tempering Monte Carlo

The flowchart for the Parallel Tempering Monte Carlo routine is presented in Figure 2.1. As discussed in Section 1.10, the energy of a system during a Monte Carlo cycle is dependent on the temperature, and temperatures are propagated independently, defining paths of evolution for the Monte Carlo simulation. The simulation using Spherical Boundary Conditions (SBC) accommodates a maximum of 2000 atoms in `mPTMC`. Swapping configurations among neighboring trajectories, `mPTMC` calculate interaction energies as functions of temperature. Finally, an implementation of the actual n-body potentials is necessary to utilize `mPTMC` , as described in Section 1.3.

`mPTMC` requires a single input file that provides job specifications and atomic/molecular configuration. Executing

```
$ ./mPTMC YOURINPUTFILE.in
```

reads job specifications from `YOURINPUTFILE.in`. This input file should include the necessary information to run any Parallel Tempering Monte Carlo simulations and must maintain the correct extension.

2.2.1 Input dissection

We analyze the input file in two sections, describing *system-dependent* and *system-independent* settings, File 2.1.

System-Independent Settings

Line 1, number of Monte Carlo cycles: The number of Monte Carlo steps for average ensemble sampling is specified in Line 1 (`INTEGER8`). After the system

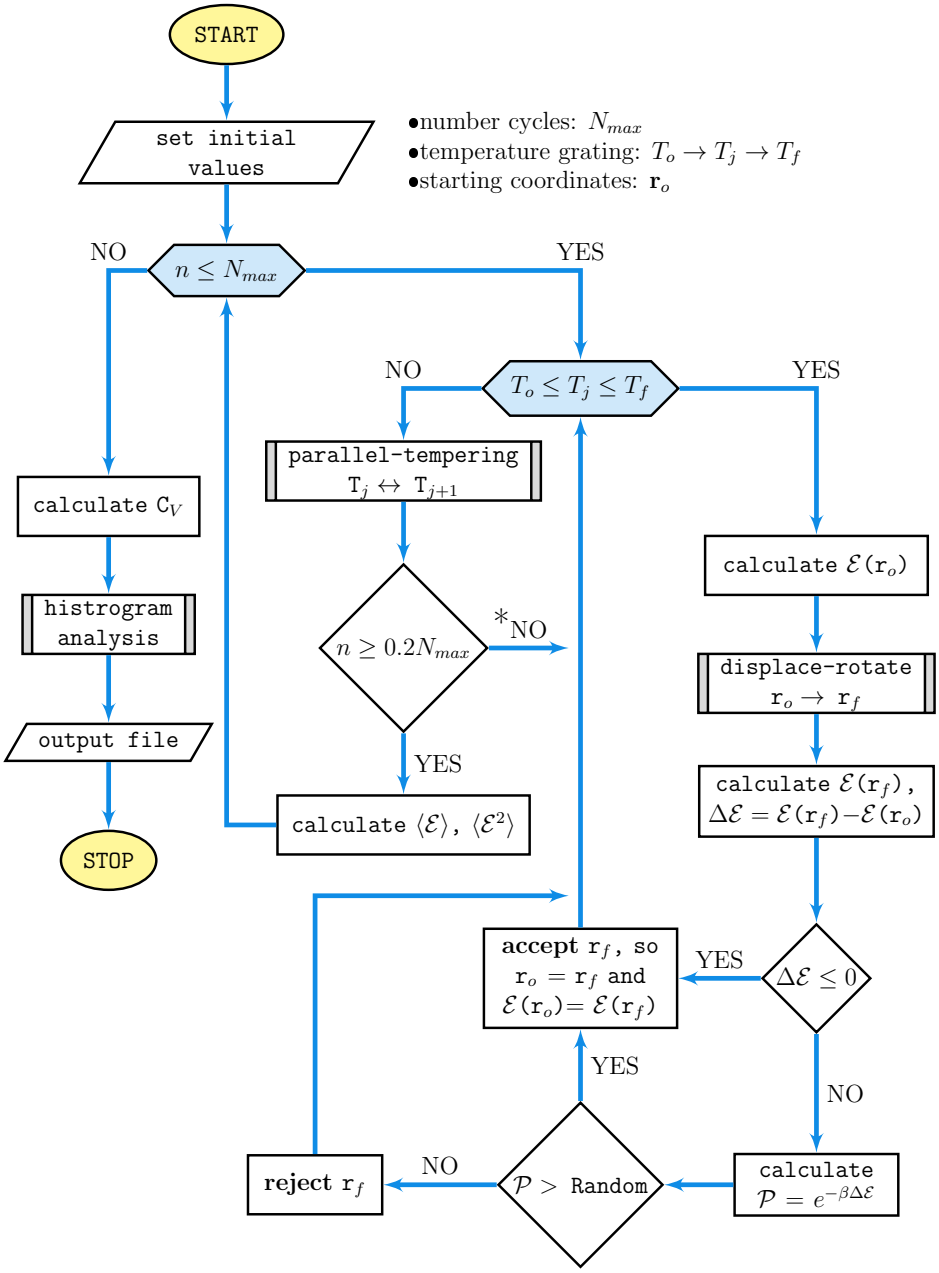

Figure 2.1: Parallel Tempering Monte Carlo flowchart. The blue shapes and the double-lined rectangles indicate counting loops and a subroutine, respectively. The computation of average quantities (*) is only performed after the equilibrium has been reached ($n \geq 0.2N_{max}$). We denote by `Random` a random number in the range [0, 1).

reaches equilibrium, averaging begins, and the total number of cycles is increased by 20% of the original number of Monte Carlo steps by default.

Line 2, temperature range and number of trajectories: The minimum (T_{min}) and maximum (T_{max}) temperatures for the simulation are specified as `REAL8` values. The third field is the number of temperatures/trajectories, n_{traj}, (`INT8`).

```
10000000
70.0 270.0 30
-1
-1
TIP4P
10.0
1.0 5.0
3
ion1              1
35    0.0000000    0.0000000    0.0000000
water1            3
8    -0.1055897    2.4520891   -0.0095455
1    -0.2270981    3.3682276    0.2397696
1    -0.3724307    1.9554441    0.7639993
water2            3
8     0.8811418   -0.8114464   -2.1422247
1     1.4310477   -0.9701245   -2.9094644
1     1.4018936   -0.2280436   -1.5902368
```

File 2.1: Example of an input file for $Br(H_2O)_2$, to run a `mPTMC` simulation.

The temperature grating for the simulation is, by default, a geometric progression. Therefore, temperature values are defined by

$$T(i) = T_{min}\left(\frac{T_{max}}{T_{min}}\right)^{\frac{i}{n_{\text{traj}}-1}} \tag{2.1}$$

where $i = 0, 1, 2, \ldots, (n_{\text{traj}} - 1)$. The geometric distribution is denser at lower temperatures compared to the arithmetic temperature distribution, as shown in Figure 2.2. For the same T_{min} and T_{max} temperatures, an arithmetic progression of equally spread temperatures is given by

$$T(i) = T_{min} + \frac{i}{n_{\text{traj}} - 1}(T_{max} - T_{min}) \tag{2.2}$$

Line 3, saving configuration: The number of configurations saved by `mPTMC` is specified as a positive `INTEGER8` value. A positive integer value indicates how often configurations are saved. However, using a small number to store several configurations will generate excessively large data files. Nevertheless, the configuration files contain a wealth of information about the phase transition.

Line 4, random seed: It is an integer (`INTEGER8`) to initialize the random number generator. Any integer value less or equal to zero means that the random seed will be based on system time.

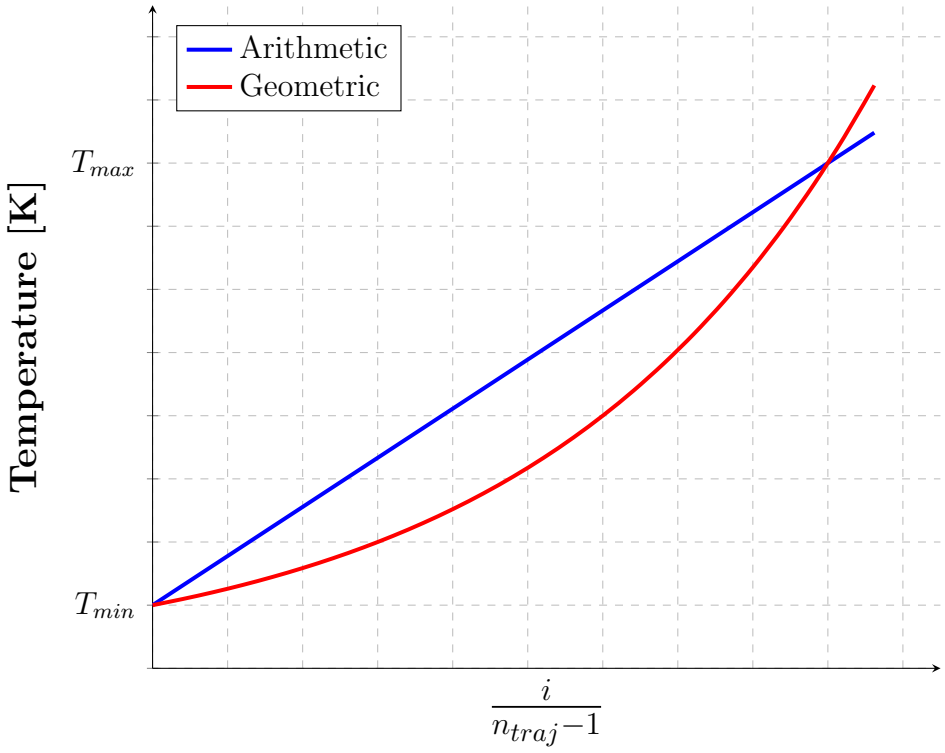

Figure 2.2: Geometric and arithmetic temperature grating schemes.

System-Dependent Settings

Line 5, two-body Potential: The two-body potential is defined as a character without embedded blanks (`CHARACTER(len=20)`). Currently, `mPTMC` includes the extended Lennard-Jones potential for the four noble gases (ELJ-Ne, ELJ-Ar, ELJ-Kr, and ELJ-Xe), as described in Section 1.3 and Appendix A.1. For water, we implemented the Transferable Intermolecular Potential (TIP3P, TIP4P, TIP4P-ice, TIP5P, and TIP6P), as detailed in Appendix A.2. Any other implementations for the two- and three-body potentials can be easily added by defining a function called `EnergyFunction` that returns the energy as a `REAL(8)` type for interatomic distances $|\mathbf{r}_a - \mathbf{r}_b|$ as input.

Line 6, sphere radius: The boundary condition for finite systems is specified as a `REAL8` value, and `mPTMC` uses Spherical Boundary Condition (SBC). Since the system evolves randomly, any movement of an atom outside the sphere (boundary condition) is rejected. SBCs are used in `mPTMC` because clusters are not stable to particle loss. If the sphere radius is too large, the evaporation of a single molecule/atom can lead to additional peaks on the heat capacity curves. On the other hand, a small radius

puts external pressure on the system, which increases the melting point.

Line 7, maximum displacement and rotation angle: Two real values are required, specified as `REAL8`. The first value corresponds to the maximum displacement in Angstroms for each center of mass on a given random motion, while the second value represents the maximum rotation in degrees of the principal axes of each molecule in a given random motion. The second field is not considered for a single atom.

Line 8, the total number of independent atoms/molecules: The total number of independent units in the system is specified as a positive `INTEGER8` value. A unit is defined as an atom or a molecule as a whole. In the case of atomic clusters, each atom must be considered an independent unit. For systems in which atoms are interacting with molecules, each atom (not part of a molecule) should be considered a unit, and each molecule should also be considered a unit.

Line 9, unit nickname and number of atoms: A character without embedded blanks (`CHARACTER(len=10)`) is used as a nickname for each unit (atom/molecule, Section 2.2.1). The second field is a positive integer (`INTEGER8`) indicating the total number of atoms in each unit.

Line 10, atomic number and Cartesian coordinates: The atomic number is specified as a positive integer (`INTEGER8`) from Hydrogen (1) to Oganesson (118). `mPTMC` can run a Monte Carlo simulation for any atom depending on the implementation of the potential energy function. The last three fields are specified as reals (`REAL8`) and represent the Cartesian coordinates (x, y, z) in Å.

The remaining lines are used to input the next molecule/atom and their Cartesian coordinates, without blank lines in between. For this specific example, **line 11** indicates the unit nickname and the number of atoms (water1 and 3, respectively), and **lines 12–14** represents the atomic number and Cartesian coordinates for one Oxygen and two Hydrogen atoms in the first water molecule, respectively. The remaining water molecules are entered in the same manner.

```
------------------------------------------------------------
Traj  T (K)     <E(T)> (kJ/mol)    Cv(T) (kJ/mol/K)
  1     70.0      -2.927478E+02        1.901182E-01
  2     75.2      -2.921061E+02        1.918446E-01
  3     80.7      -2.907020E+02        1.947924E-01
  4     86.6      -2.899388E+02        1.956457E-01
  5     93.0      -2.883251E+02        1.993989E-01
  6     99.9      -2.874375E+02        2.012598E-01
  7    107.2      -2.854636E+02        2.073695E-01
  8    115.1      -2.844192E+02        2.103462E-01
  9    123.6      -2.832991E+02        2.130148E-01
 10    132.7      -2.807932E+02        2.240865E-01
 11    142.4      -2.794164E+02        2.294507E-01
 12    152.9      -2.744829E+02        2.737941E-01
 13    164.2      -2.695909E+02        3.837099E-01
 14    176.3      -2.662145E+02        4.779797E-01
 15    189.3      -2.616999E+02        6.111249E-01
 16    203.2      -2.487103E+02        7.997212E-01
 17    218.2      -2.410640E+02        7.489722E-01
 18    234.2      -2.274456E+02        5.589124E-01
 19    251.5      -2.216274E+02        5.079860E-01
 20    270.0      -2.099786E+02        4.759778E-01
------------------------------------------------------------
 Energy Histogram Analysis within
    [  -3.055179E+02,  -1.136750E+02 ] kJ/mol
 Number of Configuration with Energy
    Below:   -3.055179E+02 kJ/mol,          0 Config
    Above:   -1.136750E+02 kJ/mol,          6 Config
 Energy Histogram Resolution:   500
------------------------------------------------------------
 Date and time: 2020-03-07, 23:59:29
 WALL time used: 0 days 2 hours 40 minutes 3.2574 seconds
```

File 2.2: Last lines of `mPTMC`'s output from a Monte Carlo simulation of $(H_2O)_8$ cluster (TIP4P) using 20 parallel tempering trajectories geometrically progressed between 70 and 270 K, and 10^6 Monte Carlo cycles.

2.2.2 Output Files

Upon completion, `mPTMC` generates several output files, including the general output file, the initial and lowest-energy configuration file, and energy histogram files.

The general output file is named after the input file, but with an `.out` extension. It contains general information about the initial conditions, lowest and highest accepted energies, count of accepted, exchanged, and out-of-boundary configurations, thermodynamic properties (e.g., heat capacity), energy histogram boundaries, and execution times for each trajectory $\tau = 1, 2 \ldots, N_{\text{bins}}$. File 2.2 contains an example of this output file.

The configuration file, containing the accepted lowest energy configuration, is generated by `mPTMC`. It is also possible to save accepted configurations periodically,

or all of them, by specifying a saving period, as explained in Section 2.2.1. In this case, they are stored in several files named `configuration_t.xyz`, where `t` indicates the temperature. By default, the XYZ format is used, which specifies the molecule geometry by providing the number of atoms with Cartesian coordinates on the first line, a comment on the second line, and the atomic number and coordinates on the following lines (atomic number, x, y, and z coordinates separated by spaces).

Energy histogram files, named `histE.t` and `histE.data`, store histogram information and are used as input files for the auxiliary programs that perform the multi-histogram analysis described in Section 2.2.5. Additionally, after every 5% of the number of sampling cycles, `mPTMC` writes status information to a file named `status_YOURINPUTFILE`.

2.2.3 Displacement and Rotation

The main concept behind `mPTMC` is to create a large number of potential solid or liquid arrangements using randomness. In atomic codes, this involves only random displacements of atoms, but in molecular codes, the relative orientation of the molecule also needs to be considered. The initial coordinates of the system of interest are used to generate these arrangements according to a Markov chain. The subroutine `displace-rotate` is then employed to randomly select an atom or molecule and displace and rotate its coordinates from r_o to r_f, as shown in Figure 2.1. When dealing with a many-body system, Jacobi coordinates are used, which involves displacing the center of mass and rotating the principal axes, as described in Jacobi and Euler-Rodrigues rotation.[56,57]

While `mPTMC` can simulate atomic, molecular, or mixed clusters, it is not necessary to rotate a single atom or calculate its center of mass (as atoms are considered points). Therefore, the following explanation will focus on molecules. The `displace-rotate` procedure involves three steps to displace and rotate an atom or molecule. Firstly, a random molecule is selected, and its center of mass is

```
1  !selecting a random molecule
2  sm=FLOOR(1+NM*Random(seed))      !NM: total number of molecules
3  !center of mass (RCM)
4  DO k=1,3                         !coordinate x(k=1),y(k=2),z(k=3)
5     !Initialization
6     TotalWeight=0.0               !Total molecular mass
7     RCM(k)=0.0
8     !Loop: Atom inside a Molecule
9     DO j=1,NA(sm)                 !NA: number of atoms
10       TotalWeight=TotalWeight+AtomicMass(Z(sm,j))
11       RCM(k)=RCM(k)+ro(sm,j,k)*AtomicMass(Z(sm,j))
12    ENDDO
13    RCM(k)=RCM(k)/TotalWeight
14 ENDDO
```

File 2.3: Simplified Fortran code visualization of the center of mass calculation for a random molecule (sm). `RCM` are the coordinates of the center of mass.

calculated using Jacobi coordinates. For a molecule containing N atoms, the center of mass is

$$\mathbf{R}_{\text{CM}} = \frac{1}{W}\sum_{k}^{N} A_k \mathbf{r}_k \tag{2.3}$$

where $W = \sum_k A_k$ is the total molecular mass; A_k is the atomic mass and $\mathbf{r}_k$ are the Cartesian coordinates for the k-th atom, respectively. In total, we have `NM` molecules and each molecule consists of `NA` atoms. File 2.3 shows a basic Fortran algorithm to compute the center of mass. The function `AtomicMass` returns the atomic mass, `REAL(8)`, for an atom with atomic number `Z` (line 10, File 2.3). `ro` is a three indices array. The first index, `sm`, specifies a molecule the set of `NM` molecules; the second, `j`, defines an atom from a system of `|`NA— atoms in the molecule; and last, `k`, defines each Cartesian component x (`k` $= 1$), y (`k` $= 2$), or z (`k` $= 3$). Line 11, File 2.3.

After calculating the center of mass, the second step is to displace it, randomly. Line 5 and Line 6 in File 2.4 show a random move of the center of mass, where `Random` is a uniform pseudo-random number generated in the range $[0, 1)$ [58] and `maxDisplace` is the maximum displacement allowed (line 7, File 2.2.1). The movement must be inside a sphere of defined radius (line 6, File 2.2.1). A displacement of $\mathbf{R}_{\text{CM}}$ is in the sphere with center (h_1, h_2, h_3) and radius r_{SBC} if and only if

$$r_{\text{SBC}}^2 > \left[(R_{\text{CM}}^{(x)} - h_1)^2 + (R_{\text{CM}}^{(y)} - h_2)^2 + (R_{\text{CM}}^{(z)} - h_3)^2\right] \tag{2.4}$$

```
1  counter=0
2  DO
3     DO k=1,3
4        Displace(k)=(2.0*Random(seed)-1.0)*maxDisplace
5        RCM(k)=RCM(k)+Displace(k)
6     ENDDO
7     r2=( (RCM(1)-h(1))**2 + (RCM(2)-h(2))**2 + (RCM(3)-h(3))**2  )
8     IF ( rsbc**2 > r2 ) THEN
9        !Exiting from the first loop
10       EXIT
11    ELSE
12       DO k=1,3
13          RCM(k)=RCM(k)-Displace(k)
14       ENDDO
15       counter=counter+1
16       IF ( counter > 100000 ) CALL ABORT
17    ENDIF
18 ENDDO
```

File 2.4: Simplified Fortran code visualization of the random displacement of a center of mass (`RCM`) inside a sphere of radius `rsbc`.

(lines 9 and 10, File 2.4). Based on the initial coordinates `ro`, `mPTMC` computes the coordinates origin (h_1, h_2, h_3). By default, to move the center of mass within the sphere, a maximum of one hundred thousand attempts can be made.

In the same fashion as the displacement of the center of mass, the rotation is also performed randomly. In line 3 File 2.5, `maxRotat` is the maximum rotation allowed for the molecular principal axes (defined in the input file, line 7 File 2.2.1). Those axes represent the position of any atom in the molecular frame of reference when the coordinates of the center of mass define the origin. The principal axes can be found by simple vectorial analysis; by definition, the principal axes are $\mathbf{r}_{pi} = \mathbf{r}_{oi} - \mathbf{R}_{\mathrm{CM}}$ $(i = 1, 2, 3)$, $\mathbf{r}_o$ are the initial coordinates, Figure 2.3A. The random displacement (`displace`), accepted for the center of mass in the Equation (2.4), is explicitly shown in line 6, File 2.5 to calculate the principal axes (`rp`).

Any orientation can be reached, starting from the reference orientation of principal axes, using a specific sequence of intrinsic rotations, whose magnitudes are the Euler angles, Figure 2.3. The Euler angles describe the orientation of a rigid molecule to a fixed internal coordinate system.

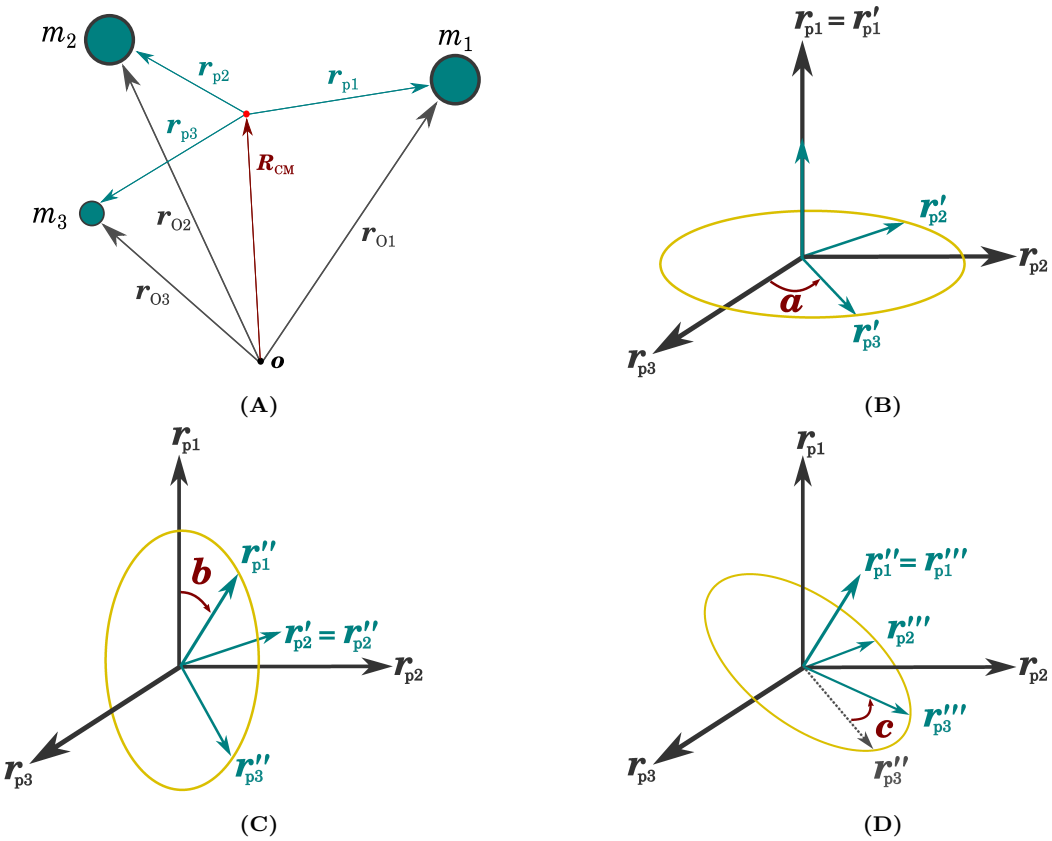

Figure 2.3: Geometrical definition of the Euler angles. A) Set of principal axes for a three-body problem; the principal axes are $\mathbf{r}_{p1}$, $\mathbf{r}_{p2}$, $\mathbf{r}_{p3}$ (blue-green), the center of mass is $\mathbf{r}_{\mathrm{CM}}$ (red), and the initial coordinates are $\mathbf{r}_{o1}$, $\mathbf{r}_{o2}$, $\mathbf{r}_{o3}$ (gray). The principal axes are shown in black, the rotating system is shown in blue-green. $_{\mathrm{CM}}$ (red), and the initial coordinates are $\mathbf{r}_{o1}$, $\mathbf{r}_{o2}$, $\mathbf{r}_{o3}$ (gray). The principal axes are shown in black, the rotating system is shown in blue-green. B) first rotation around $\mathbf{r}_{p1}$, C) second rotation around $\mathbf{r}'_{p2}$, and D) third rotation around $\mathbf{r}''_{p1}$. The rotation through the angles a and c are counterclockwise.

We can obtain the matrix representations of this transformation, and apply them sequentially as a matrix product to obtain the overall effect of the rotation. As a result, the rotation of the principal axis coordinates is as follows

1. The coordinates are rotated about the $\mathbf{r}_{p1}$ axis counterclockwise through an angle a in the range $0 \leq a < 2\pi$, onto new axes denoted by $\mathbf{r}_{p1}$, $\mathbf{r}'_{p2}$, $\mathbf{r}'_{p3}$. Figure 2.3 (a). Where the first rotation matrix is

$$\mathcal{S}_1(a) = \begin{pmatrix} \cos(a) & \sin(a) & 0 \\ -\sin(a) & \cos(a) & 0 \\ 0 & 0 & 1 \end{pmatrix} \tag{2.5}$$

causes $\mathbf{r}'_{p2}$ and $\mathbf{r}'_{p3}$ to remain in the same plane, and the $\mathbf{r}_{p1}$ ($=\mathbf{r}'_{p1}$) axis is not changed.

2. The coordinates are then rotated about the $\mathbf{r}'_{p2}$ axis clockwise through an angle b in the range $0 \leq b \leq \pi$, onto new axes denoted by $\mathbf{r}''_{p1}$, $\mathbf{r}'_{p2}$, $\mathbf{r}''_{p3}$. Figure 2.3 (b). The second rotation matrix is

$$\mathcal{S}_2(b) = \begin{pmatrix} \cos(b) & 0 & -\sin(b) \\ 0 & 1 & 0 \\ \sin(b) & b & \cos(b) \end{pmatrix}. \tag{2.6}$$

It is applied to the coordinate system as it exists after the first rotation. The $\mathbf{r}'_{p2}$ ($=\mathbf{r}''_{p2}$) axis is not changed under this rotation.

3. The third rotation is like the first, but with rotation around c. The coordinates are now rotated about the $\mathbf{r}''_{p1}$ axis counterclockwise through an angle c in the range $0 \leq c < 2\pi$, into the final axes, denoted $\mathbf{r}''_{p1}$, $\mathbf{r}'''_{p2}$, $\mathbf{r}'''_{p3}$. Figure 2.3 (c). The $\mathbf{r}''_{p1}$ ($=\mathbf{r}'''_{p1}$) axis is not changed. Finally, the third rotation matrix is

$$\mathcal{S}_3(c) = \begin{pmatrix} \cos(c) & \sin(c) & 0 \\ -\sin(c) & \cos(c) & 0 \\ 0 & 0 & 1 \end{pmatrix}. \tag{2.7}$$

Equivalently, the total rotation matrix is described by the triple matrix product

$$\mathcal{S}(a, b, c) = \mathcal{S}_1(a) \cdot \mathcal{S}_2(b) \cdot \mathcal{S}_3(c) \tag{2.8}$$

File 2.5 show a simplified Fortran code visualization of the random rotation (lines 13–15, 19–21, and 25–27). The rotated coordinates of the i-th principal axes are

$$\mathbf{r}_{pi}^{\text{rot}} = \mathcal{S} \cdot \mathbf{r}_{pi} \tag{2.9}$$

where $i = 1, 2, 3$, and $\mathbf{r}_{pi}^{\text{rot}} = \mathbf{r}'''_{pi}$ (Figure 2.3). As a result, after displacement and rotation, the final coordinates are (lines 17, 23 and 29 File 2.5)

$$\mathbf{r}_f = \mathbf{r}_{pi}^{\text{rot}} + \mathbf{R}_{\text{CM}}. \tag{2.10}$$

Finally, lines 32–42 (File 2.5) include a loop to guarantee there is no atomic

```
1  DO
2     DO k=1,3
3        !principal axes for rotation
4        DO j=1,NA(sm)
5           rp(sm,j,k)=ro(sm,j,k)+Displace(k)-RCM(k)
6        ENDDO
7        !euler rotation angles
8        Rotate(k)=(2.0*Random(seed)-1.0)*MaxRotat
9     ENDDO
10    a=Rotate(1) ; b=Rotate(2) ; c=Rotate(3) !a(k=1), b(k=2), c(k=3)
11    !Rotating principal axes
12    DO j=1,NAtoms(sm)
13       rp(sm,j,1)=rp(sm,j,1)*( COS(a)*COS(b)*COS(c) - SIN(a)*SIN(c) )+&
14                  rp(sm,j,2)*(-COS(a)*COS(b)*SIN(c) - SIN(a)*COS(c) )+&
15                  rp(sm,j,3)*( COS(a)*SIN(b)                        )
16       !Final coordinates (x, k=1) after move and rotate
17       rf(sm,j,1)=rp(sm,j,1)+RCM(1)
18
19       rp(sm,j,2)=rp(sm,j,1)*( SIN(a)*COS(b)*COS(c) + COS(a)*SIN(c) )+&
20                  rp(sm,j,2)*(-SIN(a)*COS(b)*SIN(c) + COS(a)*COS(c) )+&
21                  rp(sm,j,3)*( SIN(a)*SIN(b)                        )
22       !Final coordinates (y, k=2) after moving and rotate
23       rf(sm,j,2)=rp(sm,j,2)+RCM(2)
24
25       rp(sm,j,3)=rp(sm,j,1)*(-SIN(b)*COS(c)                        )+&
26                  rp(sm,j,2)*( SIN(b)*SIN(c)                        )+&
27                  rp(sm,j,3)*( COS(b)                               )
28       !Final coordinates (z, k=3) after moving and rotate
29       rf(sm,j,3)=rp(sm,j,3)+RCM(3)
30    ENDDO
31    Overlap=0
32    DO i=1,NM                        !loop over all molecules
33       IF ( i == sm ) CYCLE          !avoiding self-counting
34       DO jsm=1,NA(sm)               !jsm is for all atoms in sm
35          DO ji=1,NA(i)              !ji is for all atoms in i
36             d(jsm,ji,i)=( (rf(sm,jsm,1) - ro(i,ji,1))**2 + &
37                           (rf(sm,jsm,2) - ro(i,ji,2))**2 + &
38                           (rf(sm,jsm,3) - ro(i,ji,3))**2    )
39             IF( cutoff > d(jsm,ji,i) )  Overlap=Overlap+1
40          ENDDO
41       ENDDO
42    ENDDO
43    IF ( Overlap == 0 ) EXIT   !Exiting from the first loop
44 ENDDO
```

File 2.5: Simplified Fortran code visualization of the random rotation about the axes of a coordinate system; that is, rotations of principal axes (`rp`) according to the three Euler angles `a, b` and `c`.

overlapping; that is,

$$|\mathbf{r}_f - \mathbf{r}_o^{(m)}| > r_{\text{cutoff}} \tag{2.11}$$

where $\mathbf{r}_o^{(m)}$ are the coordinates for all the molecules ($\{1, 2, \ldots, m, \ldots, \texttt{NM}\}$) and r_{cutoff} is the maximum approach distance. For a point nucleus model, $r_{\text{cutoff}} = 0$ and any value larger than zero means a hard-sphere atomic radius. In terms of interaction, the pair potentials between atoms converge rapidly at distances larger than zero (`cutoff` in line 39, File 2.5).

2.2.4 Parallel Tempering

Parallel tempering, also known as replica exchange, is a procedure aimed at improving the thermodynamic behavior of the Monte Carlo method. At higher temperatures, Monte Carlo simulations can sample a phase space more efficiently than at lower temperatures. At lower temperatures, a simulation can get trapped in local regions resulting in a non-ergodic sampling of phase space. Parallel tempering improves the sampling by allowing configuration exchange. This enable that the lower temperature trajectories can "jump" between different local regions.[59]

The essence of the method consists of the following. Our Monte Carlo simulation is propagated simultaneously for several trajectories (n_{traj}), so we have n_{traj} replicas (copies of the system), each at a different temperature T_i. Then, the exchange of configurations at different neighboring temperatures is attempted and accepted based on a Metropolis criterion.

Exchanges between neighboring trajectories with temperature T_i and T_j are accepted with the probability[60]

$$\mathcal{P}(T_i \leftrightarrow T_j) = MIN\left[1, e^{(\beta_i - \beta_j)(\mathcal{E}_i - \mathcal{E}_j)}\right] \tag{2.12}$$

where β is the inverse temperature $1/k_B T$. File 2.6 shows a simplified Fortran code visualizing the parallel tempering scheme.

As a rule of thumb, an exchange is attempted 10% of the time (Equation (2.12)). The exchange is efficient when the energy histograms of neighboring temperatures overlap. Therefore, the geometric distribution of temperatures is usually taken.[61,62]

```
!probability of attempting an exchange 0.1
IF ( 0.1 > Random(seed) ) THEN
    !traj to exchange in the range [1:ntraj-1]
    ExTraj=1+FLOOR( (ntraj-1)*Random(seed) )
    !b(T)=1/kT. ! Boltzmann factor
    DB=B(ExTraj)-B(ExTraj+1)
    DE=Etot(ExTraj)-Etot(ExTraj+1)
    ExAccept=MIN( 1.0,EXP(DB*DE) )
    !is it a good exchange?
    IF ( ExAccept > Random(seed) ) THEN
       ! swap configurations; between accepted configuration (rf)
       DO i=1,NM
          DO j=1,NA(i)
             DO k=1,3
                !for r
                rex(ExTraj,i,j,k) =rf(ExTraj,i,j,k)   !temporary
                rf(ExTraj,i,j,k)  =rf(ExTraj+1,i,j,k) !rf(t)  =rf(t+1)
                rf(ExTraj+1,i,j,k)=rex(ExTraj,i,j,k)  !rf(t+1)=rex
             ENDDO
          ENDDO
       ENDDO
       !swap Energies
       Eex           =Etot(ExTraj)      !temporary
       Etot(ExTraj)  =Etot(ExTraj+1)    !E(t)  =E(t+1)
       Etot(ExTraj+1)=Eex               !E(t+1)=E_ex
    ENDIF
ENDIF
```

File 2.6: Simplified Fortran code visualization of the parallel tempering scheme. If the exchange is accepted between T_t and T_{t+1}, this procedure swaps adjacent configurations, so `rf(t)` $\leftrightarrow$ `rf(t+1)`, and energyies `Etot(t)` $\leftrightarrow$ `Etot(t+1)`.

2.2.5 Multi-Histogram Analysis

At the end of a Monte Carlo simulation, `mPTMC` computes energies and estimates average energies (Equation (1.111)) and heat capacities (Equation (1.112)) at each temperature. However, the uncertainties in the average properties measured in this way are typically large and slow to converge. To examine the physical behavior of our systems, we apply the optimal multi-histogram analysis. This technique uses the fact that the energy distribution of sampled configurations at each temperature contains a significant amount of useful information.[63]

The advantage of the multi-histogram analysis is that it uses multiple temperature measurements to estimate the density of states. This allows reliable determination of key thermodynamic properties of the system from a single Monte Carlo simulation. Using this method, we obtain results of quality similar to that of multiple runs using the more conventional variance methods, which require some predetermined knowledge of the transition temperature.[64]

Here, we provide a brief description of the method and show some

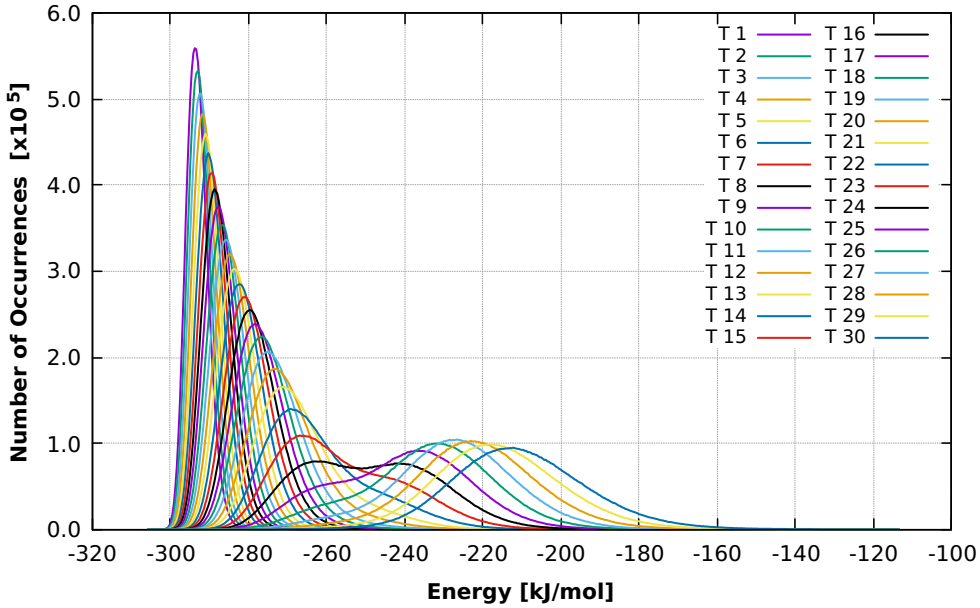

Figure 2.4: Energy histograms in dependence on the temperature for water octamer cluster $(H_2O)_8$. In the simulation, we used 30 parallel tempering trajectories that geometrically progressed between 70 and 270 K, 10^6 Monte Carlo cycles, and TIP4P.

characteristic analyses. The basic idea behind the multi-histogram technique is to store the frequency with which the system visits particular energy states in a two-dimensional histogram. This approach is a fairly straightforward adaptation of the multi-histogram approach used to solve a wide variety of problems in lattice gauge theories, chemistry, and biology, as well as statistical mechanics.[63]

We start by examining a full Monte Carlo simulation run at a set of temperatures, T_i. At each temperature T_i, a histogram of energies is created with bin widths of

$$\Delta\mathcal{E}_{\text{hist}} = \frac{\mathcal{E}_{max} - \mathcal{E}_{min}}{N_{\text{bins}}} \tag{2.13}$$

where $\mathcal{E}_{max}$ and $\mathcal{E}_{min}$ are the maximum and minimum energy values, respectively, calculated before equilibration. By default, the number of discrete energy bins is set to $N_{\text{bins}} = 500$. Thus, the energy distribution index is

$$h = \texttt{int}\left(\frac{\mathcal{E}(T_i) - \mathcal{E}_{min}}{\Delta\mathcal{E}_{\text{hist}}}\right) \tag{2.14}$$

where `int` is a function to convert any value to an integer type and $\mathcal{E}(T_i)$ is the total energy for an accepted configuration at temperature T_i (Figure 2.4). File 2.7 shows a simplified Fortran code visualization to compute the number of occurrences.

```
!h: frequency index
h=INT( (Etot(t) - Emin) / DEhist )
IF ( h >= 0 .AND. h <= Nbins ) THEN
    !counter
    hits(t,h)=hits(t,h)+1
ENDIF
```

File 2.7: Simplified Fortran code visualization to compute the energy distribution index (`h`) and the number of occurrences (`hits`). The total energy (`Etot(t)`) is calculated during the Monte Carlo cycle and after equilibration (for each trajectory `t`).

The energy histogram files created (`histE.t`, Section 2.2.2) have two columns and 500 lines. The first column is the energy distribution ($\mathcal{E}_{min} + h \times \Delta\mathcal{E}_{\text{hist}}$) and the last one is the number of occurrences (`hits`). Figure 2.4.

After collecting those energy histogram files, one can simply run a compiled version of the auxiliary program `multihist.f`* from the command line to compute some thermodynamic quantities such as $\mathcal{E}$ and C_V, based on the multi-histogram analysis.

The output files from `multihist.f` are `U.NVT`, the total internal energy; `Cv.NVT`, the heat capacity; `dCv.NVT`, the first derivative of the heat capacity to temperature; and `S`; the entropy. All the values are calculated in the canonical ensemble, for 400 temperatures T between T_{min} and T_{max}.

As illustrated in Figure 2.5, finding the temperature where C_V is a maximum (Section 1.9) is simpler with a smooth representation of C_V. Although the Equation (1.112) estimator does generally have a peak value near $T_{\text{melting}} = 200$ K – as determined by the histogram method, the solid blue line in Figure 2.5 – the extreme jagged behavior of this indicates that the variance method is not yet fully converged. Although this brief introduction captures the general spirit of the multi-histogram approach, a more detailed description to fully appreciate the methodology, as well as its implementation, can be found in Landau and Binder[48], Conrad and De Pablo[64]

*This is one of Florent's auxiliary programs to do the multi-histogram analysis.

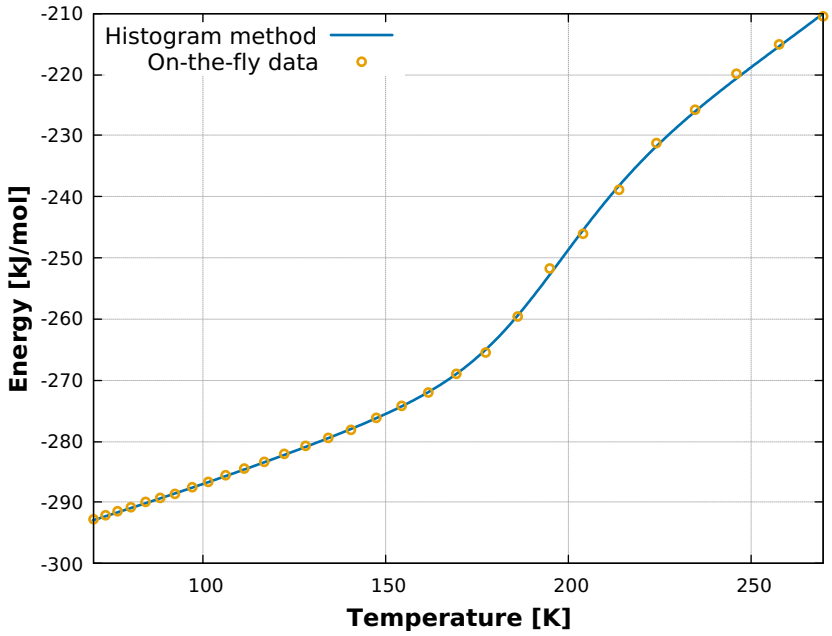

(A)

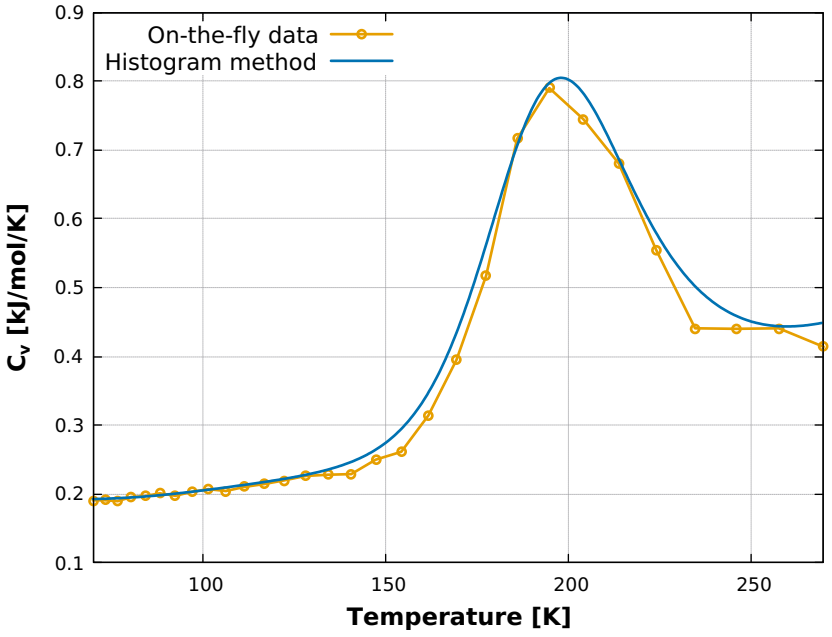

(B)

Figure 2.5: Thermal properties of the water octamer cluster $(H_2O)_8$ computed from Equations (1.111) and (1.112) (dotted yellow line), and multi-histogram method (solid blue line). A) potential energy and B) heat capacity. We used 30 parallel tempering trajectories that geometrically progressed between 70 and 270 K, and 10^6 Monte Carlo cycles.

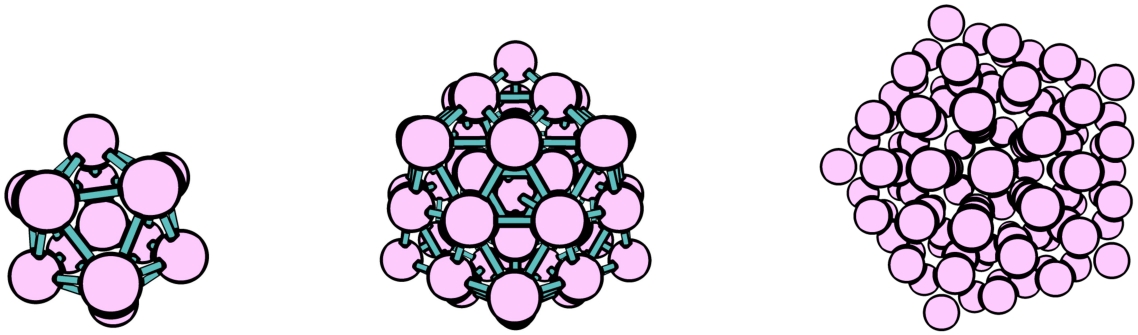

(A) (B) (C)

Figure 2.6: Geometrical shell closings, Icosahedral symmetry, for noble gas clusters according to the magic number series (Equation (2.15)). (a) $n = 13$, (b) $n = 55$, and (c) $n = 147$. Distances are not shown at scale.

2.3 Noble Gas Clusters

Noble gas (Ng) clusters show special stability at magic numbers of atoms corresponding to Mackay icosahedral structures.[65] They are characterized by S closed shells of atoms around a central atom. The number of atoms n in a Mackay structure with S shells is[66]

$$n = 1 + 2\sum_{x=1}^{S}(5x^2 + 1) = \frac{1}{3}(10S^3 + 15S^2 + 11S + 3). \tag{2.15}$$

The first magic clusters have 13, 55 and 147 atoms and are considered here. Figure 2.6 shows noble gas clusters which exhibit a geometrical shell closing (icosahedral symmetry).

In Parallel Tempering Monte Carlo simulations of noble gas clusters (Ne, Ar, Kr, and Xe), we used 2 million Monte Carlo cycles and 30 parallel trajectories in a geometrical progression between 2–40 K for Ne, 10–60 K for Ar, 30–100 K for Kr, and 60–130 K for Xe. For all cluster sizes, we used the initial structure was the global minimum of the corresponding Lennard-Jones (LJ) cluster from The Cambridge Energy Landscape Database.[67]

For spherical boundary conditions, we used

$$r_{\text{SBC}} = (S + 1) \times r_{min} \tag{2.16}$$

Table 2.1: Melting temperature (K) for the noble gas clusters (Ng_n). Experimental bulk values are 24.6, 83.8, 115.8, and 161.3 K for Ne, Ar, Kr, and Xe, respectively.

		Melting temperature		
Ng_n	n	This work	Florent's code[69]	Execution time (s)[a]
Ne	13	12.1	11.6	1535.9
	55	12.2	12.2	50 894.4
	147	15.1	14.9	672 975.3
Ar	13	40.9	38.8	1222.3
	55	41.3	40.9	50 810.6
	147	51.4	49.7	664 688.9
Kr	13	57.1	55.0	1230.5
	55	57.8	54.5	50 208.7
	147	70.3	68.4	660 764.5
Xe	13	84.3	82.2	2605.6
	55	86.3	86.9	111 015.5
	147	105.5	106.8	1 497 006.9

[a] In an Intel® Core™ i5-6200U processor, 6th Generation (3 MB cache, 2.80 GHz).

where S is the number of shells (Equation (2.15)) and r_{min} is the equilibrium distances of two-body interaction potential. The interaction potential used was the extended Lennard-Jones (ELJ) potential, Equation (1.10), with coefficients obtained from ab initio data without any experimental input whatsoever (Table A.1). The others parameters were taken as shown in File 2.1.

Our results for the melting temperature of noble gas clusters are presented in Table 2.1. We have plotted the melting curves or heat capacities for the clusters Ne_n, Ar_n, Kr_n, and Xe_n, where n is equal to 13, 55, and 147, as a function of temperature in Figures 2.7 and 2.8. These curves exhibit a single peak for all noble gas clusters, and the heat capacity curves of small clusters show a peak at the melting temperature. The finite width of the heat capacity curve is due to the finite number of atoms in the cluster. As the cluster size increases, the melting peaks become sharper, and one approaches a discontinuity in the internal energy and a delta function in heat capacity, which would be the case for an infinite system.[68]

We observed that due to the cluster's finite size, a significant fraction of

molecules tends to be present at the surface of the lattice rather than in the bulk. This leads to forces experienced by surface molecules being quite different from those experienced by molecules in the bulk. As a result, the melting points found are lower than the bulk melting temperature. In previous studies, Pahl et al.[69] and Labastie and Whetten[70] also observed well-defined single peaks in the heat capacity, which became higher, more intense, and narrower as the cluster size increased (Figures 2.7 and 2.8).

In Figures 2.7 and 2.8, the sharp peaks of the heat capacity curves result from both atomic re-arrangements and configurational energy fluctuations within two nearby thermodynamic regions, where the cluster is either entirely liquid- or entirely solid-like. The multi-histogram results suggested that the coexistence of both phases can be described as a situation in which the system fluctuates between being entirely liquid- or entirely solid-like at the melting transition. The entropy of melting also has a discontinuity at the transition temperature, indicating that the internal configuration mechanism of each cluster involves diffusive atomic motion at the surface, and depends on bond stiffness and structural order. As the temperature increases across the transition region, the number of solid-like configurations gradually decreases in favor of the liquid-like structure. In contrast, the phase transition of bulk systems contains both phases at the same time.[70]

Our study determined the melting temperature of noble gas clusters, and the results are presented in Table 2.1. We found that our melting temperature calculations are in agreement with those previously reported by Florent Calvo's original PTMC code and other studies.[69,70] The melting temperatures have a small uncertainty of approximately 2 K, and our results were consistent with each other. Additionally, we observed that our methodology had an advantage in terms of execution time compared to Florent's code. Specifically, our code demonstrated a reduction in computer time of up to 6%, 11%, and 17% for $n = 13$, $n = 55$, and $n = 147$, respectively (Table 2.1).

This successful application demonstrates the reliability and capability of our

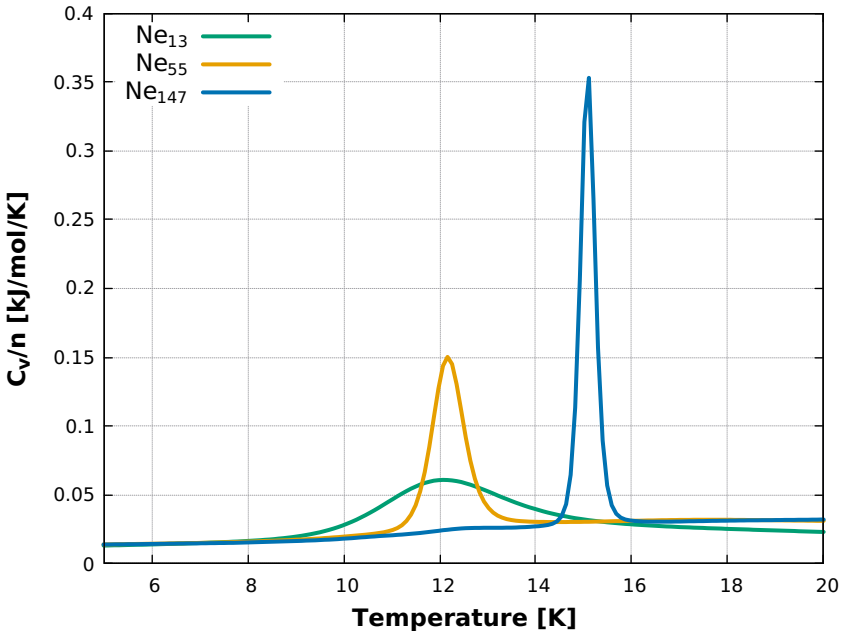

(A)

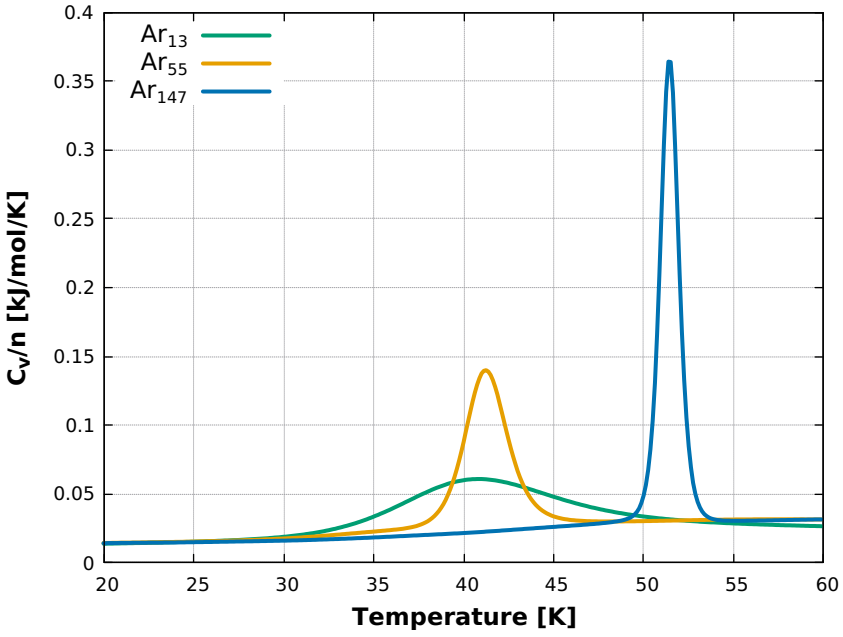

(B)

Figure 2.7: Heat capacities for noble gas clusters (C_V/n), where $n = 13, 55$, and 147. A) Ne_n and B) Ar_n. All the curves are normalized by the total number, n, of atoms in the cluster.

parallel tempering Monte Carlo code in simulating the phase transition of atomic clusters and expanding our study to the first applications of molecular systems. Our next section will describe the initial results for small water clusters.

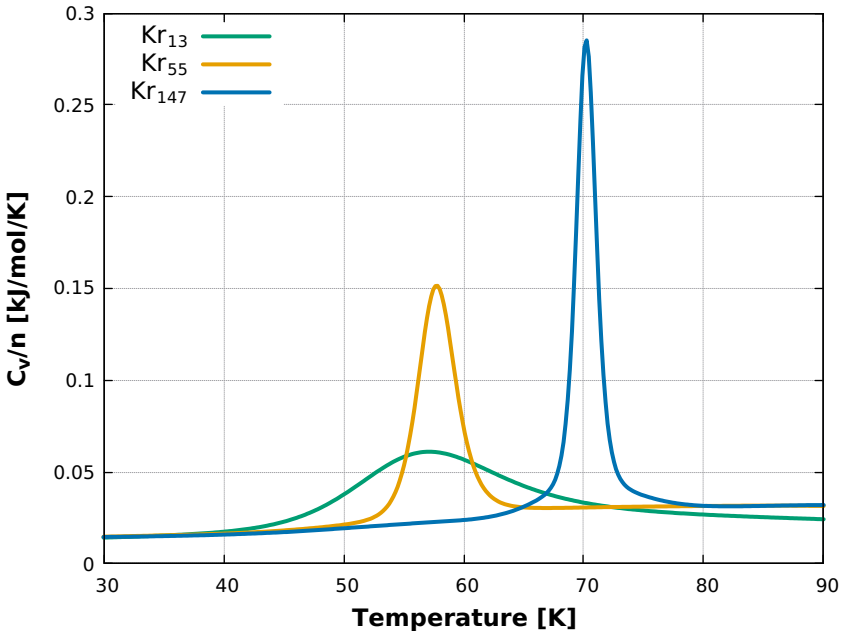

(A)

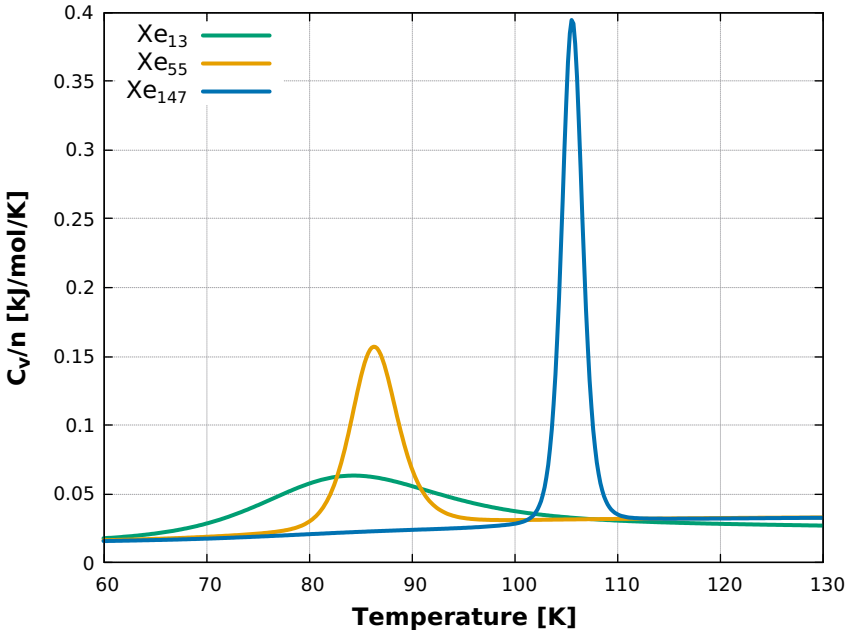

(B)

Figure 2.8: Heat capacities for noble gas clusters (C_V/n), where $n = 13, 55$, and 147. A) Kr_n and B) Xe_n. All the curves are normalized by the total number, n, of atoms in the cluster.

2.4 Small Water Clusters

We conducted simulations on water clusters, specifically $(H_2O)_n$ clusters with a cluster size of $n = 8$ and 12. We used the Transferable Intermolecular Potentials (TIPxP), where x takes values 3, 4, 5, and 6, as well as TIP4P-ice potentials, as described in Appendix A.2. Similar to our previous simulations on noble gas clusters, each water cluster was confined in a boundary sphere with a radius of 10

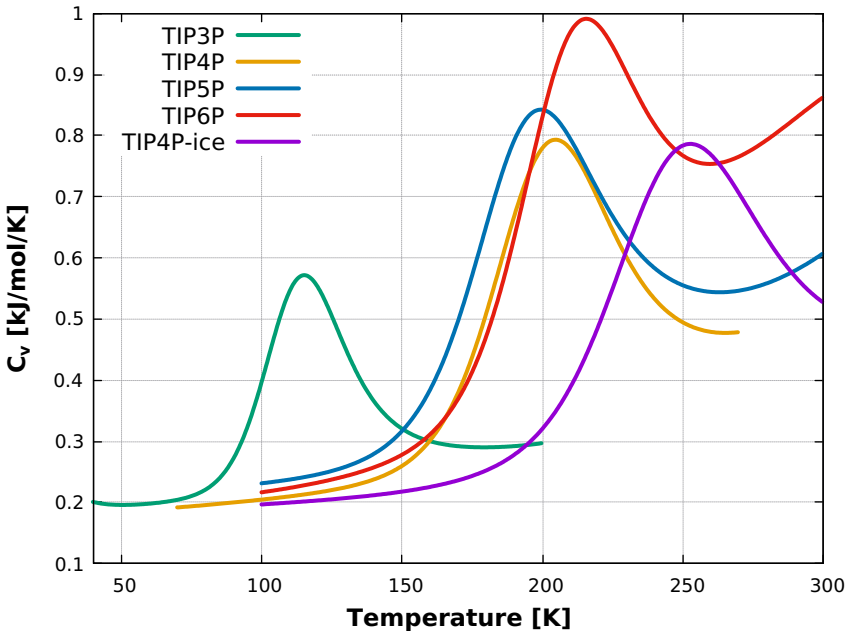

(A)

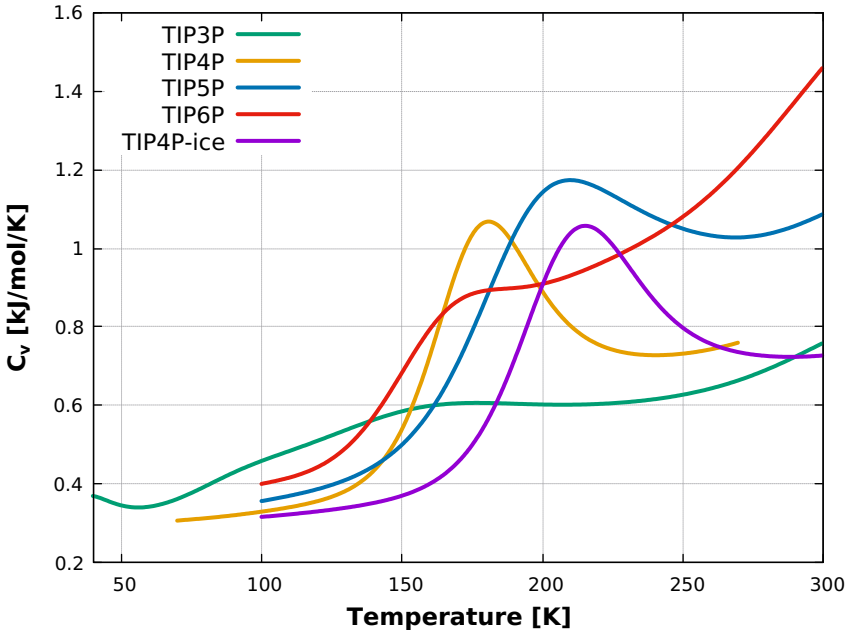

(B)

Figure 2.9: Heat capacities for A) water octamer, $(H_2O)_8$ and B) water dodecamer, $(H_2O)_{12}$.

and 12 Å for $n = 8$ and 12, respectively. We performed 10^6 Monte Carlo cycles and an additional 20% steps for equilibration and ran 30 parallel tempering trajectories that progressed geometrically between 40 and 300 K for TIP3P, 70–270 K for TIP4P, and 100–300 K for TIP5P, TIP6P, and TIP4P-ice. We obtained the initial coordinates for the water molecules in the clusters from the Cambridge Cluster Database,[71] which provides the global minima of these clusters at 0 K.

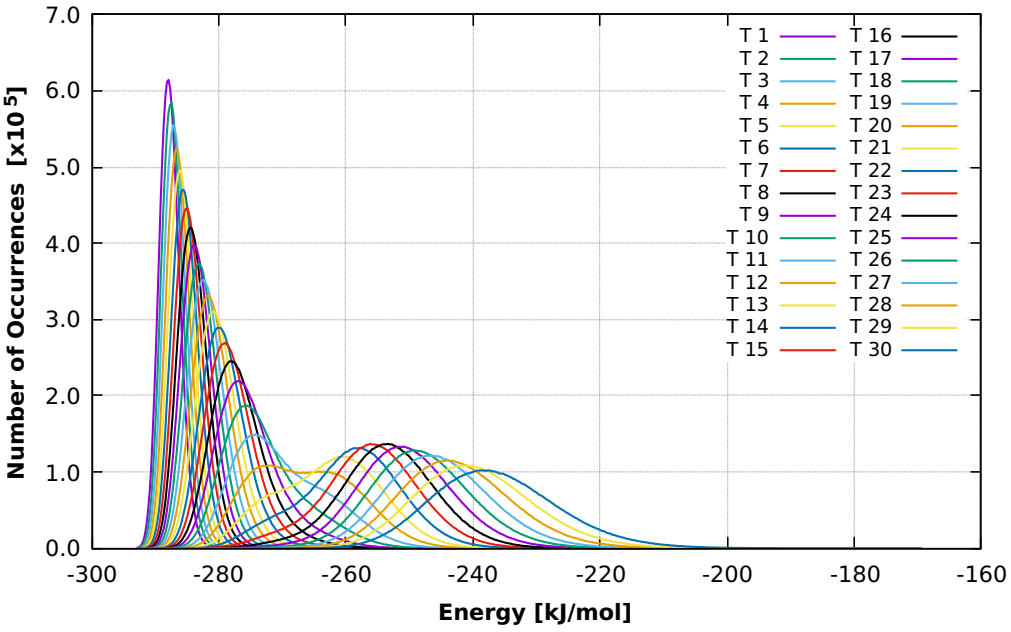

(A)

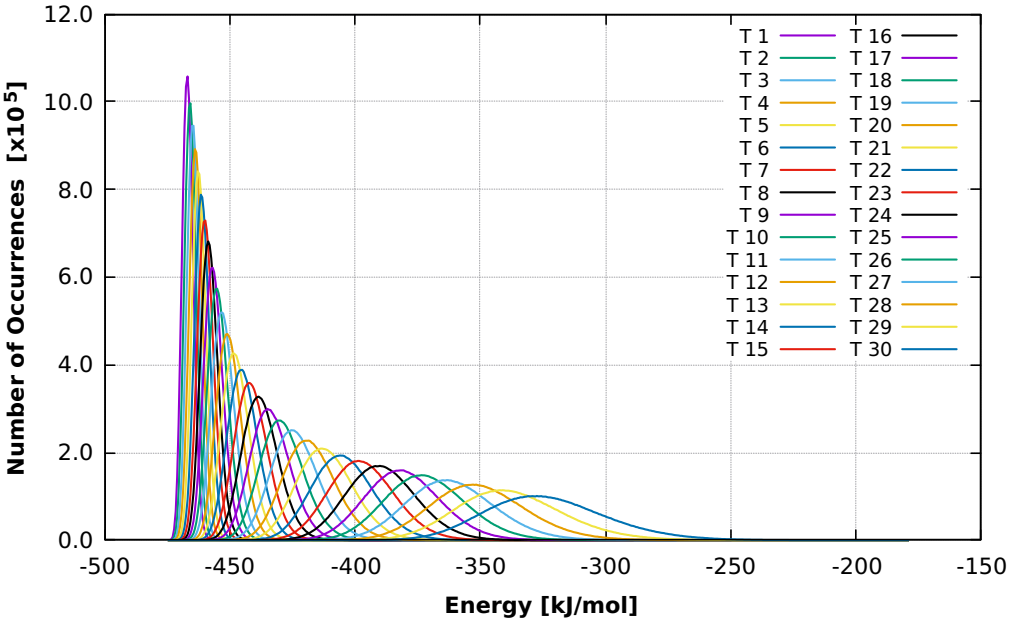

(B)

Figure 2.10: Multi-histogram analysis of the energy distribution for A) water octamer, $(H_2O)_8$ and B) water dodecamer, $(H_2O)_{12}$ using the TIP3P model.

The melting curves for water clusters $(H_2O)_n$, with cluster size $n = 8$ and 12, are shown in Figure 2.9. Unlike the noble gas clusters (Figures 2.7 and 2.8), not all of the curves exhibit a well-defined single peak in the heat capacity. However, the melting peak is still clear for the water octamer $(H_2O)_8$. The water octamer and dodecamer melt gradually over a broad temperature interval, which is expected due to their small cluster size.

Table 2.2: Melting temperature (K) for the water clusters $(H_2O)_n$.

n	Model	This work	References
8	TIP3P	115.2	123[a]/170[c]
	TIP4P	204.5	202[a]/181.6[b]/168[d]
	TIP5P	199.5	199[a]
	TIP6P	215.5	
	TIP4P-ice	252.5	248[a]
12	TIP3P	176.8	97[a]
	TIP4P	181.0	175[a]/164.6[b]/205[d]
	TIP5P	210.0	202[a]
	TIP6P	186.5	
	TIP4P-ice	215.0	214[a]

[a] Microcanonical Monte Carlo and molecular dynamics from Gelman-Constantin et al.[72]. [b] Molecular dynamics, from Kaneko et al.[55]. [c] Path-integral Monte Carlo including quantum effects, from Frantsuzov and Mandelshtam[73]. [d] Molecular dynamics and DFT, from Adeagbo and Entel[74].

In Figure 2.10, we present a multi-histogram analysis for both clusters using the TIP3P model. The observed sharpness of the transition is explained by the separate stability limits of the solid and liquid phases. For the water octamer using TIP3P, the multi-histogram analysis shows two regions of sampled cluster configuration at low and high energies, which correspond to the melting temperature of 115.1 K, T20 in Figure 2.10, A. In contrast, for the water dodecamer using TIP3P, the multi-histogram analysis indicates a more continuous change between high- and low-energy configurations, which correspond to the melting temperature of 176.8 K, T22 in Figure 2.10, B.

We note that the use of refined TIP potentials, TIP5P and TIP6P, leads to an additional peak or a shoulder at a higher temperature than the melting transition (post-melting). This behavior can be attributed to liquid-liquid phase transitions, which mostly consist of surface rearrangements and occur after melting. The post-melting feature is due to the presence of surface layering in the liquid cluster.[68]

We have summarized our results for the transition temperatures obtained in our Parallel Tempering Monte Carlo simulations with different water models in

Table 2.2. We computed melting temperatures for the water octamer and dodecamer calculated by different methodologies available in the literature. In contrast with the reported results by Gelman-Constantin et al.[72] (except for TIP6P), our results showed deviations that are not higher than 6%. The only significant deviation in the melting temperature was for the water dodecamer using the TIP3P model. Furthermore, to our knowledge, here we present for the first time calculated melting temperatures obtained from parallel tempering Monte Carlo simulations in the canonical ensemble of $(H_2O)_8$ and $(H_2O)_{12}$ using the TIP6P model.

As for noble gas clusters, our simulations suggest that the melting behavior of small water clusters is highly size-dependent. Although these clusters show a non-linear behavior in transition temperature with the cluster size comparable with results obtained with the model potential, this makes extrapolation to the bulk impossible at such small cluster sizes. We observed that there are not any magic numbers for water molecules, as was observed for noble gas clusters. Adeagbo and Entel[74] suggested that this behavior is due to the internal flexibility of the water molecule and the complexity of water connected with the formation of the hydrogen bonding networks, which requires further work.

2.5 Melting of Neon in High Magnetic Fields

2.5.1 Introduction

Noble gases play an important role in understanding the evolutionary processes in star and planet formation. Here, not only high pressures and temperatures have to be considered, but also high magnetic fields up to 10^{12} Tesla (in atomic units, 1 $a.u.$ = 2.35×10^5 Tesla) as found for example in magnetar systems.[75] For comparison, in lab systems, magnetic fields of up to about 1000 Tesla (or 10^{-3} $a.u.$) can be reached, with the largest field pulses in the micro-second time frame by explosive flux compression experiments.[76] In interstellar clouds near such high magnetic fields, the chemical and physical behavior of atoms and molecules is changed substantially.

There is little known about the chemical and physical properties of atoms, molecules, and condensed phases in high magnetic fields.[77–80] Even chemical bonding is affected, most interestingly one finds so-called perpendicular paramagnetic bonding, giving rise to molecules that do not exist on Earth. Noble gas systems present an ideal testing ground for condensed matter calculations where one can go beyond the limit of accuracy reached in typical density functional calculations.[81–84]

In this work, we used a many-body expansion of the total interaction energy between the atoms, which for weakly interacting systems converges rapidly in the long range.[10,85] It was shown recently, that such an expansion can achieve J/mol accuracy for the cohesive energy of solid argon, and correctly predicts the fcc structure as the most stable phase.[83]

2.5.2 The Many-body expansion of the interaction energy

The Helmholtz free energy $F(V,T,\boldsymbol{B})$ for a bulk system in dependence of volume V, temperature T, and a homogeneous magnetic field $\boldsymbol{B}$ may be divided into the static part of the interaction energy $E_{\text{int}}^{\text{stat}}(V,\boldsymbol{B})$ and a dynamic contribution, the latter consisting of a temperature-independent part $E_{\text{int}}^{\text{dyn}}(V,\boldsymbol{B})$ containing the zero-point energy effects (ZPE) and the thermal Boltzmann correction term $E_{\text{therm}}^{\text{dyn}}(V,T,\boldsymbol{B})$,[86,87] as a results,

$$F(V,T,\boldsymbol{B}) = E_{\text{int}}^{\text{stat}}(V,\boldsymbol{B}) + E_{\text{int}}^{\text{dyn}}(V,\boldsymbol{B}) + E_{\text{therm}}^{\text{dyn}}(V,T,\boldsymbol{B}) \tag{2.17}$$

The static part of the cohesive energy per atom is evaluated directly from a many-body expansion of the total interaction energy at a certain particle number N,

$$
\begin{aligned}
E_{\mathrm{int}}^{\mathrm{stat}}(N,\boldsymbol{B}) &= \frac{1}{N}\sum_{n=2}^{N}\Delta E^{(n)}(N,\boldsymbol{B}) \\
&\cong \frac{1}{N}\sum_{i<j}^{N}\Delta E^{(2)}(R_{ij},\boldsymbol{B}) \\
&+ \frac{1}{N}\sum_{i<j<k}^{N}\Delta E^{(3)}(R_{ij},R_{ik},R_{jk},\boldsymbol{B}) + \ \ldots
\end{aligned}
\tag{2.18}
$$

which for $\lim_{N\to\infty}(E^{\mathrm{stat}} + E^{\mathrm{dyn}})$ approaches the cohesive energy in the bulk limit. Here, $\Delta E^{(n)}(N,\boldsymbol{B})$ defines the n-body contribution per atom to the total interaction energy originating from the n-atomic fragment with internuclear distances R_{ij} between the atoms i and j (which for the bulk defines the volume) at given magnetic field vector $\boldsymbol{B}$. This expansion is formally exact if all n-body terms are taken into account.

For the two-body force, the magnetic field dependence can be reduced to a three-dimensional problem,

$$
\begin{aligned}
\Delta E^{(2)}(R_{ij},\boldsymbol{B}) &= \Delta E^{(2)}(R_{ij},B,\theta) \\
&= E^{(2)}(R_{ij},B,\theta) - 2E^{(1)}(B)
\end{aligned}
\tag{2.19}
$$

where $B = |\boldsymbol{B}|$ is the magnetic field scalar, the angle θ is defined through the scalar product $\cos\theta = \mathbf{e}_{\mathrm{M}} \cdot \mathbf{e}_{\mathrm{B}}$ of the two unit vectors between the molecular axis $\boldsymbol{M}$ and the magnetic field $\boldsymbol{B}$ directions, and $E^{(1)}(B)$ is the atomic total electronic energy in a homogeneous magnetic field $\boldsymbol{B}$.

The two-body term for neon is known very accurately with no magnetic field.[88] It is, however, a formidable task to perform accurate coupled-cluster calculations for a complete 3D hypersurface for the two-body interaction in a magnetic field. For the hypersurface we therefore only consider the change due to the finite magnetic field $\boldsymbol{B}$ ($R \equiv R_{ij}$),

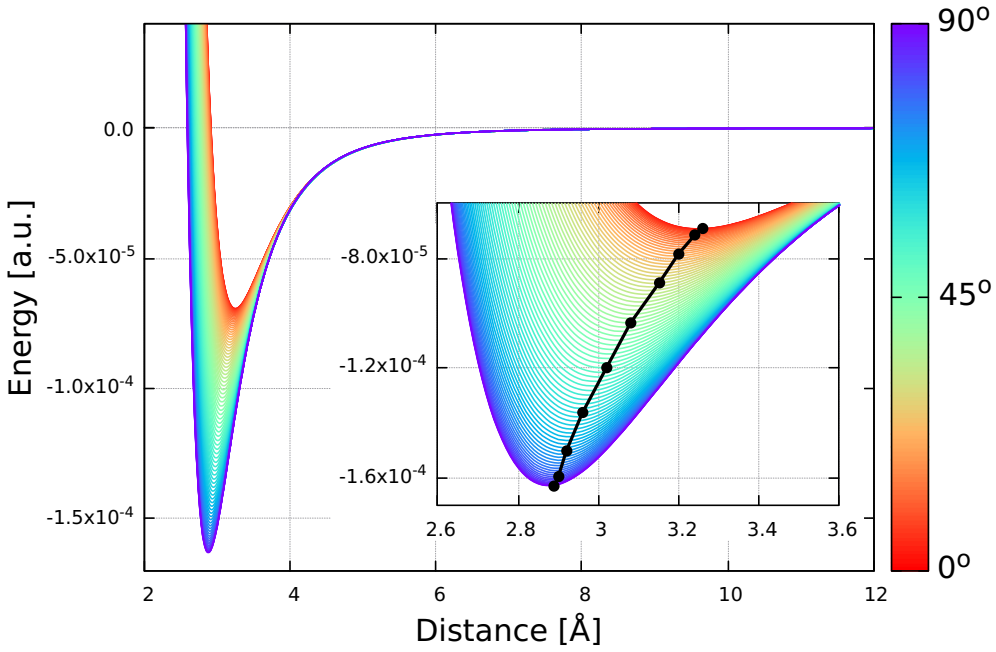

Figure 2.11: Two-body potential energy surface for Neon in a homogeneous magnetic field in z direction ($B_z = 0.30$ *a.u.*). The angle of rotation is regarding the magnetic field [in degrees]. The black points show the minimum distance for the Neon dimer regarding the rotation in the magnetic field.

$$\Delta E^{(2)}(R, \Delta B, \theta) = \Delta E^{(2)}(R, B, \theta) - \Delta E^{(2)}(R, B = 0) \tag{2.20}$$

where $\Delta E^{(2)}(R, \Delta B, \theta)$ is determined from second-order Møller-Plesset calculations with the u-aug-cc-pVQZ basis set (Figure 2.11). Accurate coupled-cluster calculations for a few selected points can be used at a subsequent stage to re-adjust the $\Delta E^{(2)}(R, \Delta B, \theta)$ surface. At $B_z = 0.2$ *a.u.*, we computed the coupled-cluster energy, CCSD and CCSD(T) with the aug-cc-pVTZ basis set. Finally, in the field-free case, we used the extended Lennard–Jones potential, with coefficients obtained from CCSD(T) energies with the aug-cc-pV5Z basis set,[89] according to the extended Lennard–Jones Potential from Schwerdtfeger et al.[90]

The three-body force is more complicated. Here one has to deal with a six-dimensional problem for non-zero magnetic fields,

$$\begin{aligned}
&\Delta E^{(3)}(R_{ij}, R_{ik}, R_{jk}, \boldsymbol{B}) = \Delta E^{(3)}(R_{ij}, R_{ik}, R_{jk}, B, \alpha, \beta) \\
&= E^{(3)}(R_{ij}, R_{ik}, R_{jk}, B, \alpha, \beta) \\
&- \sum_{lm \in \mathrm{cyc}(ijk)} E^{(2)}(R_{lm}, B, \theta_{\boldsymbol{M}_{lm}\boldsymbol{B}}) + 3E^{(1)}(B)
\end{aligned} \tag{2.21}$$

with α being the angle between the $\boldsymbol{B}$ vector and the plane normal defined by the three atoms, and β the rotation of the plane around its normal.

From previous calculations by Helgaker and co-workers we know that the electron density becomes more localized around the atoms and the molecular axis in high magnetic fields.[80] We might therefore expect that three-body forces become less important with increasing magnetic fields $\boldsymbol{B}$. For the field-free case, in the long-range the dominant three-body term is the Axilrod-Teller triple-dipole term,[91] which has a well-defined angular dependence. In this work, we also included the three-body short range by using a polynomial expansion with the following analytical form (extended Axilrod-Teller, EAT),[92–94]

$$\begin{aligned}
&\Delta E_3^{\mathrm{EAT}}(i,j,k) = g\left(R_g, R_s\right) f(\theta_i, \theta_j, \theta_k) \\
&= \left\{ c_0 R_g^{-9} + e^{-c_n R_s} \sum_{m=1}^{n-1} c_m R_g^m \right\} \left(1 + 3\cos\theta_i \cos\theta_j \cos\theta_k\right) \\
&\text{with} \quad f_\theta = \left(1 + 3\cos\theta_i \cos\theta_j \cos\theta_k\right), \\
&R_g = \left(R_{ij} R_{jk} R_{ik}\right)^{1/3}, \quad \text{and} \quad R_s = R_{ij} + R_{jk} + R_{ik}
\end{aligned} \tag{2.22}$$

with R_{ij} being the distance between two atoms i and j, and θ_i the corresponding angle between the vectors $\vec{R}_{ij}$ and $\vec{R}_{ik}$, Figure 2.12. Schwerdtfeger and Hermann[94] showed that this potential (together with an accurate two-body potential) describes precisely the equation of state for solid neon even in the high-pressure range. The magnetic field dependence can now be introduced through the expansion coefficients c_m $(m = 0, ..., n)$,

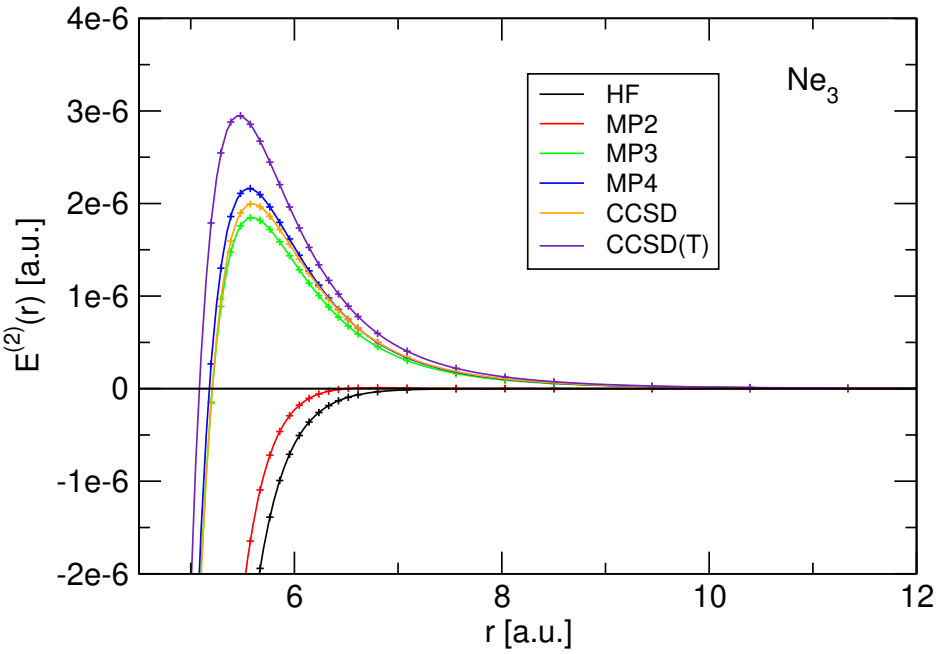

Figure 2.12: Three-body potential curves for the equilateral triangle of Ne_3 at various levels of theory from CBS limit calculations.

$$
\begin{aligned}
& g\left(R_g, R_s, B, \alpha, \beta\right) = c_0\left(B, \alpha, \beta\right) R_g^{-9} \\
& + e^{-c_n(B,\alpha,\beta)R_s} \sum_{m=1}^{n-1} c_m\left(B, \alpha, \beta\right) R_g^m \qquad (2.23) \\
& \text{with} \quad c_m\left(B, \alpha, \beta\right) = c_m\left(0, 0, 0\right) + h_m\left(B, \alpha, \beta\right)
\end{aligned}
$$

This reduces the problem to three-dimensional fits for the magnetic auxiliary functions $h_m\left(B, \alpha, \beta\right)$, which now becomes computationally accessible. The coefficients c_m are already known at the coupled cluster level for a zero magnetic field.[94] They have been determined from calculations of Ne_3 keeping the positions in an ideal triangle (D_{3h} symmetry), fitting it to the $g\left(R_g, R_s\right)$ function and multiplying it to the angular dependent part $f(\theta_i, \theta_j, \theta_k)$, Figure 2.12. The magnetic field dependent functions can be obtained in a similar way considering only Ne_3 with $R = R_{12} = R_{13} = R_{23}$ and placing it into a magnetic field $\boldsymbol{B}$. Note that three-body dispersive interactions require at least third-order perturbation theory in the electron correlation treatment; i.e., at least MP3 is required.[95,96]

Equation (2.23) requires a non-linear fit, which is cumbersome. A simpler analytical form for a fit procedure is given by,

$$g\left(R_g, R_s, B, \alpha, \beta\right) = \\ \left[1 + h\left(B, \alpha, \beta\right)\right] \left\{ c_0 R_g^{-9} + e^{-c_n R_s} \sum_{m=1}^{n-1} c_m R_g^m \right\} \tag{2.24}$$

with $h\left(0, \alpha, \beta\right) = 0$. This needs to be explored further. For the dynamic part, we adopt the Born-Oppenheimer approximation and consider vibrational effects by using the Einstein approximation.[97]

2.5.3 Computational Details

We considered neon clusters (Ne_n) of size n = 13, 55, 147, 309, 561, and 923. They show special stability at magic numbers of atoms corresponding to Mackay icosahedral structures. They are characterized by S closed shells of atoms around a central atom. The number of atoms n in a Mackay structure[66] with S shells is

$$n = 1 + 2\sum_{x=1}^{S}(5x^2 + 1) = \frac{1}{3}(10S^3 + 15S^2 + 11S + 3). \tag{2.25}$$

For finite-size clusters, we used spherical boundary conditions

$$r_{\text{SBC}} = (S + 1) \times r_{min} \tag{2.26}$$

where S is the number of shells (Equation (2.25)) and r_{min} is the equilibrium distances of the two-body interaction potential.

We refined two million Monte Carlo cycles for the largest cluster (n = 561 and 923) and four million for all the others (n = 13, 55, 147, and 309) using Parallel Tempering Monte Carlo in a canonical ensemble. Furthermore, we explore the convergence for n = 13,55, and 147, using 100 million Monte Carlo cycles. We propagated forty parallel tempering trajectories geometrically progressing around the melting region for each cluster. For all cluster sizes, the initial structure was

the global minimum of the corresponding Lennard–Jones (LJ) cluster and was taken from The Cambridge Energy Landscape Database[67].

Accurately defining a phase is a challenging task. Nonetheless, thermodynamic changes that occur during a phase transition can be described. The caloric curve, which represents the temperature and magnetic field dependence of the average potential energy, can provide insights into these changes. A peak in heat capacity corresponds to a discontinuity in the caloric curve. Therefore, a phase transition can be identified as the temperature at which the heat capacity reaches its maximum.

In this study, we analyzed the behavior of finite-size Ne_n clusters, which exhibit both an ordered solid-like phase at low temperatures and a disordered liquid-like phase upon heating. As a system reaches thermodynamic equilibrium, its configuration continuously changes and various states of total energy are visited with the corresponding Boltzmann probability. The internal energy of the system is equivalent to the average of all these energies. Our research focused on calculating the temperature and magnetic field dependence of the average potential energy, which is represented by a caloric curve.

Here, we used the optimal multi-histogram analysis to investigate the physical behavior of systems, as uncertainties in the direct estimation of average properties measured by Monte Carlo simulation can be slow to converge.[98] The multi-histogram analysis utilizes information from the energy distribution of sampled configurations at each temperature, allowing for the reliable determination of key thermodynamic properties from a single simulation.[64] Results using this method are comparable to conventional variance methods but do not require prior knowledge of the transition temperature. Here, we present a concise methodology, a simple adaptation of the multi-histogram approach, which has been successfully applied to a wide range of problems in various fields, including the investigation of molecular dynamics,[99–101] the analysis of phase transitions,[102,103] and the study of protein,[104,105] among others.[106,107]

Table 2.3: Melting temperature [K] for Ne_n clusters at MP2 and CC level in an external magnetic field up to 0.3 *a.u.* and relative energy to the global energy minimum at MP2 level and $B_z = 0.00$ a.u.

	MP2							CCSD	CCSD(T)	
n	B_Z=0.00	0.05	0.10	0.15	0.20	0.25	0.30	0.20	0.00[a]	0.20
13	6.82	6.94	7.34	7.90	8.72	9.67	10.55	10.13	12.32	12.53
55	6.94	6.94	7.36	7.98	8.93	10.07	11.50	10.36	12.39	13.11
147	8.66	8.78	9.18	9.91	11.27	12.79	14.80	12.84	15.60	16.12
309	9.64	9.88	10.44	11.34	12.62	14.66	16.84	14.78	17.28	18.28
561	11.14	11.18	11.91	13.16	14.68	16.40	19.20	16.55	19.76	20.48
923	12.19	12.46	13.00	13.36	15.31	17.86	20.51	18.11	21.00	22.24
ext1[b]	16.38	16.66	17.45	18.73	20.53	23.66	27.36	24.11	27.62	29.29
ext2[c]	17.98	18.24	18.79	19.85	22.03	25.06	29.01	25.59	29.71	31.16
	Relative energy [10^{-5} *a.u.*] to MP2 level and $B_z = 0.00$ *a.u.*									
	0.00	-2.16	-8.77	-20.20	-37.13	-60.45	-91.21	-53.68	-82.84	–

[a] Two-body energy according the extended Lennard–Jones Potential from Schwerdtfeger et al.[90]. [b] Extrapolation made with four points of the melting temperatures $n = 147 - 923$. [c] Extrapolation made with three points of the melting temperatures $n = 147 - 923$. Figure A.2 shows the extrapolation of melting temperature in a homogeneous magnetic field.

2.5.4 Results

The melting curves and heat capacities are shown for the Neon clusters (Ne_n) as a function of temperature (Figures 2.13 and 2.14). Our results show melting curves with a well-defined single peak for small Ne_n clusters ($n = 13, 55, 147$) and one pre-melting peak for the largest ones. The heat capacity curves of small clusters have a major peak at the melting temperature. The finite width of the heat capacity curve is due to the finite number of atoms in the cluster. The melting peaks become sharper for increasing cluster size (for the infinite system) and one gets to a discontinuity in the internal energy and heat capacity[68]. Figure A.1 shows heat capacities for Ne_n cluster based on the two-body energy from the coupled-cluster level of theory. Table 2.3 shows the numerical values for the melting temperatures of Neon gas clusters.

The sharp peaks of the heat capacity curves are due to both atomic re-arrangements and the configurational energy fluctuations within two nearby thermodynamic regions so that the cluster is either liquid- or all-solid-like. The multi-histogram results suggest the coexistence of both phases is described as the situation in which the system fluctuates between being entirely liquid- or entirely

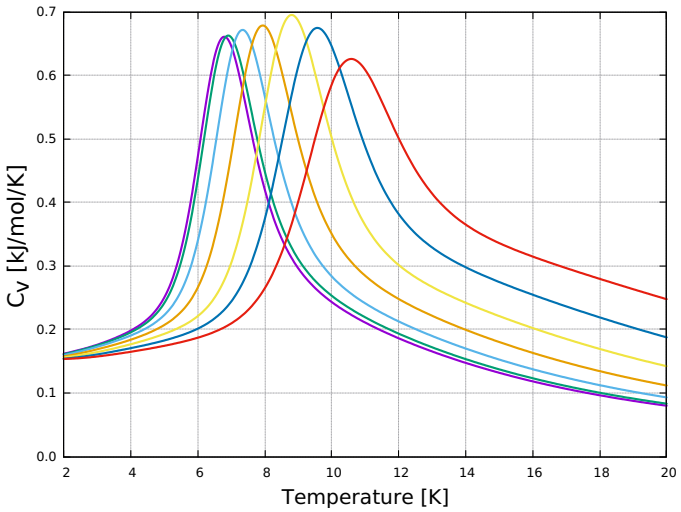

(A)

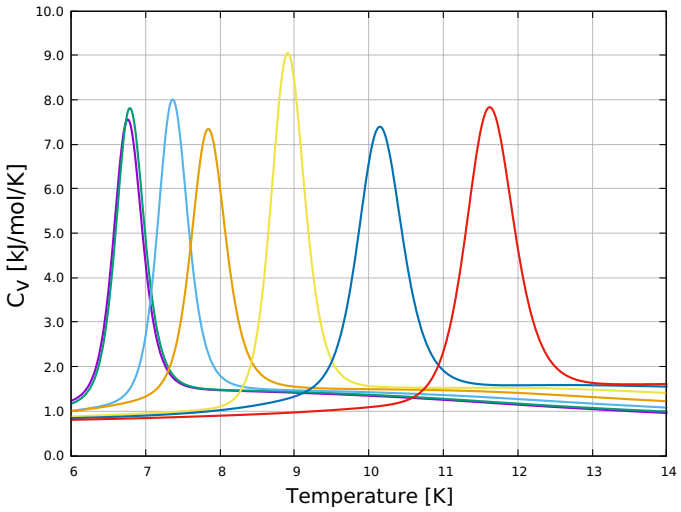

(B)

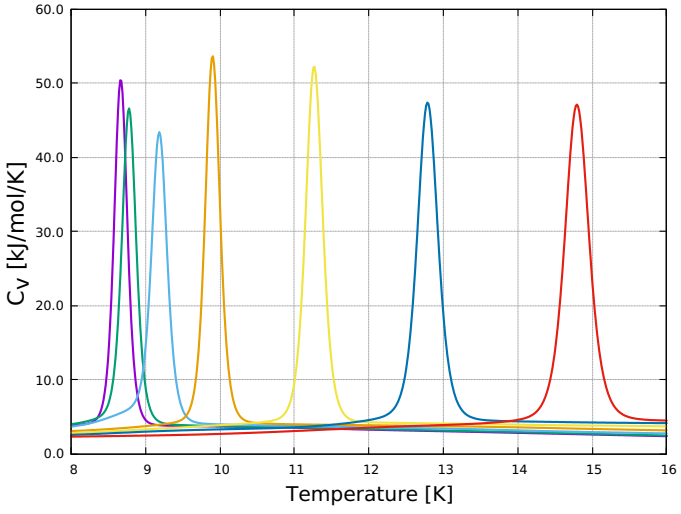

(C)

Figure 2.13: Heat capacity for A) Ne_{13}, B) Ne_{55}, and C) Ne_{147} in a homogeneous magnetic field (B_z, in *a.u.*). From left to right, the magnetic field strength is 0.0 (purple), 0.05 (green), 0.1 (light blue), 0.15 (golden), 0.2 (light yellow), 0.25 (blue), and 0.3 (red).

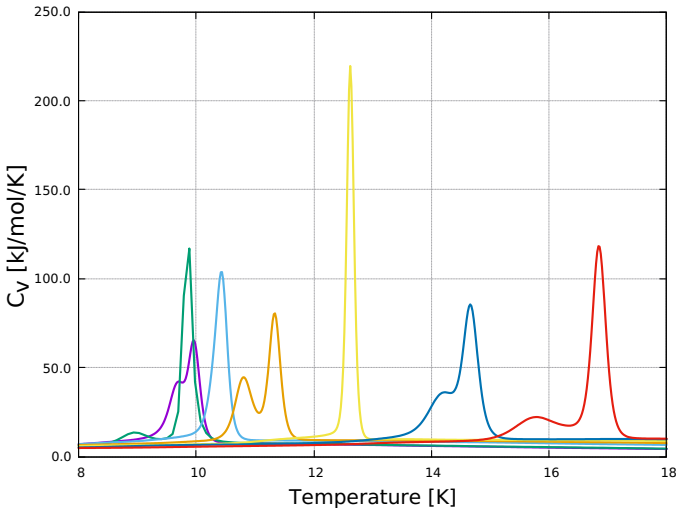

(A)

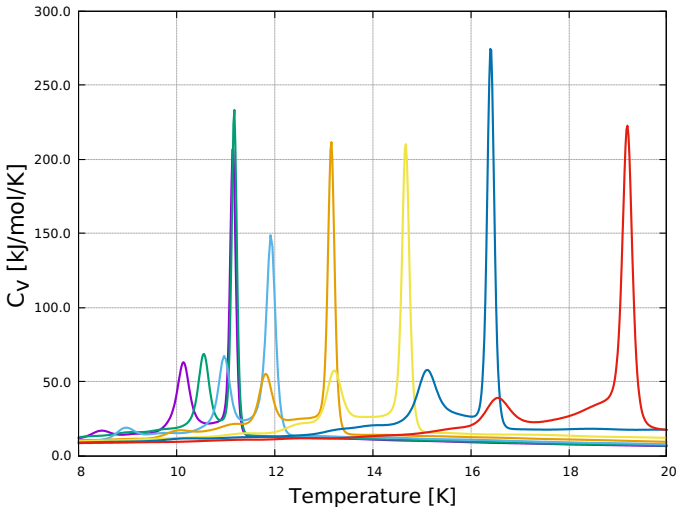

(B)

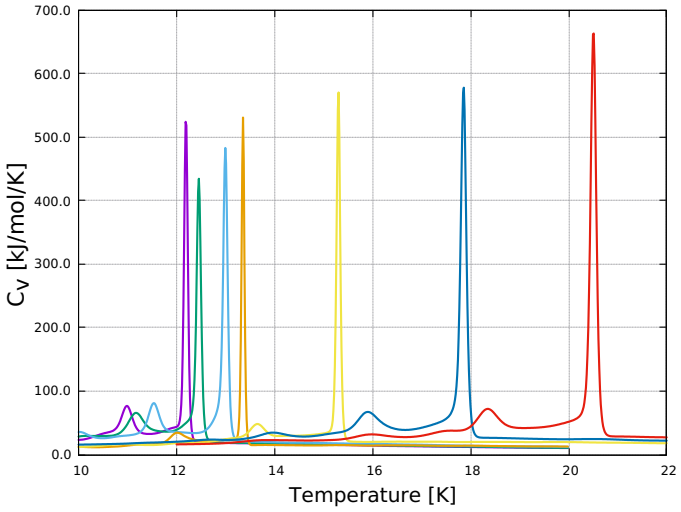

(C)

Figure 2.14: Heat capacity for A) Ne_{309}, B) Ne_{561}, and C) Ne_{923} in a homogeneous magnetic field (B_z, in *a.u.*). From left to right, the magnetic field strength is 0.0 (purple), 0.05 (green), 0.1 (light blue), 0.15 (golden), 0.2 (light yellow), 0.25 (blue), and 0.3 (red).

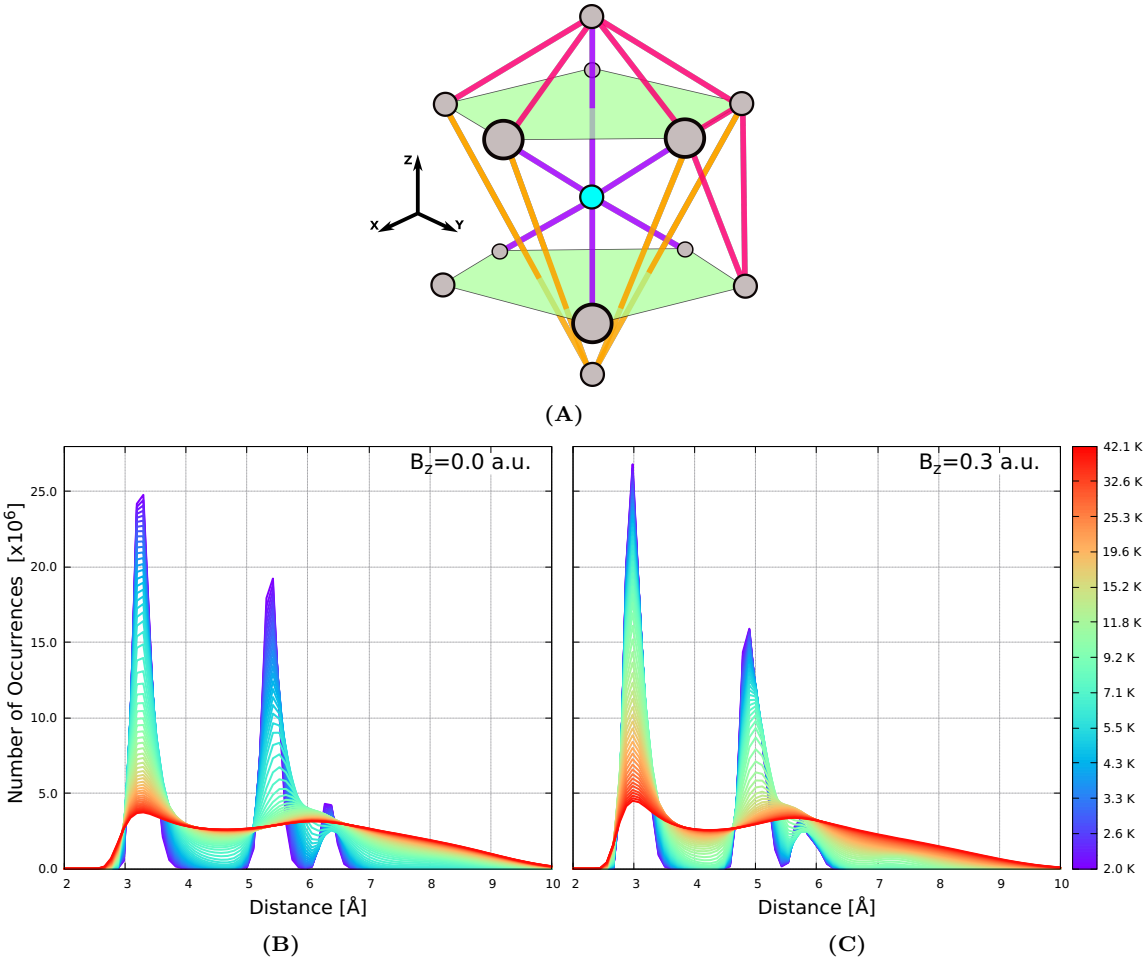

Figure 2.15: Distances for the icosahedral structure of the Ne_{13}. A) Geometrical distances for icosahedral Ne_{13} and atomic distance distribution for Ne_{13} in a homogeneous magnetic filed in z direction B) $B_z = 0.0$ *a.u.* and C) $B_z = 0.3$ *a.u.*.

solid-like at the melting transition.

As the fraction of surface atoms decreases with increasing cluster size, the melting peak is expected to converge towards the bulk value by increasing linearly with the surface/volume ratio, that is, with the inverse cluster radius $N^{1/3}$. The cluster finite size means that a large fraction of the molecules can be expected at the surface of the lattice rather than in the bulk. Forces experienced by surface molecules are quite different from molecules in the bulk. Therefore, one could find melting points that are lowered to the bulk melting temperature (Figure A.2). In this work, for ten million Monte Carlo cycles, the uncertainty of melting temperatures is approximately 2 K.

The Mackay clusters exhibit a geometrical shell closing, icosahedral symmetry,

with one central atom. This geometric structure is one of the most important molecular arrangements for the melting process.[65,108] For example, the icosahedral structure for 13 atoms has two types of atoms: the central one and any of those around it (Figure 2.15A). As a result of the icosahedral geometry, there are four different types of distances: *i*) the shortest distance is that among the central atom and any other on the shell (blue line); *ii*) among the atoms on the shell and their closest neighbor on the shell (red line); *iii*) among the atoms on the shell and their second-closest neighbor on the shell (yellow line); and *iv*) among the atoms on the shell and their furthest neighbor on the shell (any line connecting two atoms on the shell through the central atom).

Based on the previous description for Ne_{13} (Figure 2.15A), we describe inter-atomic distances using an atomic distance distribution with three regions corresponding with several types of distances. For the field-free case, B_z=0 *a.u.*, the first two types of distances – type-*i* and -*ii* – are approximately similar, and they are around 3.3 Å. The type-*iii* and -*iv* distances are around 5.4 Å and 6.3 Å, respectively (Figure 2.15B). In a homogeneous magnetic field (B_z) these maxima of the atomic distance distribution are shifted to the shortest distances in a continuous process (Figure 2.15C).

The atomic distance distribution displays two distinct structural behaviors: solid-like and liquid-like, before and after melting. At low temperatures before melting, the blue and green lines in Figure 2.15B depict ordered configurations or solid-like behavior. However, as the temperature increases and we reach the melting point, the kinetic energy increases, leading to more disordered configurations or liquid-like behavior, represented by the orange and red lines in Figure 2.15C. The magnetic field is another critical property that influences the order-disorder configuration of Neon clusters.

As a result, increasing the magnetic field strength from 0 to 0.3 *a.u.*, the average inter-atomic distance is reduced up to 20% and the number of configurations with shorter average distance increases proportionally to the field

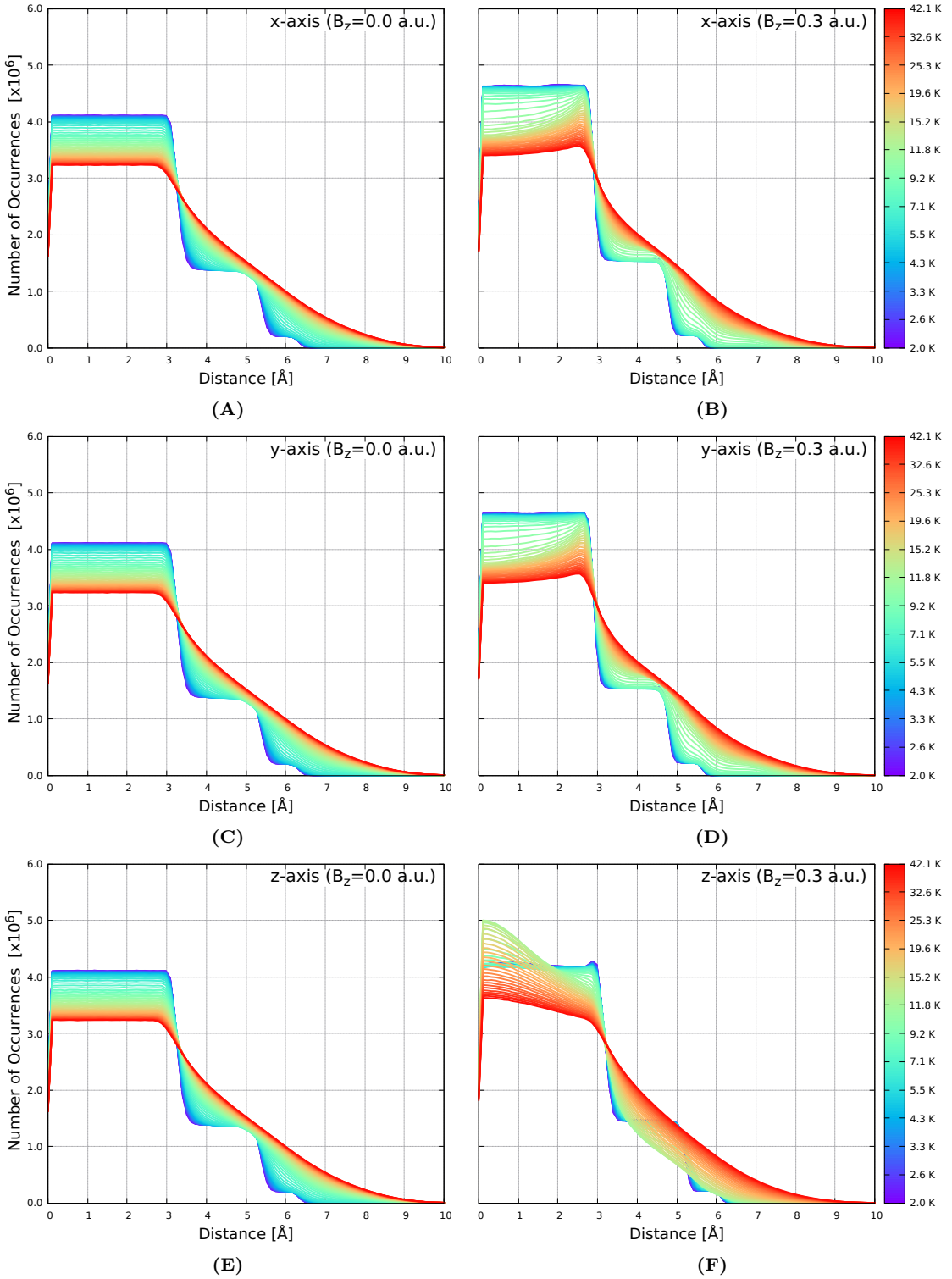

Figure 2.16: Atomic distance distribution for Ne_{13} in a homogeneous magnetic field. Filed direction across the axes x (top), y (middle), and z (bottom) at $B_z = 0.0$ *a.u.* (left) and $B_z = 0.3$ *a.u.* (right).

strength for every temperature. In Figure 2.15C, we get a higher pick around 3 Å and smaller picks around 5 and 6 Å regarding the field-free case (Figure 2.15B).

These findings indicate that a magnetic field causes structural compression in Neon clusters, resulting in shorter distances across all temperatures. In the absence of a magnetic field, all directions are equivalent and fewer configurations with short distances are present as the temperature rises, Figure 2.16 (top). However, when a strong magnetic field (B_z=0.3 $a.u.$) is applied, the anisotropy leads to distinct inter-atomic distance distributions. An analysis of each coordinate reveals that this distance reduction mainly occurs in the z direction, Figure 2.16 (bottom). The magnetic field mainly squeezes the Neon clusters in the z direction, leading to an increase in the number of configurations with shorter distances upon melting. In the y and z directions, there is a slight compression (less than 0.1 Å) compared to the field-free case, regardless of temperature.

The concept of entropy is often related to the level of order within a system, and in the context of this study, entropy plays a crucial role in the arrangement of atoms with and without a magnetic field. In general, atoms in a solid state are more ordered than the same atoms when heated. The magnetic field has a significant impact on reducing the degree of freedom in the system by compressing the Neon atoms across the z direction. The entropy of a neon cluster in a magnetic field is lower than that of a field-free cluster.

The entropy of a system $S(T)$ increases with temperature. As the temperature increases, the internal configuration mechanism of each cluster undergoes diffusive atomic motion at the surface, which depends on bond stiffness and structural order.[109–111] As the temperature rises across the transition region, the number of solid-like configurations decreases while the number of liquid-like configurations increases. This is in contrast to bulk systems, where both phases exist at the same time during the phase transition.[112]

2.5.5 Conclusions

Our findings show that when we increase the magnetic field the entropy decreases, Figure 2.17. The thermodynamical parameter $dS/dT = C_V/T$ shows how the entropy changes before, on, and after melting. In the absence of a magnetic field,

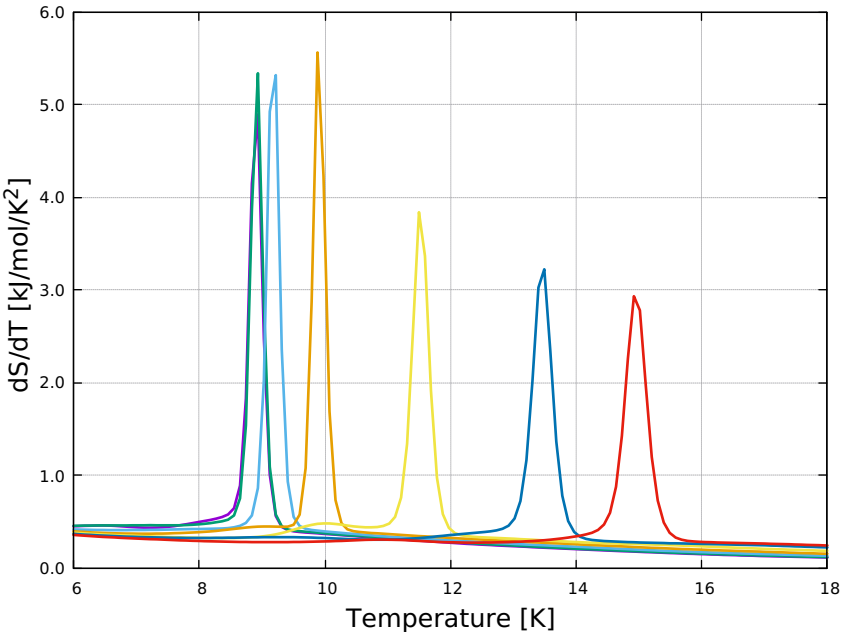

Figure 2.17: Variation of the entropy to the temperature for the Ne_{147} cluster in a homogeneous magnetic field in z direction (B_z in *a.u.*): 0.0 (purple), 0.05 (green), 0.1 (light blue), 0.15 (golden), 0.2 (light yellow), 0.25 (blue), and 0.3 (red).

the entropy of a neon cluster is maxima when the system undergoes a phase transition. However, for high magnetic fields dS/dT is reduced by approximately 60 %.

The icosahedral structure of Mackay clusters with a central atom and atoms around it influences the melting process. The atomic distance distribution before and after melting displays solid-like and liquid-like behaviors, respectively, and is affected by the magnetic field strength. Increasing the magnetic field strength reduces the average inter-atomic distance and leads to more configurations with shorter average distances.

We found that the melting temperature of the Neon cluster increases when we increase the size of the cluster and when we increase the strength of the magnetic field. The heat capacity of Mackay clusters exhibits sharp peaks due to atomic rearrangements and configurational energy fluctuations between liquid-like and solid-like phases. The melting transition of the system is described as the fluctuation between these two phases. Earlier studies on the melting temperatures of noble gas clusters Pahl et al.[113] and Labastie and Whetten[112], also showed

well-defined single peaks in the heat capacity, which become higher, more intense, and narrower as the cluster size increases. Our results show a good agreement between the melting temperatures computed in this work and those calculated Pahl et al.[113] and Labastie and Whetten[112].

In conclusion, the results of this study indicate that the presence of a magnetic field causes structural compression in Neon clusters, leading to shorter inter-atomic distances. The magnetic field primarily squeezes the cluster in the z direction, which increases the number of configurations with shorter distances upon melting. The effect of the magnetic field on the entropy of the cluster is significant, reducing the degree of freedom in the system and leading to a lower entropy compared to the field-free cluster.

Chapter 3

The Super-Heavy Element Flerovium*

As early as 1975, Pitzer suggested that copernicium, flerovium, and oganesson are volatile substances behaving noble-gas-like because of their closed-shell configurations and accompanying relativistic effects. It is, however, precarious to predict the chemical bonding and physical behavior of a solid by knowledge of the atomic or molecular properties only. The melting of copernicium and oganesson has been analyzed very recently by the Auckland group. Both are predicted to be semiconductors and volatile substances with rather low melting and boiling points, which may justify a comparison with the noble gas elements. We, therefore, decided to study closed-shell flerovium in detail to predict solid-state properties including the melting point from a decomposition of the total energy into many-body forces derived from relativistic coupled-cluster and density functional theory. The convergence of such a decomposition for flerovium is critically analyzed, and the problem of using density functional theory is highlighted. We predict that flerovium is in many ways not behaving like a typical noble gas element despite its closed-shell $7p_{1/2}^2$ configuration and resulting weak interactions. Unlike the noble gases, the many-body expansion in terms of the interaction energy is not converging smoothly. This makes the accurate prediction of phase transitions very difficult. Nevertheless, the first prediction by Monte-Carlo simulation estimates the melting point at 284 ± 50 K. Furthermore, calculations for the electronic band gap suggest that flerovium is a semiconductor similar to copernicium.

3.1 Introduction

Ever since Lewis introduced the electron sharing/pairing concept between atoms in 1916[114–116] and the first description of interatomic interactions via the newly developed theory of quantum mechanics in 1927 by Heitler and London[117], the study of the nature of chemical bonding in molecules, clusters, aggregates or infinite systems, such as solids or liquids, became of fundamental importance to chemistry.[118–122] Pauling, who followed up the work of Lewis, Heitler and London with a series of seminal contributions on chemical bonding,[123–131] defines chemical bonding in his most influential book on *The Nature of the Chemical Bond*,[118] as *There is a chemical bond between two atoms or groups of atoms in the case that the forces acting between them are such as to lead to the formation of an aggregate with sufficient stability to make it convenient for the chemist to consider it as an independent molecular species*. It is apparent from such a (rather loose) definition that chemical bonding is (and remains) a fuzzy concept in chemistry (see Frenking and others for critical analysis and historical account on chemical bonding[120,121,132–134]). For example, we would not consider the dimer He_2, which accommodates just one single vibrational level in the diatomic potential curve, as an independent molecular species.

From a quantum mechanical point of view, the term "chemical bond" does *not* correspond to a physical observable (i.e. a self-adjoint operator on a Hilbert space). Second, electrons are indistinguishable, and only within a single-particle approximation such as Hartree-Fock or Kohn-Sham, we may distinguish between different molecular orbitals or densities between valence and core electrons involved in chemical bonding.[132] Here we quote Coulson:[135] *Sometimes it seems to me that a bond between two atoms has become so real, so tangible, so friendly, that I can almost see it. Then I awake with a little shock, for a chemical bond is not a real thing. It does not exist. No one has ever seen one. No one ever can. It is a figment of our imagination.* Besides these fundamental (or philosophical)

*Reproduced with the permission of AIP Publishing from Florez, Edison, Odile R. Smits, Jan-Michael Mewes, Paul Jerabek, and Peter Schwerdtfeger. *"From the gas phase to the solid state: The chemical bonding in the superheavy element flerovium."* The Journal of Chemical Physics 157, no. 6 (2022). doi.org/10.1063/5.0097642

issues, chemical bonding concepts are undoubtedly the most important tools chemists have to discuss to the predict chemical and physical properties of compounds in different aggregate states.

The beauty in chemical bonding theory is that we have (besides classical and empirical methods) a plethora of different wavefunction or density functional-based models at hand that give deep insight into the behavior of a chemical compound. In turn, chemical bonding theory can also lead to major controversies between different "philosophical" schools. The reason here lies in the many different approximations used, such as different decompositions of the Hamiltonian or the total electronic energy, or the wavefunction or density of the system, that can often lead to very different interpretations,[136,137] albeit (mostly) valid within the bonding picture chosen. An example here is the bonding for the ground state of the C_2 molecule and the recent debate if the molecule contains a quadruple bond or not[138–140]. There are many such examples in the literature which often lead to fierce debates.[141,142] In our opinion, such controversies are both useful and important for the progress of chemistry as a discipline, and for the development of critical thinking skills and understanding of chemical concepts to science students.

Chemists traditionally think of molecules when discussing chemical bonding, although, over the past few decades, solid-state physics has moved into the chemistry domain, mainly because of its importance to material science.[143] Many (if not all) bonding models can be successfully transferred into the solid state.[144,145] These include models for covalent, ionic, metallic, and Van der Waals (weak or dispersive) types of interactions. A typical link here, for example for ionic bonding, is the ligand-field theory for molecules compared to the crystal-field theory for the solid-state.[146,147] Moreover, by comparing different approximations one can discuss in detail the influence of electron correlation effects (Hartree-Fock versus the exact result from the Schrödinger or Dirac equation), relativistic effects (Schrödinger versus Dirac results either at the Hartree-Fock or correlated level), or even smaller effects such as quantum electrodynamic contributions to the stability of a chemical bond between atoms in molecules or the solid state.[148,149] Such

effects are experimentally not accessible but important for the discussion of the chemical and physical behavior of atoms, molecules, and the solid state.

As a prime example of the influence of relativistic effects on chemical bonding, we take the interaction between the two metal atoms cesium and gold. CsAu is ionic because gold behaves like a pseudohalide because its electronegativity is relativistically increased from 1.9 to 2.4.[150] As a result, CsAu forms orange crystals adopting a CsCl lattice, and behaves like a semi-conductor (specific resistivity of 10^{-5} Ωm compared to a typical metal of $10^{-7} - 10^{-8}$ Ωm) with an optical gap of 2.6 eV[151]. Hence the bonding between two metals does not necessarily result in a metallic bond due to relativistic effects.[149,152,153] This implies that one has to be very careful when predicting the bonding behavior in condensed systems purely from the knowledge of the chemical behavior of the elements involved.

As a second prime example for both relativistic and electron correlation effects in chemical bonding, we take mercury, which becomes important for our discussion on flerovium. The mercury dimer is Van der Waals bound with a dissociation energy of only 4.69 kJ/mol and a rather large bond distance of 3.69 Å.[154] At the Hartree-Fock level, Hg_2 is unbound, in agreement with the fact that dispersion interactions originate from electron correlation.[155] Even for the bulk system, mercury is unbound at the Hartree-Fock (or Dirac-Hartree-Fock) level,[156] thus the chemical bonding in mercury is purely due to electron correlation.[155,157]

However, the nature of the chemical bond changes dramatically from the dimer to the solid state[158] as the solid/dimer ratios between the cohesive and dissociation energies $E_{\mathrm{coh}}/D_{\mathrm{e}}$ and the nearest neighbor and the equilibrium distances $r_{\mathrm{NN}}/r_{\mathrm{e}}$ show, cf. Figure 3.1 and Figure 3.2.

Furthermore, relativistic effects have a substantial influence on chemical bonding and without relativity, mercury would not be a liquid at room temperature. In fact, relativistic effects on the melting temperature are predicted

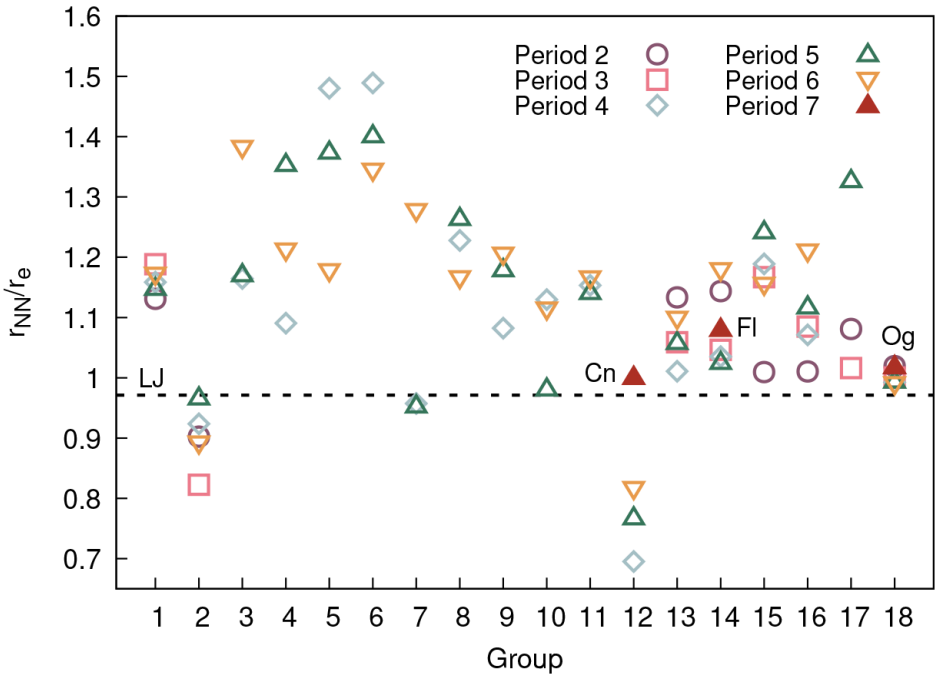

Figure 3.1: Ratio between the bulk nearest neighbor distance and the equilibrium distance of the corresponding diatomic compound, $r_{\mathrm{NN}}/r_{\mathrm{e}}$, for the main group and transition metals in the periodic table. The value for the (6,12) Lennard-Jones (LJ) potential is given as a straight line. Experimental data (if available) for the diatomics were taken from Huber and Herzberg [1], and for the solid state from Kittel and McEuen [2].

to be as high as $\Delta_R T_{\mathrm{MP}} = T_{\mathrm{MP}}^{\mathrm{NR}} - T_{\mathrm{MP}}^{\mathrm{R}} \sim 400$ K.[159–161] Even more dramatic is the relativistic change in the boiling point, $\Delta_R T_{\mathrm{BP}} = \sim 600$ K.[161,162]

The simulation of solid-to-liquid-to-gas phase transitions requires an accurate treatment of the interactions between the atoms and molecules involved, which is a formidable task. Only for the noble gas elements melting points close to the experimental values have been achieved through a many-body expansion of the total energy applying relativistic coupled-cluster theory with no empirical parameters involved.[163–165]

Figures 3.1 and 3.2 deserve some further discussion at this point. For most elements, the bond distance increases when moving from the diatomic to the solid state. Exceptions are found only for the Group 2 and 12 elements, as we go from Van der Waals bonding to the metallic state, Pd which is closed-shell, and interestingly for two of the Group 7 elements. The ratio of the (12,6) Lennard-Jones potential for an fcc lattice,[166] $r_{\mathrm{NN}}/r_{\mathrm{e}} = (L_{12}/L_6)^{1/6} r_{\mathrm{e}} = 0.9712 r_{\mathrm{e}}$,

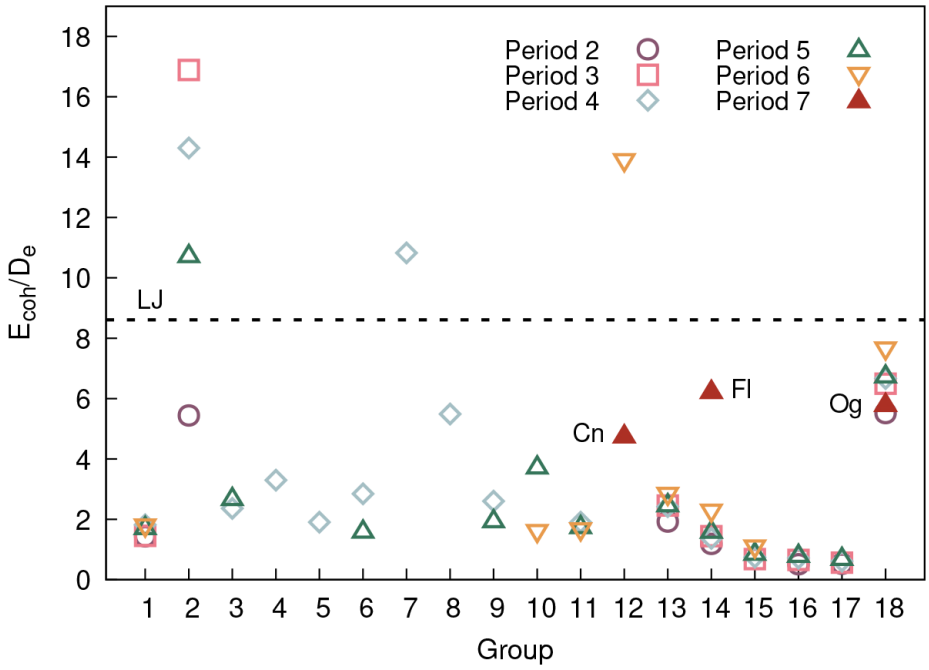

Figure 3.2: Ratio between the bulk cohesive energy and the dissociation energy of the corresponding diatomic compound, $E_{\mathrm{coh}}/D_{\mathrm{e}}$, for the main group and transition metals in the periodic table. For clarity, the two Group 12 elements not shown in this figure are Zn and Cd with $E_{\mathrm{coh}}/D_{\mathrm{e}}$ =44.9 and 28.6 respectively. The value for the (6,12) Lennard-Jones (LJ) potential is given as a straight line. Experimental data (if available) for the diatomics were taken from Huber and Herzberg[1], and for the solid state from Kittel and McEuen[2].

is smaller than 1.0 because of the additional attractive non-nearest neighbor interactions. Here L_6 and L_{12} are the Lennard-Jones-Ingham coefficients (or lattice sums).[167,168] The noble gas elements are LJ-like and accumulate around $r_{\mathrm{NN}}/r_{\mathrm{e}} = 1$.

Concerning the ratio of binding energies, we compare the binding for a diatomic to the bulk cohesive energy. In the latter, we get stabilization in the bulk due to additional interactions between the atoms in the solid state. For the ratio of the cohesive energy to the binding energy per atom the values shown in Figure 3.2 must be multiplied by a factor of 2. Again, it is illuminating to take the (12,6) Lennard-Jones ratio of $2E_{\mathrm{coh}}/D_{\mathrm{e}} = (L_6^2/L_{12})D_{\mathrm{e}} = 17.220$[166] as a reference. The noble-gas elements are close to this Lennard-Jones ratio as one expects, and only a few elements lie above which are mainly the group 2 and 12 elements. Most elements, however, have a decreased cohesive energy. The reason for this lies in the importance of many-body forces for the solid-state,[10] which we will discuss in detail for flerovium.

In 1975, Pitzer asked the question if the elements 112, 114, and 118 are relatively inert gases.[169,170] All three elements adopt a closed-shell configuration, Cn ($7s^2$), Fl ($7s^2p_{1/2}^2$) (At the scalar relativistic or non-relativistic level flerovium is an open-shell with a $^3P_0$ ground state) and Og ($7s^2p_{1/2}^2p_{3/2}^4$).[171–173] Pitzer gives a promotion (excitation) energy for Fl of 6.12 eV (Cn of 8.57 eV, Og of 8.8 or 4.89 eV depending on the valence state) based on DHF calculations, compared to an estimated bond (dissociation) energy of 4 eV (5-6 eV for Cn, 1.8 eV for Og) from extrapolation of the lighter congeners, which lead to the prediction of these elements to be gases or volatile liquids bound by dispersion.

From recent and more accurate quantum chemical calculations we have promotion energies of (in eV) 4.44 for Cn, 3.27 for Fl, and 4.20 for Og,[174–176] compared to much smaller bond energies of (in eV) 0.078 for Cn, 0.080 for Fl and 0.078 for Og.[177] Although the values shift significantly, they are still in line with Pitzer's original prediction. The static dipole polarizabilities are also interesting to compare[178] as these determine the dispersive interactions between atoms, i.e. (in atomic units) 27.4 for Cn, 30.6 for Fl and 58.0 for Og,[179,180] compared to 33.1 for Hg, 47.1 for Pb and 35.3 for Rn.[164,181,182]

Concerning the solid state, the ratio $E_{\mathrm{coh}}/D_{\mathrm{e}}$ shown in Figure 3.2 puts flerovium close to the noble gas elements. Nevertheless, from all these data it is very difficult to predict if Fl is a volatile substance behaving like a noble gas element as Pitzer suggested.[169] The noble-gas-like behavior is best described by chemical inertness compared to the other elements of the periodic table due to the closed shell structure,[183] the inter-atomic interactions mediated through mostly dispersive forces, which are well described by the Lennard-Jones potential,[184] and, for the solid state, fast convergence of the many-body expansion of the interaction energy at the equilibrium distance.[10,185]

The Auckland group recently analyzed the solid and liquid state behavior of both Cn[161,186,187] and Og.[4,188] It was found that these elements are

semiconductors but with very low melting and boiling points, e.g. T_{MP}(Cn)= 284 K, T_{BP}(Cn)= 340 K, T_{MP}(Og)= 324 K, T_{BP}(Og)= 453 K.[161,188] This supports at least in part Pitzer's original claim.[169] The remaining missing link is flerovium, which requires an accurate treatment of spin-orbit coupling. From recent atom-at-a-time experiments of flerovium adsorption on a gold surface it was concluded that flerovium is a volatile metal.[189–191] Regarding the volatility, theoretical simulations indeed suggest that the adsorption energies are very similar between the three elements Cn, Fl, and Og.[179,192–195] For recent reviews on the chemistry of superheavy elements see Türler and Pershina[196], Pershina[197].

In this chapter, we study the interaction between flerovium atoms using a many-body expansion (MBE) of the total energy in terms of relativistic coupled-cluster and density functional theory (DFT), as well as projector augmented wave (PAW) DFT calculations for the solid-state properties of flerovium. We specifically address the problem if such an expansion is valid and if density functional theory correctly predicts the individual n-body interaction terms. We also present a first estimate of the melting point of flerovium.

3.2 Methods and Computational Details

All atomic calculations were carried out with the program packages GRASP[3] and DIRAC.[198,199] For constructing the many-body potentials for Fl_2, Fl_3 and Fl_4 we carried out relativistic DFT and coupled-cluster (CC) calculations within the exact 2-component version (X2C) as implemented in the DIRAC program package.[198] For the DFT calculations we chose the local density functional approximation (LDA),[200,201] the Perdew-Becke-Enzerhofer (PBE) gradient corrected functional (GGA) including exact exchange (PBE0),[202,203] and the Becke-Lee-Yang-Parr hybrid functional (B3LYP)[204,205] together with Dyall's uncontracted double-zeta (2Z) $(26s23p17d11f)$, triple-zeta (3Z) $(30s29p20d13f1g)$ and quadruple-zeta (4Z) $(35s35p24d16f3g1h)$ basis set for flerovium.[206] For the more expensive second-order Møller-Plesset (MP2) and coupled-cluster singles-doubles calculations

including triple substitutions (CCSD(T)), we had to restrict the basis set to double-zeta quality[206] for the three-body force.

The active orbital space chosen is within the energy range of $[-2, 50]$ a.u., which includes the $6d7s7p$ orbitals in the active space. For the MBE solid-state calculations, we used the program SAMBA. Further, solid-state calculations at the spin-orbit relativistic (SO)-DFT level were carried out using the program VASP.[207–210] The core region was modeled using the PAW approach of Blöchl, Kresse and Joubert[211,212] with the potential for Fl published recently.[195] The functionals PBE0, PBEsol, and PBE-D3,[202,203,213] containing the Grimme D3 dispersion correction with Becke-Johnson damping[214] and recently published atomic parameters for Fl[195] were employed.

All structural optimizations are conducted at the SO-DFT level with the highest numerical precision settings, converged k-grids (7^3 for optimizations, 9^3 for final energies of the fcc lattice, $7 \times 7 \times 4$ for optimizations and $9 \times 9 \times 5$ for final energies of the hcp lattice), and using a plane-wave cutoff of 600 eV to remedy Pulay stress. Bulk moduli are calculated via a Birch-Murnahagan fit to five-volume/energy pairs (98%, 99%, 100%, 101%, and 102% of the optimized volume). We also carried out self-consistent quasi-particle GW calculations to refine the electronic band gap calculated at the DFT level.[215–217] The GW calculations use reduced energy cutoffs (300 eV) to limit the computational effort and start from converged PBE orbitals.

Atomistic Electron Localization Function Calculations

The Electron Localization Function (ELF) $D_\sigma(\vec{r})$ is a useful chemical bonding analysis tool to visualize the electronic structure of atoms, molecules and periodic systems.[218–220] It is formulated as a measure for the inverse conditional probability of finding an electron in the vicinity of another same-spin electron located at a given position $\vec{r}$:

$$D_\sigma(\vec{r}) = \left[1 + \left(\frac{\tau_\sigma(\vec{r})\rho_\sigma(\vec{r}) - \frac{1}{4}|\vec{\nabla}\rho_\sigma(\vec{r})|^2}{\rho_\sigma(\vec{r})\tau_\sigma^{\mathrm{TF}}(\vec{r})}\right)^2\right]^{-1} \tag{3.1}$$

Here σ = spin $\uparrow$ or spin $\downarrow$, ρ_σ the electron spin density, τ_σ the kinetic energy density, $\vec{\nabla}\rho_\sigma$ the electron density gradient, and $\tau_\sigma^{\mathrm{TF}}$ the Thomas-Fermi kinetic energy (of the uniform electron gas). In the relativistic case where spin is not a good quantum number anymore, σ should be replaced by the Kramers component. Moreover, for the kinetic energy term, the nonrelativistic expression is used similar to what is described by Pilmé et al.[221], and for Pb and Fl at the scalar relativistic and nonrelativistic level we use restricted (spin-unpolarized) Kohn-Sham theory with an occupation of $ns^2p_{1/2}^{2/3}p_{3/2}^{4/3}$, n =6 or 7.

The ELF generally assumes values between 0 and 1, where a value close to 1 indicates that the probability of finding two same-spin electrons close to each other is very low (high level of electron localization), and the ELF value of 0.5 corresponding to the limit of a hypothetical uniform Fermi gas of the same density (high level of electron delocalization).

In molecular systems, the ELF is usually utilized to allow the distinction between bonding electron pairs and lone pairs. However, ELF calculations are sensitive enough to be able to resolve the spatial regions corresponding to electronic shell separations in atoms – when calculated with sufficiently high resolution, that is.

In this work, we performed ELF calculations for the atoms Hg, Pb, Rn, Cn, Fl, and Og, respectively, based on non-relativistic (NR), scalar-relativistic (SR) and fully relativistic (R) DFT calculations employing the relativistic *ab-initio* quantum chemistry program DIRAC,[198,199] for which we utilized the PBE density functional[202] in conjunction with fully uncontracted relativistic Dyall 4Z all-electron basis sets.[222–225] For the fully relativistic computations we made use of DIRAC's 4-component DFT routine[226] and explicitly included the small-component integrals as well as the two-electron Gaunt term. The choice to

obtain the converged electron densities for the ELF calculations via DFT rather than (D)HF theory was made in order to include electron correlation to a certain degree.

We note that for the NR and SR cases, only the densities of the large component were considered in the ELF calculations, whereas in the fully relativistic four-component case (R) the total one-particle density was obtained by adding the small-component to the large-component densities.

Many-body Expansion of the Total Energy

For the solid-state calculations, we decompose the total electronic energy of the system into individual n-body interaction contributions,

$$E^T = \sum_{i=1}^{\infty} E_i^T \tag{3.2}$$

We subtract the one-body atomic contribution, rearrange the terms in Equation (2.18), and use translational symmetry for the fcc lattice such that we obtain the cohesive energy (per atom) for a monatomic compound

$$\begin{aligned} E_{\text{coh}} = \sum_{i=2}^{\infty} E_i = \frac{1}{2}\sum_{i=1}^{\infty} V_2(R_{0i}) + \frac{1}{3}\sum_{i<j}^{\infty} V_3(R_{0i}, R_{0j}, R_{ij}) \\ + \frac{1}{4}\sum_{i<j<k}^{\infty} V_4(R_{0i}, R_{0j}, R_{0k}, R_{ij}, R_{ik}, R_{jk}) + ... \end{aligned} \tag{3.3}$$

where we arbitrarily chose one atom as the center of origin from which we start our summation. The distances R_{ij} in the solid belong to a graph connecting all n atoms (line for the two-body, triangle for the three-body, tetrahedron for the four-body) with $n(n-1)/2$ distances (edges). This expansion needs to converge relatively fast[10] as going beyond four-body terms becomes computationally intractable. In fact, as the number of n-body contributions for the cohesive energy scale like $\mathcal{O}(N^{n-1})$ with N being the number of atoms considered, each n-body contribution should roughly be an order of magnitude smaller compared to the

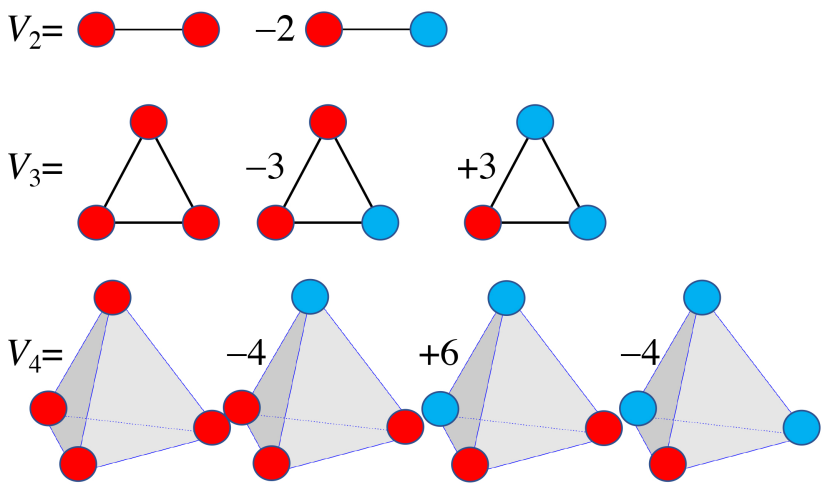

Figure 3.3: Schematic presentation of the many-body contributions to the total potential energy. Atoms in red and ghost atoms are required for the Boys-Bernardi counterpoise correction in blue. For simplification, the contributions are shown for the ideal symmetries only, i.e. diatomic ($D_{\infty h}$), ideal triangle (D_{3h}), and ideal tetrahedron (T_d). The number of contributions follows the row numbers of Pascal's triangle with alternating signs.

previous $(n-1)$ one to ensure convergence. We will see that in contrast to the noble gas elements this is indeed a problem in the bonding region for flerovium.

The individual n-body terms are defined by,

$$V_2(R_{0i}) = E_2(R_{0i}) - 2E_1 \tag{3.4}$$
$$V_3(R_{0i}, R_{0j}, R_{ij}) = E_3(R_{0i}, R_{0j}, R_{ij})$$
$$- E_2(R_{0i}) - E_2(R_{0j}) - E_2(R_{ij}) + 3E_1$$

and similar to the four-body force. E_n is the total electronic energy of the atom $(n = 1)$, diatomic $(n = 2)$, or cluster $(n > 2)$ obtained for example from relativistic coupled-cluster or density functional calculations. This scheme can easily be extended to include ghost atoms for accounting for basis set superposition errors,[227,228] e.g. see Figure 3.3 which summarizes the contributions for the high-symmetry arrangements.

Two-body potential and fitting routine

The quadruple-zeta (4Z) PBE0 and triple-zeta (3Z) CCSD(T) data points were point-wise fitted to an extended Lennard-Jones (ELJ) potential[166]

$$V_2^{\mathrm{ELJ}}(R) = \sum_{k=6}^{n} C_k^{\mathrm{ELJ}} R^{-k} \tag{3.5}$$

by a linear least-squares procedure, where R is the inter-nuclear distance and C_k are the fitting parameters listed in Table 3.1. To ensure that the long-range is correctly described by the London dispersion force[229], the C_6 parameter of the attractive C_6R^{-6} term of the potential is fixed to the dispersion coefficient[230] and the C_7R^{-7} term is not included in the potential. Furthermore, to ensure correct repulsive asymptotic behavior in the short range, the highest-order fitting parameter must be positive. Note that for the PBE0 potential, this boundary condition was omitted to improve accuracy around the equilibrium distance and therefore this potential is not valid for distances shorter than 1.6 Å.

In general, the CCSD(T) method still suffers from the basis set incompleteness and the restriction of active space chosen in the electron correlation procedure. However, the calculations reveal that our active space chosen is sufficiently accurate. To make the point we report BSSE corrected CCSD(T) dissociation energies for Fl_2 and a DZ basis set level at the hcp nearest neighbor distance of 3.834 Å reported by Hermann et al.[231] for the following active orbital energy ranges (in a.u.) : [-0.4,+50.0] 0.0787 eV, [-0.4,+100.0] 0.0787 eV, and [-3.0,+50.0] 0.0770 eV, [-3.0,+100.0] 0.0770 eV, [-10.0,+50.0] 0.0781 eV, [-10.0,+100.0] 0.0780 eV. Therefore, we expect the basis set incompleteness to be the largest source of error and corrected our CCSD(T) two-body potential energies by the complete basis set limit (CBS) approximation (denoted as CCSD(T)*) as follows,

$$V_2^{\mathrm{CCSD(T)^*}} = V_2^{\mathrm{CCSD(T)}} + \Delta V_2^{\mathrm{CBS}} \tag{3.6}$$

Here, $\Delta V_2^{\mathrm{CBS}}$ at the HF level is derived from the formula given by Feller[232], Williams et al.[233]

Table 3.1: Fitting parameters for the PBE0/4Z and coupled-cluster CCSD(T)/3Z derived two-body (ELJ) potential and for the CBS corrected CCSD(T)* results (in a.u.).

ELJ	PBE0/4Z	CCSD(T)/3Z	CCSD(T)*
C_6	-339.643483831	-344.0	-344.0
C_8	1177531.1415	-770391.8502765	-110621.5019612
C_9	-52018617.7654	43077393.39481	4023445.547618
C_{10}	1155631543.57	-1002843991.432	-41492884.78204
C_{11}	-16188552995.9	12735792196.18	-387745374.8124
C_{12}	146566750227.3	-99788509014.52	10316968487.99
C_{13}	-849420907097.0	512163870304.3	-76337297937.02
C_{14}	3076916940736.0	-1731590910598.0	255739280363.9
C_{15}	-6520784516725.0	3626205025279.0	-350507219160.8
C_{16}	6552227093983.0	-3783119151841.0	28695054176.34
C_{18}	-3798072698274.0	2622535615368.0	578047205008.7

$$V_2^{\mathrm{CBS/HF}} = V_2^{\mathrm{HF/2Z}} - \frac{\left(V_2^{\mathrm{HF/2Z}} - V_2^{\mathrm{HF/3Z}}\right)^2}{\left(V_2^{\mathrm{HF//2Z}} - 2V_2^{\mathrm{HF/3Z}} + V_2^{\mathrm{HF/4Z}}\right)} \tag{3.7}$$

and for the pure electron correlation part from the formula given by Helgaker et al.[234]

$$\Delta V_2^{\mathrm{CBS/cor}} = \Delta V_2^{\mathrm{cor/3Z}} - \frac{8}{19}\left(\Delta V_2^{\mathrm{cor/2Z}} - \Delta V_2^{\mathrm{cor/3Z}}\right) \tag{3.8}$$

Three-body potential and fitting routine

For the three-body potential we used an extended Axilrod-Teller-Muto potential (EATM)[91,235,236]

$$V_3^{\mathrm{EAT}}(ijk) = f_\theta\left[C_{\mathrm{AET}} R_g^{-9} + e^{-\alpha R_s}\sum_{k=0}^{m} A_{2k} R_g^{2k}\right] \tag{3.9}$$

$$\text{with } f_\theta = (1 + 3\cos\theta_i \cos\theta_j \cos\theta_k)$$

$$\text{and } R_g = (R_{ij}R_{jk}R_{ik})^{1/3}, R_s = \frac{1}{3}(R_{ij} + R_{jk} + R_{ik})$$

The Axilrod-Teller triple-dipole function $f_\theta C_{\mathrm{EAT}} R_g^{-9}$ is the dominating term in the long-range compared to other three-body interactions.[237] Hence, the parameter C_{EAT} is determined by fitting the long-range data points to this function, after which the other parameters α, A_0, A_2, A_4 and A_6 are determined

Table 3.2: Fitting parameters for the 4Z PBE0 and 2Z CCSD(T) derived three-body EATM potential (in a.u.).

EATM	PBE0	CCSD(T)	CCSD(T)*
C_{EAT}	23349.86591	9106.676863	8952.307205
α	2.612993685	2.891226892	2.930823379
A_0	-7294.665949	-2330.438604	747.1528685
A_2	753.4515046	-598.7559746	-1430.647198
A_4	-42.46646972	91.28651736	165.4699656
A_6	0.813522220	-5.363525164	-8.436634719
A_8	0.0	0.1181645184	0.1689106734

using the full range of equilateral data-points. The parameters are listed in Table 3.2. The ab-initio calculations are produced for an ideal D_{3h} structure with varying R such that $R_{ij} = R$ and $\theta = 120^o$, for which we get $R_g = R, R_s = 3R$ and $f_{120^o} = 5/8$.

For the three-body potential it was not feasible to extend the active space in the coupled-cluster procedure or to use 3Z basis sets because of the computational resources required. However, we could estimate the CBS limit at the HF level from 2Z and 3Z calculations (at short-range we did not achieve convergence with the 4Z basis set). Here we used Feller's exponential CBS correction with fixed exponential as suggested by Jensen[238]

$$V_3^{\mathrm{CBS/HF}} \approx V_3^{\mathrm{HF/3Z}} - 0.3273 \left(V_3^{\mathrm{HF/2Z}} - V_3^{\mathrm{HF/3Z}} \right) \tag{3.10}$$

which we added to our CCSD(T)/2Z results. We refer to this as CCSD(T)* in the following.

Four-body potential and fitting routine

As an approximation for the four-body potential, we make use of the extended quadruple dipole (EQD) four-body potential V_4^{EQD}. The dominant long-range (LR) four-body contribution is the fourth-order (quadruple) dipole (QD) term for the interaction of four atoms i, j, k and l as derived from the classical quadruple dipole Drude model[185]

$$V_4^{\mathrm{QD}}(ijkl) = \omega\left[f(ijkl) + f(ijlk) + f(ikjl)\right] \tag{3.11}$$

with

$$\begin{aligned} f(ijkl) = (R_{ij}R_{jk}R_{kl}R_{il})^{-3}\big[&(\vec{u}_{ij}.\vec{u}_{jk})^2 + (\vec{u}_{ij}.\vec{u}_{kl})^2 \\ &+ (\vec{u}_{ij}.\vec{u}_{li})^2 + (\vec{u}_{jk}.\vec{u}_{kl})^2 + (\vec{u}_{jk}.\vec{u}_{li})^2 + (\vec{u}_{kl}.\vec{u}_{li})^2 \\ &- 3(\vec{u}_{ij}.\vec{u}_{jk})(\vec{u}_{jk}.\vec{u}_{kl})(\vec{u}_{kl}.\vec{u}_{ij}) - 3(\vec{u}_{ij}.\vec{u}_{jk})(\vec{u}_{jk}.\vec{u}_{li})(\vec{u}_{li}.\vec{u}_{ij}) \\ &- 3(\vec{u}_{ij}.\vec{u}_{kl})(\vec{u}_{kl}.\vec{u}_{li})(\vec{u}_{li}.\vec{u}_{ij}) - 3(\vec{u}_{jk}.\vec{u}_{kl})(\vec{u}_{kl}.\vec{u}_{li})(\vec{u}_{li}.\vec{u}_{jk}) \\ &+ 9(\vec{u}_{ij}.\vec{u}_{jk})(\vec{u}_{jk}.\vec{u}_{kl})(\vec{u}_{kl}.\vec{u}_{li})(\vec{u}_{li}.\vec{u}_{ij}) - 1\big] \end{aligned} \tag{3.12}$$

In order to also describe the short-range reasonably well, we introduce a distance-dependent factor $g(ijkl)$ such that the total four-body interaction is given by

$$V_4^{\mathrm{EQD}} = \omega g(ijkl)[f(ijkl) + f(ijlk) + f(ikjl)] \tag{3.13}$$

The short-range function $g(ijkl)$ is chosen as

$$g(ijkl) = g(R_s, R_g) = 1 - e^{b_1(R_s+b_2)^2}\sum_{k=0}^{m} a_k R_g^k \tag{3.14}$$

with the distances defined as

$$R_g = (R_{ij}R_{ik}R_{il}R_{jk}R_{jl}R_{kl})^{1/6} \tag{3.15}$$

and

$$R_s = \frac{1}{6}(R_{ij} + R_{ik} + R_{il} + R_{jk} + R_{jl} + R_{kl}) \tag{3.16}$$

The 4Z PBE0 calculations are produced for an ideal T_d structure with varying R. In this case, the expression for the four-body interaction is simplified to

$$V_4^{\mathrm{EQD}}(R) = \frac{27\omega}{16} g(R, R). \tag{3.17}$$

The exponent in the short-range function $g(ijkl)$ takes the form of a gaussian

Table 3.3: Fitting parameters for the PBE0 derived three-body EQD four-body potential.

EQD	PBE0	EQD	PBE0
ω	-7992722.55619003	a_0	129597.573335952
a_1	-275214.064486529	a_2	262259.700306389
a_3	-147690.171082272	a_4	54436.4255351231
a_5	-13724.0901018183	a_6	2397.26033547513
a_7	-286.554888314985	a_8	22.4411938961907
a_9	-1.04023664629066	a_{10}	0.02168849665813
b_1	-0.33759027067181	b_2	-2.98392301962817

when both parameters b_1 and b_2 are negative, such that $g(ijkl)$ goes to unity at a large distance and the Drude function becomes the dominant term. Hence, to ensure correct asymptotic behavior, initially, the long-range data points are fitted to the Drude function, which contains only ω as a fitting parameter.

The previously published argon four-body potential[185] can be linearly scaled by the parameters γ_x and γ_y, $\gamma_y E^4(\gamma_x R)$, such that it approximately overlaps with the flerovium data-points. This was used to fix the parameters b_1 and b_2 of the function $g(R, R)$, i.e. we have $b_1^{Fl} = b_1^{Ar}\gamma_x^2$ and $b_2^{Fl} = b_2^{Ar}/\gamma_x$. The scaling factor is determined by the ratio between the minimum of the flerovium and argon potentials, $R_{\text{min}}^{\text{Ar}}/R_{\text{min}}^{\text{Fl}} = \gamma_x = 0.765$. Then, as a last step, the fitting parameters of the polynomial, a_k are determined by the least squares fit.

Unfortunately, we were only able to obtain very few CCSD(T)/2Z points with a much restricted active orbital space of $[-2, 20]$ a.u. and without BSSE correction, and we present the PBE0 parameters only in Table 3.3. As we shall see this suffices for our discussion on the many-body decomposition.

Solid-State Calculations using Many-Body Potentials

The analytical expression for the two-body cohesive energy is given by

$$E_2^{\text{ELJ}}(R_0) = \frac{1}{2}\sum_{n\geq 6} C_n^{\text{ELJ}} L_n R_0^{-n} \tag{3.18}$$

where R_0 is the nearest neighbor distance of the lattice $R_0 = \min\{R_{0i}\}$. This

expression can be evaluated analytically for the cubic lattices and for the ideal hexagonal closed packed (hcp) structure from so-called lattice sums L_n, which can be computed to computer precision through Bessel function expansions.[168] Lattice sums for the hcp structure with $c/a \neq \sqrt{8/3}$ are currently being derived in our group and are therefore not yet available, and a numerical treatment has been chosen instead. The three- and four-body forces also have to be determined numerically by summing over 20,000 and 5,000 atoms respectively in the crystal. This restriction does not affect the accuracy of the values reported in this work. The minimum nearest neighbor distance is obtained analytically through lattice summations if possible, and by Fletcher and Powell[239] described an optimization procedure if higher-body forces are included.

Monte-Carlo Method

In this work, the parallel tempering Monte-Carlo (PTMC) method is applied to cells with periodic boundary conditions. For these types of simulations, the melting temperatures of the cells converge rapidly and earlier studies on the noble gases showed that cells with 864 atoms converged to the bulk melting temperature.[164,165,188] For the noble gases, the inclusion of two and three-body interactions were sufficient to successfully obtain agreement with the experimental values. For flerovium, the situation is slightly different as the four-body interactions are non-negligible. Hence simulations performed here will serve as a first estimate.

The simulations are performed in the isobaric-isothermal ensemble (NPT); that is, the number of atoms, N, and temperature T is held constant, but the sample cells are allowed to change volume, V, in order to remain at atmospheric pressure ($P = 1$ bar) throughout the simulation. Starting with fcc sample cells with periodic boundary conditions, random configurations are generated by arbitrarily moving atoms and scaling the volume of the simulated cell. New configurations are accepted with the Boltzmann probability

$$\alpha(x \to x') = \min[1, \exp^{-\beta[\Delta E + P\Delta V] + N\ln(V/V')}] \tag{3.19}$$

with $\beta = 1/(k_B T)$. In total, 32 temperature trajectories are propagated simultaneously spanning the temperature interval of the melting transition. For each simulated temperature 3×10^6 MC cycles are performed and statistical data is collected from the last 1×10^6 cycles. Exchanges of configurations are attempted of near-lying temperatures according to the parallel tempering method in order to overcome ergodicity problems and improve convergence. The inner energy $U(T)$ and volume $V(T)$, the enthalpy $H(T)$, and the heat capacity at constant pressure, $C(T)$ are obtained as a continuous function of temperature T using the histogram re-weighting technique.

The total N-body interaction energy E_i, for micro-state i, is calculated by summing over all two- and three-body energies interactions up to a spherical cut-off distance of $R_c = \frac{1}{2}L$, where L is the length of a simulation cell at 0 K. Four-body terms are not considered in our MC simulations because of the very high computational demand required. The internal energy U is defined as the statistical mean value of energies E_i, $U = \langle E_i \rangle$ and the heat capacities are obtained from the relation

$$C(T) = \left.\frac{\partial H(T)}{\partial T}\right|_p = \frac{\langle H(T)^2 \rangle - \langle H(T) \rangle^2}{k_B T^2} \tag{3.20}$$

where the enthalpy is given by $H(T) = U(T) + PV(T)$. The temperature at which the solid-liquid phase transition occurs can be identified from a sudden increase in the inner energy, which corresponds to the temperature where the heat capacity curve $C(T)$ has a peak. However, the absence of impurities and a surface shifts the solid-to-liquid phase-transition temperature, T_{SL}, to an increased value, referred to as superheating. We adopt the superheating correction factor as introduced by Koči et al.[240] to obtain the bulk melting temperature.

$$\frac{T_{SL}}{T_{MP}} = 1 + \frac{\ln 2}{3} \approx 1.231. \tag{3.21}$$

Although the superheating correction factor comes from the high-pressure

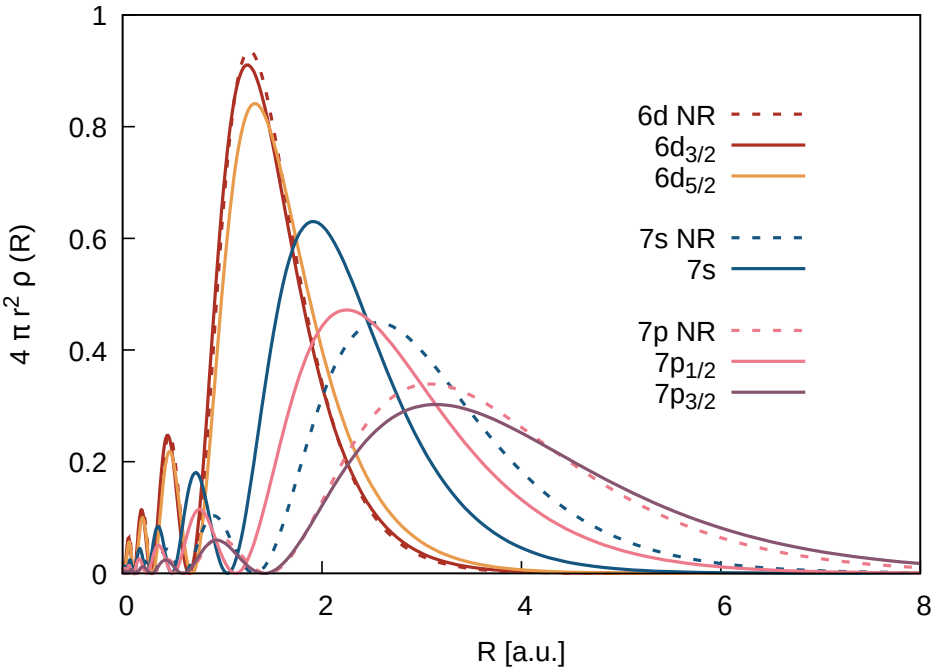

Figure 3.4: Relativistic and nonrelativistic valence radial densities of flerovium from multi-reference calculations[3] distributing the two $7p$ electrons over the $7p_{1/2}$ and $7p_{3/2}$ levels.

limit, this approximation worked extremely well for determining the melting points of the heavier noble gases.[164,165] For a general theory of melting as a dislocation-mediated phase transition see Burakovsky et al.[241].

3.3 Results and Discussion

The Flerovium atom

The flerovium atomic electronic structure has already been discussed by many authors.[173,182,196,242–252] We only point out the most important features as shown in Figure 3.4.

Using Fock-space coupled-cluster theory, Landau et al.[173] calculated the $^3P_0(7p_{1/2}^2) \rightarrow {}^3P_1(7p_{1/2}^1 p_{3/2}^1)$ excitation energy at 3.27 eV, a rather large value for the 7p spin-orbit splitting (for comparison, the $^3P_0 \rightarrow {}^3P_1$ excitation energy for Pb is 0.97 eV[253]), which is seen in the spatial separation between the $7p_{1/2}$ and the $7p_{3/2}$ orbitals in Figure 3.4.

A comparison between the nonrelativistic ($\langle r \rangle^{\mathrm{NR}}_{7p}$ = 1.983 Å) and the corresponding relativistic r-expectation values ($\langle r \rangle^{\mathrm{R}}_{7p_{3/2}}$ = 2.098 Å and $\langle r \rangle^{\mathrm{R}}_{7p_{1/2}}$ = 1.444 Å) shows that this is mainly due to the strong relativistic contraction and stabilization of the $7p_{1/2}$ orbital, and is because the $7p_{1/2}$ orbital has a substantial density close to the nucleus where the relativistic perturbation operators act.[254,255] Moreover, we see that the $7p_{1/2}$ orbital is more compact and extends less into the valence space compared to the nonrelativistic $7p$ orbital.

The ionization potential has been estimated at 8.65 eV[252] above that of Pb (7.42 eV), but still below the noble gases including Og with 8.91 eV[192]. Concerning the dipole polarizabilities, we have 30.6 a.u. for Fl, and for comparison for Og 46.3 a.u.[192] However, Fl has a zero electron affinity unlike Pb (0.36 eV) or Og (0.076 eV).[256,257] We note that the 7s orbital relativistically contracts ($\langle r \rangle^{\mathrm{R}}_{7s}$ = 1.165 Å compared to $\langle r \rangle^{\mathrm{NR}}_{7s}$ = 1.594 Å) and stabilizes substantially as expected for a superheavy element. In fact, energetically $7s$ and $6d_{5/2}$ orbitals are very close and core-like (orbital energy $\epsilon^{\mathrm{R}}_{7s}$ = −19.6 eV and $\epsilon^{\mathrm{R}}_{6d_{5/2}}$ = −21.6 eV). Hence we expect that Fl with a $7p^2_{1/2}$ is chemically more inert than its lighter congeners, but not as inert as some of the noble gases.

Figures 3.5 to 3.7 show the ELFs for the heaviest group 12, 14, and 18 atoms at the nonrelativistic (NR), scalar relativistic (SR) and fully relativistic (R) PBE level of theory for comparison. We have recently argued that the large spin-orbit splitting in the 7p electronic shell of Og (10.13 eV) is responsible for this superheavy element showing a uniform-gas-like behavior in the valence region[180], although this was criticized later on by Kaygorodov et al.[257] Nevertheless, we see from Figures 3.5 and 3.7 that relativistic effects lead to the smearing out of electron density, which becomes more electron gas-like. Flerovium is no different in this respect compared to Cn and Og, except for Fl and Og the influence of strong spin-orbit effects is visible. For Fl, the nonrelativistic and scalar relativistic ELF pictures do not differ substantially.

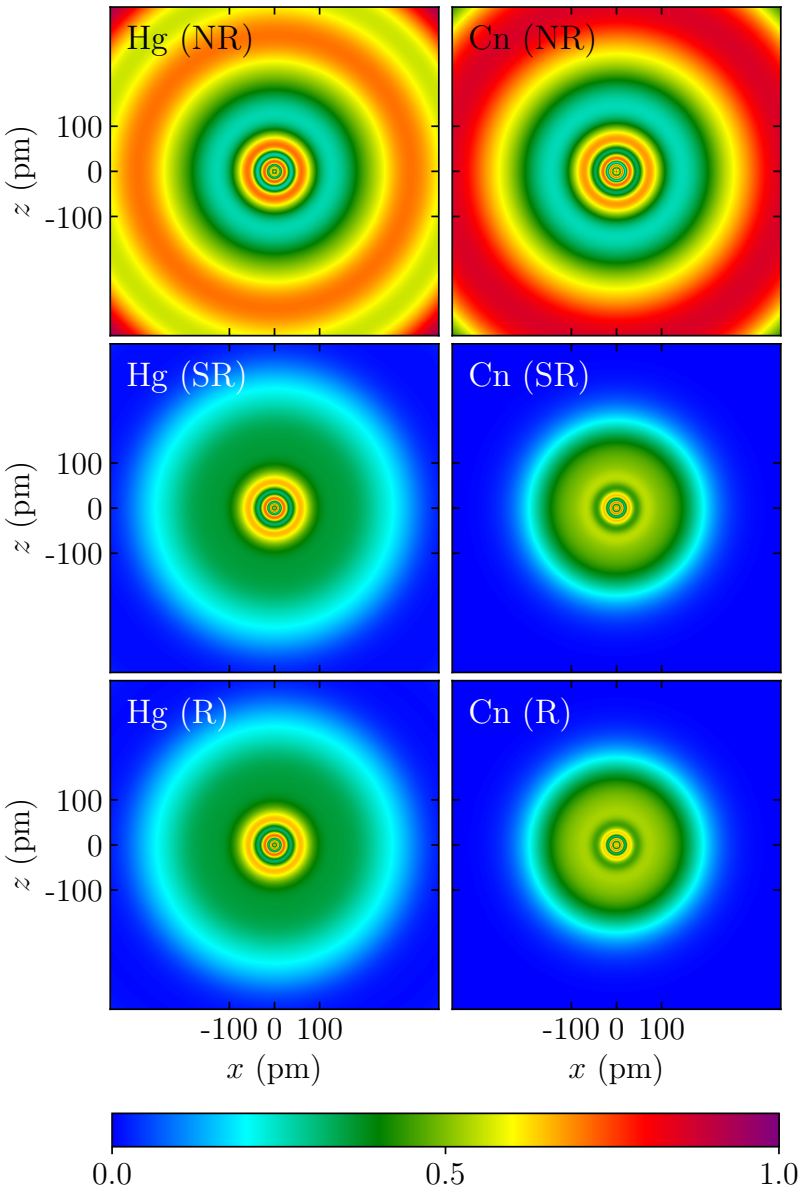

Figure 3.5: ELFs $D(r)$ from nonrelativistic (NR), scalar relativistic (SR) and fully relativistic (R) DFT calculations at PBE/dyall.ae4z level of theory. A) Hg (left) and Cn (right). B) Pb (left) and Fl (right). C) Rn (left) and Og (right).

Potential energy curves and molecular properties for the flerovium dimer

The potential energy curves for the diatomic Fl_2 at different levels of theory are shown in Figure 3.8A, and the corresponding equilibrium molecular properties are listed in Table 3.4.

Like the noble-gas dimers,[4] or the Group 2 or 12 dimers,[156] Fl_2 is unbound at the HF level and electron correlation is entirely responsible for the chemical

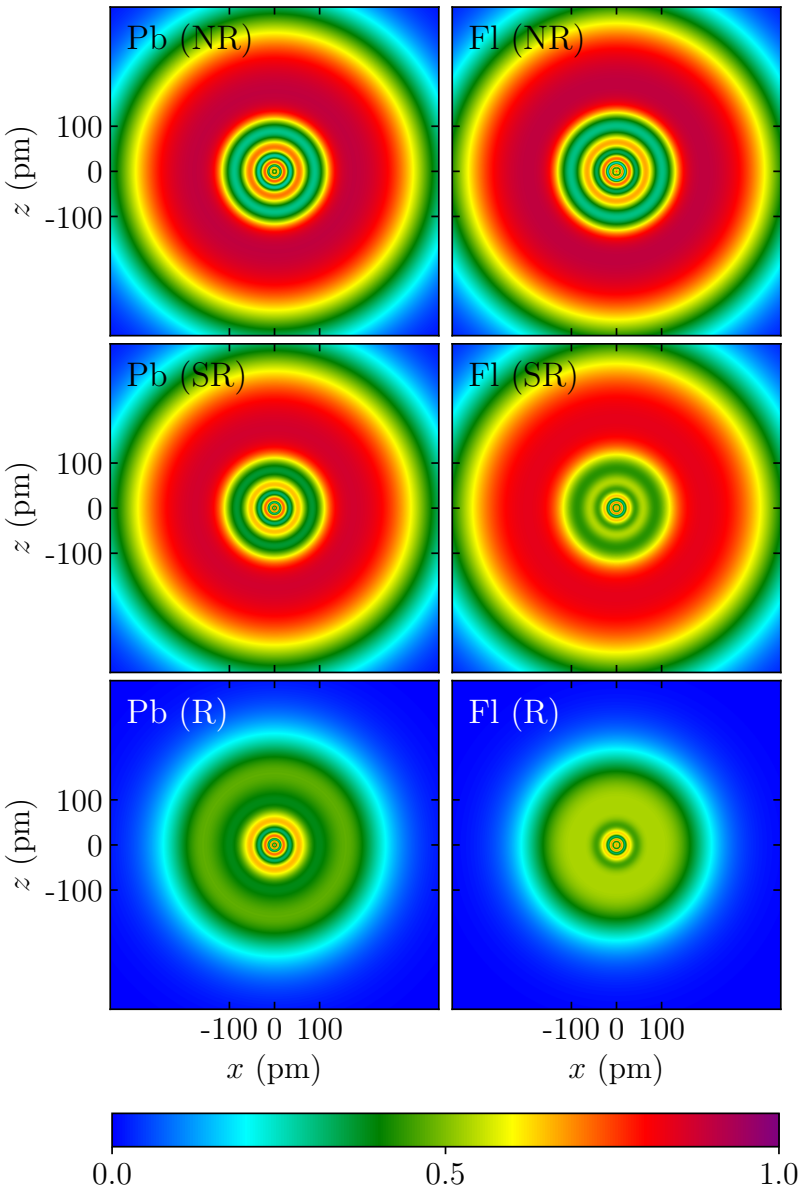

Figure 3.6: ELFs $D(r)$ from nonrelativistic (NR), scalar relativistic (SR) and fully relativistic (R) DFT calculations at PBE/dyall.ae4z level of theory. A) Hg (left) and Cn (right). B) Pb (left) and Fl (right). C) Rn (left) and Og (right).

bonding (there is a tiny minimum at 5.721 Å with a depth of 3×10^{-5} eV at the HF/4Z level of theory, which we regard as an artifact of the method). As expected, the performance of DFT varies greatly for such a weakly interacting system, see Table 3.4. LDA overbinds while B3LYP underbids compared to our best-coupled cluster curve. We point out that changing the basis set from $2Z \rightarrow 3Z \rightarrow 4Z$ lowers the repulsive wall at all levels of theory leading to stronger binding as one expects. Further, the CBS coupled-cluster result improves the dissociation energy considerably and lowers the bond distance.

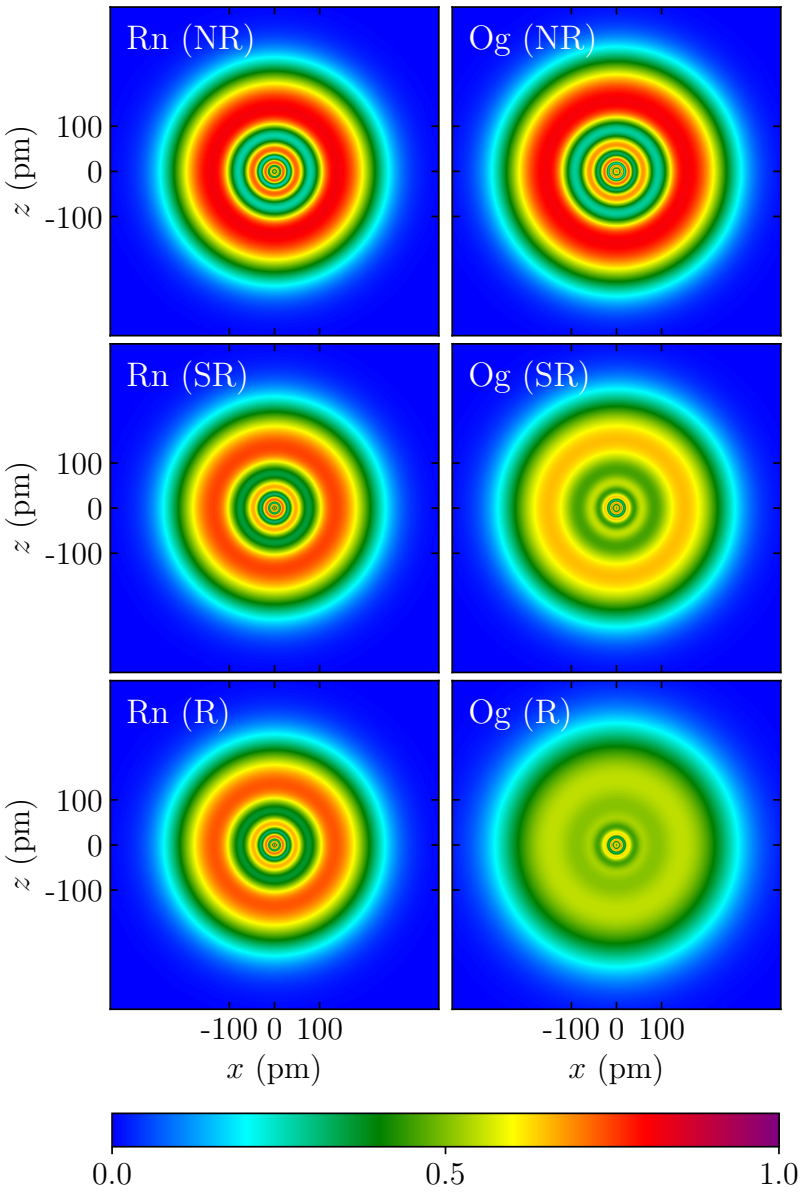

Figure 3.7: ELFs $D(r)$ from nonrelativistic (NR), scalar relativistic (SR) and fully relativistic (R) DFT calculations at PBE/dyall.ae4z level of theory. A) Hg (left) and Cn (right). B) Pb (left) and Fl (right). C) Rn (left) and Og (right).

Faegri Jr[258] used a dual family basis set which is similar to our 3Z basis set, but their basis set is slightly extended in the g-space. A comparison of our CBS coupled-cluster results to that of Borschevsky gives a scaling factor of $\lambda_E = 1.206$ for the energy and $\lambda_R = 0.989$ for the equilibrium distance. Anyway, the CBS limit coupled cluster potential energy curve presented here is the best approximation we currently have for the flerovium dimer.

Table 3.4: Molecular properties for Fl_2. Equilibrium distance R_e in Å, dissociation energy D_e in eV (not corrected for zero-point vibrational energy), and force constant k_e in N/m obtained from DFT and CCSD(T) calculations using Dyall's double-zeta (2Z), triple-zeta (3Z) and quadruple-zeta (4Z) basis sets. FDF denotes a Faegri dual type $27s24p18d14f6g$ basis set.[6] For the basis set used by Liu et al.[7]. CCSD(T)(ext) indicates an extended active space of $[-10, 50]$ a.u. was chosen for the 2Z basis set. CCSD(T)* is corrected to the CBS limit. For comparison, results from other authors and for Cn_2 and Og_2 are also provided.

Method		R_e	D_e	k_e
plane-wave/PAW	*Cutoff*			
PBEsol	600 eV	3.333	0.210	–
PBE	600 eV	3.481	0.140	–
PBE-D3	600 eV	3.476	0.177	–
PBE0	600 eV	3.460	0.133	–
PBE0-D3	600 eV	3.454	0.172	–
GTO/all-electron	*Basis*			
LDA	2Z	3.259	0.341	27.9
	3Z	3.249	0.347	28.4
	4Z	3.246	0.352	28.5
PBE	2Z	3.508	0.138	12.5
	3Z	3.495	0.140	11.8
	4Z	3.491	0.143	12.2
PBE0	2Z	3.557	0.096	8.87
	3Z	3.543	0.099	9.03
	4Z	3.536	0.101	9.49
B3LYP	2Z	3.695	0.053	6.05
	3Z	3.680	0.053	6.00
	4Z	3.676	0.054	6.27
MP2	2Z	3.507	0.129	11.1
	3Z	3.461	0.142	12.0
CCSD(T)	2Z	3.634	0.085	7.43
	3Z	3.606	0.092	7.47
CCSD(T)(ext)	2Z	3.640	0.084	7.31
CCSD(T)*	CBS	3.588	0.096	8.53
other work				
CCSD(T)[6]	FDF	3.547	0.117	
PP-CCSD(T)[7]	PPBS	3.732	0.07	6
BDF-BP[7]	DFT	3.463	0.12	14
Cn_2 CCSD(T)[6]	FDF	3.461	0.084	-
Og_2 CCSD(T)[4]	QZ	4.314	0.078	8.68

If we compare the atomic polarizabilities we have (in a.u.) α(Cn)=27.4 $< \alpha$(Fl)=31.9 $< \alpha$(Og)=58.0. However, in terms of the binding energy, we have a different ordering, D_e(Og)$<$ D_e(Cn)$<$ D_e(Fl). The dispersion (dipole-dipole) interaction is given by $V_{\mathrm{DD}} = -c\alpha^2/R^6$,[259] and for the trend in binding energies one has to consider not only the atomic polarizabilities but also the bond

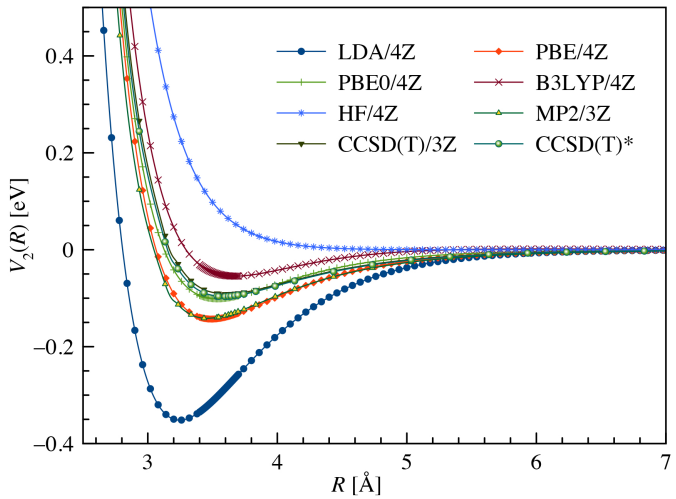

(A)

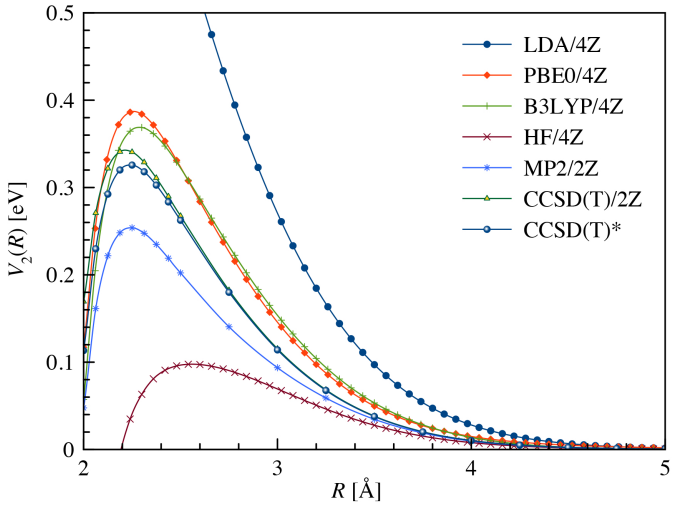

(B)

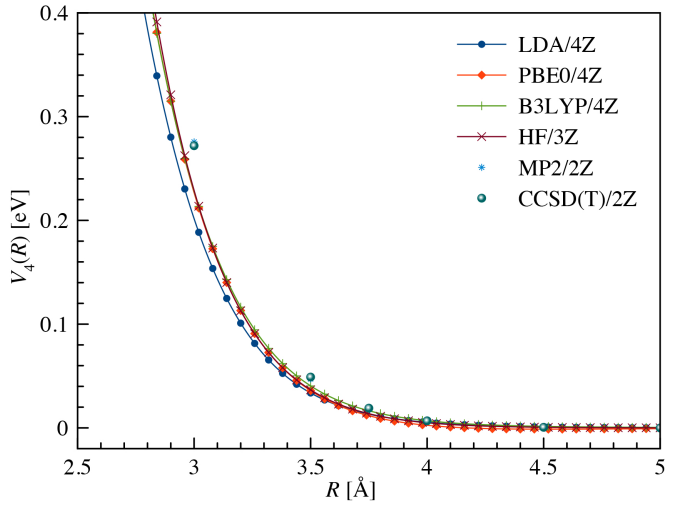

(C)

Figure 3.8: Two- (A), three (B), and four-body (C) potentials at various DFT, HF, MP2 and CCSD(T) levels of theory.

distances, which enter as the inverse sixth power(!), and the coupling constants c related to the frequency of the oscillating dipole (or the dispersion coefficient C_6).

For the coupling constant, we derived the following values from the dissociation energies in Table 3.4 (in a.u.) c(Cn)= 0.32, c(Fl)= 0.38 and c(Og)= 0.14 (for Fl we obtain $c = 0.40$ from the $C_6 = c/\alpha^2$ value in Table 3.1 and the polarizability from Schwerdtfeger and Nagle[178] which is in good agreement). In this sense, Fl is more closely related to Cn (and Hg) than to Og. The rather short bond distance we obtain for the flerovium dimer will cause problems for the many-body expansion of the interaction energy (as found for Hg for example Hermann et al.[10]) as we shall see in the following.

Many-Body Expansion and the Flerovium Trimer and Tetramer

Figures 3.8B and 3.8C demonstrate that, around the two-body potential minimum, the three- and four-body interactions are quite large compared to the two-body potential, which will have consequences for the convergence of the many-body expansion towards the solid state. For the three-body potential, we see large variations between the different DFT results as this is the case for the two-body curves. Here we see a lesser agreement between the CCSD(T)* and the PBE0 curves with CCSD(T)* being less repulsive in energy. This agrees with a previous analysis by Tkatchenko and von Lilienfeld[260] who pointed out that for the noble gas elements, the three-body Axilrod-Teller term is, compared to coupled-cluster theory, too repulsive in the long-range for all functionals applied. LDA results in the most repulsive interaction. Tkatchenko and von Lilienfeld[260] describe this as follows:

The "paradox" of the remarkable performance of LDA in describing solid state properties and in failing to describe molecular systems seems - at least partially - to be due to the fortuitous cancellation of many-body contributions errors with two-body errors in the bulk.

Concerning the (repulsive) four-body interactions we see that surprisingly all curves obtained at different levels of theory agree with each other extremely well, that is the difference between different levels of theory is less pronounced here. Because of computer time and hardware requirements, we were only able to obtain a few points at the 2Z level for the four-body potential (with no BSSE correction), where we had to reduce the active orbital space to $[-2, 30]$ a.u. These points are included in Figure 3.8C, showing at least that they do not deviate much from all the other curves including HF. This implies that electron correlation or dispersion forces play a rather minor role in the four-body quadruple-dipole force which is dominated by the HF contribution.

Table 3.5 lists the equilibrium distances and atomization energies for Fl_3 and Fl_4 at various levels of theory, and Figure 3.9 summarizes the evolution of the bond distances from the dimer to the tetramer at various levels of theory. The bond distances vary widely at different levels of theory, but the overall trend remains the same. A comparison to Oganesson shows the same trend of increasing bond distances from the dimer to the tetramer. In comparison for flerovium, we observed far shorter bond distances as one expects from a relativistically stabilized and contracted $7p_{1/2}$ shell, Figure 3.4. At shorter bond distances the convergence of the many-body expansion deteriorates, as we shall see for the solid-state results presented in the next section.

Bulk Properties

Structure and Stability

To explore the stability of the bulk phases we consider the fcc and hcp lattices with plain and dispersion-corrected SO-DFT/PAW methods as well as with CCSD(T)- and PBE0-derived (dispersion-exclusive) MBE potentials including up to 4-body interactions. In the following, we will first discuss the MBE results and then start a critical comparison with the DFT/PAW results.

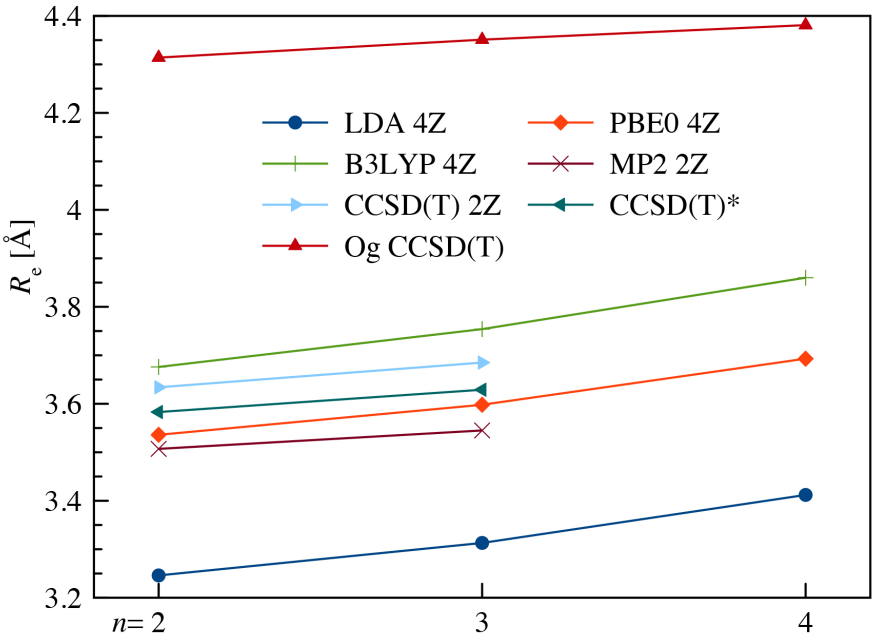

Figure 3.9: Bond distances for $Fl_n (n = 2, 3, 4)$. For comparison, the data for Og_n are also shown (obtained from the many-body potentials of Jerabek et al.[4]).

Table 3.5: Molecular properties for Fl_3 and Fl_4. Equilibrium distance R_e in Å and atomization energy ΔE_a in eV, from DFT and CCSD(T) calculations using Dyall's basis sets (see Table 3.4 for details). For CCSD(T)* for Fl_3 the DZ three-body and the CCSD(T)* 3Z/4Z two-body terms were used for the total interaction energy.

Molecule	Method	Basis	R_e	ΔE_a
Fl_3	LDA	2Z	3.328	0.869
		3Z	3.317	0.886
		4Z	3.313	0.898
Fl_4	LDA	2Z	3.427	1.427
		3Z	3.416	1.455
		4Z	3.412	1.475
Fl_3	PBE0	2Z	3.623	0.245
		3Z	3.607	0.254
		4Z	3.598	0.261
Fl_4	PBE0	2Z	3.718	0.401
		3Z	3.705	0.420
		4Z	3.693	0.433
Fl_3	B3LYP	2Z	3.782	0.127
		3Z	3.761	0.129
		4Z	3.754	0.132
Fl_4	B3LYP	2Z	3.889	0.194
		3Z	3.872	0.198
		4Z	3.860	0.203
Fl_3	MP2	2Z	3.545	0.354
	CCSD(T)	2Z	3.685	0.230
	CCSD(T)*	CBS	3.629	0.261

Table 3.6: Nearest neighbor distance R_{NN} (in Å), volume (in $\mathrm{cm}^3/\mathrm{mol}$), cohesive energy E_{coh} (in eV) and bulk modulus B (in GPa) for the *face-centered cubic* (fcc) structure of flerovium obtained from DFT/PAW and MBE (many-body expansion). Results at CCSD(T) level use the 3Z basis set, while at the PBE0 level, the 4Z basis set. CCSD(T)* 2+3+4-body results use the PBE0 4-body term. The DFT/PAW structure used in all further calculations is set in bold.

method	V	R_{NN}	$-E_{\mathrm{coh}}$	B
DFT/PAW				
PW91 [231]		3.897	0.487	12.5
PW91 *this work*[a]	26.60	3.949	0.349	10.1
PBEsol	23.22	3.792	0.491	13.6
PBE	27.18	3.997	0.294	9.8
PBE-D3	24.87	3.880	0.575	12.8
PBE0	26.51	3.963	0.265	9.6
PBE0-D3	24.51	3.861	0.577	14.9
MBE				
PBE0 2-b	17.76	3.472	0.705	29.9
PBE0 2+3-b	25.26	3.900	0.264	9.1
PBE0 2+3+4-b	28.36	4.053	0.223	7.7
CCSD(T) 2-b	18.40	3.509	0.720	26.8
CCSD(T) 2-b	18.07	3.488	0.764	29.8
CCSD(T) 2+3-b	22.92	3.776	0.451	13.7
CCSD(T) 2+3+4-b	26.10	3.943	0.380	11.1

[a]This work employs a different PAW than Hermann et al. [231].

Figure 3.10A summarizes the cohesive energies as a function of the nearest-neighbor distance for the fcc structure, underlining the importance of the higher N-body forces to the cohesive energy. The data are collected in Table 3.6. Of course, we neglect five- (and higher) body forces and the correct angular dependence, which was taken from a simple Drude dipole interaction model. [259] Nevertheless, the results show that the cohesive energy is not converging fast to the MBE in contrast to, for example, the lighter noble gas elements. What is evident from Figure 3.10A is that the rather short distance between the flerovium atoms upsets the convergence of the MBE.

Turning to the hcp structure we show the cohesive energy as a function of the c/a ratio for the MBE at the PBE0 and CCSD(T)* level of theory in Figure 3.10B. The data are collected in Table 3.7. The two-body curves have a minimum very close to the ideal hcp $c/a = \sqrt{\frac{8}{3}}$ ratio, i.e. if we define $c/a = \sqrt{\frac{8}{3}} + \Delta_{c/a}$ we obtain $\Delta_{c/a} = -4.2 \times 10^{-4}$ (PBE0) and 1.2×10^{-3} (CCSD(T)*).

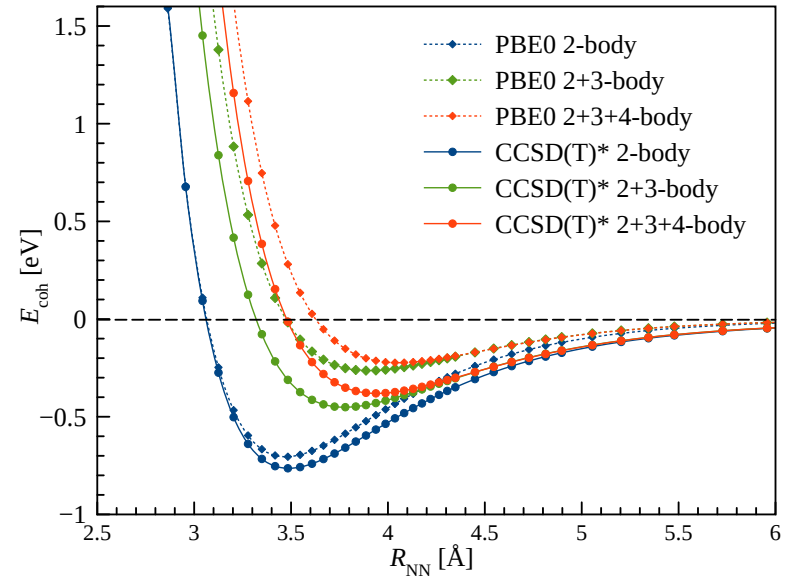

(A)

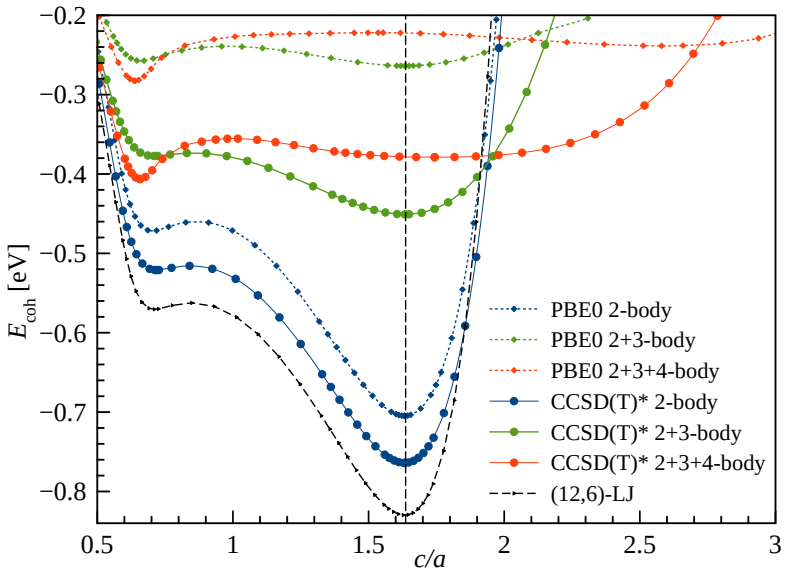

(B)

Figure 3.10: Cohesive energy curves. A) $E_{\mathrm{coh}}(R_{\mathrm{NN}})$ against the nearest neighbor distance R_{NN} for the PBE0 (dotted lines) and CCSD(T)* (solid lines) many-body contributions to the fcc structure. B) along the ratio of lattice constants c/a line for hcp flerovium at the PBE0 (dotted lines) and CCSD(T)* (solid lines) levels of theory and for different many-body contributions. The vertical line shows the ratio of $c/a = \sqrt{8/3}$ for the ideal hcp structure. The (12,6)-LJ curve (dashed line) is also shown using the dissociation energy and equilibrium distance from the CCSD(T)* result shown in Table 3.4.

In fact, for an ideal (12,6)-LJ potential we obtain from lattice summations $\Delta_{c/a} = -2.30 \times 10^{-4}$.[261] What is of interest here is that the two-body potential shows a *second* metastable minimum at a rather small ratio of c/a =+0.703 (which

we term *inv* c/a for the following as we have $c/a \approx \sqrt{\frac{3}{8}})$ and E_{coh} =-0.472 eV at the PBE0 level of theory, and c/a =0.719 and $E_{\text{coh}} = -0.521$ eV for CCSD(T)*. This second metastable minimum is also in the region where the nearest neighbor distance is dominated by the cell parameter c, i.e. $R_{\text{NN}} = \min\{R_{ij}\} = c$, in the region $c/a \leq \frac{2}{3}$.

$$R_{\text{NN}} = \min\left\{a, c, \sqrt{\frac{a^2}{3} + \frac{c^2}{4}}\right\} \tag{3.22}$$

Figure 3.10B also demonstrates that the basic (12,6)-LJ potential has the same topological feature compared to the more accurate ELJ potential. A detailed analysis of general LJ potentials in terms of lattice sums will be published elsewhere.[261]

This can be easily derived from the relation of the nearest neighbor distances to the c, a cell parameters for the hcp structure adding the three-body force, we obtain the same qualitative picture except for the fact that along the c/a line the cohesive energy curve becomes extremely shallow with the main maximum close to ideal hcp structure, i.e. $\Delta_{c/a} = +1.7 \times 10^{-3}$ for PBE0 and $+1.2 \times 10^{-3}$ for CCSD(T)*. The metastable minimum for PBE0 is at $c/a = 0.660$ with E_{coh} =0.257 eV and for CCSD(T)* level it is located at $c/a = 0.709$ and E_{coh} =0.377 eV, very close in energy to the deeper lying minimum, see Table 3.7.

Finally, adding the PBE0 four-body force to our coupled-cluster results, the metastable minimum now becomes the lowest lying minimum (within hcp or fcc), with a c/a ratio of 0.640 for PBE0 and 0.657 for CCSD(T)*. The transition state (towards the second metastable minimum) lies at only 0.061 eV (PBE0) and 0.051 eV (CCSD(T)*) above that minimum, with the metastable state now being at $c/a = 2.580$ (PBE0) and 1.744 (CCSD(T)*).

This transition state lies close to the ideal c/a ratio for PBE0. There is obviously a subtle interplay between the many-body forces leading to this unique topological feature. However, this should be taken with a grain of salt since the

Table 3.7: Cell parameters a and c and nearest neighbor distance R_{NN} (in Å), volume (in $\mathrm{cm}^3/\mathrm{mol}$), cohesive energy E_{coh} (in eV) and bulk modulus B (in GPa) for the *hexagonal close-packed* (hcp) structure of flerovium obtained from DFT/PAW and MBE. The CCSD(T)* 2+3+4-body results use the 3Z basis set and PBE0 4-body term, PBE0 results use the 4Z basis set. For some of the hcp structures, both relevant minima with different c/a ratios are shown. The nearest neighbor distance R_{NN} is given by Equation (3.22). The DFT/PAW structure used in all further calculations is set in bold.

method/comment	a	c	V	R_{NN}	$-E_{\mathrm{coh}}$	B
DFT/PAW						
PW91 [231]	4.126	6.014	26.70	3.834	0.504	14.6
PW91 *this work*[a]	3.995	6.211	25.29	3.863	0.349	6.0
PW91 *inv.* c/a [b]	5.708	3.682	31.05	3.763	0.371	9.1
PBEsol	3.850	5.952	23.03	3.847	0.489	16.8
PBEsol *inv.* c/a	5.510	3.523	27.84	3.622	0.498	13.9
PBE	3.995	6.473	27.05	3.995	0.300	8.1
PBE *inv.* c/a	5.725	3.705	31.57	3.781	0.314	7.7
PBE-D3	3.876	6.351	24.86	3.872	0.578	12.5
PBE-D3 *inv.* c/a	5.537	3.692	29.37	3.689	0.530	11.1
PBE-D3 *small* c	3.890	6.187	24.53	3.890	0.578	12.6
PBE0	3.924	6.506	26.43	3.924	0.264	9.6
PBE0-D3	3.813	6.389	24.27	3.812	0.576	14.9
PBE0-D3 *small* c	3.873	6.165	24.30	3.873	0.575	13.5
MBE						
PBE0 2-b	3.473	5.670	17.77	3.473	0.705	29.9
PBE0 2+3-b	3.899	6.373	25.17	3.899	0.264	9.2
PBE0 2+3+4-b	5.587	3.572	28.96	3.572	0.282	-
	3.626	9.398	31.98	3.626	0.239	-
CCSD(T) 2-b	3.510	5.730	18.34	3.510	0.721	26.7
CCSD(T) 2-b	3.488	5.695	18.00	3.488	0.764	28.5
CCSD(T) 2+3-b	3.775	6.169	22.84	3.775	0.451	13.7
CCSD(T) 2+3+4-b	5.401	3.550	26.90	3.550	0.406	-
	3.862	6.736	26.10	3.862	0.379	-

[a] This work employs a different PAW than Hermann et al. [231].
[b] This second minimum was obtained by restarting the optimization after swapping the length of the a and b vectors. It corresponds to the leftmost minimum shown in Figure 3.10B.

previously discussed VASP DFT-D3 calculations show the global minimum close to the ideal c/a ratio, which may hint towards inconsistencies in our 4-body force and perhaps the underestimation of the cohesive energy for our two-body potential which favors the ideal c/a ratio (see discussion of the DFT results below). A further warning should be added here, as other distortions from the hcp structure may occur when larger unit cells are employed.

We note that in general, large deviations from the ideal $c/a = \sqrt{\frac{8}{3}}$ ratio are more typical for metallic systems. For example, Häussermann and Simak investigated the c/a ratios for Group 2 and 12 metals at fixed experimental volume.[262] Their results show that Mg adopts the ideal hcp structure, while for Be, Zn, and Cd a symmetry breaking is observed to either lower (c/a =1.568 for Be) or higher ratios (c/a=1.856 for Zn and 1.886 for Cd, see also discussion in Mewes et al.[187] for Hg and Cn) at the DFT level of theory. They related their results to *s*-*p* hybridization effects.

Figure 3.11 shows the two hcp structures for the lowest and largest c/a ratios considered here and observe a significant structural change at both ends of the c/a scale compared to the ideal hcp structure as shown in Figure 3.11. At large c/a values we have the situation of weakly interacting hexagonal (2-dimensional closed-packed) flerovium sheets, while at small c/a values we see weakly interacting one-dimensional flerovium chains.

Concerning the VASP/DFT results, plain dispersion-uncorrected DFT methods predict the minimum at very low c/a ratios close to 0.6 to be lower in energy than the more common one, dispersion-corrected DFT methods, which favor the ideal hcp structure. We report the presence of two difference minima with near-ideal c/a ratios, see Table 3.7.

For example, the c/a ratios optimized with PBE-D3 are 1.590 and 1.639, and 1.592 and 1.676 with PBE0-D3, all of which are distinctly lower in energy by $\approx$ 0.05 eV than the minima near $c/a \approx 0.6$. Similarly, the dispersion-inclusive CCSD(T)-derived 2+3-body MBE result shows the global minimum at the near ideal c/a-ration, and only a meta-stable and very shallow minimum near $c/a \approx 0.6$. With the corresponding 2+3-body MBE potential the two minima are nearly degenerate. The inclusion of PBE0-derived 4-body term strongly favors the minimum near $c/a \approx 0.6$ in both MBEs on a very shallow $E_{\mathrm{coh}}(c/a)$ curve, and in the case of the pure PBE0-derived MBE the minimum near the ideal c/a ratio vanished entirely.

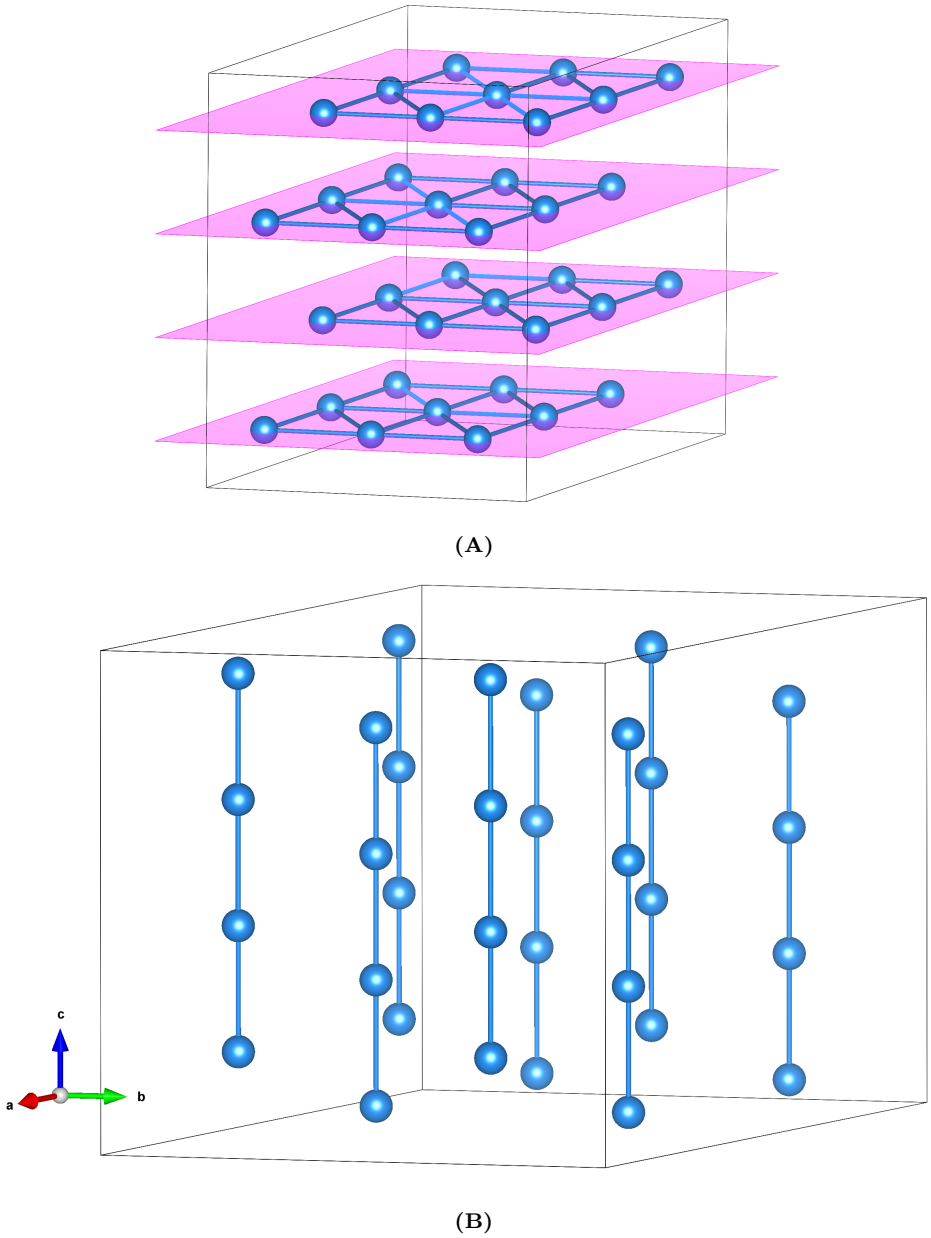

Figure 3.11: The hcp lattice for the two cases of (A) c/a=2.0 shows weakly interacting hexagonal sheets, and (B) c/a=0.5 shows weakly interacting one-dimensional chains.

Concerning the previously reported DFT/PAW structure of Hermann and coworkers,[231] who employed the PW91 functional and a different PAW potential. This method combination predicts the hcp structure to be considerably more stable than fcc, and generally rather large cohesive energies of ca. -0.5 eV considering that the plain PW91 functional does not include dispersion effects. The PAW from Trombach et al.[195] with the same PW91 functional provides considerably smaller cohesive energies for both hcp and fcc of ca. -0.35 eV and

the two phases become near degenerate.

Anticipating the problem with correctly describing the c/a-ratio of the minimum hcp structure, we further explored the hcp lattice and located another minimum structure by swapping the length of the a and c vectors followed by re-optimization (*inv.* c/a). This minimum is now considerably more stable with PW91 and all other dispersion-uncorrected functionals compared to the hcp minimum with a near-ideal c/a-ratio.

Moving to further density-functional approximations, the energetic ordering of the structures is essentially the same with all dispersion-uncorrected density functionals. The main difference between the DFT methods is that PBEsol generally provides more dense and more strongly bound structures, whereas the opposite is the case with PBE (and PBE0).

The most significant changes occur when London dispersion effects are included via Grimmes D3 correction with the parameters presented in Trombach et al.[195] The D3 correction leads to a doubling of the cohesive energies, which is not at all surprising since Fl is a large and polarizable element with a large dispersive type of interaction. More importantly, in contrast to plain functionals, the dispersion-corrected variants PBE-D3 and PBE0-D3 predict the common hcp structure (with c/a ratio close to its ideal value) to be well below the c/a-inverted one, and the fcc and hcp lattices to be virtually degenerate.

Upon closer investigation of the PBE-D3 and PBE0-D3 calculations for the hcp lattice converged on different minima (a slight variation of the c/a ratio due to smaller c in the PBE-D3 result). We assume this is related to the general shallowness of the potential-energy surface near the ideal c/a ratio as shown in Figure 3.10B for the MBE results. To further investigate this issue, we reoptimized the PBE0-D3 optimized structure with PBE-D3 and vice versa. In both cases, these additional optimizations converged very slowly but eventually converged, confirming the existence of a second near-degenerate local minimum, which we

indicate as *small c* in Table 3.7. In the following and for the band-gap calculations, we will use the energetically slightly favored PBE0-D3 structure set in bold.

Regarding the agreement between DFT/PAW and the MBE potentials, we note that the results obtained with DFT/PAW level are very consistent with the 2+3-body MBE potentials, that is if only up to three-body interactions are included. The PBE0-derived MBE, which can be regarded as analog to dispersion-uncorrected DFT/PAW, provides structures, bulk moduli, and cohesive energies that are in good agreement with DFT/PBE0 and DFT/PBE for both fcc and hcp lattices. Similarly, CCSD(T)-derived MBE potential, which includes dispersion effects, provides structures and properties that are consistent with PBE0-D3 and PBE-D3. However, in the case of both MBEs, including 4-body effects results in more pronounced inconsistencies between the MBE and DFT/PAW results.

These manifest in the form of much too low cohesive energies in the 2+3+4-body MBEs compared to the respective DFT/PAW calculations, too large interatomic distances, and, most importantly, a strong overstabilization of the hcp-minimum with very low c/a-ratios, as evident from Figure 3.10B. In this respect, in particular, the comparison between DFT/PBE0 and the PBE0-derived MBE is illustrative.

Although both the DFT/PAW and MBE approaches rely on more or less severe approximations and thus have associated issues and inherent uncertainties, the good consistency between these very different approaches at the level of up to three-body interactions in the MBE evolution lends some credibility to the results of both methods. The inconsistency lies perhaps in the inclusion of the PBE0 4-body effects in the MBE, but as discussed the various DFT 4-body curves agreed with each other to a certain extent. One possible issue is that due to computational limitations, the 4-body terms for the CCSD(T)-MBE are calculated at the PBE0 level, which provides an incomplete description due to the lack of dispersion.

Having discussed the performance and relation of the DFT/PAW and MBE approaches, let us now move on to structural features. Regarding the near degeneracy of fcc and hcp, it should be noted that this is reminiscent of the noble gases, where zero-point vibrational energy (ZPVE) contributions are decisive.[185] We mention that flerovium has a rather high molar mass ($M \approx 289$ *amu* for the currently most stable isotope[263]), which results in only small vibrational corrections (see discussion below), i.e. we obtain for the fcc lattice the Einstein frequency of $4{\times}10^{-4}$ eV for the CCSD(T)* two-body potential using the mass of the most stable isotope Fl-289, which is rather small and can therefore be neglected compared to the errors inherent in all the other approximations we made. Including the ZPVE in the crystal structure optimization increases the nearest neighbor distance by only 0.01 Å.

To estimate the final cohesive energy important for future adsorption studies,[189,190,264–266] our best CCSD(T)* value is $E_{\mathrm{coh}} = -0.38$ eV for the fcc structure and -0.41 eV for hcp. If we scale ($\lambda_E = 1.206$ and $\lambda_R = 0.989$) the 2-body curve to the result of Borschevsky et al.[6], we obtain $E_{\mathrm{coh}} = -0.469$ eV for the fcc structure and -0.502 eV for hcp (c/a=0.657) including the three- and four-body forces.

The DFT calculations including dispersion via the D3 model provide cohesive energies ranging from -0.575 to -0.578 eV. Hence, the best estimate we currently have is $E_{\mathrm{coh}} = -0.5 \pm 0.1$ eV which compares well with the proposed sublimation energy of $\Delta H^{298}_{\mathrm{subl}} = 0.26^{+023}_{-0.10}$ eV of Eichler[264]. After all, the cohesive energy of flerovium is similar to that of oganesson (-0.45 eV),[4] and most likely higher than the value for Cn (-0.38 eV),[186] but below that of Hg (-0.79 eV).[157]

The volume varies widely between the different methods. Using our CCSD(T)* and DFT-D3 results we estimate the volume for the solid state to be at 25.3±0.8 cm^3/mol. Using the mass of the most stable isotope Fl-289, we obtain a density of 11.4±0.3 $\mathrm{g/cm}^3$ which is very close to that of Pb (11.34 $\mathrm{g/cm}^3$).

The electronic bandgap

To explore the size of the electronic bandgap E_g of Fl and its dependence on the structure and functional, we first consider the results of our DFT/PAW calculations for the fcc structure. Afterward, we move to include additional self-consistent GW/PBE calculations conducted for the PBE0-D3 optimized structures and eventually repeat the analysis for the hcp lattice.

Inspection of the results summarized in Table 3.8 reveals a strong dependency of E_g on (i) the structural parameter(s), (ii) the employed density functional, and (iii) the k-point grid. Only for the most compact fcc structure with the LDA-like PBEsol functional, E_g vanishes, and a metallic system is found. For the same PBEsol structure, the PBE functional affords a small E_g of 0.08 eV, which increases to 0.23 eV for the less dense PBE-optimized structure and decreases to 0.20 eV for the slightly more compact PBE-D3 optimized structure. Moving from the GGAs to the hybrid functional PBE0, E_g shows the typical increase to 0.7-1.1 eV. Again, the value strongly depends on the lattice parameter, explaining the difference between the PBE0 and PBE0-D3 optimized structures.

Further PBE calculations with different k-point grids for the PBE0-D3 optimized structure (which we will use as the reference in all further considerations) illustrate the convergence of E_g: Apparently, a k-point grid of 11^3 is required for converged results, which is, however, too expensive for practical calculation times at the hybrid level, and even more so for the GW calculations. Therefore, we conducted GW calculations with 7^3, 8^3, and $9^3$$k$-points with different numbers of bands included (196, 256, 512, 1024) and extrapolate to an infinite number of bands and fine k-point grid as detailed in the supporting information.

Combining the result of the GW method of 1.51 eV for infinite bands at $9^3$$k$-points with the k-point convergence at the PBE level to $11^3$$k$-points we arrive

at a final theoretical best estimate of $E_g = 1.4 \pm 0.5$ eV for the fcc structure. Since all high-level structures of fcc summarized in Table 3.6 are less dense than the PBE0-D3 optimized structure, which is correlated with a widening of bandgap leads us to the conclusion that fcc Fl is presumably a semiconductor. We note in passing that obtaining accurate fundamental band gaps is a notoriously difficult problem for solid-state calculations.[267]

For hcp, the value and dependencies of E_g are comparable to those of the fcc structure, albeit lower by about 0.6 eV in line with previous calculations for solid argon.[268] Again, only PBEsol provides the most compact structure and, in turn, a vanishing band gap. However, for the same PBEsol structure, already PBE predicts a small but non-zero gap. The largest value for E_g at the DFT/PAW level of 0.69 eV is obtained with PBE0, which is no surprise since this level also predicts the least dense structure. Upon including dispersion effects via the D3 model, the PBE0-D3 structure becomes more compact and E_g decreases to 0.16 eV for the local minimum with the small c/a-ratio, and 0.26 eV for the slightly more stable structure with the larger c/a-ratio. These values are distinctly smaller than those for the fcc structure at the same level, which is presumably a result of the shorter Fl-Fl distances that appear to strongly influence E_g.

PBE calculations for the PBE0-D3 structure with an increasingly fine k-point grid demonstrate that E_g of the hcp structure is less sensitive to the k-grid. GW calculations with a similar number of bands (196-1024) and k-grids ($7 \times 7 \times 4$ to $9 \times 9 \times 5$) confirm the hypothesis that E_g is generally smaller for the hcp structure compared to fcc. Combining the number-of-bands-extrapolated GW results and k-grid dependency, we arrive at the theoretical best estimate of $E_g = 0.8 \pm 0.3$ eV for the hcp structure.

First attempt at melting flerovium

To give an initial estimate for the melting and boiling temperatures we make use of the linear relation derived in earlier work for the phase transition (PT),[187]

Table 3.8: Electronic band gaps E_g from various DFT and self-consistent *GW* calculations (in eV) for the fcc (top) and hcp (bottom) structures. DFT calculations employ a plane-wave cut-off of 600 eV, and *GW* calculations use a lower value of 300 eV as this does not have a significant influence. A leading * in the row indicates that the structure from the previous row has been used.

method	k-grid	a	c	E_g
fcc				
PBEsol	9^3	3.792		0.00
*PBE	9^3	3.792		0.08
PBE	9^3	3.997		0.23
PBE-D3	9^3	3.880		0.20
PBE0	9^3	3.963		1.11
PBE0-D3	9^3	3.861		0.71
*PBE	7^3	3.861		0.57
*PBE	8^3	3.861		0.32
*PBE	9^3	3.861		0.14
*PBE	11^3	3.861		0.04
*PBE	13^3	3.861		0.04
*GW/PBE	7^3	3.861		1.73
*GW/PBE	8^3	3.861		1.56
*GW/PBE	9^3	3.861		1.51
best estimate		3.861		$\mathbf{1.4 \pm 0.5}$
hcp				
PBEsol	$9 \times 9 \times 5$	3.850	5.952	0.00
*PBE	$9 \times 9 \times 5$	3.850	5.952	0.06
PBE	$9 \times 9 \times 5$	3.995	6.473	0.06
PBE-D3*	$9 \times 9 \times 5$	3.890	6.187	0.06
PBE-D3	$9 \times 9 \times 5$	3.876	6.351	0.03
PBE0	$9 \times 9 \times 5$	3.924	6.506	0.69
PBE0-D3*	$9 \times 9 \times 5$	3.873	6.165	0.28
PBE0-D3	$9 \times 9 \times 5$	3.813	6.389	0.26
*PBE	$7 \times 7 \times 4$	3.813	6.389	0.08
*PBE	$8 \times 8 \times 5$	3.813	6.389	0.03
*PBE	$9 \times 9 \times 5$	3.813	6.389	0.05
*PBE	$11 \times 11 \times 7$	3.813	6.389	0.08
*PBE	$13 \times 13 \times 9$	3.813	6.389	0.08
*GW/PBE	$7 \times 7 \times 4$	3.813	6.389	1.01
*GW/PBE	$8 \times 8 \times 5$	3.813	6.389	0.94
*GW/PBE	$9 \times 9 \times 5$	3.813	6.389	0.73
best estimate		3.813	6.389	$\mathbf{0.8 \pm 0.3}$

$$k_B T_{\mathrm{PT}} = c_{\mathrm{PT}} E_{\mathrm{coh}} \tag{3.23}$$

which gives that if the potential interaction is linearly scaled, the melting temperature scales accordingly. Although in the periodic table, the potentials for

the elements do not exactly linearly relate to one another, the linear regression is approximately observed.[161] On the other hand, for the (12,6)-LJ potential with scaled potential D_e the linear regression holds precisely. Using Monte-Carlo simulations, Mastny and de Pablo obtained a T_{MP} of 0.7793(4) in reduced units.[269] Using the relation between the cohesive and dissociation energy in terms of lattice sums for the fcc crystal, $E_{\mathrm{coh}} = D_e L_6^2/2L_{12} = 8.6093 D_e$, we thus get for the LJ potential $c_{\mathrm{MP}}^{\mathrm{LJ}}/k_B$= 1050 K/eV.

Figure 3.12 shows the cohesive energies versus the melting and boiling points of the group 14 elements. For these elements, the linear regression is c_{MP}/k_B= 416 K/eV and c_{BP}/k_B= 683 K/eV with R^2 of 0.924 for the melting points and 0.967 for the boiling points.

If we take the cohesive energy by Hermann et al.[231] with 0.487 eV for the fcc structure and use the group 14 linear regression, a first estimate sets the transition temperatures at $T_{\mathrm{MP}} \approx 200^{+50}_{-110}$ K and $T_{\mathrm{BP}} \approx 330^{+150}_{-50}$ K, which hints at flerovium being a volatile liquid at room temperature. However, these estimates have rather large uncertainties.

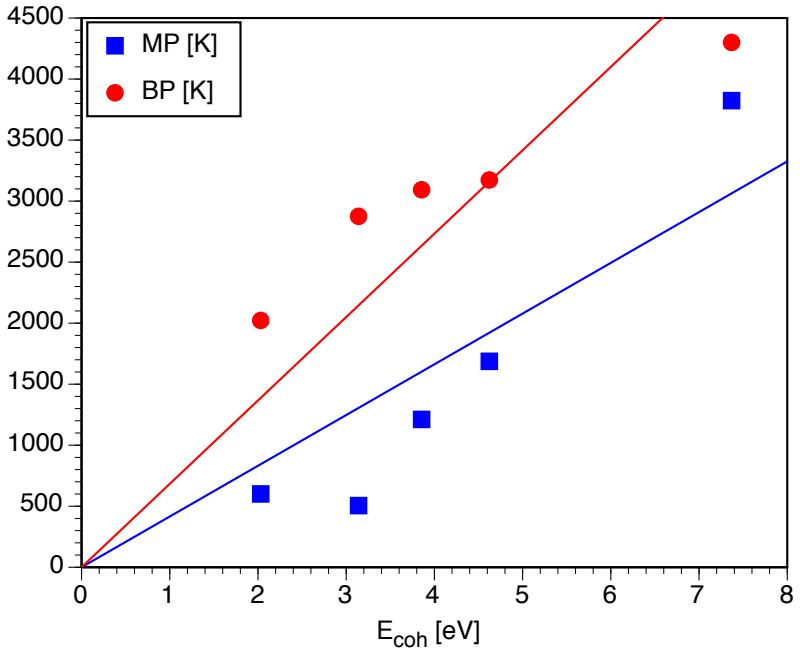

Figure 3.12: Correlation between the cohesive energies of the group 14 elements and the melting and boiling points.

Therefore, we investigated the melting temperature of flerovium using the PTMC method using a many-body expansion derived from coupled-cluster theory. The PTMC method has been shown to provide accurate melting temperatures of noble gases. Here, we use the same approach to obtain a first estimate of the melting temperature of flerovium.

Monte Carlo melting simulations were performed for the PBE0 and CCSD(T)* potentials, with potential parameters as given in Tables 3.1 and 3.2. Two-body simulations were performed for cells with N = 108, 256, 500, and 864 atoms. Due to the high computational demand, simulations with the two and three-body potential were performed with the 108 and 256 atomic cells only. The melting temperatures of these cells, corrected for superheating are given in Table 3.9, and the heat capacity curves can be found in Appendix A.3.2. In the following, we focus our discussion on the more accurate CCSD(T)* potential.

For the N = 256 simulation cell the melting temperatures shifts by -416 K due to three-body interactions, which is used as a correction to the two-body simulation performed with the N = 864 cell. Based on these results our first estimate of the melting temperature of Fl is 272 K. If we correct our two+three-body result for the four-body interaction using the difference in cohesive energies shown in Tables 3.6 and 3.7, i.e. $\Delta_{3,4} = -0.07$ eV, we obtain a four-body correction for the melting temperature of ≈ -30 K using c_{MP}/k_B= 416 K/eV from above. This sets the final melting point to ca. 242 K. On the other hand, our cohesive energy could be underestimated by about 0.1 eV, which leads to an increase according to Equation (3.23) by 42 K. Hence we put our final estimate to 284 ± 50 K. This means that flerovium is most likely a liquid at room temperature with a melting point in-between that of Cn with 230 K[161,187] and Og with 325 K.[188]

From the three-body corrected PTMC simulation, we obtain before melting starts a solid density of ρ_s^{2560K} = 11.4 g/cm^3 (25.2 cm^3/mol), which decreases to ρ_l^{270K} = 10.6 g/cm^3 (27.2 cm^3) for the liquid phase. The density curves can be

Table 3.9: Melting temperatures in Kelvin were obtained by MC simulations for cells with N = 108, 256, and 500 atoms. The transition temperatures are corrected for superheating.

	cell size	108	256	500	864
PBE0	2b	652	663	674	675
	2b + 3b	70	98		
CCSD(T)*	2b	665	680	688	689
	2b + 3b	239	264		

found in Appendix A.3.3.

3.4 Conclusions

We presented a comprehensive but challenging study of the interaction between flerovium atoms including the solid state using two very different approaches, density functional theory and many-body expansions of the total energy. DFT calculations showed that the dispersion correction is very important, i.e. it increases $|E_{\mathrm{coh}}|$ by about 100%. However, the remaining error in the accurate determination of lattice properties still lies within density functional theory. As the treatment of electron correlation for small band-gap systems including metals is problematic, albeit some progress has been made through incremental methods,[157,270–272] we chose to use the MBE of the total energy which works well for the lighter noble gases[185,236] and allows coupled-cluster theory to be used.

The problem here is the huge computational costs to obtain accurately the two-, three- and four-body forces. Only for the two-body force we were able to use larger basis sets and estimate the basis set superposition and incompleteness error at the correlated level, for the three-body force we corrected for basis set effects only at the HF level, and for the four-body force, we used the PBE0 functional. Another problem arose from the convergence of the MBE (for a general discussion see Hermann et al.[10]) around the bonding distance of flerovium. Nevertheless, the solid-state PBE0 MBE results agree well with PBE0/PAW results from VASP calculations, suggesting that higher than four-body forces might actually be small. Such convergence problems were already encountered for Og[4,188] and are more

pronounced for flerovium.

While Cn was found to be a liquid at room temperature[161,187] and Og a solid (just) with a very low melting point,[188] and therefore not gases at room temperature, flerovium is most likely a liquid at room temperature, although the boiling point still needs to be determined. All three superheavy elements have a strong tendency to be volatile in agreement with adsorption studies on gold surfaces.[190,195,264,265] Similar to Fl having a rather small band gap of 0.8±0.3 eV for the hcp structure, Og is a semi-conductor[273] as well with an estimated band gap of E_g=1.5±0.6 eV, while Cn is predicted to be an insulator with E_g= 6.4 eV.[187] This distinguishes the three superheavy elements from their lighter congeners. In the case of flerovium, this is due to the large spin-orbit splitting of the $7p$ shell leading to a closed $7p_{1/2}$ shell. For Cn, this is mainly due to the large relativistic $7s$ contraction, and for Og due to the soft and spin-orbit destabilized $7p_{3/2}$ shell.

It took almost 50 years to shed some light on Pitzer's original question if the elements Cn, Fl, and Og behave like noble gas or not. As discussed, the findings do not provide a clear-cut answer. The results put Fl somewhere in-between Cn and Og, and in terms of the many-body expansion of the interaction energy, we see a rather slow convergence around the equilibrium nearest neighbor distance. The next logical step now is to perform more extensive melting and boiling simulations using scaled density functional theory as suggested by Mewes and Schwerdtfeger[161], Mewes and Smits[162], Mewes et al.[187]

Chapter 4

Probing High Oxidation States in Noble Gas Fluorides

We present a systematic study of relativistic and electron correlation effects for the decomposition of the noble gas fluorides $NgF_n \rightarrow NgF_{n-2}+F_2$ (Ng=Ar, Kr, Xe, Rn and Og). Concerning this decomposition reaction, the stability of all fluorides increases down the group 18 elements, and, in agreement with experimental studies, shows stability from xenon onward. A sole exception of this trend is found for OgF_6, where the strong spin-orbit splitting of the 7p shell, together with the relativistic $7p_{1/2}$ stabilization and contraction, destabilize the oxidation state +6. While electron correlation effects lead to a general stabilization of noble gas fluorides as one expects, several fluorides are already stable at the Hartree-Fock level.

4.1 Introduction

The synthesis and chemistry of the noble gas fluorides have a long history.[274] Kossel speculated in 1916 about the existence of Kr and Xe fluorides.[275] After several unsuccessful attempts to isolate noble gas compounds (see Refs.[274,276–281] for historical accounts), Bartlett succeeded in 1962 to oxidize Xe with PtF_6[282], resulting most likely in a mixture of $XeF^+PtF_6^-$ and $XeF^+Pt_2F_{11}^-$[283]. Subsequently, many noble gas fluorides have been synthesized, isolated and studied,[274] mostly those of xenon[284–293] with a few exceptions for krypton[294–299] or radon[300]. For the lighter noble gas fluorides, there are few studies in the gas

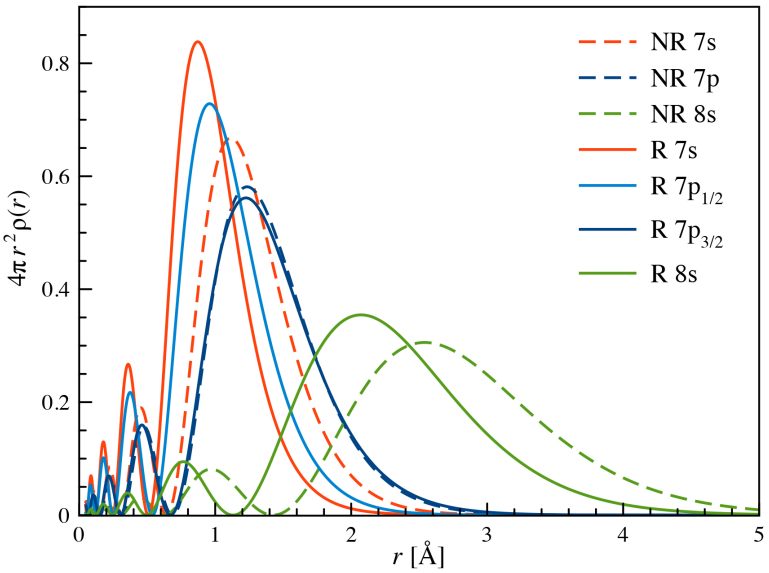

Figure 4.1: Nonrelativistic (NR) and relativistic (R) radial densities for oganesson.

phase, such as for the argon molecule HArF, which was identified in matrix isolation.[301,302] Theoretical studies predict that HNeF and HHeF should also be observable in the gas phase,[303,304] but so far no experimental studies have been reported for these compounds. The highest oxidation state that can be achieved for the noble gases is +6 such as XeF_6 or $XeOF_4$,[292,305,306] while XeF_8 has been predicted to be thermodynamically unstable.[307] On the other hand, the noble gases can be encapsulated in fullerenes such as C_{60},[308,309] but such species should be seen as a confined system with rather weak bonding with the carbon cage[310,311]. Some more recent advances in noble gas chemistry are described by Gomila and Frontera[312] or Mazej[313]. Noteworthy here is the synthesis of $AuXe_4^{2+}(Sb_2F_{11}^-)_2$ by Seidel and Seppelt[314], Pyykkö[315].

Experimental enthalpies of the formation for the gas phase xenon fluorides show XeF_2, XeF_4 and XeF_6 are thermodynamically stable.[316] One naively expects that the thermodynamic stability of the closed shell noble gas fluorides would increase[317] with increasing atomic number as the valence *p*-electrons become more diffuse and therefore chemically more accessible.[318] The first ionization potentials or polarizabilities suggested from He to Og are (in eV) 24.587, 21.565, 15.760, 14.000, 12.130, 10.749, and 8.88, respectively.[319,320] However, strong spin-orbit effects lead to a substantial stabilization of the $p_{1/2}$ valence electrons and a rather

large spin-orbit splitting in the valence shell for the heaviest of the noble gas elements. Figure 4.1 demonstrates the large spin-orbit splitting in the $7p$ shell for the superheavy element Og, as well as the very large relativistic stabilization of the $7s$ and $8s$ shells. Due to this, the $7p_{1/2}$ electrons become chemically inert for Og, and not accessible for chemical bonding. Relativistic calculations for RnF_6 by Filatov and Cremer[321] already showed that strong spin-orbit coupling effects reduce the decomposition energy into RnF_4 and F_2 by 14 kcal/mol.

There have been several computational studies on the noble gas fluorides already.[307,321–329] The main geometries that these fluorides adopt are $D_{\infty h}$ for NgF_2, D_{4h} and T_d for NgF_4, and O_h for NgF_6. Figure 4.2 shows their corresponding Molecular Orbital (MO) diagrams. All the noble gas tetrafluoride adopt D_{4h} symmetry energetically well above the T_d arrangement,[307] except for OgF_4 which has been predicted to have a slight preference for the tetrahedral symmetry due to spin-orbit effects.[330] Concerning the hexafluorides, XeF_6 can undergo a second-order Jahn-Teller distortion, i.e. HOMO$\{a^*_{1g}$[Xe($5s$)F($2p$)]$\}\otimes$LUMO$\{t_{1u}$[Xe($5p$)F($2sp$)]$\}$, through a $O_h \leftrightarrow C_{2v} \leftrightarrow C_{3v}$ path from the active t_{1u} mode,[331–338] see Figure 4.3A. This distortion will be very sensitive to the relativistic valence ns contraction and np shell spin-orbit splitting in the noble gas atom, Figure A.7. Indeed, Kaupp et al.[339] pointed out that this Jahn-Teller distortion depends on a delicate balance between electron correlation, relativistic and basis set effects. Cheng et al.[340] and Peterson et al.[341] showed from scalar relativistic coupled-cluster calculations that the Jahn-Teller hypersurface for XeF_6 is very shallow with a slight preference of the C_{3v} by about 1 kcal/mol over the O_h structure. Additionally, Grant et al.[307] showed from coupled-cluster calculations that XeF_2, XeF_4 and XeF_6 are all stable to the loss of F_2 but the highest oxidation state, XeF_8 decomposes into XeF_6 and F_2.

Introducing the spin representation and spin-orbit coupling can change the point group representation and symmetry of atomic or molecular systems by introducing new symmetry operations. This can cause the splitting or merging of

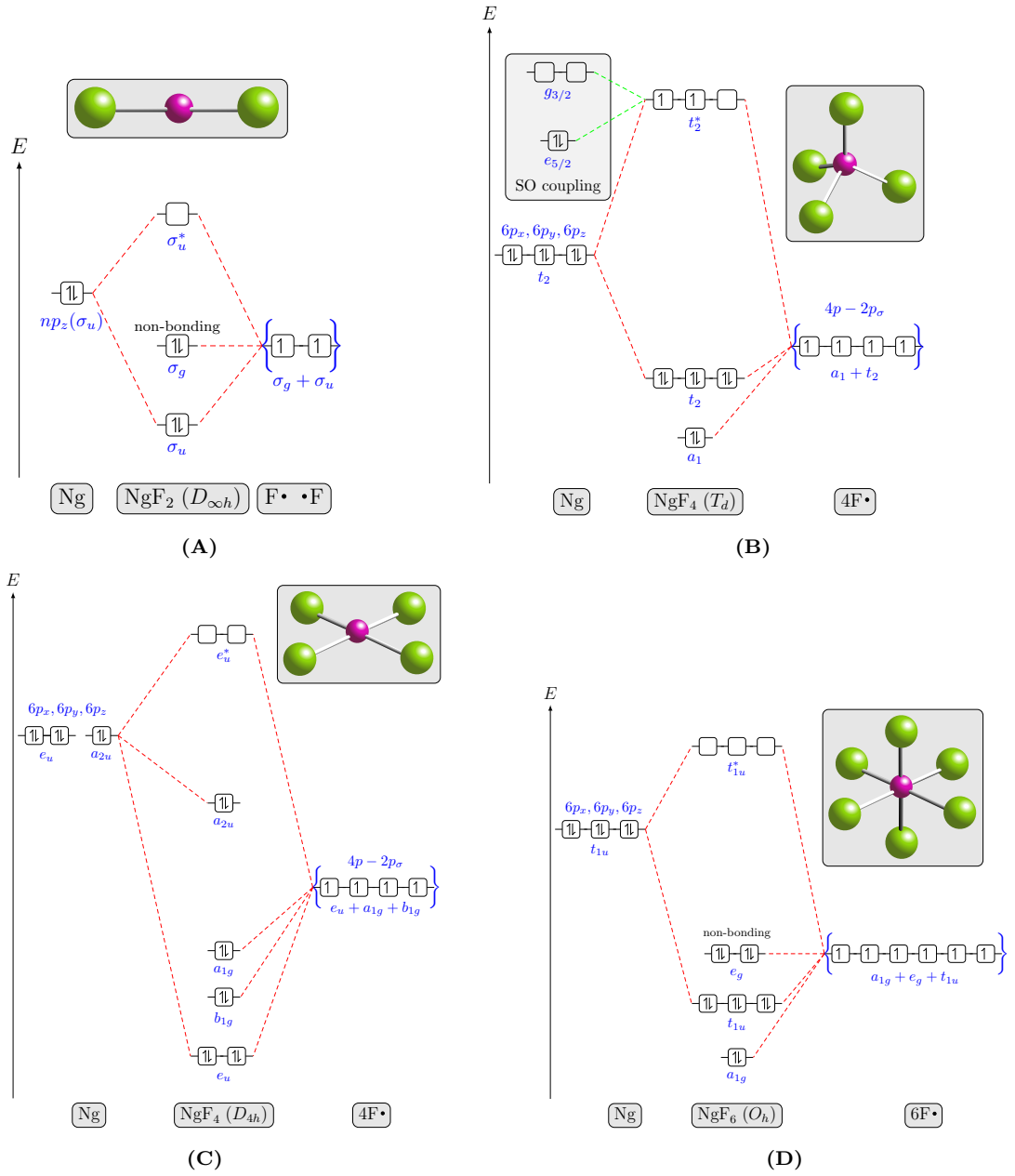

Figure 4.2: Non-relativistic symmetry adapted Molecular Orbital (MO) energy level sketch for RnF_m (Rn in red and F in green), where $m = 2, 4, 6$. MOs derived from Rn $6p$ orbitals and F $2p_\sigma$ orbitals. Symmetry adapted MOs for (a) RgF_2 with symmetry $D_{\infty h}$, (b) RnF_4 with symmetry T_d and spin-orbit (SO) coupling, (c) RnF_4 with symmetry D_{4h} and (d) RnF_6 with symmetry O_h. The energy levels are at CCSD/def2QZVPPD order.

representations, and the spin representation can introduce spin-dependent symmetry operations.[342,343] These changes can have a significant impact on the symmetry of the molecule. In the presence of spin-orbit coupling, the interaction between the orbital and spin angular momentum of electrons, may affect the splitting of energy levels. This effect is important in atomic or molecular systems, leading to changes in the symmetry and point group representation of the

system.[344,345]

The effects of spin-orbit coupling can be significant in molecules with heavy atoms or in a strong electric field, such as those found near large nuclei. In these cases, the spin-orbit coupling can lead to changes in the geometry of the molecule and can play a crucial role in determining its reactivity and chemical properties.[346] Because of the electron spin in a relativistic framework, these systems can also display time reversal symmetry in addition to spatial symmetry and the group representation for each symmetry extends to the language of double groups.[347–349]

The double group is a generalization of the point group that includes time-reversal symmetry. Figures 4.3C and 4.3D showed the symmetry-adapted HOMO-LUMO orbitals in the language of the double groups, constructed by the direct product with the irreducible representation of the spin function $e_{1/2}$ (aka Γ_6).[347,350] The extra orbital splitting for T_d symmetry generates a double-group (T_d^*), where

$$e_{1/2} \otimes t_2 = e_{5/2} \oplus g_{3/2} \tag{4.1}$$

and O_h^* double-group

$$\begin{aligned} e_{1/2g} \otimes a_{1g} &= e_{1/2g} \\ e_{1/2g} \otimes t_{1u} &= e_{1/2u} \oplus g_{3/2u} \end{aligned} \tag{4.2}$$

The extra-reducible representations $e_{5/2}$ and $e_{1/2}$ are two-dimensional, and $g_{3/2}$ is four-dimensional (Figures 4.3C and 4.3D).

In order to study the trend in stability for the noble gas fluorides and the role of both electron correlation and relativistic effects including spin-orbit coupling, we decided to use both wave-function-based and coupled cluster theory for the decomposition reaction $NgF_n \rightarrow NgF_{n-2} + F_2$ (Ng = Ar – Og and $n = 2, 4, 6$). For NgF_6, we mainly considered the octahedral arrangement and for XeF_6, we analyzed C_{3v} and C_{2v} symmetries separately.

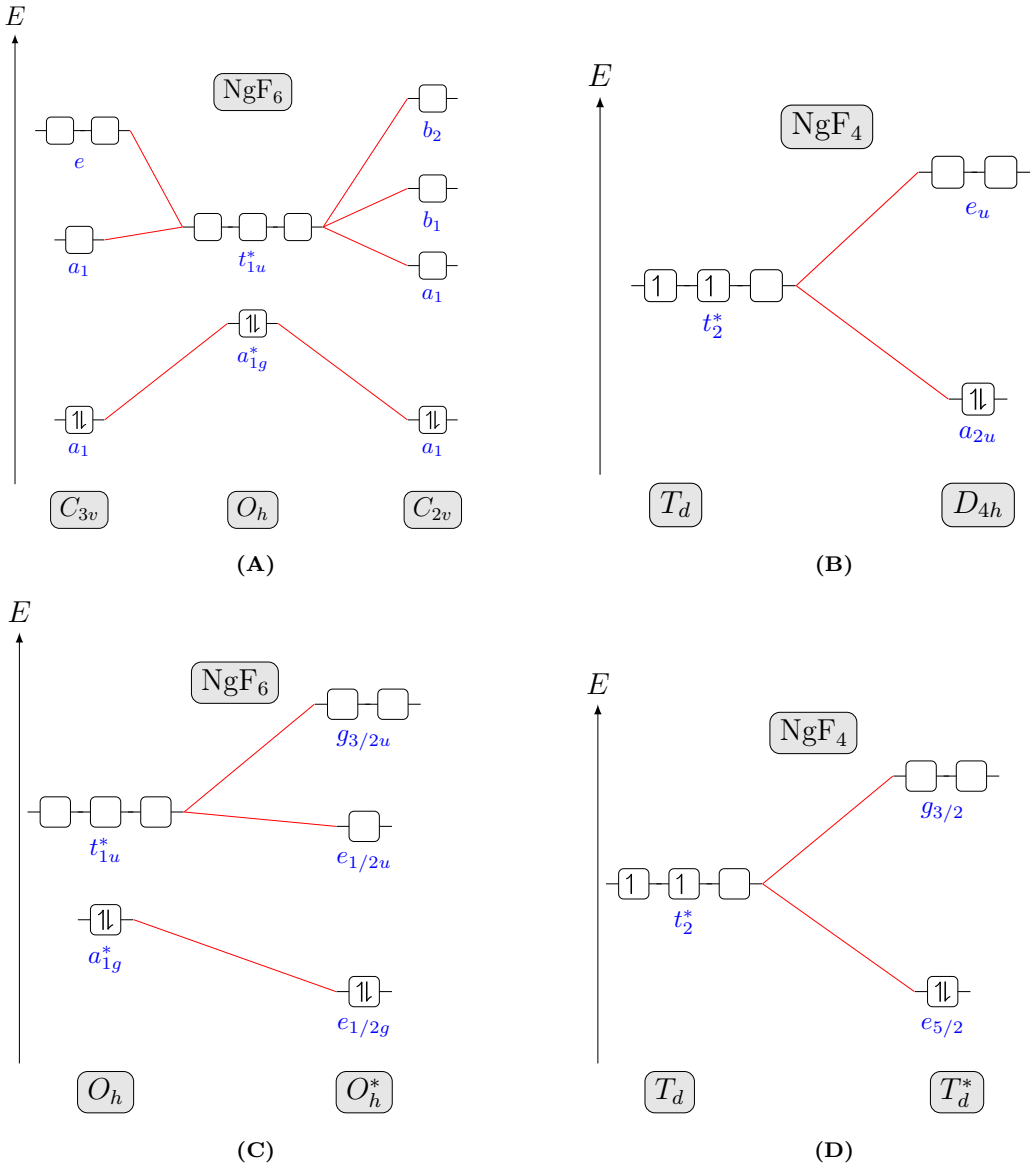

Figure 4.3: Schematic splitting of HOMO and LUMO orbitals for $RnF_{4,6}$ molecules reducing the symmetry of the molecule (top panel) and introducing spin-orbit coupling (bottom panel) referring to the symmetry-adapted Molecular Orbitals (MOs) diagrams in Figure 4.2. Symmetry reduction from (a) $C_{3v} \leftarrow O_h \rightarrow C_{2v}$ and (b) $T_d \rightarrow D_{4h}$. Spin-orbit coupling, see Equations (4.1) and (4.2) for the double group (c) T_d^* and (d) O_h^*, respectively.

4.2 Computational Details

We explored exhaustively the Potential Energy Surface (PES) for the molecular systems formed between noble gas (Ng) and two, four and six fluoride atoms, NgF_n ($n = 2, 4, 6$). We used a stochastic search algorithm to explore each PES under annealing conditions with an adapted Metropolis acceptance test as implemented in the ASCEC program[351–353] (Spanish acronym Annealing Simulado con Energía Cuántica).

We performed quadruplicated runs of the ASCEC algorithm to generate candidate structures for each system using PBE0 functional[354] and cc-pVDZ for fluoride in conjunction with Stuttgart/Dresden ECPmMDF[355,356] pseudo-potential and TZVP basis set for Ar and Kr ($m = 10$), Xe ($m = 28$), Rn ($m = 60$), and Og ($m = 92$). The ASCEC has been quite successful in exploring a wide variety of atomic and molecular systems with complex interactions such as clusters linked via hydrogen bonding networks,[357–364] microsolvation of heavy ions and cations,[365–367] carbenes,[368] metallic clusters,[369–371] and clusters joined via van der Waals interactions.[372]

After exhaustive exploration of the PES of NgF_n systems, all the afforded structures were refined by gradient-following methods. We optimized these structures for the closed-shell noble gas fluorides, NgF_n, in their corresponding symmetries $D_{\infty h}$ for NgF_2, D_{4h} and T_d for NgF_4, and O_h for NgF_6 at various levels of the theory. For the F, Ar, and Kr, we used Ahlrichs triple and quadruple basis sets (Def2xZVPPD with x = T, Q).[373] For Xe, Rn, and Og, we used the multi-electron adjusted scalar relativistic Stuttgart/Dresden ECPmMDF pseudo-potential with 28, 60 and 92 electrons (m) treated as the core, respectively. For the 26 valence electrons, we used the cc-pVTZ basis set,[355,356] as the best compromise between accuracy and computational expense.

The following density functionals were applied: the hybrid functional PBE0,[354] CAM-B3LYP (a long-range-corrected version of B3LYP using the Coulomb-attenuating method),[374] ωB97X-D with empirical dispersion,[375] and the double hybrid PBEQIDH with exact HF exchange and MP2-like correlation.[376] For the wavefunction-based method, we chose second-order Møller-Plesset theory (MP2)[377] and coupled-cluster theory (CC)[378,379] with single and double excitations (full active space). In all cases, except for the coupled cluster, we assured that true minima were obtained through the eigenvalues of the Hessian matrix. However, the NgF_n molecules in T_d symmetry are often saddle points. We used Gaussian16[380] software package for these calculations.

To discuss relativistic and electron correlation effects more consistently, we used the DIRAC21[198] program suite at both, the scalar (spin-free, SF[381]) and spin-orbit (eXact Two Component, X2C[382]) formalisms. We performed a distance scan using a grid of 1×10^{-3} Å for highly symmetric systems, $D_{\infty h}$ for NgF_2, D_{4h} and T_d for NgF_4, and O_h for NgF_6. We applied the all-electron Dyall cv2z and cv3z basis set[383,384] with and without electron correlation using PBE0 functional. We used a simple Gaussian function for the finite nuclear charge distribution as detailed by Visscher.[385] To compute the binding energy, we introduced the electron correlation at the MP2[386] and CCSD[387] level of theory. We used lowest-energy geometries for each symmetry as stated above and for F_2 an experimental bond distance of 1.4112 Å.

4.3 Results and Discussion

4.3.1 Bond Length and Symmetry

In Table 4.1, we present the optimized geometries of noble gases fluorides (NgF_n, where $n = 2, 4, 6$ and Ng = Ar, Kr, Xe, Rn, and Og) using three different density functional theory (DFT) functionals PBE0, CAM-B3LYP, and PBEQIDH, and coupled-cluster singles and doubles (CCSD) at the scalar-relativistic level. To ensure the stability of the geometries, we conducted a vibrational analysis for each geometry and found that the geometries of symmetries $D_{\infty h}$, D_{4h}, and O_h are true minima, while the ones with T_d symmetry displayed at least one imaginary frequency. For true minima geometries, we found that the Ng–F bond length increases following the predicted periodic trend. Our results showed that the Ar–F bond length is on average 1.77 ± 0.01 Å, while Kr–F is 1.84 ± 0.01 Å, Xe–F is 1.94 ± 0.02 Å, Rn–F is 2.01 ± 0.03 Å, and Og–F is 2.10 ± 0.05 Å. For a given noble gas, the Ng–F bond length is the longest for T_d symmetry, followed by $D_{\infty h}$, then D_{4h}, and finally O_h symmetry. Thus, the Ng–F bond length evolves according to the trend $T_d > D_{\infty h} > D_{4h} > O_h$ (Figure 4.4 Å).

The Ng–F bond lengths are contracted by about 0.03 Å when we improved the

description of the electron correlation by using double-hybrid functional PBEQIDH or CCSD methods. This bond length contraction is larger for Rn or Og. However, there is no change in Ng–F bond length when we used Ahlrichs Def2QZPPV or Stuttgart/Dresden ECPxMDF pseudo-potential (x = 28, 60, and 92 for Xe, Rn, and Og, respectively). Additionally, long-range (CAM-B3LYP) or dispersion (ωB97X-D) corrections do not change the Ng–F bond length computed by using the PBE0 functional.

In Table 4.2, we show the effect of electron correlation and relativistic contributions to the Ng–F bond distances for the symmetries considered. To analyze these effects, we computed the energy minima for each symmetry with and without electron correlation, using the PBE0 functional and Hartree-Fock at the non-relativistic (NR), spin-free (SF), and two-component (X2C) levels of theory. Our findings reveal that with some exceptions (Table 4.1 and Figure 4.4 A), the bond lengths increase including either relativistic or correlation effects explicitly. Additionally, we observed that relativistic effects increase the bond lengths of Ng–F for $D_{\infty h} > D_{4h} > O_h$ symmetries, while the T_d symmetry remains mostly unchanged (Figure 4.4 B).

Our results suggest that electron correlation and relativistic effects play a significant role in expanding the Ng–F bond lengths. While electron correlation contributions are more significant for lighter atom systems such as ArF_n and Kr_n, relativistic effects are crucial for heavy atom systems such as Rn_n and Og_n, with the Xe–F bond length being affected by both effects.

The bond distances in the noble gas fluorides (NgF_n) depend on the level of theory applied in the calculation. In general, when electron correlation is taken into account, the Ng–F bond length increases regarding the Hartree-Fock calculation. The electronic correlation effect has a strong impact on the Ar–F and Kr–F bond lengths, increasing them by approximately 0.08 and 0.06 Å, respectively. In contrast, the Xe–F, Rn–F, and Og–F bond lengths experience only a small increase of approximately 0.04, 0.02, and 0.01 Å, respectively. Similarly,

Table 4.1: Optimized bond distances [Å] for the noble gas fluorides NgF_n, where Ng = Ar, Kr, Xe, Rn and $n = 2, 4, 6$. Ahlrichs all-electron Def2QZVPPD basis sets for F, Ar, Kr and the appropriate all-electron Hamiltonians were used, as well as For the scalar relativistic pseudo-potential calculations for Ng = Xe, Rn, and Og we used Stuttgart/Dresden energy consistent ECPxMDF pseudo-potentials (x = 28, 60, and 92 for Xe, Rn, and Og, respectively) and corresponding TZVP basis sets for the valence electrons together with aug-cc-pVTZ for the fluorine atom. All structures are true minima except for those with T_d symmetry.

Ng	Level	Pseudo-Potential	NgF_2 ($D_{\infty h}$)	NgF_4 (D_{4h})	NgF_4 (T_d)[a]	NgF_6 (O_h)
Ar	PBE0	Def2QZPPV	1.766	1.757	1.978	1.768
	CAM-B3LYP	Def2QZPPV	1.765	1.754	1.952	1.762
	ωB97X-D	Def2QZPPV	1.760	1.750	1.963	1.762
	PBEQIDH	Def2QZPPV	1.757	1.759	1.911	1.786
	CCSD	Def2QZPPV	1.759	1.764	1.972	1.808
Kr	PBE0	Def2QZPPV	1.862	1.836	2.005	1.832
	CAM-B3LYP	Def2QZPPV	1.861	1.834	1.990	1.828
	ωB97X-D	Def2QZPPV	1.858	1.832	1.991	1.828
	PBEQIDH	Def2QZPPV	1.844	1.822	1.935	1.824
	CCSD	Def2QZPPV	1.842	1.816	2.000	1.818[b]
Xe	PBE0	Def2QZPPV	1.976	1.936	2.057	1.921
		ECP26MDFQ	1.986	1.949	2.073	1.934
	CAM-B3LYP	Def2QZPPV	1.976	1.936	2.049	1.919
		ECP26MDFQ	1.986	1.948	2.066	1.931
	ωB97X-D	Def2QZPPV	1.975	1.936	2.051	1.921
		ECP26MDFQ	1.984	1.947	2.066	1.933
	PBEQIDH	Def2QZPPV	1.958	1.920	2.001	1.908
		ECP26MDFQ	1.966	1.930	2.017	1.920
	CCSD	Def2QZPPV	1.956	1.915	2.032	1.908[b]
		ECP26MDFQ	1.966	1.926	2.050	1.914
Rn	PBE0	Def2QZPPV	2.057	2.010	2.107	1.977
		ECP60MDFQ	2.069	2.024	2.127	1.992
	CAM-B3LYP	Def2QZPPV	2.058	2.009	2.102	1.976
		ECP60MDFQ	2.070	2.022	2.122	1.990
	ωB97X-D	Def2QZPPV	2.060	2.011	2.104	1.977
		ECP60MDFQ	2.070	2.024	2.122	1.993
	PBEQIDH	Def2QZPPV	2.040	1.994	2.057	1.962
		ECP60MDFQ	2.049	2.005	2.076	1.975
	CCSD	Def2QZPPV	2.039	1.991	2.082	1.963[c]
		ECP60MDFQ	2.047	2.000	2.099	1.968
Og	PBE0	ECP92MDFQ	2.162	2.106	2.188	2.057
	CAM-B3LYP	ECP92MDFQ	2.163	2.105	2.183	2.057
	ωB97X-D	ECP92MDFQ	2.164	2.106	2.185	2.058
	PBEQIDH	ECP92MDFQ	2.144	2.089	2.143	2.042
	CCSD	ECP92MDFQ	2.145	2.088	2.164	2.038

[a] Geometries with at least one imaginary frequency. [b] At the MP4(DQ)/Def2QZVPPD instead. [c] Using Ahlrichs Def2TZVPPD basis set instead.

relativistic effects increase the Ng–F bond lengths. X2C calculations result in the longest bond distances, while NR calculations give the shortest bond distances. Although the bond lengths of Ar–F and Kr–F are almost unchanged by relativistic effects, the bond lengths of Xe–F, Rn–F, and Og–F are significantly impacted.

Our systematic comparison of the Ng–F bond lengths at various levels of

Table 4.2: Bond distances [Å] obtained from a scan using a grid of 1×10^{-3} Å for the noble gas fluorides NgF_n, where Ng = Ar, Kr, Xe, Rn and $n = 2, 4, 6$ at the Non-Relativistic (NR), Spin-Free (SF) and Exact Two Components (X2C) using Hartree-Fock (HF) or PBE0 levels of theory and the Dyall cv3z all-electron basis sets.

Ng	Level	NgF_2 ($D_{\infty h}$)	NgF_4 (D_{4h})	NgF_4 (T_d)	NgF_6 (O_h)
Ar	HF/NR	1.693	1.680	1.910	1.705
	HF/SF	1.693	1.680	1.916	1.705
	HF/X2C	1.693	1.680	1.904	1.705
	PBE0/NR	1.768	1.760	1.982	1.770
	PBE0/SF	1.768	1.755	1.982	1.768
	PBE0/X2C	1.768	1.757	1.970	1.767
Kr	HF/NR	1.802	1.772	1.922	1.775
	HF/SF	1.803	1.772	1.922	1.775
	HF/X2C	1.803	1.772	1.910	1.775
	PBE0/NR	1.864	1.836	2.006	1.833
	PBE0/SF	1.865	1.836	2.006	1.830
	PBE0/X2C	1.865	1.838	1.986	1.830
Xe	HF/NR	1.924	1.885	1.998	1.890
	HF/SF	1.931	1.890	1.998	1.880
	HF/X2C	1.935	1.890	1.998	1.880
	PBE0/NR	1.970	1.935	2.064	1.930
	PBE0/SF	1.977	1.940	2.064	1.925
	PBE0/X2C	1.980	1.940	2.049	1.925
Rn	HF/NR	2.005	1.960	2.046	1.958
	HF/SF	2.023	1.975	2.046	1.940
	HF/X2C	2.045	1.990	2.058	1.947
	PBE0/NR	2.046	2.005	2.112	1.990
	PBE0/SF	2.063	2.015	2.118	1.980
	PBE0/X2C	2.085	2.015	2.100	1.990
Og	HF/NR	2.086	2.040	2.070	2.040
	HF/SF	2.124	2.065	2.130	2.015
	HF/X2C	2.192	2.125	2.148	2.065
	PBE0/NR	2.118	2.075	2.124	2.065
	PBE0/SF	2.154	2.095	2.178	2.095
	PBE0/X2C	2.209	2.148	2.163	2.120

theory, including non-relativistic, spin-free, and two-component, gives valuable insights into the mechanisms responsible for changes in the geometry and symmetry of these compounds. Our findings show that relativistic effects have expanded the bond lengths for Rn and Og, and have impacted the bond length trends for different symmetries, emphasizing the need to take relativistic effects into account in these systems. Our approach demonstrates the independent contributions from electron correlation, spin-free (scalar relativistic) and spin-dependent operators. We will further analyze these findings in the following section (Section 4.3.2).

Although the spin-free level accounts for scalar relativistic effects (e.g.

mass-velocity and Darwin terms) and provides more accurate results compared to the non-relativistic level, this level of approach to the spin-free level does not account for the effects of spin-orbit coupling.[388,389] The two-component level (X2C), on the other hand, considers both scalar relativistic and spin-orbit coupling effects, resulting in the most accurate predictions of molecular geometry. In principle, the X2C relativistic Hamiltonian produces identical energies to those produced by the four-component one-electron Hamiltonian, given that both are used with the same large component basis set and restricted kinetic balance. Furthermore, the X2C Hamiltonian provides the same distinction between spin-free (scalar relativistic) and spin-orbit-like contributions as the four-component Hamiltonian.[46,390] This difference indicates that the spin-same-orbit correction, included in the X2C calculations, plays a crucial role in determining bond distances in the heavy atoms fluoride systems. This is expected from the relativistic $p_{3/2}$ expansion, see Figure 4.1.

This comparison of the results obtained from non-relativistic, spin-free, and two-component levels highlights the importance of taking into account relativistic effects in the study of the geometries and symmetries of fluorides of noble gases. These findings can contribute to our understanding of the behavior of these compounds and the role of relativistic effects in molecular physics.

4.3.2 Molecular Decomposition Energy

We computed the molecular decomposition energy according to the following decomposition reaction,

$$\mathrm{NgF}_n \rightarrow \mathrm{NgF}_{n-2} + \mathrm{F}_2 \tag{4.3}$$

where Ng = Ar, Kr, Xe, Rn, and $n = 2, 4, 6$ with symmetry $D_{\infty h}$, D_{4h}, T_d, and O_h. The molecular decomposition energy is defined as the amount of energy that must be supplied to separate a molecule into its constituents atoms/molecules, and it can be calculated by subtracting the total energy of the molecule (NgF_n) from

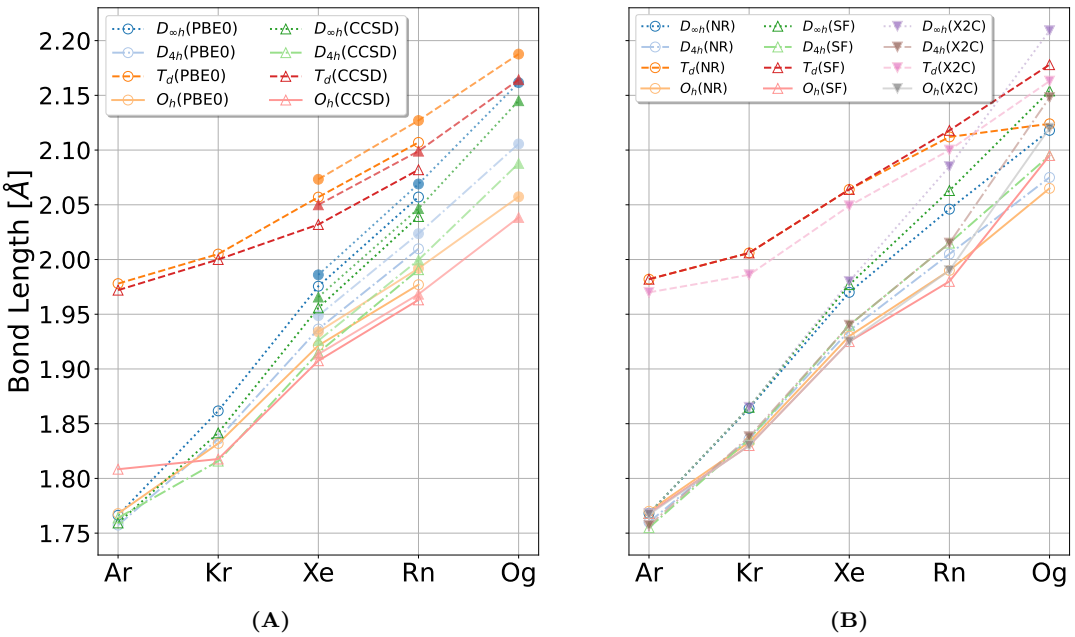

Figure 4.4: Optimized bond distances from NgF_n, where Ng = Ar, Kr, Xe, Rn, and $n = 2, 4, 6$ with symmetry $D_{\infty h}$, D_{4h}, T_d, and O_h. A) obtained at the PBE0 and CCSD level of theory with Pseudo-Potentials, where DEF2QZPPVD is represented with transparent markers and ECPxMDFQ uses solid colors. B) Calculations at PBE0 and cv3z all-electron basis set from nonrelativistic (NR), scalar relativistic spin-free (SF) and relativistic (X2C) level.

the total energy of the individual constituents (NgF_{n-2} and F_2). Then,

$$\Delta E = E\left[NgF_{n-2}\right] + E\left[F_2\right] - E\left[NgF_n\right] \tag{4.4}$$

The calculation of the decomposition energy was performed at specific levels of theory for each symmetry. As a result, the more energy that is required to break a molecule into its constituent atoms, the more stable the molecule is considered to be (positive ΔE). The molecular decomposition energy is an important measure of the stability of a molecule, it is opposite to the formation energy and related to the binding energy.

Our findings reveal a notable distinction in the stability of difluorides and tetrafluorides among noble gases. Specifically, it is observed that difluorides, denoted as NgF_2 ($D_{\infty h}$) and tetrafluorides, denoted as NgF_4 (D_{4h}), are unstable towards decomposition in the cases of Ar and Kr. However, an intriguing contrast emerges when considering Xe, Rn, and Og as these noble gases exhibit stability in both their difluoride and tetrafluoride forms, see Figure 4.5.

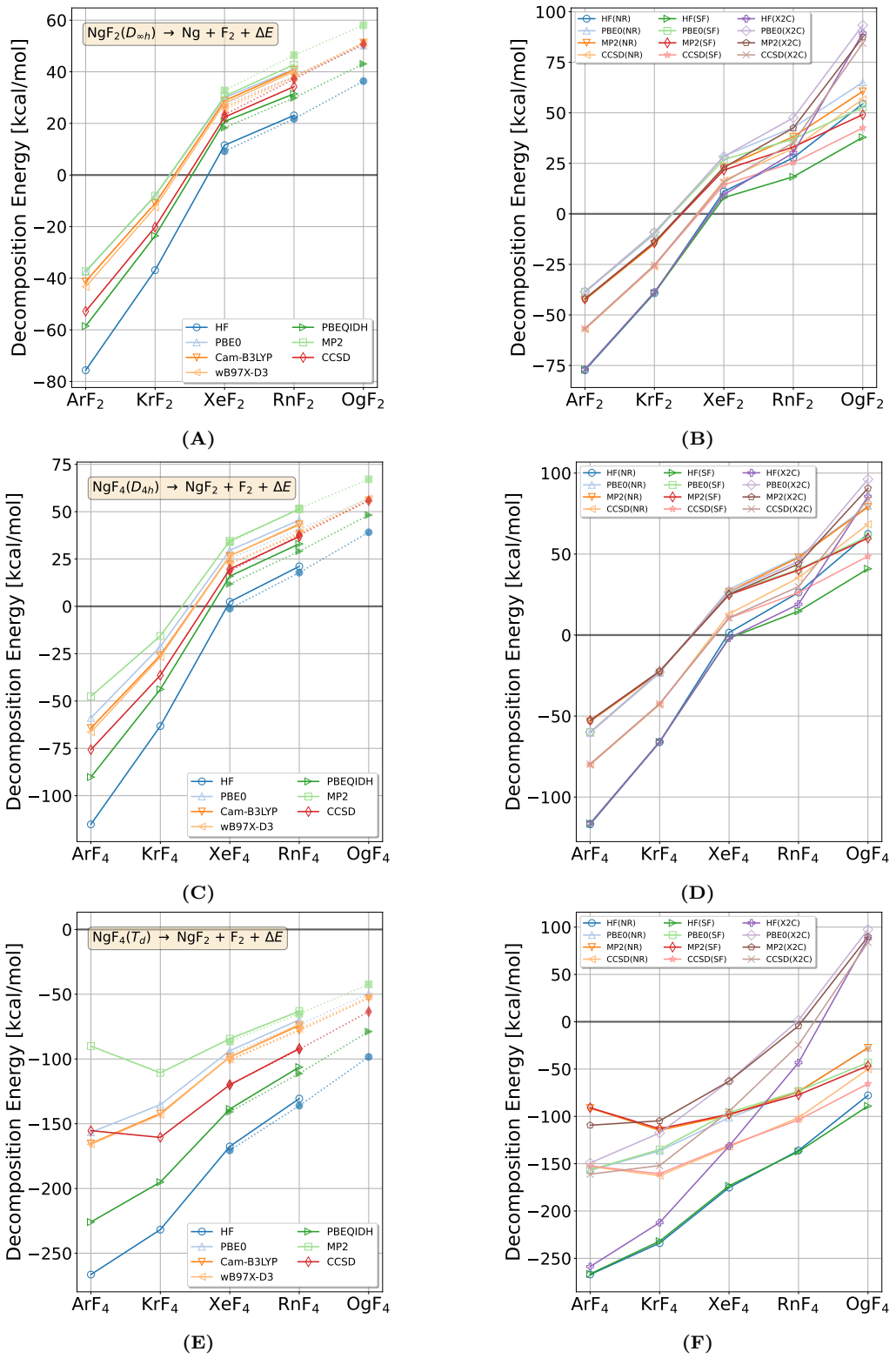

Figure 4.5: Molecular decomposition energies [in kcal/mol] for $NgF_n \rightarrow NgF_{n-2}$ ($n = 2, 4$). The left panel shows energies computed using Pseudo-Potentials, where DEF2QZPPVD is represented with transparent markers and ECPxMDFQ uses solid colors. The right panel shows energies computed using cv3z all-electron basis set from nonrelativistic (NR), scalar relativistic spin-free (SF) and relativistic (X2C) levels. A,B) decomposition from NgF_2 with symmetry $D_{\infty h}$; C,D) decomposition from NgF_4 with symmetry D_{4h}; and D,E) decomposition from NgF_4 with symmetry T_d.

Moreover, in Figure 4.5E, tetrafluoride compounds with tetrahedral symmetry show a trend of instability towards decomposition across all noble gases, except for Oganesson tetrafluoride OgF_4 (T_d). This unique stability in the case of tetrahedral OgF_4 can be attributed to the influence of relativistic effects, see Figure 4.5F.

Regarding the decomposition of hexafluorides, NgF_6 (O_h), our results reveal that while ArF_6 and KrF_6 compounds exhibit instability and decompose into F_2 and NgF_4 with D_{4h} symmetry, XeF_6 and RnF_6 compounds demonstrate stability, see Figure 4.6. Notably, considering the decomposition into the tetrahedral NgF_4 (T_d), we observed that Ar, Kr, Xe, and Rn hexafluorides remain stable. Conversely, due to relativistic effects (spin-orbit contribution), OgF_6 becomes unstable and decomposes into F_2 and NgF_4, either with D_{4h} or T_d symmetry, see Figures 4.6B and 4.6D.

Previously, Haiduke et al.[327] and Han and Lee[325] discussed how relativistic effects affect chemical properties such as geometry and heat of formation for XeF_2 and tetrafluorides of heavier noble gases.[316,391] Also, Malli et al.[323], Malli[326] pointed out that XeF_2 and RnF_6 are unstable at the uncorrelated level. Moreover, RnF_6 is likely to be nonvolatile and the Rn–F bonds become quite polar due to relativistic effects.[392] Highly fluorine-bridged structures might exist in the solid, resulting in the nonvolatility of radon-fluorides compounds.[393,394]

We found that for NgF_n compounds with symmetries $D_{\infty h}$, D_{4h}, and T_d, electron correlation and relativistic effects boost the stability of the molecules, pushing to positive decomposition energy values. Conversely, for hexafluorides NgF_6, electron correlation and relativistic effects contribute in opposite directions, where spin-orbit contribution drives the decomposition energy to negative values. For $NgF_{2,4}$ compounds, Tables A.3 and A.5 show numerical results for electron correlation and relativistic effects on decomposition energy and Tables A.4 and A.6 for NgF_6.

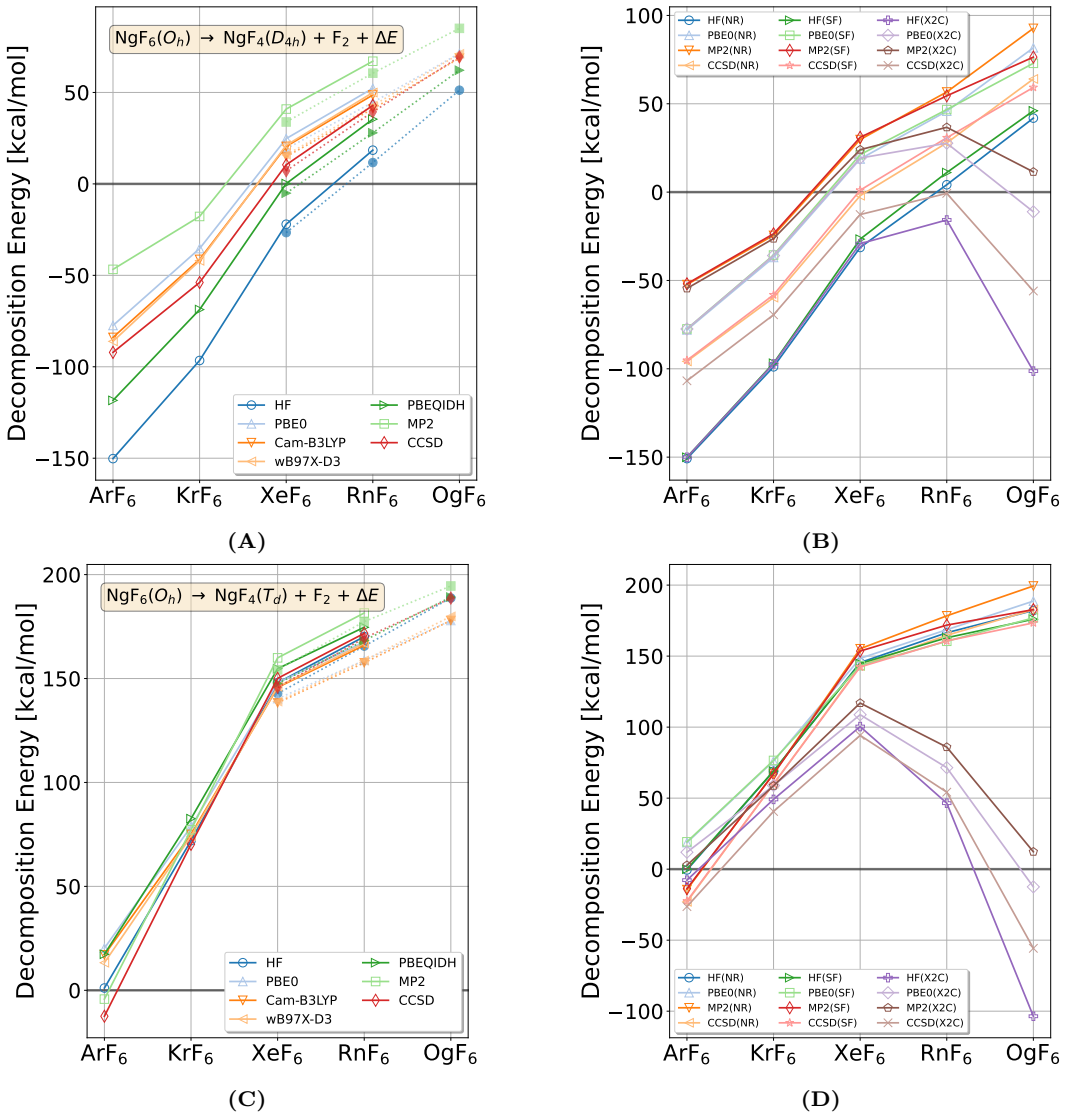

Figure 4.6: Molecular decomposition energies [in kcal/mol] for A-B) $NgF_6(O_h) \rightarrow NgF_4(D_{4h})$ and C-D) $NgF_6(O_h) \rightarrow NgF_4(T_d)$. The left panel shows energies computed using pseudo-potentials, where DEF2QZPPVD is represented with transparent markers and ECPxMDFQ uses solid colors. The right panel shows energies computed using cv3z all-electron basis set from nonrelativistic (NR), scalar relativistic spin-free (SF) and relativistic (X2C) levels.

4.3.3 Decomposition Analysis of the Electron Correlation and Relativistic Effects

Although different research about the atomic and molecular system has proven that relativistic and electron correlation effects are non-additive,[395–402] in 2005 Gourlaouen et al.[403] proposed a decomposition scheme to compute the independent role of the electron correlation and relativistic effects on a given property ($\mathcal{X}$) and to estimate the number of non-additive effects. The relativistic, electron correlation and non-additive effects are calculated according to the

following energy decomposition scheme

$$\Delta\mathcal{X} = \Delta\mathcal{X}_o + \Delta\mathcal{X}_{corr} + \Delta\mathcal{X}_{rel} + \Delta\mathcal{X}_{nonadd} \tag{4.5}$$

where $\Delta\mathcal{X}$ is considered as the reference value of the property of interest (e.g. bond length or decomposition energy), $\Delta\mathcal{X}_o$ is the property calculated at the Hartree-Fock level of theory with any further contribution, $\Delta\mathcal{X}_{corr}$ is the contribution of pure electron correlation effects, $\Delta\mathcal{X}_{rel}$ is the contribution of pure relativistic effects, and $\Delta\mathcal{X}_{nonadd}$ is the non-additive electron correlation and relativistic effects term.

For instance, when we compute a property $\mathcal{X}$ at the Hartree-Fock (HF) and PBE level of theory, using a non-relativistic (NR) and relativistic (REL) scheme and an all-electron (AE) basis set, $\Delta\mathcal{X}_{[REL(PBE)/AE]}$ is the reference value built from $\Delta\mathcal{X}_o = \Delta\mathcal{X}_{[NR(HF)/AE]}$ and the pure electron correlation

$$\Delta\mathcal{X}_{corr} = \Delta\mathcal{X}_{[NR(PBE)/AE]} - \Delta\mathcal{X}_{[NR(HF)/AE]} \tag{4.6}$$

and pure relativistic effects contributions

$$\Delta\mathcal{X}_{rel} = \Delta\mathcal{X}_{[REL(HF)/AE]} - \Delta\mathcal{X}_{[NR(HF)/AE]} \tag{4.7}$$

Therefore, from Equations (4.5) to (4.7), the non-additive electron correlation contribution is

$$\begin{aligned}\Delta\mathcal{X}_{nonadd} = \Delta\mathcal{X}_{[REL(PBE)/AE]} &- \Delta\mathcal{X}_{[NR(PBE)/AE]} \\ &- \Delta\mathcal{X}_{[REL(HF)/AE]} + \Delta\mathcal{X}_{[NR(HF)/AE]}\end{aligned} \tag{4.8}$$

On the other hand, when the relativistic effects (scalar) are included using pseudopotential (PP) methods, we only can recover the contribution of electron correlation effects, $\Delta\mathcal{X}_{corr} = \Delta\mathcal{X}_{[NR(PBE)/PP]} - \Delta\mathcal{X}_{[NR(HF)/PP]}$.

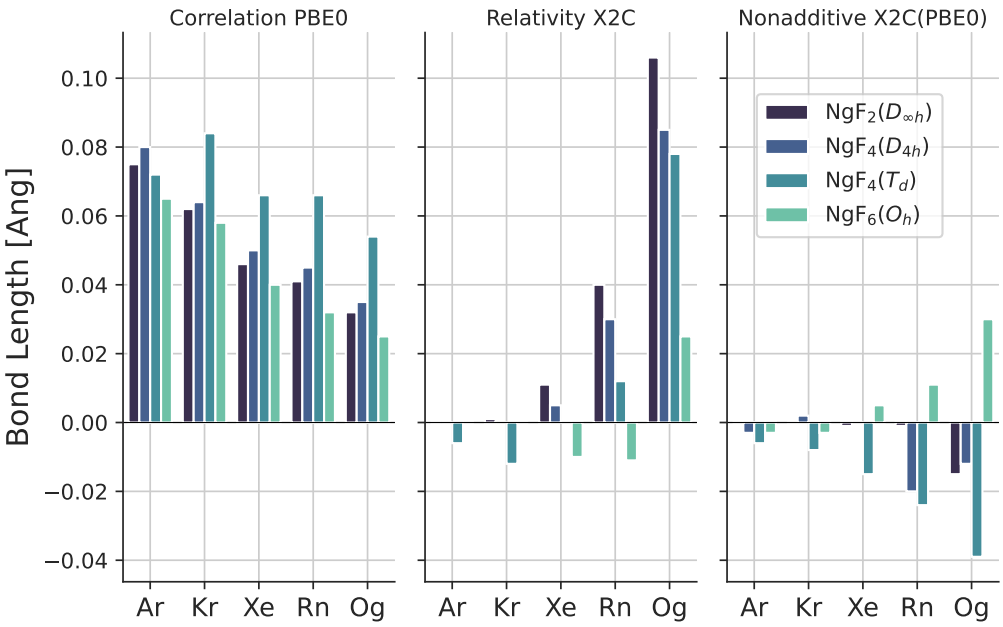

(A)

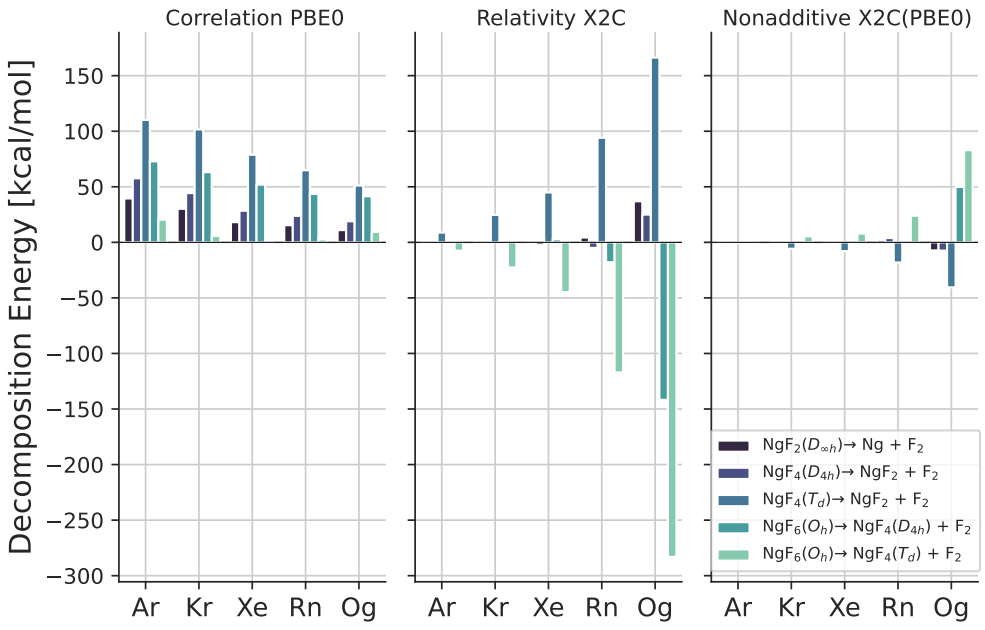

(B)

Figure 4.7: Decomposition analysis of the electron correlation and relativistic effects on the bond length and decomposition energy for NgF_n where $n = 2, 4, 6$ and Ng = Ar, Kr, Xe, Rn, and Og. The electron correlation, relativistic effects, and non-additive terms were computed according to Equations (4.6) to (4.8), respectively.

In Figure 4.7A, we present the individual contribution of pure electron correlation at the PBE0 level of theory, the contribution of pure relativistic effects at the X2C level of theory, and the non-additive term. Our findings showed that electron correlation contributions decrease and relativistic effects increase from Ar

to Og for the Ng–F bond lengths. Furthermore, both pure electron correlation and pure relativistic effects extend the Ng–F bond lengths by up to 0.1 Å and they contribute in the same scale. However, the non-additive term slightly reduces the Ng–F bond lengths, except for the hexafluoride NgF_6 with symmetry O_h (Ng = Xe, Rn, and Og).

Similarly, we found that as we go from Ar to Og, the contribution of electron correlation decreases and the contribution of relativistic effects increases the decomposition energy. However, for the hexafluoride NgF_6 with O_h symmetry, the contribution of relativistic effects reduces the decomposition energy (Figure 4.7B). The relativistic effects contribution for RnF_6 and OgF_6 is three times and six times larger, respectively, than the contribution of electron correlation.

4.3.4 Geometry Distortion of the Xenon Hexafluoride

Previously, we introduced how the Jahn-Teller effect distorts the molecular geometry of XeF_6, by splitting the degenerate states, enabling the molecule to have a lower symmetry. The concept of a second-order Jahn-Teller effect, or pseudo-Jahn-Teller effect, refers to the energetic stabilization of a molecule in a nondegenerate ground state by symmetry lowering. The second-order Jahn-Teller distortion allows a larger energy gap between the highest occupied molecular orbital (HOMO) and the lowest unoccupied molecular orbital (LUMO).

This effect increases the HOMO (a_{1g}^*)/LUMO (t_{1u}^*) splitting by allowing a mixing of the HOMO and LUMO orbitals that is only possible in XeF_6 distorted structure, C_{3v} or C_{2v}. The symmetry distortion by mixing the HOMO and LUMO lowers the overall energy in C_{3v} or C_{2v} symmetry where the HOMO and LUMO belong to the same symmetry species (a_1) and the extent of distortion is the delicate balance between energy-raising effects and stabilization of a molecule in a nondegenerate ground state.[392,404]

We performed an exhaustive search of the potential energy surface of XeF_6

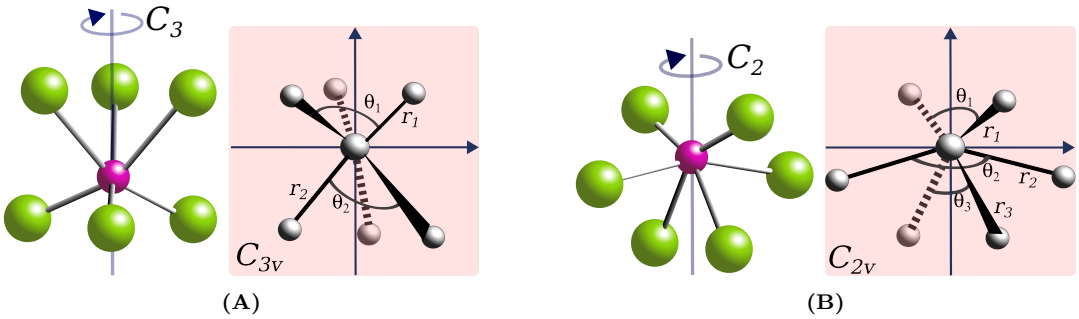

Figure 4.8: Geometry of NgF_6 according to A) C_{3v} symmetry and B) C_{2v} symmetry. The green spheres represent the fluorine atoms and the red spheres are the noble gas atoms.

using Simulated Annealing with Metropolis Monte Carlo (see Section 4.2) to generate candidate structures. A trigonally distorted geometry is observed, which is attributed to the presence of a stereochemically active lone pair of electrons from Xe and the need to accommodate seven electron pairs in the valence shell, Figure 4.8. Xenon hexafluoride has a unique molecular structure and is not monomeric in the solid, liquid, or dissolved state. While most hexafluorides adopt the octahedral structure.[405]

In Table 4.3, we show the optimized geometry of XeF_6 in O_h, C_{3v}, and C_{2v} symmetries and found that C_{3v} is the global minimum. Our results show that both the O_h and C_{3v} structures of XeF_6 are true minima on the potential energy surface, with the C_{2v} structure being a transition state. Furthermore, the energy difference between the O_h and C_{3v} symmetry is 2.90 kcal/mol and between the C_{2v} (saddle point) and C_{3v} symmetry is 1.14 kcal/mol.

This result suggests that for XeF_6 the small energy difference between the C_{3v} and O_h structures is due to the subtle changes in the electronic structure caused by the stereochemically active lone pair. The structures and vibrational frequencies of XeF_6 do not change significantly when going from C_{3v} to C_{2v} to O_h, indicating that the bonding between Xe and F atoms remains relatively stable.[341] This type of stereochemically active lone pair is not seen in similar systems, such as BrF_6^- or ClF_6^-, compound with octahedral geometry due to electron correlation effects.[339,406–411]

Table 4.3: Optimized geometry (bond distance in Å and angles in degrees) and relative energy (ΔE_r) to C_{3v} symmetry [kcal/mol] of XeF_6 molecule using Ahlrichs Def2TZVPPD basis set all-electron for F and scalar relativistic pseudo-potentials with 28 core electrons for Xe.

Symmetry	parameter	CAM-B3LYP	PBEQIDH	CCSD	CCSD(T)[a]	Composite[b]
C_{3v}	ΔE_r	0.0	0.0	0.0	0.0	0.0
	r_1	1.879	1.842	1.832	1.842	
	r_2	1.959	1.949	1.949	1.950	
	θ_1	83.9	82.3	81.9	82.1	
	θ_2	106.6	108.52	110.7	109.3	
O_h	ΔE_r	0.43	0.04	2.90	3.61	1.80
	r	1.926	1.910	1.908	1.917	
C_{2v}^c	ΔE_r	0.49	0.74	1.14	1.23	1.08
	r_1	1.974	1.965	1.972	1.968	
	r_2	1.906	1.888	1.872	1.886	
	r_3	1.870	1.848	1.834	1.845	
	θ_1	114.1	118.2	126.9	122.1	
	θ_2	167.2	166.0	163.7	164.7	
	θ_3	81.2	80.0	78.1	79.08	

[a] Peterson et al.[341] value at the CCSD(T)-F12b/VQZ-F12 level of theory with $\gamma = 1.4$ for both frozen-core and 4d-correlated calculations. [b] Total composite value including several contribution such as CCSD(T)-F12b/VQZ-F12, ΔCV (4d), ΔCV (1s of F, 4s4p of Xe), and DK-CCSD(T)/awCVTZ-DK according to Peterson et al.[341]. [c] XeF_6 molecule with symmetry C_{2v} has one imaginary frequency.

4.4 Conclusion

The bond distances in the noble gas fluorides (NgF_n) are influenced by both electron correlation and relativistic effects. Electron correlation has a greater impact on the bond distances of lighter atom systems like ArF_n and KrF_n, whereas relativistic effects have a more significant effect on heavy atom systems like RnF_n and OgF_n. The Xe–F bond length is impacted by both effects. The results of this study suggest that there are differences in bond distances depending on the level of theory applied in the calculation. For example, when considering relativistic effects, the bond lengths are longer in the exact two-components (X2C) calculation and shorter in the non-relativistic (NR) calculation. This indicates that the two-electron spin-same-orbit corrections, which are included in X2C calculations, play a crucial role in determining bond distances in the heavy atoms fluoride systems.

Despite the consensus that XeF_6 geometry is stereochemically active with a fluctuating lone pair, the debate about the significance of the O_h and C_{3v} structures and the impact of relativistic effects and electron correlation on the molecule's structure continues. For NgF_6, a Jahn-Teller distortion is observed when nonrelativistic Hartree-Fock theory is used, and even using a large basis set favored the C_{3v} structure. However, relativistic effects and electron correlation both favored the O_h structure, resulting in small differences between the two structures in their calculated energies. These suggest that both structures, O_h and C_{3v}, may coexist.

Noble gas difluorides NgF_2 ($D_{\infty h}$), tetrafluorides NgF_4 (D_{4h}) and hexafluorides NgF_6 (O_h) are generally stable, except for Ar and Kr, which are unstable and decompose to F_2 and NgF_{n-2}. In contrast, tetrahedral NgF_4 (T_d) are generally unstable, except for OgF_4 which is stable due to the influence of large relativistic effects. Moreover, OgF_6 is unstable and decomposes into F_2 and NgF_4 with symmetry either D_{4h} or T_d.

Our results suggested that OgF_6 is unstable and RnF_6 is likely the highest fluoride possible and may be an octahedral compound, even at the Hartree-Fock level, due to strong relativistic effects. These show the interplay role of relativistic effects and electron correlation effects in the geometrical distortion of NgF_6 molecule.

Appendix A

Appendix

A.1 The Extended Lennard–Jones Potential for Noble Gases

Table A.1: Fitting parameters for the two-body potentials of the noble gases (from Ne to Xe) according to ELJ model, Equation (1.10). C_k is given in a.u. and equilibrium distances (r_{eq}) are in Å. Data were taken from Refs.[8,9]

	Neon	Argon	Krypton	Xenon
C_6	−10.5097942564988	−123.635101619510	−227.476410584751	−301.7
C_8	989.725135614556	21262.8963716972	50281.6033768459	−26816.402071
C_9				−29141425.4118978
C_{10}	−101383.865938807	−3239750.64086661	−9549691.98083359	2525729440.60837
C_{11}				−93157553751.1815
C_{12}	3918846.12841668	189367623.844691	658170535.750904	1958061699137.66
C_{13}				−25959603531187.9
C_{14}	−56234083.4334278	−4304257347.72069	−17524714507.3525	225015902487099.0
C_{15}				−1292921381781360.0
C_{16}	288738837.441765	35315085074.3605	166980981478.238	4526862108942420.0
C_{17}				−9182845674164360.0
C_{18}				8100817151233585.0
r_{eq}	3.130	3.837	4.052	4.552

A.2 Transferable Intermolecular Potential

Although water is a chemically simple molecule, it is notoriously difficult to model. In 1933, Bernal-Fowler was one of the first attempts to describe water as a collection of point charges.[412] Since then, more than one hundred different water models/potentials have been proposed.[413] Generally, each model is developed to

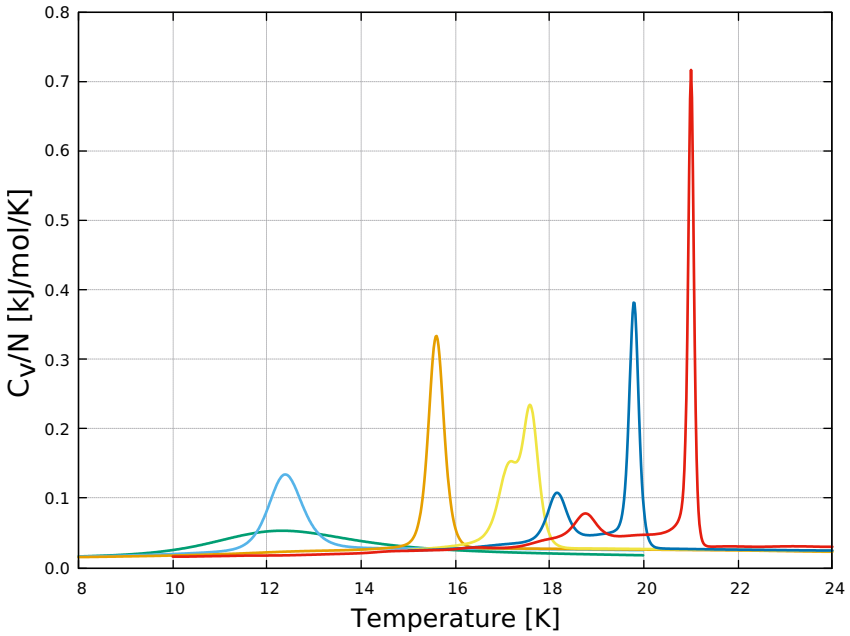

(A)

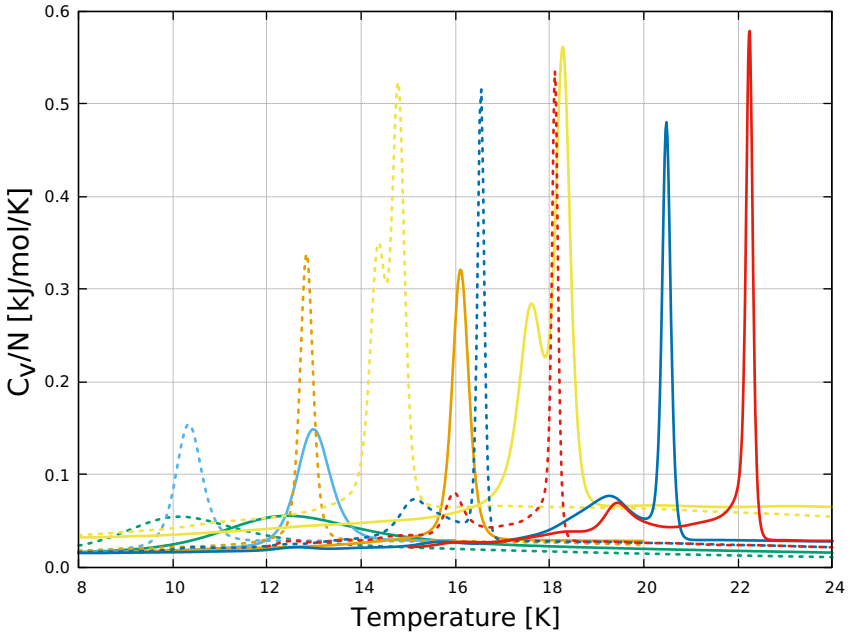

(B)

Figure A.1: Heat capacity for Ne_n cluster based on the two-body energy from the coupled-cluster level of theory in a homogeneous magnetic field in z direction. A) $B_z = 0.0$ *a.u.* at CCSD(T)/aug-cc-pV5Z level and B) $B_z = 0.2$ *a.u.* at CCSD (dashed) and CCSD(T) (solid) with the aug-cc-pVTZ basis set. From the left to the right : Ne_{13} (green), Ne_{55} (light blue), Ne_{147} (golden), Ne_{309} (light yellow), Ne_{561} (blue), and Ne_{923} (red), respectively.

fit one particular physical structure or parameter well, for example, the density anomaly, radial distribution function or critical parameters. Consequently, these models work well to reproduce the properties of the macroscopic systems according to the conditions in which they are parameterized.[414] The low computational cost

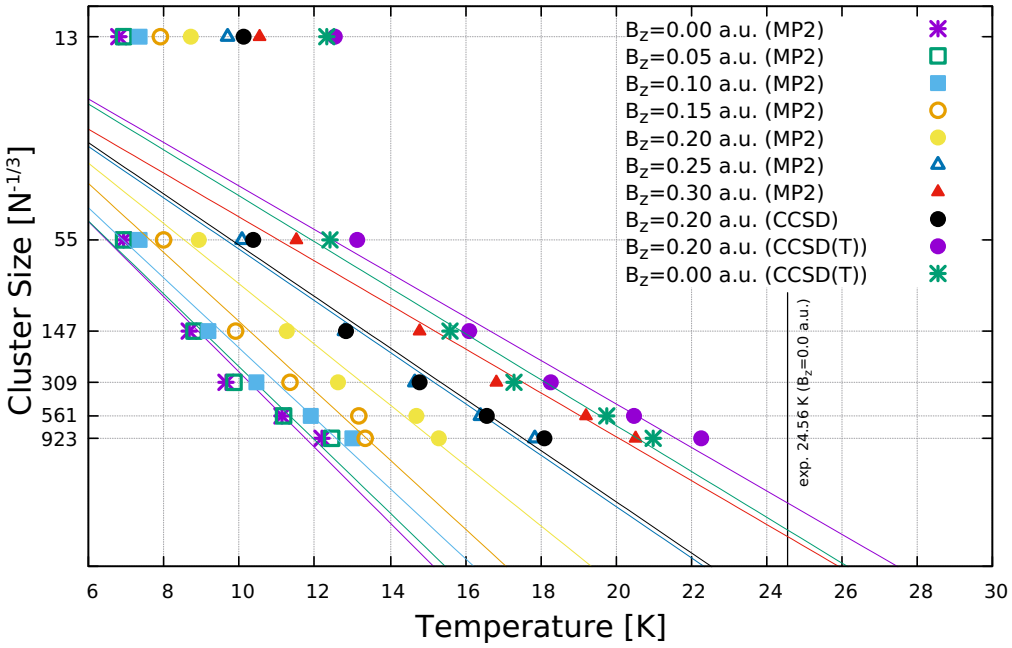

Figure A.2: Neon melting temperature size dependence ($N^{-1/3}$) and extrapolation in a homogeneous magnetic field. The experimental melting points of the bulk (24.56 K at field free) showed using a vertical line.

associated with these models would make them the preferred choice for the most computationally demanding applications. Several excellent reviews already exist that cover all attempts to accurately model water to date.[413–416] Here, we will look further into one specific family of water models.

One of the most widely used molecular potentials is the Transferable Intermolecular Potential (TIP) used to describe the interaction between two water molecules.

The Transferable Intermolecular Potential or TIPnP (where $n = 3 - 6$) involves rigid water monomers that are represented by three, four, five or six interaction sites (Figure A.3). Transferable Intermolecular Potentials are a two-body potential energy function for monomers M and N, so

$$\mathcal{E}^{\mathrm{TIP}}(ij) = \sum_{i}^{\text{in } M} \sum_{j}^{\text{in } N} \left\{ \frac{q_i q_j}{|\mathbf{r}_i - \mathbf{r}_j|} + 4\varepsilon_o \left[\left(\frac{\sigma_o}{|\mathbf{r}_i^o - \mathbf{r}_j^o|} \right)^{12} - \left(\frac{\sigma_o}{|\mathbf{r}_i^o - \mathbf{r}_j^o|} \right)^{6} \right] \right\} \tag{A.1}$$

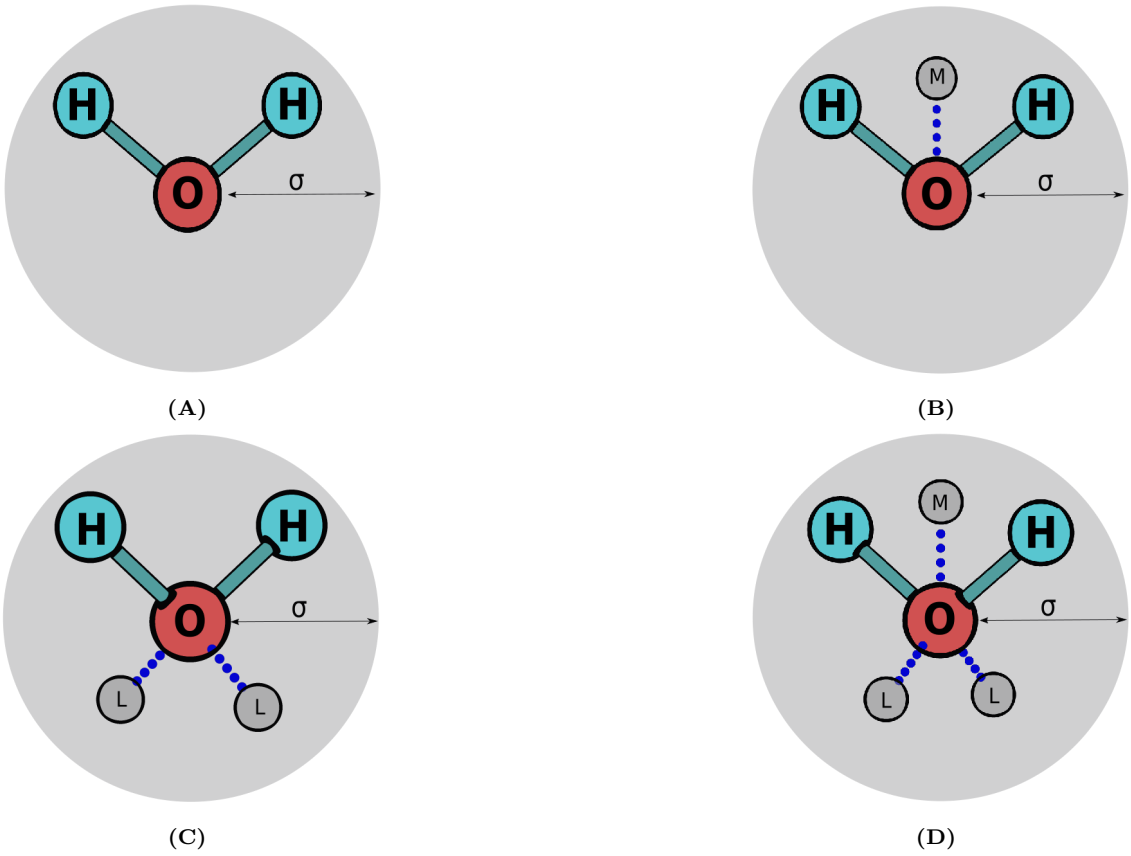

Figure A.3: Schematic illustration of a water molecule for Transferable Intermolecular Potentials. A) 3-site model (TIP3P), B) 4-site model (TIP4P), C) 5-site model (TIP5P), D) 6-site model (TIP6P). Model types (A) and (B) are all planar whereas types (C) and (D) are almost tetrahedral. The distance OH is 0.9572 Åand the angle HOH is 104.52 degrees for all models. For TIP6P, there are two different σ parameters, one for oxygen and another for hydrogen atoms (Table A.2).

This family of potentials describes a Coulombic interaction between all intermolecular pairs of charges along with a single LJ term between the oxygens. The original TIP3P site model has positive charges on the hydrogen atom and a negative charge on the oxygen atom($q_o = -2q_{\mathrm{H}}$).[417] In all TIPnP models, there is a charge equilibrium; that is, $\sum_i q_i = 0$ (Table A.2). The TIP4P model has four interaction points by adding one dummy atom (M-site) close to the oxygen, along with the bisector of the HOH angle; to displace the negative charge towards the hydrogens.[418] This M-site only has a negative charge (Figure A.3 b). The TIP5P model replaces the M-site with two tetrahedral negative charge sites (L-site), to mimic the lone pairs of water (Figure A.3 c).[419] In Figure A.3 d, the TIP6P model combines M- and L-sites, and includes an additional LJ term between Hydrogens ($\mathbf{r}^{\mathrm{H}}$, ϵ_{H} and σ_{H}).[420] An additional model was used here, the TIP4P-ice, specifically designed to deal with solid-phase properties, using different parameters

Table A.2: Parameters for the Transferable Intermolecular Potentials (Figure A.3).

	TIP3P	TIP4P	TIP4P-ice	TIP5P	TIP6P
σ_o (Å)	3.1506	3.1536	3.1668	3.12	3.15
σ_{H} (Å)					0.673
ϵ_o (kJ/mol)	0.6364	0.648	0.8822	0.6694	0.7149
ϵ_{H} (kJ/mol)					0.1154
q_o (e)	−0.834				
q_{H} (e)	0.417	0.52	0.5897	0.241	0.477
q_{M} (e)		−1.04	−1.1794		−0.866
q_{L} (e)				−0.241	−0.044
Distance OM (Å)		0.15	0.1577		0.23
Angle HOM (deg)		52.26	52.26		52.26
Distance OL (Å)				0.7	0.8892
Angle LOL (deg)				109.47	111.00

for the 4-sites model.[421]

TIPnP potentials are one of the most uncomplicated models used to study water behavior, but outside of the conditions in which they are parameterized, they are not very accurate predictors. However, they have a low computational cost for a large number of water molecules. Many works published with these models show that they can predict phase transitions, densities, enthalpy of vaporization, heat capacities and dielectric constants across phases.[72,422,423]

Although TIPnP models are of great utility, neither transferability nor universal applicability can be identified at this time. They work using a rigid water model, and it gives an excessive stabilization of the interatomic interactions.[424] Clearly, water is a polarizable molecule, and it also has internal vibrations; water is a flexible molecule. TIPnP models do not include these characteristics. Therefore, the predictive value of these water models and their general application should be approached with caution.

A.3 The chemical bonding in the superheavy element flerovium

A.3.1 Potential energy curves

The N-body (N=2,3,4) potential energy curves $V(R)$ for the dimer, trimer (D_{3h} symmetry) and tetramer (T_d symmetry) at various levels of theory using different basis sets are provided on a downloadable excel spread-sheet file (PotentialCurvesFl.xlsx). Distances are in Å and energies in eV. For the three-body potential, the numbers in red are estimated because we faced difficulties in the HF convergence at the X2C level of theory. The data also contains the fcc solid-state cohesive energy curves $E_{\mathrm{coh}}(R)$ at different levels of theory.

A.3.2 Heat capacities

Heat capacity curves obtained with the PBE0 and CCSD(T)* potentials are shown in Figures A.4 and A.5 respectively. Top, two-body simulations with cells with N = 108, 256, 500 and 864 atoms, bottom two+three-body simulations for the N=108 and 256 atomic cell.

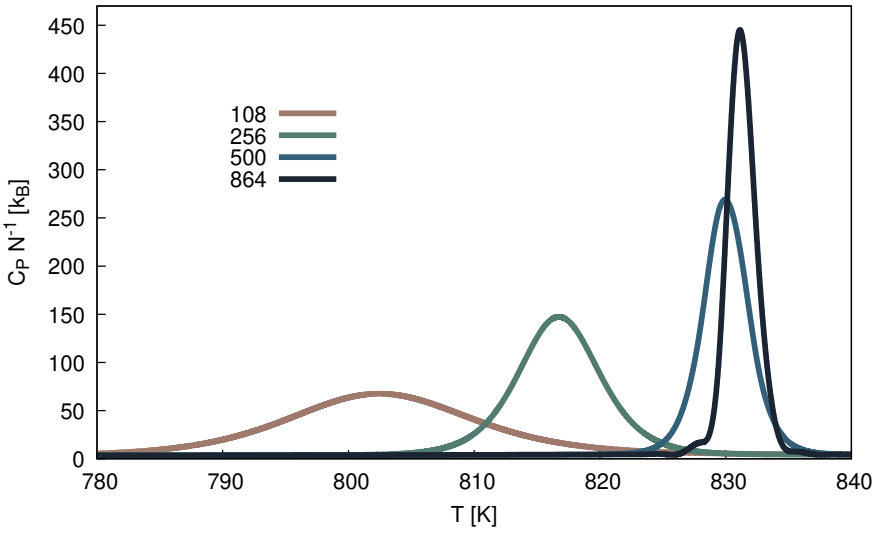

(A)

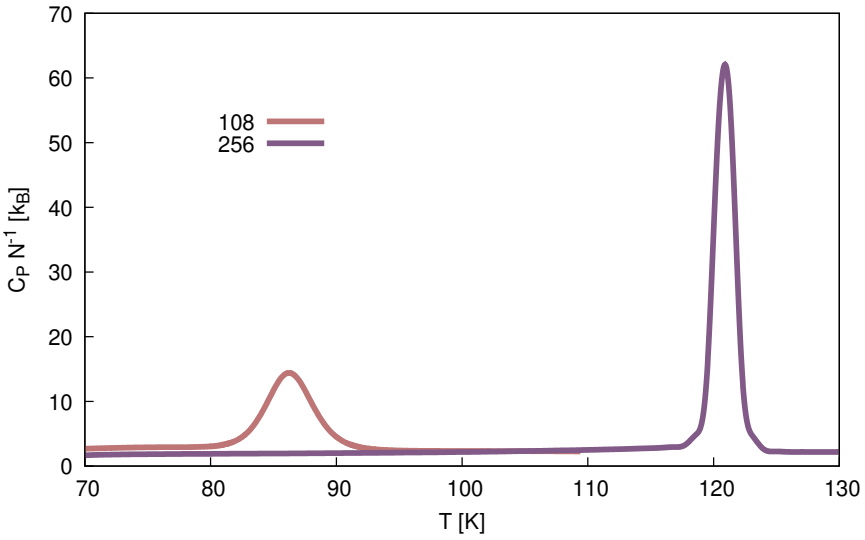

(B)

Figure A.4: Heat capacities per atom as a function of the simulation temperature not corrected for superheating. A) heat capacity curves obtained considering two-body PBE0 ELJ interactions only. B) obtained heat capacities considering two and three-body interactions, computed with the PBE0 ELJ and EATM potentials respectively.

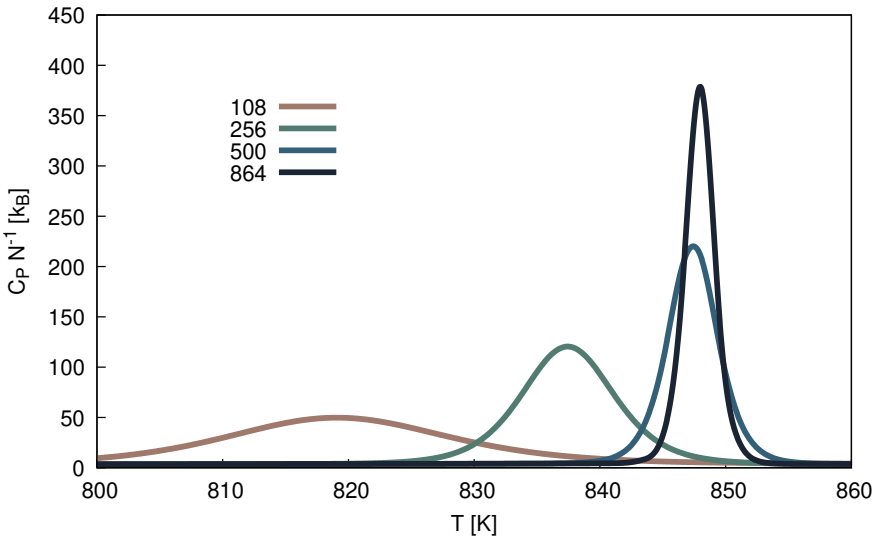

(A)

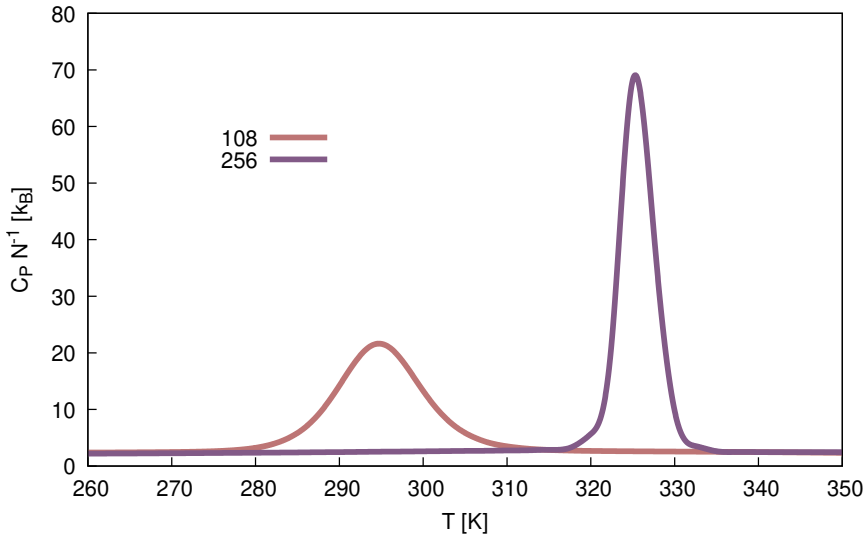

(B)

Figure A.5: Heat capacities per atom as a function of the simulation temperature not corrected for superheating. A) heat capacity curves obtained considering two-body CCSD(T)* ELJ interactions only. B)heat capacities considering two and three-body interactions, computed with the CCSD(T)* ELJ and EATM potentials, respectively.

A.3.3 Densities

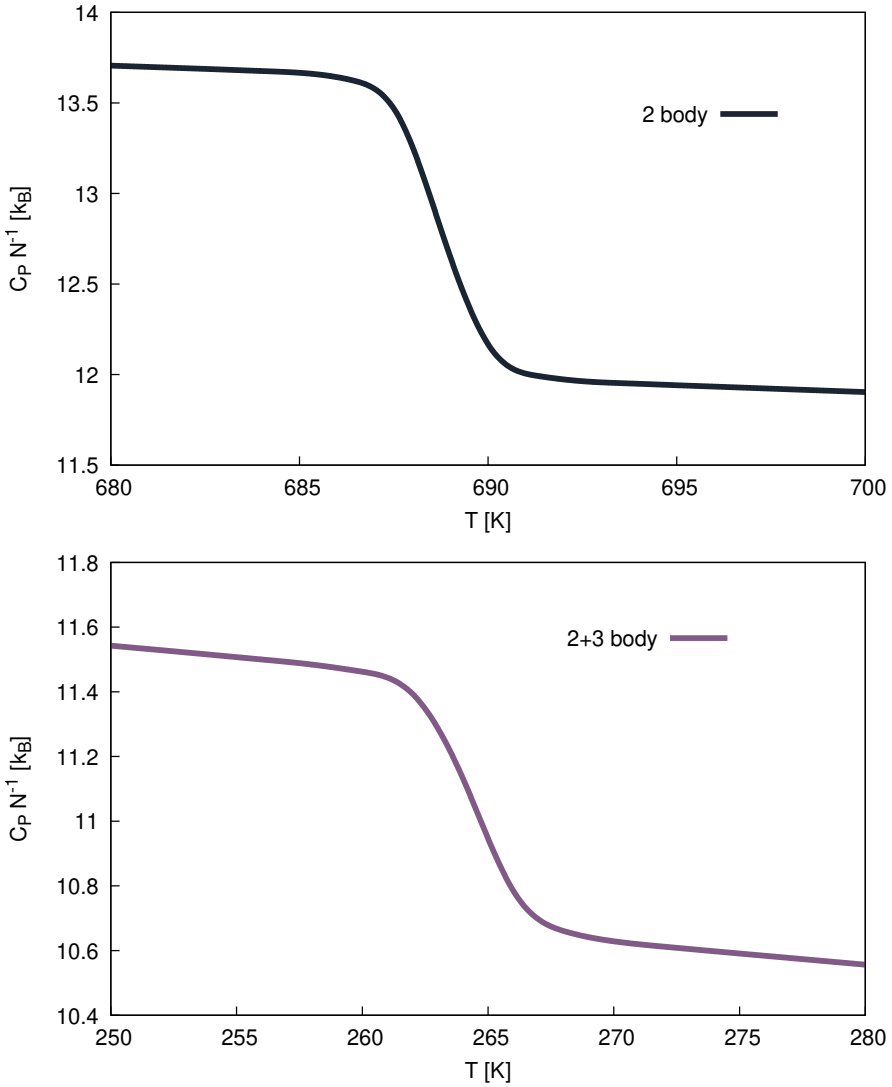

Figure A.6: Densities as a function of the simulation temperature corrected for superheating. A) density obtained considering two-body CCSD(T)* ELJ interactions only, extracted from the $N = 864$ simulation cell. B) density obtained considering two and three-body interactions, computed with the CCSD(T)* ELJ and EATM potentials respectively, extracted from the $N = 256$ simulation cell.

A.4 Probing High Oxidation States in Noble Gas Fluorides

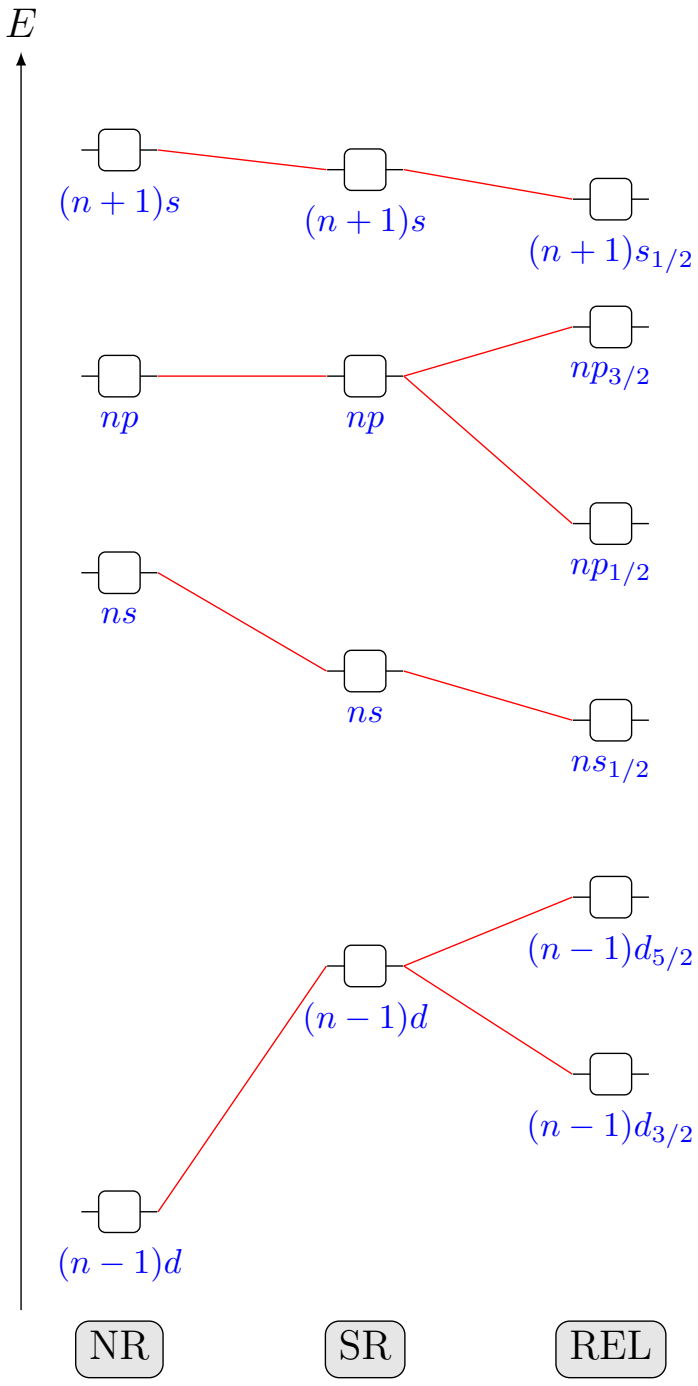

Figure A.7: Relativistic corrections to the atomic orbital energy levels for the $^1S_0$ ground state of a noble gas (Kr, Xe, Rn, or Og) from nonrelativistic (NR) and scalar-relativistic (SR) Hartree-Fock, and Dirac-HartreeFock (REL) calculations according to Jerabek et al.[5]

Table A.3: Electron correlation effects on decomposition energy [kcal/mol] for $NgF_{2,4}$, where Ng = Ar, Kr, Xe, Rn, Og. Using Ahlrichs Def2TZVPPD (TZ), Def2QZVPPD (QZ) basis set and the Stuttgart/Dresden ECPxMDF pseudo-potential (x = 28, 60, and 92 for Xe, Rn, and Og, respectively) and TZVP basis set for the valence electrons for Ng and aug-cc-pVTZ for Fluorine atom.

	Basis set	HF	PBE0	CAM-B3LYP	ωB97X-D	PBEQIDH	MP2	CCSD
$NgF_2(D_{\infty h}) \rightarrow Ng + F_2$								
Ar	TZ	-76.6	-38.3	-42.1	-43.8	-59.4	-39.9	-54.7
	QZ	-75.7	-37.5	-41.3	-43.3	-58.5	-37.3	-52.8
Kr	TZ	-38.5	-9.3	-12.3	-13.7	-25.1	-8.4	-20.8
	QZ	-36.9	-8.0	-11.0	-12.5	-23.6	-8.0	-20.2
Xe	TZ	7.8	26.8	25.7	25.0	17.2	25.5	17.6
	QZ	11.5	29.9	28.8	27.7	20.7	30.5	22.4
	ECP	9.2	27.1	26.1	25.3	18.3	32.8	23.4
Rn	TZ	20.2	38.7	38.3	38.1	28.8	40.3	31.6
	QZ	23.1	41.1	40.8	40.1	31.5	42.8	34.3
	ECP	21.8	38.2	38.2	37.7	29.9	46.4	37.2
Og	ECP	36.4	50.1	51.3	51.0	43.1	58.1	50.7
$NgF_4(D_{4h}) \rightarrow NgF_2 + F_2$								
Ar	TZ	-116.3	-60.0	-65.4	-67.2	-91.3	-50.6	-77.8
	QZ	-115.1	-59.0	-64.3	-66.5	-90.2	-47.5	-75.7
Kr	TZ	-65.4	-23.0	-27.8	-28.5	-45.9	-16.7	-37.5
	QZ	-63.2	-21.2	-25.9	-26.8	-43.8	-15.7	-36.4
Xe	TZ	-2.7	25.3	22.4	22.6	11.0	27.9	13.1
	QZ	2.4	29.6	26.7	26.6	15.9	34.6	19.7
	ECP	-1.2	25.2	22.3	22.6	11.9	33.8	18.6
Rn	TZ	16.7	41.9	39.5	40.4	28.8	47.2	32.3
	QZ	21.1	45.5	43.2	43.7	33.0	51.3	36.8
	ECP	17.8	40.6	38.4	39.2	29.1	51.7	37.6
Og	ECP	39.1	57.1	56.0	57.0	48.2	67.1	55.8
$NgF_4(T_d) \rightarrow NgF_2 + F_2$								
Ar	TZ	-266.7	-156.9	-165.6	-165.8	-226.2	-89.6	-152.0
	QZ	-266.5	-156.6	-165.3	-165.8	-225.9	-90.0	-155.4
Kr	TZ	-232.7	-136.0	-142.8	-143.5	-196.0	-110.0	-157.8
	QZ	-231.8	-135.3	-142.2	-143.0	-195.1	-110.7	-160.6
Xe	TZ	-171.1	-96.4	-101.3	-100.8	-142.0	-88.3	-122.6
	QZ	-167.5	-93.6	-98.6	-98.3	-138.7	-84.4	-120.0
	ECP	-170.6	-95.9	-101.0	-100.4	-140.8	-86.5	-119.9
Rn	TZ	-133.8	-72.2	-76.6	-75.4	-109.2	-65.9	-94.2
	QZ	-130.6	-69.8	-74.1	-73.3	-106.3	-63.1	-92.0
	ECP	-136.1	-73.6	-78.1	-76.7	-111.2	-65.1	-92.5
Og	ECP	-98.4	-49.5	-53.1	-51.7	-78.8	-42.4	-63.5

Table A.4: Electron correlation effects on decomposition energy [kcal/mol] for NgF_6 with symmetry O_h, where Ng = Ar, Kr, Xe, Rn. Using Ahlrichs Def2TZVPPD (TZ) and Def2QZVPPD (QZ) basis set.

Noble gas (Ng)	Basis set	HF	PBE0	CAM-B3LYP	ωB97X-D	PBEQIDH	MP2	CCSD
$NgF_6(O_h) \rightarrow NgF_4(D_{4h}) + F_2$								
Ar	TZ	-150.8	-78.0	-84.5	-86.3	-119.0	-49.1	-93.1
	QZ	-150.2	-77.4	-83.9	-86.1	-118.4	-46.7	-92.1
Kr	TZ	-98.8	-37.3	-43.3	-43.8	-70.8	-19.9	-54.8
	QZ	-96.6	-35.4	-41.3	-42.1	-68.7	-17.8	-53.9
Xe	TZ	-27.5	20.1	15.7	16.8	-5.0	33.6	3.9
	QZ	-22.1	24.8	20.5	21.1	0.2	40.9	10.4
	ECP	-26.6	19.2	15.0	15.9	-5.1	33.9	7.2
Rn	TZ	12.6	47.5	43.7	45.5	30.0	61.3	36.9
	QZ	18.4	52.2	48.6	49.9	35.4	67.1	42.9
	ECP	11.7	44.6	41.0	42.7	27.9	60.5	39.4
Og	ECP	51.2	71.4	68.7	71.1	62.1	85.1	69.4
$NgF_6(O_h) \rightarrow NgF_4(T_d) + F_2$								
Ar	TZ	-0.3	18.9	15.6	12.4	16.0	-10.1	-18.9
	QZ	1.1	20.3	17.1	13.3	17.4	-4.2	-12.5
Kr	TZ	68.5	75.7	71.7	71.3	79.3	73.4	65.5
	QZ	72.0	78.7	75.0	74.1	82.6	77.2	70.2
Xe	TZ	140.8	141.8	139.3	140.2	148.0	149.7	139.6
	QZ	147.9	148.0	145.7	146.0	154.7	159.9	150.1
	ECP	142.8	140.3	138.3	138.9	147.6	154.2	145.7
Rn	TZ	163.0	161.6	159.8	161.3	168.0	174.3	163.4
	QZ	170.2	167.5	166.0	166.9	174.7	181.5	171.7
	ECP	165.6	158.7	157.6	158.7	168.3	177.4	169.5
Og	ECP	188.7	177.9	177.9	179.9	189.2	194.5	188.7

Table A.5: Electron correlation and relativistic effects on decomposition energy [kcal/mol] for $NgF_{2,4}$ where Ng = Ar, Kr, Xe, Rn. Using all-electron Dyall.cv2z (DZ) and Dyall.cv3z (TZ) basis set.

		Non–Relativistic				Spin–Free				Exact Two Component			
	Basis	HF	PBE0	MP2	CCSD	DHF	PBE0	MP2	CCSD	DHF	PBE0	MP2	CCSD
$NgF_2(D_{\infty h}) \rightarrow Ng + F_2$													
Ar	DZ	-87.3	-46.7	-54.4	-67.8	-86.8	-46.3	-53.9	-67.3	-86.8	-46.2	-53.9	-67.3
	TZ	-77.4	-38.9	-42.5	-57.1	-77.0	-38.5	-42.1	-56.8	-77.0	-38.5	-42.1	-56.8
Kr	DZ	-47.9	-16.8	-27.4	-37.7	-47.2	-15.8	-26.3	-36.8	-46.8	-15.4	-26.0	-36.5
	TZ	-39.3	-10.1	-14.8	-26.0	-39.1	-9.5	-14.2	-25.6	-38.7	-9.2	-13.9	-25.3
Xe	DZ	-1.2	17.5	6.1	-0.1	-2.9	17.2	5.8	-1.0	-1.4	18.5	7.1	0.2
	TZ	11.1	28.6	23.2	16.6	8.0	26.9	21.7	14.4	9.5	28.4	22.9	15.7
Rn	DZ	16.1	32.0	21.4	16.1	10.2	29.5	19.4	12.3	22.3	40.2	28.8	22.1
	TZ	27.8	42.7	38.2	32.4	18.3	37.0	33.1	25.4	30.2	47.5	42.5	35.2
Og	DZ	49.9	61.3	50.2	46.5	35.7	50.7	40.5	34.8	88.9	92.4	79.5	77.1
	TZ	54.5	65.1	60.6	56.7	37.9	52.6	49.1	42.6	89.4	93.4	87.4	84.4
$NgF_4(D_{4h}) \rightarrow NgF_2 + F_2$													
Ar	DZ	-127.9	-69.2	-66.7	-91.2	-127.4	-68.7	-66.2	-90.7	-127.4	-68.6	-66.2	-90.7
	TZ	-116.9	-60.4	-53.2	-80.1	-116.4	-59.9	-52.7	-79.7	-116.4	-59.9	-52.7	-79.7
Kr	DZ	-78.9	-33.0	-38.9	-57.9	-78.2	-32.2	-37.9	-56.9	-78.2	-32.0	-37.8	-56.9
	TZ	-66.1	-23.4	-23.0	-42.9	-65.9	-22.9	-22.4	-42.5	-65.9	-22.8	-22.3	-42.4
Xe	DZ	-18.5	11.6	2.9	-10.2	-20.3	11.1	2.6	-11.2	-20.2	11.4	2.8	-11.0
	TZ	1.5	28.3	26.8	13.1	-2.0	26.1	24.9	10.5	-1.9	26.6	25.1	10.7
Rn	DZ	7.2	32.5	24.4	12.4	-0.1	28.4	20.8	7.2	4.3	33.4	24.6	11.0
	TZ	26.3	48.6	47.9	35.4	14.7	40.5	40.1	26.2	19.1	45.4	43.9	29.9
Og	DZ	55.6	76.2	67.6	56.3	37.3	59.3	52.0	40.6	82.5	94.9	82.6	75.3
	TZ	62.4	79.8	79.1	68.4	40.9	60.9	59.8	48.6	85.6	96.2	90.6	84.0
$NgF_4(T_d) \longrightarrow NgF_2 + F_2$													
Ar	DZ	-264.3	-154.0	-80.5	-135.4	-263.7	-153.7	-80.3	-135.0	-255.1	-146.0	-104.1	-137.8
	TZ	-267.1	-157.1	-91.2	-152.9	-266.5	-156.6	-90.9	-152.4	-258.7	-149.3	-109.3	-161.0
Kr	DZ	-244.5	-138.6	-132.1	-179.0	-236.3	-137.0	-115.4	-159.2	-216.7	-119.6	-109.1	-153.8
	TZ	-233.9	-136.6	-114.8	-162.7	-231.9	-135.0	-113.0	-160.6	-212.3	-117.6	-104.7	-152.0
Xe	DZ	-193.1	-109.3	-117.6	-150.3	-186.3	-106.9	-108.1	-141.3	-147.1	-73.9	-80.1	-111.1
	TZ	-175.3	-101.4	-98.7	-132.1	-173.4	-95.9	-97.7	-130.8	-131.5	-62.9	-62.8	-94.8
Rn	DZ	-154.5	-86.6	-93.3	-120.5	-151.1	-84.4	-90.7	-117.6	-59.1	-10.5	-24.1	-43.6
	TZ	-136.0	-74.2	-73.8	-101.4	-137.1	-73.2	-77.2	-103.7	-43.2	1.6	-4.4	-24.5
Og	DZ	-81.7	-30.0	-39.2	-60.0	-91.7	-43.5	-53.9	-72.1	85.2	96.7	82.4	75.5
	TZ	-77.8	-27.3	-27.6	-50.2	-89.1	-43.1	-46.5	-65.5	87.9	97.5	89.9	83.9

Table A.6: Electron correlation and relativistic effects on decomposition energy [kcal/mol] for NgF_6 with symmetry O_h, where Ng = Ar, Kr, Xe, Rn, Og. Using Dyall.cv2z (DZ) and Dyall.cv3z (TZ) basis set.

		Non–Relativistic				Spin–Free				Exact Two Component			
	Basis	DHF	PBE0	MP2	CCSD	DHF	PBE0	MP2	CCSD	DHF	PBE0	MP2	CCSD
$NgF_6(O_h) \longrightarrow NgF_4(D_{4h}) + F_2$													
Ar	DZ	-155.1	-82.1	-62.4	-100.2	-154.4	-81.6	-61.9	-99.7	-154.4	-81.6	-62.0	-99.7
	TZ	-150.8	-78.0	-52.3	-95.8	-150.1	-77.4	-51.9	-95.2	-150.1	-77.5	-54.5	-106.8
Kr	DZ	-107.9	-43.5	-37.5	-70.1	-105.8	-42.2	-36.4	-68.4	-106.1	-42.4	-36.6	-68.6
	TZ	-98.9	-37.0	-24.5	-59.7	-96.8	-35.6	-23.6	-58.2	-97.2	-35.9	-26.3	-69.4
Xe	DZ	-52.2	1.6	4.9	-25.0	-46.6	5.1	7.5	-20.9	-49.0	3.3	6.0	-22.7
	TZ	-31.3	18.8	29.7	-2.0	-26.6	21.2	31.0	1.1	-29.2	19.3	24.0	-12.7
Rn	DZ	-18.4	27.3	29.0	1.6	-9.1	31.3	30.8	7.4	-34.2	13.5	16.6	-10.6
	TZ	4.2	45.8	56.7	27.9	11.1	46.7	54.5	30.8	-15.8	27.7	36.7	-0.7
Og	DZ	37.2	80.4	81.4	53.6	40.8	71.5	69.8	51.4	-103.2	-10.6	11.3	-46.7
	TZ	41.9	81.7	92.7	64.0	46.0	72.9	76.4	59.2	-101.3	-11.1	11.4	-56.0
$NgF_6(O_h) \longrightarrow NgF_4(T_d) + F_2$													
Ar	DZ	-18.8	2.7	-48.6	-56.1	-18.1	3.3	-47.8	-55.3	-26.7	-4.3	-24.0	-52.6
	TZ	-0.6	18.7	-14.4	-23.0	0.0	19.2	-13.8	-22.4	-7.7	11.9	2.8	-26.4
Kr	DZ	57.6	62.1	55.7	51.1	52.3	62.7	41.1	33.9	32.4	45.2	34.7	28.2
	TZ	68.9	76.1	67.2	60.0	69.1	76.5	67.1	60.0	49.1	58.9	58.7	40.6
Xe	DZ	122.4	122.6	125.4	115.0	119.5	123.1	118.1	109.1	77.9	88.7	88.8	77.4
	TZ	145.4	148.4	155.2	143.1	144.8	143.3	153.5	142.4	100.4	108.7	117.0	94.2
Rn	DZ	143.3	146.4	146.7	134.6	141.9	144.2	142.3	132.2	29.2	57.3	65.4	44.0
	TZ	166.5	168.6	178.4	164.6	162.9	160.5	171.8	160.7	46.5	71.5	85.9	54.2
Og	DZ	174.5	186.6	188.2	170.0	169.8	174.3	175.7	164.1	-105.9	-12.3	11.5	-46.9
	TZ	182.1	188.7	199.4	182.6	176.0	176.9	182.7	173.4	-103.6	-12.5	12.2	-55.7

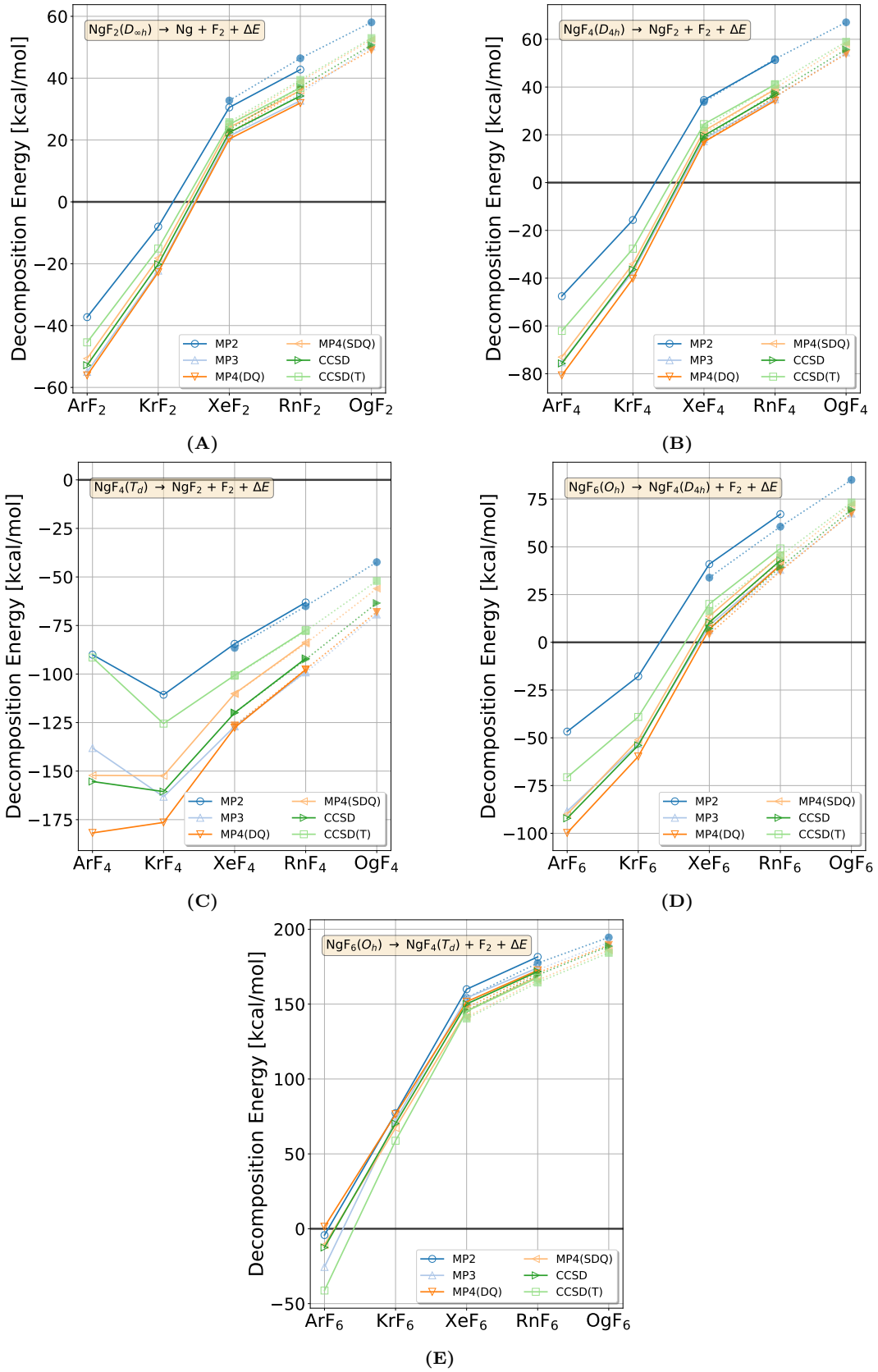

Figure A.8: Molecular decomposition energies [kcal/mol] at MP2, PM3, MP4(DQ), MP4(SDQ), CCSD, and CCSD(T) using Pseudo-Potentials, where DEF2QZPPVD is represented with transparent markers and ECPxMDFQ uses solid colors. For NgF_n where Ng = Ar, Kr, Xe, Rn, and Og and $n = 2, 4, 6$, A) NgF_2 with symmetry $D_{\infty h}$, B) NgF_4 with symmetry $D_{\infty h}$, C) NgF_4 with symmetry T_d, and D) NgF_6 with symmetry O_h.

MASSEY UNIVERSITY
TE KUNENGA KI PŪREHUROA
UNIVERSITY OF NEW ZEALAND

GRADUATE RESEARCH SCHOOL

STATEMENT OF CONTRIBUTION
DOCTORATE WITH PUBLICATIONS/MANUSCRIPTS

We, the student and the student's main supervisor, certify that all co-authors have consented to their work being included in the thesis and they have accepted the student's contribution as indicated below in the Statement of Originality.

Student name:	Edison Ferney Florez Hincapie
Name and title of main supervisor:	Distinguished Professor Peter Schwerdtfeger
In which chapter is the manuscript/published work?	Chapter 3: The Super-Heavy Element Flerovium
What percentage of the manuscript/published work was contributed by the student?	80%

Describe the contribution that the student has made to the manuscript/published work:

Edison's contribution was significant and multifaceted. He played a critical role in data generation and curation, ensuring the data used in the study was reliable and valid. Additionally, his contributions in statistical methods and quantum chemistry was essential in generating atomic and molecular calculations, many-body potentials, analyzing the data, and drawing meaningful conclusions. Finally, his involvement in the investigation phase of the research helped ensure the research questions were answered accurately and thoroughly.

Please select one of the following three options:

(X)	**The manuscript/published work is published or in press** Please provide the full reference of the research output: Florez, Edison, Odile R. Smits, Jan-Michael Mewes, Paul Jerabek, and Peter Schwerdtfeger. "From the gas phase to the solid state: The chemical bonding in the superheavy element flerovium." The Journal of Chemical Physics 157, no. 6 (2022): 064304. DOI: 10.1063/5.0097642
( )	**The manuscript is currently under review for publication** Please provide the name of the journal:
( )	**It is intended that the manuscript will be published, but it has not yet been submitted to a journal**

Student's signature:	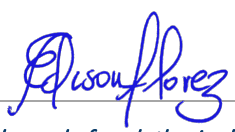	Main supervisor's signature:	

This form should appear at the end of each thesis chapter/section/appendix submitted as a manuscript/ publication or collected as an appendix at the end of the thesis.

Bibliography

[1] KP Huber and G Herzberg. Molecular structure and molecular spectra. iv. constants of diatomic molecules. *Van Rostrand-Reinhold, New York*, 1979.

[2] Charles Kittel and Paul McEuen. *Introduction to solid state physics*. John Wiley & Sons, 2018.

[3] K.G. Dyall, I.P. Grant, C.T. Johnson, F.A. Parpia, and E.P. Plummer. GRASP: A general-purpose relativistic atomic structure program. *Comput. Phys. Commun.*, 55(3):425–456, 1989. ISSN 0010-4655. doi: http://dx.doi.org/10.1016/0010-4655(89)90136-7. URL http://www.sciencedirect.com/science/article/pii/0010465589901367.

[4] Paul Jerabek, Odile R. Smits, Jan-Michael Mewes, Kirk A. Peterson, and Peter Schwerdtfeger. Solid oganesson via a many-body interaction expansion based on relativistic coupled-cluster theory and from plane-wave relativistic density functional theory. *J. Phys. Chem. A*, 123(19):4201–4211, 05 2019. doi: 10.1021/acs.jpca.9b01947. URL https://doi.org/10.1021/acs.jpca.9b01947.

[5] Paul Jerabek, Bastian Schuetrumpf, Peter Schwerdtfeger, and Witold Nazarewicz. Electron and nucleon localization functions of oganesson: approaching the thomas-fermi limit. *Physical Review Letters*, 120(5):053001, 2018.

[6] A. Borschevsky, V. Pershina, E. Eliav, and U. Kaldor. Relativistic coupled cluster study of diatomic compounds of hg, cn, and fl. *J. Chem. Phys.*, 141(8):084301, 2014. doi: 10.1063/1.4893347. URL https://doi.org/10.1063/1.4893347.

[7] Wenjian Liu, Christoph van Wüllen, Young Kyu Han, Yoon Jeong Choi, and Yoon Sup Lee. Spectroscopic constants of pb and eka-lead compounds: comparison of different approaches. *Adv. Quantum Chem.*, 39:325–355, 2001.

[8] Peter Schwerdtfeger, Nicola Gaston, Robert P Krawczyk, Ralf Tonner, and Gloria E Moyano. Extension of the lennard-jones potential: Theoretical investigations into rare-gas clusters and

crystal lattices of he, ne, ar, and kr using many-body interaction expansions. *Physical Review B*, 73(6):064112, 2006.

[9] Paul Jerabek, Odile Smits, Elke Pahl, and Peter Schwerdtfeger. A relativistic coupled-cluster interaction potential and rovibrational constants for the xenon dimer. *Molecular Physics*, 116(1):1–8, 2018.

[10] Andreas Hermann, Robert P. Krawczyk, Matthias Lein, Peter Schwerdtfeger, I. P. Hamilton, and James J. P. Stewart. Convergence of the many-body expansion of interaction potentials: From van der waals to covalent and metallic systems. *Phys. Rev. A*, 76:013202, Jul 2007. doi: 10.1103/PhysRevA.76.013202. URL http://link.aps.org/doi/10.1103/PhysRevA.76.013202.

[11] John Edward Lennard-Jones. On the determination of molecular fields. ii. from the equation of state of gas. *Proc. Roy. Soc. A*, 106:463–477, 1924.

[12] Peter Schwerdtfeger, Antony Burrows, and Odile R. Smits. The lennard-jones potential revisited: Analytical expressions for vibrational effects in cubic and hexagonal close-packed lattices. *The Journal of Physical Chemistry A*, 125(14):3037–3057, 04 2021. doi: 10.1021/acs.jpca.1c00012. URL https://doi.org/10.1021/acs.jpca.1c00012.

[13] BM Axilrod and Ei Teller. Interaction of the van der waals type between three atoms. *The Journal of Chemical Physics*, 11(6):299–300, 1943.

[14] EE Polymeropoulos, J Brickmann, L Jansen, and R Block. Analysis of three-body potentials in systems of rare-gas atoms: Axilrod-teller versus three-atom exchange interactions. *Physical Review A*, 30(4):1593, 1984.

[15] Andreas Köster, Peter Mausbach, and Jadran Vrabec. Premelting, solid-fluid equilibria, and thermodynamic properties in the high density region based on the lennard-jones potential. *The Journal of chemical physics*, 147(14):144502, 2017.

[16] Alison N Leonard, Andrew C Simmonett, Frank C Pickard IV, Jing Huang, Richard M Venable, Jeffery B Klauda, Bernard R Brooks, and Richard W Pastor. Comparison of additive and polarizable models with explicit treatment of long-range lennard-jones interactions using alkane simulations. *Journal of chemical theory and computation*, 14(2):948–958, 2018.

[17] Thomas C OĆonnor, Jan Andzelm, and Mark O Robbins. Airebo-m: A reactive model for hydrocarbons at extreme pressures. *The Journal of chemical physics*, 142(2):024903, 2015.

[18] Patsy V Ramírez-González and Vladimir Alonso Escobar-Barrios. Viscosity and normal stress forces of lennard-jones chains using reverse non-equilibrium molecular dynamics. *Molecular Physics*, 115(23):2970–2977, 2017.

[19] John G Kirkwood, Victor A Lewinson, and Berni J Alder. Radial distribution functions and the equation of state of fluids composed of molecules interacting according to the lennard-jones potential. *The Journal of Chemical Physics*, 20(6):929–938, 1952.

[20] Andrew M Teale, Trygve Helgaker, Andreas Savin, Carlo Adamo, Bálint Aradi, Alexei V Arbuznikov, Paul W Ayers, Evert Jan Baerends, Vincenzo Barone, Patrizia Calaminici, et al. Dft exchange: sharing perspectives on the workhorse of quantum chemistry and materials science. *Physical chemistry chemical physics*, 24(47):28700–28781, 2022.

[21] John P Perdew and Karla Schmidt. Jacob's ladder of density functional approximations for the exchange-correlation energy. In *AIP Conference Proceedings*, volume 577, pages 1–20. American Institute of Physics, 2001.

[22] Jianwei Sun, Richard C Remsing, Yubo Zhang, Zhaoru Sun, Adrienn Ruzsinszky, Haowei Peng, Zenghui Yang, Arpita Paul, Umesh Waghmare, Xifan Wu, et al. Accurate first-principles structures and energies of diversely bonded systems from an efficient density functional. *Nature chemistry*, 8(9):831–836, 2016.

[23] Michael G Medvedev, Ivan S Bushmarinov, Jianwei Sun, John P Perdew, and Konstantin A Lyssenko. Density functional theory is straying from the path toward the exact functional. *Science*, 355(6320):49–52, 2017.

[24] Gabriel R Schleder, Antonio CM Padilha, Carlos Mera Acosta, Marcio Costa, and Adalberto Fazzio. From dft to machine learning: recent approaches to materials science–a review. *Journal of Physics: Materials*, 2(3):032001, 2019.

[25] Igor Ying Zhang and Xin Xu. On the top rung of jacob's ladder of density functional theory: Toward resolving the dilemma of sie and nce. *Wiley Interdisciplinary Reviews: Computational Molecular Science*, 11(1):e1490, 2021.

[26] Kamal Sharkas, Julien Toulouse, and Andreas Savin. Double-hybrid density-functional theory made rigorous. *The Journal of chemical physics*, 134(6), 2011.

[27] Neil Qiang Su, Zhenyu Zhu, and Xin Xu. Doubly hybrid density functionals that correctly describe both density and energy for atoms. *Proceedings of the National Academy of Sciences*, 115(10):2287–2292, 2018.

[28] Stefan Grimme, Andreas Hansen, Jan Gerit Brandenburg, and Christoph Bannwarth. Dispersion-corrected mean-field electronic structure methods. *Chemical reviews*, 116(9): 5105–5154, 2016.

[29] Stefan Grimme. Density functional theory with london dispersion corrections. *Wiley Interdisciplinary Reviews: Computational Molecular Science*, 1(2):211–228, 2011.

[30] II Mazin, Harald O Jeschke, Frank Lechermann, Hunpyo Lee, Mario Fink, Ronny Thomale, and Roser Valentí. Theoretical prediction of a strongly correlated dirac metal. *Nature communications*, 5(1):4261, 2014.

[31] E Engel and RM Dreizler. Relativistic density functional theory. *Density Functional Theory II: Relativistic and Time Dependent Extensions*, pages 1–80, 2005.

[32] Rodney J Bartlett. Many-body perturbation theory and coupled cluster theory for electron correlation in molecules. *Annual review of physical chemistry*, 32(1):359–401, 1981.

[33] Riccardo Borghi. The variational method in quantum mechanics: an elementary introduction. *European Journal of Physics*, 39(3):035410, 2018.

[34] Maria Esteban, Mathieu Lewin, and Eric Séré. Variational methods in relativistic quantum mechanics. *Bulletin of the American Mathematical Society*, 45(4):535–593, 2008.

[35] Thomas Sommerfeld. Lorentz trial function for the hydrogen atom: a simple, elegant exercise. *Journal of Chemical Education*, 88(11):1521–1524, 2011.

[36] Raghunath O Ramabhadran and Krishnan Raghavachari. Extrapolation to the gold-standard in quantum chemistry: computationally efficient and accurate ccsd(t) energies for large molecules using an automated thermochemical hierarchy. *Journal of chemical theory and computation*, 9(9):3986–3994, 2013.

[37] Patton L Fast, Jose C Corchado, María L Sánchez, and Donald G Truhlar. Multi-coefficient correlation method for quantum chemistry. *The Journal of Physical Chemistry A*, 103(26): 5129–5136, 1999.

[38] Krishnan Raghavachari, Gary W Trucks, John A Pople, and Martin Head-Gordon. A fifth-order perturbation comparison of electron correlation theories. *Chemical Physics Letters*, 157(6):479–483, 1989.

[39] Peter Schwerdtfeger. *Relativistic Electronic Structure Theory: Part 2. Applications*. Elsevier, 2004.

[40] Pekka Pyykkö. Relativistic effects in chemistry: more common than you thought. *Annual review of physical chemistry*, 63:45–64, 2012.

[41] Peter Schwerdtfeger, Odile R Smits, and Pekka Pyykkö. The periodic table and the physics that drives it. *Nature reviews chemistry*, 4(7):359–380, 2020.

[42] Stefan Knecht, Hans Jørgen Aa Jensen, and Trond Saue. Relativistic quantum chemical calculations show that the uranium molecule u2 has a quadruple bond. *Nature Chemistry*, 11(1):40–44, 2019.

[43] Kenneth G. Dyall and Knut Faegri Jr. *Introduction to relativistic quantum chemistry.* Oxford University Press, 2007.

[44] Markus Reiher and Alexander Wolf. *Relativistic quantum chemistry: the fundamental theory of molecular science.* John Wiley & Sons, 2nd edition, 2014.

[45] Markus Reiher. Relativistic douglas–kroll–hess theory. *Wiley Interdisciplinary Reviews: Computational Molecular Science*, 2(1):139–149, 2012.

[46] Stefan Knecht, Michal Repisky, Hans Jørgen Aagaard Jensen, and Trond Saue. Exact two-component hamiltonians for relativistic quantum chemistry: Two-electron picture-change corrections made simple. *The Journal of Chemical Physics*, 157(11):114106, 2022.

[47] Daoling Peng and Markus Reiher. Exact decoupling of the relativistic fock operator. *Theoretical Chemistry Accounts*, 131:1–20, 2012.

[48] David P Landau and Kurt Binder. *A guide to Monte Carlo simulations in statistical physics.* Cambridge university press, 2014.

[49] Peter Jäckel. *Monte Carlo methods in finance.* J. Wiley, 2002.

[50] Ralf Korn, Elke Korn, and Gerald Kroisandt. *Monte Carlo methods and models in finance and insurance.* CRC press, 2010.

[51] J Charles. Applications of monte carlo methodes in biolog medicine and other fields of science, 2011.

[52] Dirk P Kroese, Tim Brereton, Thomas Taimre, and Zdravko I Botev. Why the monte carlo method is so important today. *Wiley Interdisciplinary Reviews: Computational Statistics*, 6 (6):386–392, 2014.

[53] Michael P Allen and Dominic J Tildesley. *Computer simulation of liquids.* Oxford university press, 1987.

[54] Richard J. Sadus. *molecular Simulation of Fluids: Theory, Algorithms and Object-Orientation.* Elsevier, 2002.

[55] Toshihiro Kaneko, Takuma Akimoto, Kenji Yasuoka, Ayori Mitsutake, and Xiao Cheng Zeng. Size-dependent phase changes in water clusters. *Journal of chemical theory and computation*, 7(10):3083–3087, 2011.

[56] Patrick Cornille. *Advanced electromagnetism and vacuum physics*, volume 21. World Scientific, 2003. pag. 102.

[57] George B Arfken, Hans J Weber, and Frank E Harris. *Mathematical methods for physicists: a comprehensive guide.* Academic press, 2011. pag. 139.

[58] Stephen K. Park and Keith W. Miller. Random number generators: good ones are hard to find. *Communications of the ACM*, 31(10):1192–1201, 1988.

[59] David J Earl and Michael W Deem. Parallel tempering: Theory, applications, and new perspectives. *Physical Chemistry Chemical Physics*, 7(23):3910–3916, 2005.

[60] Daan Frenkel and Berend Smit. *Understanding molecular simulation: from algorithms to applications*, volume 1. Elsevier, 2001.

[61] JP Neirotti, F Calvo, David L Freeman, and JD Doll. Phase changes in 38-atom lennard-jones clusters. i. a parallel tempering study in the canonical ensemble. *The Journal of Chemical Physics*, 112(23):10340–10349, 2000.

[62] DD Frantz, David L Freeman, and JD Doll. Reducing quasi-ergodic behavior in monte carlo simulations by j-walking: Applications to atomic clusters. *The Journal of chemical physics*, 93(4):2769–2784, 1990.

[63] Alan M Ferrenberg and Robert H Swendsen. Optimized monte carlo data analysis. *Computers in Physics*, 3(5):101–104, 1989.

[64] PB Conrad and JJ De Pablo. Comparison of histogram reweighting techniques for a flexible water model. *Fluid phase equilibria*, 150:51–61, 1998.

[65] Hellmut Haberland, Thomas Hippler, Jörn Donges, Oleg Kostko, Martin Schmidt, and Bernd von Issendorff. Melting of sodium clusters: Where do the magic numbers come from? *Physical review letters*, 94(3):035701, 2005.

[66] Richard B McClurg, Richard C Flagan, and William A Goddard III. Free energy and surface tension of arbitrarily large mackay icosahedral clusters. *The Journal of chemical physics*, 102 (8):3322–3330, 1995.

[67] The cambridge energy landscape database, 2018. URL http://doye.chem.ox.ac.uk/jon/structures/LJ.html. http://doye.chem.ox.ac.uk/jon/structures/LJ.html. [Last accessed: 13 April 2018].

[68] Andrés Aguado and Martin F Jarrold. Melting and freezing of metal clusters. *Annual review of physical chemistry*, 62:151–172, 2011.

[69] Elke Pahl, Florent Calvo, Love Koči, and Peter Schwerdtfeger. Accurate melting temperatures for neon and argon from ab initio monte carlo simulations. *Angewandte Chemie International Edition*, 47(43):8207–8210, 2008.

[70] Pierre Labastie and Robert L Whetten. Statistical thermodynamics of the cluster solid-liquid transition. *Physical review letters*, 65(13):1567, 1990.

[71] The cambridge energy landscape database, 2002. URL http://www-wales.ch.cam.ac.uk/~wales/CCD/TIP4P-water.html. http://www-wales.ch.cam.ac.uk/~wales/CCD/TIP4P-water.html. [Last accessed: 13 April 2018].

[72] Julián Gelman-Constantin, Marcelo A Carignano, Igal Szleifer, Ernesto J Marceca, and Horacio R Corti. Structural transitions and dipole moment of water clusters (h 2 o) n= 4–100. *The Journal of chemical physics*, 133(2):024506, 2010.

[73] Pavel A Frantsuzov and Vladimir A Mandelshtam. Equilibrium properties of quantum water clusters by the variational gaussian wavepacket method. *The Journal of chemical physics*, 128(9):094304, 2008.

[74] WA Adeagbo and P Entel. Determination of melting of water clusters using density functional theory. *Phase Transitions*, 77(1-2):63–79, 2004.

[75] Rudolf A. Treumann, Wolfgang Baumjohann, and André Balogh. The strongest magnetic fields in the universe: how strong can they become? *Frontiers in Physics*, 2:59, 2014. ISSN 2296-424X. doi: 10.3389/fphy.2014.00059. URL https://www.frontiersin.org/article/10.3389/fphy.2014.00059.

[76] Rémy Battesti, Jerome Beard, Sebastian Böser, Nicolas Bruyant, Dmitry Budker, Scott A Crooker, Edward J Daw, Victor V Flambaum, Toshiaki Inada, Igor G Irastorza, et al. High magnetic fields for fundamental physics. *arXiv preprint arXiv:1803.07547*, 2018.

[77] Gordon R. Freeman and Norman H. March. Chemistry of multiply charged negative molecular ions and clusters in the gas phase:? terrestrial and in intense galactic magnetic fields. *J. Chem. Phys.*, 100(11):4331–4338, 1996. doi: 10.1021/jp951483+. URL https://doi.org/10.1021/jp951483+.

[78] P. Schmelcher and L. S. Cederbaum. Molecules in strong magnetic fields: Some perspectives and general aspects. *Int. J. Quantum Chem.*, 64(5):501–511, 1997. doi: 10.1002/(SICI)1097-461X(1997)64:5⟨501::AID-QUA3⟩3.0.CO;2-\#.

[79] Wei Cai and Giulia Galli. Ab initio calculations in a uniform magnetic field using periodic supercells. *Phys. Rev. Lett.*, 92:186402, May 2004. doi: 10.1103/PhysRevLett.92.186402. URL https://link.aps.org/doi/10.1103/PhysRevLett.92.186402.

[80] Kai K. Lange, E. I. Tellgren, M. R. Hoffmann, and T. Helgaker. A paramagnetic bonding mechanism for diatomics in strong magnetic fields. *Science*, 337(6092):327–331, 2012. ISSN 0036-8075. doi: 10.1126/science.1219703. URL http://science.sciencemag.org/content/337/6092/327.

[81] Krzysztof Rościszewski, Beate Paulus, Peter Fulde, and Hermann Stoll. *Ab initio* coupled-cluster calculations for the fcc and hcp structures of rare-gas solids. *Phys. Rev. B*, 62:

5482–5488, Sep 2000. doi: 10.1103/PhysRevB.62.5482. URL http://link.aps.org/doi/10.1103/PhysRevB.62.5482.

[82] P. Schwerdtfeger and A. Hermann. Equation of state for solid neon from quantum theory. *Phys. Rev. B*, 80:064106–1–064106–5, 2009. doi: 10.1103/PhysRevB.80.064106.

[83] Peter Schwerdtfeger, Ralf Tonner, Gloria E. Moyano, and Elke Pahl. Towards j/mol accuracy for the cohesive energy of solid argon. *Angew. Chem. Int. Ed.*, 55(40):12200–12205, 2016. ISSN 1521-3773. doi: 10.1002/anie.201605875. URL http://dx.doi.org/10.1002/anie.201605875.

[84] Peter Schwerdtfeger, Krista G. Steenbergen, and Elke Pahl. Relativistic coupled-cluster and density-functional studies of argon at high pressure. *Phys. Rev. B*, 95:214116, Jun 2017. doi: 10.1103/PhysRevB.95.214116. URL https://link.aps.org/doi/10.1103/PhysRevB.95.214116.

[85] Grzegorz Chałasiński and Małgorzata M. Szczęśniak. State of the art and challenges of the ab initio theory of intermolecular interactions. *Chem. Rev.*, 100(11):4227–4252, 2000. doi: 10.1021/cr990048z. URL http://dx.doi.org/10.1021/cr990048z. PMID: 11749345.

[86] Ilya G. Kaplan, Ruben Santamaria, and Octavio Novaro. Non-additive forces in atomic clusters. the case of Ag_n. *Mol. Phys.*, 84(1):105–114, 1995.

[87] Peter Schwerdtfeger, Nicola Gaston, Robert P. Krawczyk, Ralf Tonner, and Gloria E. Moyano. Extension of the lennard-jones potential: Theoretical investigations into rare-gas clusters and crystal lattices of he, ne, ar, and kr using many-body interaction expansions. *Phys. Rev. B*, 73:064112, Feb 2006. doi: 10.1103/PhysRevB.73.064112. URL https://link.aps.org/doi/10.1103/PhysRevB.73.064112.

[88] E. Bich, R. Hellmann, and E. Vogel. *Ab initio* potential energy curve for the neon atom pair and thermophysical properties for the dilute neon gas. ii. thermophysical properties for low-density neon. *Mol. Phys.*, 106:1107–1122, 2008. doi: 10.1080/00268970802302662.

[89] S. M. Cybulski and R. R. Toczyłowski. Ground state potential energy curves for he_2, ne_2, ar_2, he–ne, he–ar, and ne–ar: A coupled-cluster study. *J. Chem. Phys.*, 111:10520–10528, 1999.

[90] Peter Schwerdtfeger, Nicola Gaston, Robert P Krawczyk, Ralf Tonner, and Gloria E Moyano. Extension of the lennard-jones potential: Theoretical investigations into rare-gas clusters and crystal lattices of he, ne, ar, and kr using many-body interaction expansions. *Phys. Rev. B*, 73(6):064112, 2006.

[91] B. M. Axilrod and E. Teller. Interaction of the van der waals type between three atoms. *J. Chem. Phys.*, 11(6):299–300, 1943. doi: 10.1063/1.1723844. URL https://doi.org/10.1063/1.1723844.

[92] Yu. A. Freiman and S. M. Tretyak. Many-body interactions and high-pressure equations of state in rare-gas solids. *Low Temp. Phys.*, 33(6):545–552, 2007. doi: 10.1063/1.2746249. URL https://doi.org/10.1063/1.2746249.

[93] Martin Neumann and Marco Zoppi. Path-integral monte carlo simulations of solid neon at room temperature. *Phys. Rev. B*, 62:41–44, Jul 2000. doi: 10.1103/PhysRevB.62.41. URL https://link.aps.org/doi/10.1103/PhysRevB.62.41.

[94] P. Schwerdtfeger and Andreas Hermann. Equation of state for solid neon from quantum theory. *Phys. Rev. B*, 80:064106, Aug 2009. doi: 10.1103/PhysRevB.80.064106. URL http://link.aps.org/doi/10.1103/PhysRevB.80.064106.

[95] Grzegorz Chalasinski and Maciej Gutowski. Weak interactions between small systems. models for studying the nature of intermolecular forces and challenging problems for ab initio calculations. *Chem. Rev.*, 88(6):943–962, 1988. doi: 10.1021/cr00088a007. URL https://doi.org/10.1021/cr00088a007.

[96] P. Schwerdtfeger, B. Assadollahzadeh, and A. Hermann. Convergence of the Møller–Plesset perturbation series for the fcc lattices of neon and argon. *Phys. Rev. B*, 82:205111–1–205111–11, 2010.

[97] P. Schwerdtfeger, N. Gaston, R. P. Krawczyk, R. Tonner, and G. E. Moyano. Extension of the lennard-jones potential: Theoretical investigations into rare-gas clusters and crystal lattices of he, ne, ar and kr using many-body interaction expansions. *Phys. Rev. B*, 73: 064112–1–064112–19, 2006.

[98] A. M. Ferrenberg and R. H. Swendsen. Optimized monte carlo data analysis. *Phys. Rev. Lett.*, 63:1195–1198, 1989.

[99] Johannes Kästner. Umbrella sampling. *Wiley Interdisciplinary Reviews: Computational Molecular Science*, 1(6):932–942, 2011.

[100] Enzo Marinari and Giorgio Parisi. Simulated tempering: a new monte carlo scheme. *Europhysics letters*, 19(6):451, 1992.

[101] Sanghyun Park, Fatemeh Khalili-Araghi, Emad Tajkhorshid, and Klaus Schulten. Free energy calculation from steered molecular dynamics simulations using jarzynski's equality. *The Journal of chemical physics*, 119(6):3559–3566, 2003.

[102] Lev D Gelb, KE Gubbins, R Radhakrishnan, and M Sliwinska-Bartkowiak. Phase separation in confined systems. *Reports on Progress in Physics*, 62(12):1573, 1999.

[103] Jeffrey J Potoff and J Ilja Siepmann. Vapor–liquid equilibria of mixtures containing alkanes, carbon dioxide, and nitrogen. *AIChE journal*, 47(7):1676–1682, 2001.

[104] Shankar Kumar, John M Rosenberg, Djamal Bouzida, Robert H Swendsen, and Peter A Kollman. The weighted histogram analysis method for free-energy calculations on biomolecules. i. the method. *Journal of computational chemistry*, 13(8):1011–1021, 1992.

[105] Ayori Mitsutake, Yuji Sugita, and Yuko Okamoto. Generalized-ensemble algorithms for molecular simulations of biopolymers. *Peptide Science: Original Research on Biomolecules*, 60(2):96–123, 2001.

[106] Philippe De Forcrand and Owe Philipsen. The qcd phase diagram for small densities from imaginary chemical potential. *Nuclear Physics B*, 642(1-2):290–306, 2002.

[107] G Boyd, Jürgen Engels, Frithjof Karsch, Edwin Laermann, C Legeland, M Lütgemeier, and Bengt Petersson. Thermodynamics of su (3) lattice gauge theory. *Nuclear Physics B*, 469 (3):419–444, 1996.

[108] Olof Echt, Otto Kandler, Thomas Leisner, Werner Miehle, and Ekkehard Recknagel. Magic numbers in mass spectra of large van der waals clusters. *Journal of the Chemical Society, Faraday Transactions*, 86(13):2411–2415, 1990.

[109] Daan Frenkel. The simulation of entropic phase transitions. *Journal of Physics: Condensed Matter*, 6(23A):A71, 1994.

[110] Elena Bonetti and Michel Frémond. A phase transition model with the entropy balance. *Mathematical methods in the applied sciences*, 26(7):539–556, 2003.

[111] Fei Zhang, Hongbo Lou, Benyuan Cheng, Zhidan Zeng, and Qiaoshi Zeng. High-pressure induced phase transitions in high-entropy alloys: A review. *Entropy*, 21(3):239, 2019.

[112] P. Labastie and R.L. Whetten. Statistical thermodynamics of the cluster solid-liquid transition. *Phys. Rev. Lett.*, 65:1567 – 1570, Sep 1990. doi: 10.1103/PhysRevLett.65.1567. URL http://link.aps.org/doi/10.1103/PhysRevLett.65.1567.

[113] E. Pahl, F. Calvo, L. Koči, and P. Schwerdtfeger. Accurate Melting Temperatures for Neon and Argon from Ab Initio Monte Carlo Simulations. *Angew. Chem. Int. Ed.*, 47:8207–8210, 2008.

[114] Gilbert N. Lewis. The atom and the molecule. *J. Am. Chem. Soc.*, 38(4):762–785, 04 1916. doi: 10.1021/ja02261a002. URL https://doi.org/10.1021/ja02261a002.

[115] Gilbert Newton Lewis. *Valence and the Structure of Atoms and Molecules*. American Chemical Society Monographs Series, New York, 1923.

[116] Gilbert N Lewis. The chemical bond. *J. Chem. Phys.*, 1(1):17–28, 1933.

[117] W Heitler and F London. Interaction between neutral atoms and homopolar binding according to quantum mechanics. *Z. Phys.*, 44:140–155, 1927.

[118] Linus Pauling. *The Nature of the Chemical Bond...* Cornell university press Ithaca, NY, 1960.

[119] Ahmed Zewail. *The Chemical bond: structure and dynamics*. Elsevier, 1992.

[120] Gernot Frenking and Sason Shaik. *The Chemical Bond: Fundamental Aspects of Chemical Bonding*, volume 1. John Wiley & Sons, 2014.

[121] Gernot Frenking and Sason Shaik. *The Chemical Bond: Chemical Bonding Across the Periodic Table*, volume 2. John Wiley & Sons, 2014.

[122] Gernot Frenking. The chemical bond – an entrance door of chemistry to the neighboring sciences and to philosophy. *Isr. J. Chem.*, 62(1-2):e202100070, 2022. doi: https://doi.org/10.1002/ijch.202100070. URL https://onlinelibrary.wiley.com/doi/abs/10.1002/ijch.202100070.

[123] Linus Pauling. The shared-electron chemical bond. *Proc. Nat. Acad. Sci. USA*, 14(4):359, 1928.

[124] Linus. Pauling. The nature of the chemical bond. application of results obtained from the quantum mechanics and from a theory of paramagnetic susceptibility to the structure of molecules. *J. Am. Chem. Soc.*, 53(4):1367–1400, 04 1931. doi: 10.1021/ja01355a027. URL https://doi.org/10.1021/ja01355a027.

[125] Linus. Pauling. The nature of the chemical bond. ii. the one-electron bond and the three-electron bond. *J. Am. Chem. Soc.*, 53(9):3225–3237, 09 1931. doi: 10.1021/ja01360a004. URL https://doi.org/10.1021/ja01360a004.

[126] Linus Pauling. The nature of the chemical bond. iii. the transition from one extreme bond type to another. *J. Am. Chem. Soc.*, 54(3):988–1003, 03 1932. doi: 10.1021/ja01342a022. URL https://doi.org/10.1021/ja01342a022.

[127] Linus Pauling. The nature of the chemical bond. iv. the energy of single bonds and the relative electronegativity of atoms. *J. Am. Chem. Soc.*, 54(9):3570–3582, 09 1932. doi: 10.1021/ja01348a011. URL https://doi.org/10.1021/ja01348a011.

[128] Linus Pauling. Interatomic distances in covalent molecules and resonance between two or more lewis electronic structures. *Proc. Nat. Acad. Sci. USA*, 18(4):293–297, 1932. ISSN 0027-8424. doi: 10.1073/pnas.18.4.293. URL https://www.pnas.org/content/18/4/293.

[129] Linus Pauling and G. W. Wheland. The nature of the chemical bond. v. the quantum-mechanical calculation of the resonance energy of benzene and naphthalene and the hydrocarbon free radicals. *J. Chem. Phys.*, 1(6):362–374, 1933. doi: 10.1063/1.1749304. URL https://doi.org/10.1063/1.1749304.

[130] Linus Pauling and J. Sherman. The nature of the chemical bond. vi. the calculation from thermochemical data of the energy of resonance of molecules among several electronic structures. *J. Chem. Phys.*, 1(8):606–617, 1933. doi: 10.1063/1.1749335. URL https://doi.org/10.1063/1.1749335.

[131] Linus Pauling and J. Sherman. The nature of the chemical bond. vii. the calculation of resonance energy in conjugated systems. *J. Chem. Phys.*, 1(10):679–686, 1933. doi: 10.1063/1.1749226. URL https://doi.org/10.1063/1.1749226.

[132] Michael Weisberg, Paul Needham, and Robin Hendry. Philosophy of Chemistry. In Edward N. Zalta, editor, *The Stanford Encyclopedia of Philosophy*. Metaphysics Research Lab, Stanford University, Spring 2019 edition, 2019.

[133] Lili Zhao, W. H. Eugen Schwarz, and Gernot Frenking. The lewis electron-pair bonding model: the physical background, one century later. *Nature Rev. Chem.*, 3(1):35–47, 2019. doi: 10.1038/s41570-018-0052-4. URL https://doi.org/10.1038/s41570-018-0052-4.

[134] Lili Zhao, Sudip Pan, Nicole Holzmann, Peter Schwerdtfeger, and Gernot Frenking. Chemical bonding and bonding models of main-group compounds. *Chemi. Rev.*, 119(14):8781–8845, 07 2019. doi: 10.1021/acs.chemrev.8b00722. URL https://doi.org/10.1021/acs.chemrev.8b00722.

[135] C. A. Coulson. The contributions of wave mechanics to chemistry. *J. Chem. Soc.*, pages 2069–2084, 1955. doi: 10.1039/JR9550002069. URL http://dx.doi.org/10.1039/JR9550002069.

[136] Klaus Ruedenberg. The physical nature of the chemical bond. *Rev. Mod. Phys.*, 34:326–376, Apr 1962. doi: 10.1103/RevModPhys.34.326. URL https://link.aps.org/doi/10.1103/RevModPhys.34.326.

[137] Frank Driessler and Werner Kutzelnigg. Analysis of the chemical bond. *Theoret. Chim. Acta*, 43(1):1–27, 1976. doi: 10.1007/BF00548953. URL https://doi.org/10.1007/BF00548953.

[138] Sason Shaik, David Danovich, Wei Wu, Peifeng Su, Henry S Rzepa, and Philippe C Hiberty. Quadruple bonding in c 2 and analogous eight-valence electron species. *Nature Chem.*, 4(3):195–200, 2012.

[139] Gernot Frenking and Markus Hermann. Comment on "the quadruple bonding in c2 reproduces the properties of the molecule". *Chemistry–A European Journal*, 22(52):18975–18976, 2016.

[140] Sason Shaik, David Danovich, Benoit Braida, and Philippe C Hiberty. A response to a comment by g. frenking and m. hermann on: The quadruple bonding in c2 reproduces the properties of the molecule. *Chemistry–A European Journal*, 22(52):18977–18980, 2016.

[141] Richard F. W. Bader. Bond paths are not chemical bonds. *J. Phys. Chem. A*, 113(38):10391–10396, 09 2009. doi: 10.1021/jp906341r. URL https://doi.org/10.1021/jp906341r.

[142] Peter Politzer and Jane S. Murray. A look at bonds and bonding. *Struct. Chem.*, 30 (4):1153–1157, 2019. doi: 10.1007/s11224-019-01364-3. URL https://doi.org/10.1007/s11224-019-01364-3.

[143] Roald Hoffmann. How chemistry and physics meet in the solid state. *Angew. Chem. Int. Ed.*, 26(9):846–878, 1987.

[144] Walter A Harrison. *Electronic structure and the properties of solids: the physics of the chemical bond*. Courier Corporation, 2012.

[145] Thomas A Albright, Jeremy K Burdett, and Myung-Hwan Whangbo. *Orbital interactions in chemistry*. John Wiley & Sons, 2013.

[146] JS Griffith and LE Orgel. Ligand-field theory. *Quart. Rev. Chem. Soc.*, 11(4):381–393, 1957.

[147] CJ Ballhausen. Crystal and ligand field theory. *Int. J. Quant. Chem.*, 5(S5):373–377, 1971.

[148] P. Pyykkö. Relativistic effects in structural chemistry. *Chem. Rev.*, 88:563, 1988.

[149] Peter Schwerdtfeger. *Relativity and Chemical Bonding*, chapter 11, pages 383–404. John Wiley & Sons, Ltd, 2014. ISBN 9783527664696. doi: https://doi.org/10.1002/9783527664696.ch11. URL https://onlinelibrary.wiley.com/doi/abs/10.1002/9783527664696.ch11.

[150] Peter Schwerdtfeger. Relativistic and electron-correlation contributions in atomic and molecular properties: benchmark calculations on au and au2. *Chem. Phys. Lett.*, 183(5): 457–463, 1991. ISSN 0009-2614. doi: https://doi.org/10.1016/0009-2614(91)90409-3. URL https://www.sciencedirect.com/science/article/pii/0009261491904093.

[151] W. E. Spicer, A. H. Sommer, and J. G. White. Studies of the semiconducting properties of the compound csau. *Phys. Rev.*, 115:57–62, Jul 1959. doi: 10.1103/PhysRev.115.57. URL https://link.aps.org/doi/10.1103/PhysRev.115.57.

[152] N.E. Christensen and J. Kollar. Electronic structure of csau. *Solid State Commun.*, 46(9): 727–730, 1983. ISSN 0038-1098. doi: https://doi.org/10.1016/0038-1098(83)90516-1. URL https://www.sciencedirect.com/science/article/pii/0038109883905161.

[153] C. Koenig, N. E. Christensen, and J. Kollar. Electronic properties of alkali-metal—gold compounds. *Phys. Rev. B*, 29:6481–6488, Jun 1984. doi: 10.1103/PhysRevB.29.6481. URL https://link.aps.org/doi/10.1103/PhysRevB.29.6481.

[154] Elke Pahl, Detlev Figgen, Anastasia Borschevsky, Kirk A. Peterson, and Peter Schwerdtfeger. Accurate potential energy curves for the group 12 dimers zn2, cd2, and hg2. *Theoret. Chem. Acc.*, 129(3):651–656, 2011. doi: 10.1007/s00214-011-0912-1. URL https://doi.org/10.1007/s00214-011-0912-1.

[155] Nicola Gaston and Peter Schwerdtfeger. From the van der waals dimer to the solid state of mercury with relativistic ab initio and density functional theory. *Phys. Rev. B*, 74:024105, Jul 2006. doi: 10.1103/PhysRevB.74.024105. URL https://link.aps.org/doi/10.1103/PhysRevB.74.024105.

[156] Beate Paulus and Krzysztof Rosciszewski. Metallic bonding due to electronic correlations: a quantum chemical ab initio calculation of the cohesive energy of mercury. *Chem. Phys. Lett.*, 394(1):96–100, 2004. ISSN 0009-2614. doi: https://doi.org/10.1016/j.cplett.2004.06.118. URL https://www.sciencedirect.com/science/article/pii/S0009261404009960.

[157] Beate Paulus, Krzysztof Rosciszewski, Nicola Gaston, Peter Schwerdtfeger, and Hermann Stoll. Convergence of the ab initio many-body expansion for the cohesive energy of solid mercury. *Phys. Rev. B*, 70:165106, Oct 2004. doi: 10.1103/PhysRevB.70.165106. URL http://link.aps.org/doi/10.1103/PhysRevB.70.165106.

[158] Yixuan Wang, Heinz-Jürgen Flad, and Michael Dolg. Realistic hybrid model for correlation effects in mercury clusters. *Phys. Rev. B*, 61:2362–2370, Jan 2000. doi: 10.1103/PhysRevB.61.2362. URL https://link.aps.org/doi/10.1103/PhysRevB.61.2362.

[159] Florent Calvo, Elke Pahl, Michael Wormit, and Peter Schwerdtfeger. Evidence for low-temperature melting of mercury owing to relativity. *Angew. Chem. Int. Ed.*, 52(29):7583–7585, 2013. ISSN 1521-3773. doi: 10.1002/anie.201302742. URL http://dx.doi.org/10.1002/anie.201302742.

[160] Krista G. Steenbergen, Elke Pahl, and Peter Schwerdtfeger. Accurate, large-scale density functional melting of hg: Relativistic effects decrease melting temperature by 160 k. *J. Phys. Chem. Lett.*, 8(7):1407–1412, 2017. doi: 10.1021/acs.jpclett.7b00354. URL https://doi.org/10.1021/acs.jpclett.7b00354. PMID: 28285532.

[161] Jan-Michael Mewes and Peter Schwerdtfeger. Exclusively relativistic: Periodic trends in the melting and boiling points of group 12. *Angew. Chem. Int. Ed.*, 60(14):7703–7709, 2021. doi: https://doi.org/10.1002/anie.202100486. URL https://onlinelibrary.wiley.com/doi/abs/10.1002/anie.202100486.

[162] Jan-Michael Mewes and Odile R. Smits. Accurate elemental boiling points from first principles. *Phys. Chem. Chem. Phys.*, 22:24041–24050, 2020. doi: 10.1039/D0CP02884C. URL http://dx.doi.org/10.1039/D0CP02884C.

[163] Elke Pahl, Florent Calvo, Love Koči, and Peter Schwerdtfeger. Accurate melting temperatures for neon and argon from ab initio monte carlo simulations. *Angew. Chem. Int. Ed.*, 47(43):8207–8210, 2008.

[164] Odile R. Smits, Paul Jerabek, Elke Pahl, and Peter Schwerdtfeger. A hundred-year-old experiment re-evaluated: Accurate ab-initio monte-carlo simulations of the melting of radon. *Angew. Chem. Int. Ed.*, 57(31):9961–9964, 2018. doi: https://doi.org/10.1002/anie.201803353. URL https://onlinelibrary.wiley.com/doi/abs/10.1002/anie.201803353.

[165] O. R. Smits, P. Jerabek, E. Pahl, and P. Schwerdtfeger. First-principles melting of krypton and xenon based on many-body relativistic coupled-cluster interaction potentials. *Phys. Rev. B*, 101:104103, Mar 2020. doi: 10.1103/PhysRevB.101.104103. URL https://link.aps.org/doi/10.1103/PhysRevB.101.104103.

[166] Peter Schwerdtfeger, Nicola Gaston, Robert P. Krawczyk, Ralf Tonner, and Gloria E. Moyano. Extension of the lennard-jones potential: Theoretical investigations into rare-gas clusters and crystal lattices of he, ne, ar, and kr using many-body interaction expansions. *Phys. Rev. B*, 73:064112, Feb 2006. doi: 10.1103/PhysRevB.73.064112.

[167] J. E. Jones and A. E. Ingham. On the Calculation of Certain Crystal Potential Constants, and on the Cubic Crystal of Least Potential Energy. *Proc. R. Soc. Lond. A*, 107(744): 636–653, 1925. ISSN 0950-1207. doi: 10.1098/rspa.1925.0047. URL http://rspa.royalsocietypublishing.org/content/107/744/636.

[168] Antony Burrows, Shaun Cooper, Elke Pahl, and Peter Schwerdtfeger. Analytical methods for fast converging lattice sums for cubic and hexagonal close-packed structures. *J. Math. Phys.*, 61(12):123503, 2020. doi: 10.1063/5.0021159. URL https://doi.org/10.1063/5.0021159.

[169] Kenneth S Pitzer. Fluorides of radon and element 118. *J. Chem. Soc., Chem. Commun.*, 0: 760b–761, 1975. doi: 10.1039/C3975000760B.

[170] B Eichler. Das flüchtigkeitsverhalten von transactiniden im bereich um z= 114 (voraussage). *Kernenergie*, 19(10):307, 1976.

[171] Burkhard Fricke. Superheavy elements a prediction of their chemical and physical properties. In *Recent Impact of Physics on Inorganic Chemistry*, volume 21 of *Structure and Bonding*, pages 89–144. Springer Berlin Heidelberg, 1975. ISBN 978-3-540-07109-9. doi: 10.1007/BFb0116498. URL http://dx.doi.org/10.1007/BFb0116498.

[172] B. Fricke and G. Soff. Dirac-Fock-Slater calculations for the elements z=100, fermium, to z = 173. *At. Data Nucl. Data Tables*, 19:83–95, 1977.

[173] Arie Landau, Ephraim Eliav, Yasuyuki Ishikawa, and Uzi Kaldor. Electronic structure of eka-lead (element 114) compared with lead. *J. Chem. Phys.*, 114(7):2977–2980, 2001. doi: http://dx.doi.org/10.1063/1.1342763. URL http://scitation.aip.org/content/aip/journal/jcp/114/7/10.1063/1.1342763.

[174] T. H. Dinh, V. A. Dzuba, and V. V. Flambaum. Calculation of the spectra for the superheavy element $z = 112$. *Phys. Rev. A*, 78:062502, Dec 2008. doi: 10.1103/PhysRevA.78.062502. URL https://link.aps.org/doi/10.1103/PhysRevA.78.062502.

[175] Ephraim Eliav, Uzi Kaldor, and Anastasia Borschevsky. Electronic structure of the transactinide atoms. *Encyclopedia of Inorganic and Bioinorganic Chemistry*, pages 1–16, 2011.

[176] B. G. C. Lackenby, V. A. Dzuba, and V. V. Flambaum. Atomic structure calculations of superheavy noble element oganesson ($z = 118$). *Phys. Rev. A*, 98:042512, Oct 2018. doi: 10.1103/PhysRevA.98.042512. URL https://link.aps.org/doi/10.1103/PhysRevA.98.042512.

[177] Avijit Shee, Stefan Knecht, and Trond Saue. A theoretical benchmark study of the spectroscopic constants of the very heavy rare gas dimers. *Phys. Chem. Chem. Phys.*, 17:10978–10986, 2015. doi: 10.1039/C5CP01094B. URL http://dx.doi.org/10.1039/C5CP01094B.

[178] Peter Schwerdtfeger and Jeffrey K. Nagle. 2018 table of static dipole polarizabilities of the neutral elements in the periodic table. *Mol. Phys.*, 117(9-12):1200–1225, 2019. doi: 10.1080/00268976.2018.1535143. URL https://doi.org/10.1080/00268976.2018.1535143.

[179] V. Pershina, A. Borschevsky, E. Eliav, and U. Kaldor. Prediction of the adsorption behavior of elements 112 and 114 on inert surfaces from ab initio Dirac-Coulomb atomic calculations. *J. Chem. Phys.*, 128(2):024707, 2008. doi: http://dx.doi.org/10.1063/1.2814242. URL http://scitation.aip.org/content/aip/journal/jcp/128/2/10.1063/1.2814242.

[180] Paul Jerabek, Bastian Schuetrumpf, Peter Schwerdtfeger, and Witold Nazarewicz. Electron and nucleon localization functions of oganesson: Approaching the thomas-fermi limit. *Phys. Rev. Lett.*, 120:053001, Jan 2018. doi: 10.1103/PhysRevLett.120.053001. URL https://link.aps.org/doi/10.1103/PhysRevLett.120.053001.

[181] Dirk Goebel and Uwe Hohm. Dipole polarizability, cauchy moments, and related properties of hg. *J. Phys. Chem.*, 100(18):7710–7712, 01 1996. doi: 10.1021/jp960231l. URL https://doi.org/10.1021/jp960231l.

[182] Christian Thierfelder, Behnam Assadollahzadeh, Peter Schwerdtfeger, Sascha Schäfer, and Rolf Schäfer. Relativistic and electron correlation effects in static dipole polarizabilities for the group-14 elements from carbon to element $z = 114$: Theory and experiment. *Phys. Rev. A*, 78:052506, Nov 2008. doi: 10.1103/PhysRevA.78.052506. URL https://link.aps.org/doi/10.1103/PhysRevA.78.052506.

[183] Eric G. Hope. Coordination chemistry of the noble gases and noble gas fluorides. *Coordination Chemistry Reviews*, 257(5):902–909, 2013. ISSN 0010-8545. doi: https://doi.org/10.1016/j.ccr.2012.07.017. URL https://www.sciencedirect.com/science/article/pii/S0010854512002020. Recent Developments in Main Group Chemistry.

[184] GERALD L. POLLACK. The solid state of rare gases. *Rev. Mod. Phys.*, 36:748–791, Jul 1964. doi: 10.1103/RevModPhys.36.748. URL https://link.aps.org/doi/10.1103/RevModPhys.36.748.

[185] Peter Schwerdtfeger, Ralf Tonner, Gloria E Moyano, and Elke Pahl. Towards j/mol accuracy for the cohesive energy of solid argon. *Angew. Chem. Int. Ed.*, 55(40):12200–12205, 2016.

[186] K. G. Steenbergen, J.-M. Mewes, L. F. Pašteka, H. W. Gäggeler, G. Kresse, E. Pahl, and P. Schwerdtfeger. The cohesive energy of superheavy element copernicium determined from accurate relativistic coupled-cluster theory. *Phys. Chem. Chem. Phys.*, 19:32286–32295, 2017. doi: 10.1039/C7CP07203A. URL http://dx.doi.org/10.1039/C7CP07203A.

[187] Jan-Michael Mewes, Odile R. Smits, Georg Kresse, and Peter Schwerdtfeger. Copernicium: A relativistic noble liquid. *Angew. Chem. Int. Ed.*, 58(50):17964–17968, 2019. doi: https://doi.org/10.1002/anie.201906966. URL https://onlinelibrary.wiley.com/doi/abs/10.1002/anie.201906966.

[188] Odile R. Smits, Jan-Michael Mewes, Paul Jerabek, and Peter Schwerdtfeger. Oganesson: A noble gas element that is neither noble nor a gas. *Angew. Chem. Int. Ed.*, 59(52):23636–23640, 2020. doi: https://doi.org/10.1002/anie.202011976. URL https://onlinelibrary.wiley.com/doi/abs/10.1002/anie.202011976.

[189] Robert Eichler, N. V. Aksenov, Yu. V. Albin, A. V. Belozerov, G. A. Bozhikov, V. I. Chepigin, S. N. Dmitriev, R. Dressler, H. W. Gäggeler, V. A. Gorshkov, G.S. Henderson, and et al. Indication for a volatile element 114. *Radiochim. Acta*, 98(3):133–139, 2010. doi: doi: 10.1524/ract.2010.1705. URL https://doi.org/10.1524/ract.2010.1705.

[190] Alexander Yakushev, Jacklyn M. Gates, Andreas Türler, Matthias Schädel, Christoph E. Düllmann, Dieter Ackermann, Lise-Lotte Andersson, Michael Block, Willy Brüchle, Jan Dvorak, Klaus Eberhardt, Hans G. Essel, Julia Even, Ulrika Forsberg, Alexander Gorshkov, Reimar Graeger, Kenneth E. Gregorich, Willi Hartmann, Rolf-Dietmar Herzberg, Fritz P. Heßberger, Daniel Hild, Annett Hübner, Egon Jäger, Jadambaa Khuyagbaatar, Birgit Kindler, Jens V. Kratz, Jörg Krier, Nikolaus Kurz, Bettina Lommel, Lorenz J. Niewisch, Heino Nitsche, Jon Petter Omtvedt, Edward Parr, Zhi Qin, Dirk Rudolph, Jörg Runke, Brigitta Schausten, Erwin Schimpf, Andrey Semchenkov, Jutta Steiner, Petra Thörle-Pospiech, Juha Uusitalo, Maciej Wegrzecki, and Norbert Wiehl. Superheavy element flerovium (element 114) is a volatile metal. *Inorg. Chem.*, 53(3):1624–1629, 2014. doi: 10.1021/ic4026766. URL http://dx.doi.org/10.1021/ic4026766. PMID: 24456007.

[191] Patrick Steinegger and Robert Eichler. Radiochemical research with transactinide elements in switzerland. *CHIMIA Int. J. Chem.*, 74(12):924–931, 2020.

[192] V. Pershina, A. Borschevsky, E. Eliav, and U. Kaldor. Adsorption of inert gases including element 118 on noble metal and inert surfaces from ab initio Dirac-Coulomb atomic calculations. *J. Chem. Phys.*, 129(14):144106–1–144106–9, 2008.

[193] V Pershina, A Borschevsky, E Eliav, and U Kaldor. Prediction of the adsorption behavior of elements 112 and 114 on inert surfaces from ab initio dirac-coulomb atomic calculations. *The Journal of chemical physics*, 128(2):024707, 2008.

[194] Valeria Pershina. Reactivity of superheavy elements cn, nh, and fl and their lighter homologues hg, tl, and pb, respectively, with a gold surface from periodic dft calculations. *Inorg. Chem.*, 57(7):3948–3955, 04 2018. doi: 10.1021/acs.inorgchem.8b00101. URL https://doi.org/10.1021/acs.inorgchem.8b00101.

[195] Lukas Trombach, Sebastian Ehlert, Stefan Grimme, Peter Schwerdtfeger, and Jan-Michael Mewes. Exploring the chemical nature of super-heavy main-group elements by means of efficient plane-wave density-functional theory. *Phys. Chem. Chem. Phys.*, 21:18048–18058, 2019. doi: 10.1039/C9CP02455G. URL http://dx.doi.org/10.1039/C9CP02455G.

[196] Andreas Türler and Valeria Pershina. Advances in the production and chemistry of the heaviest elements. *Chem. Rev.*, 113(2):1237–1312, 02 2013. doi: 10.1021/cr3002438. URL https://doi.org/10.1021/cr3002438.

[197] V. Pershina. Electronic structure and properties of superheavy elements. *Nucl. Phys. A*, 944:578, 2015. ISSN 0375-9474. doi: http://dx.doi.org/10.1016/j.nuclphysa.2015.04.007.

[198] R. Bast, A. S. P. Gomes, T. Saue, L. Visscher, H. J. Aa. Jensen, I. A. Aucar, V. Bakken, K. G. Dyall, S. Dubillard, U. Ekström, E. Eliav, T. Enevoldsen, E. Fashauer, T. Fleig, O. Fossgaard, L. Halbert, E. D. Hedegard, T. Helgaker, B. Helmich-Paris, J. Henriksson,

M. Ilias, Ch. R. Jacob, S. Knecht, S. Komorovsky, O. Kullie, J. K. Lardahl, C. V. Larsen, Y. S. Lee, N. H. List, H. S. Nataraj, M. K. Nayak, P. Norman, G. Olejniczak, J. Olsen, J. M. H. Olsen, A. Papadopoulos, Y. C. Park, J. K. Pedersen, M. Pernpointner, J. V. Pototschnig, R. Di Remigio, M. Repisky, K. Ruud, P. Salek, B. Schimmelpfennig, B. Senjean, A. Shee, J. Sikkema, A. Sunaga, A. J. Thorvaldsen, J. Thyssen, J. van Stralen, M. L. Vidal, S. Villaume, O. Visser, T. Winther, and S. Yamamoto. Dirac21, May 2021. URL https://doi.org/10.5281/zenodo.4836496. v21.0, Zenodo, DOI: 10.5281/zenodo.4836496.

[199] Trond Saue, Radovan Bast, André Severo Pereira Gomes, Hans Jørgen Aa. Jensen, Lucas Visscher, Ignacio Agustín Aucar, Roberto Di Remigio, Kenneth G. Dyall, Ephraim Eliav, Elke Fasshauer, Timo Fleig, Loïc Halbert, Erik Donovan Hedegård, Benjamin Helmich-Paris, Miroslav Iliaš, Christoph R. Jacob, Stefan Knecht, Jon K. Laerdahl, Marta L. Vidal, Malaya K. Nayak, Małgorzata Olejniczak, Jógvan Magnus Haugaard Olsen, Markus Pernpointner, Bruno Senjean, Avijit Shee, Ayaki Sunaga, and Joost N. P. van Stralen. The DIRAC code for relativistic molecular calculations. *J. Chem. Phys.*, 20:204104, 2020. doi: 10.1063/5.0004844. URL http://aip.scitation.org/doi/10.1063/5.0004844.

[200] John Clarke Slater. *Quantum Theory of Molecular and Solids*, volume 4. McGraw-Hill, 1974.

[201] S. H. Vosko, L. Wilk, and M. Nusair. Accurate spin-dependent electron liquid correlation energies for local spin density calculations: a critical analysis. *Can. J. Phys.*, 58(8):1200–1211, 1980. doi: 10.1139/p80-159. URL https://doi.org/10.1139/p80-159.

[202] John P. Perdew, Kieron Burke, and Matthias Ernzerhof. Generalized gradient approximation made simple. *Phys. Rev. Lett.*, 77:3865–3868, Oct 1996. doi: 10.1103/PhysRevLett.77.3865. URL https://link.aps.org/doi/10.1103/PhysRevLett.77.3865.

[203] John P. Perdew, Matthias Ernzerhof, and Kieron Burke. Rationale for mixing exact exchange with density functional approximations. *J. Chem. Phys.*, 105(22):9982–9985, 1996. doi: 10.1063/1.472933. URL https://doi.org/10.1063/1.472933.

[204] Chengteh Lee, Weitao Yang, and Robert G. Parr. Development of the colle-salvetti correlation-energy formula into a functional of the electron density. *Phys. Rev. B*, 37:785–789, Jan 1988. doi: 10.1103/PhysRevB.37.785. URL https://link.aps.org/doi/10.1103/PhysRevB.37.785.

[205] Axel D. Becke. Density-functional thermochemistry. iii. the role of exact exchange. *J. Chem. Phys.*, 98(7):5648–5652, 1993. doi: 10.1063/1.464913. URL https://doi.org/10.1063/1.464913.

[206] Kenneth G. Dyall. Relativistic double-zeta, triple-zeta, and quadruple-zeta basis sets for the 7p elements, with atomic and molecular applications. *Theoret. Chem. Acc.*,

131(3):1172, 2012. doi: 10.1007/s00214-012-1172-4. URL https://doi.org/10.1007/s00214-012-1172-4.

[207] G. Kresse and J. Hafner. Ab initio molecular dynamics for liquid metals. *Phys. Rev. B*, 47: 558–561, Jan 1993. doi: 10.1103/PhysRevB.47.558. URL https://link.aps.org/doi/10.1103/PhysRevB.47.558.

[208] G. Kresse and J. Hafner. Ab initio molecular-dynamics simulation of the liquid-metal–amorphous-semiconductor transition in germanium. *Phys. Rev. B*, 49:14251–14269, May 1994. doi: 10.1103/PhysRevB.49.14251. URL https://link.aps.org/doi/10.1103/PhysRevB.49.14251.

[209] G. Kresse and J. Furthmüller. Efficiency of ab-initio total energy calculations for metals and semiconductors using a plane-wave basis set. *Comput. Mat. Sci.*, 6(1):15–50, 1996. ISSN 0927-0256. doi: https://doi.org/10.1016/0927-0256(96)00008-0. URL https://www.sciencedirect.com/science/article/pii/0927025696000080.

[210] G. Kresse and J. Furthmüller. Efficient iterative schemes for ab initio total-energy calculations using a plane-wave basis set. *Phys. Rev. B*, 54:11169–11186, Oct 1996. doi: 10.1103/PhysRevB.54.11169. URL https://link.aps.org/doi/10.1103/PhysRevB.54.11169.

[211] P. E. Blöchl. Projector augmented-wave method. *Phys. Rev. B*, 50:17953–17979, Dec 1994. doi: 10.1103/PhysRevB.50.17953. URL https://link.aps.org/doi/10.1103/PhysRevB.50.17953.

[212] G. Kresse and D. Joubert. From ultrasoft pseudopotentials to the projector augmented-wave method. *Phys. Rev. B*, 59:1758–1775, Jan 1999. doi: 10.1103/PhysRevB.59.1758. URL https://link.aps.org/doi/10.1103/PhysRevB.59.1758.

[213] John P. Perdew, Adrienn Ruzsinszky, Gábor I. Csonka, Oleg A. Vydrov, Gustavo E. Scuseria, Lucian A. Constantin, Xiaolan Zhou, and Kieron Burke. Restoring the density-gradient expansion for exchange in solids and surfaces. *Phys. Rev. Lett.*, 100:136406, Apr 2008. doi: 10.1103/PhysRevLett.100.136406. URL https://link.aps.org/doi/10.1103/PhysRevLett.100.136406.

[214] Stefan Grimme, Jens Antony, Stephan Ehrlich, and Helge Krieg. A consistent and accurate ab initio parametrization of density functional dispersion correction (dft-d) for the 94 elements h-pu. *J. Chem. Phys.*, 132(15):154104, 2010. doi: 10.1063/1.3382344. URL https://doi.org/10.1063/1.3382344.

[215] Lars Hedin. New method for calculating the one-particle green's function with application to the electron-gas problem. *Phys. Rev.*, 139:A796–A823, Aug 1965. doi: 10.1103/PhysRev.139.A796. URL https://link.aps.org/doi/10.1103/PhysRev.139.A796.

[216] F Aryasetiawan and O Gunnarsson. TheGWmethod. *Rep. Prog. Phys.*, 61(3):237–312, mar 1998. doi: 10.1088/0034-4885/61/3/002. URL https://doi.org/10.1088/0034-4885/61/3/002.

[217] Maxim Shishkin, Martijn Marsman, and Georg Kresse. Accurate quasiparticle spectra from self-consistent gw calculations with vertex corrections. *Phys. Rev. Lett.*, 99(24):246403, 2007.

[218] A. D. Becke and K. E. Edgecombe. A simple measure of electron localization in atomic and molecular systems. *J. Chem. Phys.*, 92(9):5397–5403, 1990. ISSN 0021-9606. doi: 10.1063/1.458517.

[219] M. Kohout and A. Savin. Atomic shell structure and electron numbers. *Int. J. Quantum Chem.*, 60:875–882, 1996. ISSN 1097-461X. doi: 10.1002/(SICI)1097-461X(1996)60:4⟨875::AID-QUA10⟩3.0.CO;2-4. URL http://dx.doi.org/10.1002/(SICI)1097-461X(1996)60:4<875::AID-QUA10>3.0.CO;2-4.

[220] A Savin, R Nesper, S Wengert, and T F Fässler. {ELF}: The Electron Localization Function. *Angew. Chem. Int. Ed. Engl.*, 36:1808–1832, 1997. doi: 10.1002/anie.199718081. URL http://dx.doi.org/10.1002/anie.199718081.

[221] Julien Pilmé, Eric Renault, Tahra Ayed, Gilles Montavon, and Nicolas Galland. Introducing the elf topological analysis in the field of quasirelativistic quantum calculations. *J. Chem. Theory Comput.*, 8(9):2985–2990, 09 2012. doi: 10.1021/ct300558k. URL https://doi.org/10.1021/ct300558k.

[222] Kenneth G. Dyall. Relativistic double-zeta, triple-zeta, and quadruple-zeta basis sets for the 5d elements hf-hg. *Theor. Chem. Acc.*, 112(5):403–409, 2004. ISSN 1432-881X, 1432-2234. doi: 10.1007/s00214-004-0607-y. URL http://link.springer.com/10.1007/s00214-004-0607-y.

[223] Kenneth G. Dyall. Relativistic quadruple-zeta and revised triple-zeta and double-zeta basis sets for the 4p, 5p, and 6p elements. *Theor. Chem. Acc.*, 115(5):441–447, 2006. ISSN 0021400601260. doi: 10.1007/s00214-006-0126-0.

[224] Kenneth G. Dyall. Relativistic double-zeta, triple-zeta, and quadruple-zeta basis sets for the 6d elements rf-cn. *Theor. Chem. Acc.*, 129(3):603–613, 2011. ISSN 1432-881X, 1432-2234. doi: 10.1007/s00214-011-0906-z. URL http://link.springer.com/10.1007/s00214-011-0906-z.

[225] Kenneth G. Dyall. Core correlating basis functions for elements 31-118. *Theor. Chem. Acc.*, 131(5):1217, 2012. ISSN 1432-881X, 1432-2234. doi: 10.1007/s00214-012-1217-8. URL http://link.springer.com/10.1007/s00214-012-1217-8.

[226] Trond Saue and Trygve Helgaker. Four-component relativistic kohn-sham theory. *J. Comp. Chem.*, 23(8):814–823, 2002. ISSN 0192-8651, 1096-987X. doi: 10.1002/jcc.10066. URL https://onlinelibrary.wiley.com/doi/10.1002/jcc.10066.

[227] S.F. Boys and F. Bernardi. The calculation of small molecular interactions by the differences of separate total energies. some procedures with reduced errors. *Mol. Phys.*, 19(4):553–566, 1970. doi: 10.1080/00268977000101561. URL https://doi.org/10.1080/00268977000101561.

[228] John F. Ouyang and Ryan P. A. Bettens. Many-body basis set superposition effect. *J. Chem. Theory Comput.*, 11(11):5132–5143, 11 2015. doi: 10.1021/acs.jctc.5b00343. URL https://doi.org/10.1021/acs.jctc.5b00343.

[229] Fritz London. The general theory of molecular forces. *Trans. Faraday Soc.*, 33:8b–26, 1937.

[230] Tim Gould and Tomáš Bučko. C6 coefficients and dipole polarizabilities for all atoms and many ions in rows 1–6 of the periodic table. *J. Chem. Theory Comput.*, 12(8):3603–3613, 2016. doi: 10.1021/acs.jctc.6b00361. URL https://doi.org/10.1021/acs.jctc.6b00361. PMID: 27304856.

[231] Andreas Hermann, Jürgen Furthmüller, Heinz W. Gäggeler, and Peter Schwerdtfeger. Spin-orbit effects in structural and electronic properties for the solid state of the group-14 elements from carbon to superheavy element 114. *Phys. Rev. B*, 82:155116, Oct 2010. doi: 10.1103/PhysRevB.82.155116. URL https://link.aps.org/doi/10.1103/PhysRevB.82.155116.

[232] David Feller. The use of systematic sequences of wave functions for estimating the complete basis set, full configuration interaction limit in water. *J. Chem. Phys.*, 98(9):7059–7071, 1993. doi: 10.1063/1.464749. URL https://doi.org/10.1063/1.464749.

[233] T. Gavin Williams, Nathan J. DeYonker, and Angela K. Wilson. Hartree-fock complete basis set limit properties for transition metal diatomics. *J. Chem. Phys.*, 128(4):044101, 2008. doi: 10.1063/1.2822907. URL https://doi.org/10.1063/1.2822907.

[234] Trygve Helgaker, Wim Klopper, Henrik Koch, and Jozef Noga. Basis-set convergence of correlated calculations on water. *J. Chem. Phys.*, 106(23):9639–9646, 1997. doi: 10.1063/1.473863. URL https://doi.org/10.1063/1.473863.

[235] Yoshio Muto. Force between nonpolar molecules. *J. Phys. Math. Soc. Japan*, 17:629, 1943.

[236] P. Schwerdtfeger and A. Hermann. Equation of state for solid neon from quantum theory. *Phys. Rev. B*, 80:064106–1–064106–5, 2009. doi: 10.1103/PhysRevB.80.064106.

[237] Michael L Klein, Michael L Klein, JA Venables, JA Venables, et al. *Rare Gas Solids*, volume 1/2. Academic Press, New York, 1976.

[238] Frank Jensen. Estimating the hartree—fock limit from finite basis set calculations. *Theoret. Chem. Acc.*, 113(5):267–273, 2005. doi: 10.1007/s00214-005-0635-2. URL https://doi.org/10.1007/s00214-005-0635-2.

[239] Roger Fletcher and Michael JD Powell. A rapidly convergent descent method for minimization. *Computer J.*, 6(2):163–168, 1963.

[240] L. Koči, R. Ahuja, and A. B. Belonoshko. *Ab initio* and classical molecular dynamics of neon melting at high pressure. *Phys. Rev. B*, 75, 2007. doi: 214108-1--214108-7.

[241] Leonid Burakovsky, Dean L. Preston, and Richard R. Silbar. Melting as a dislocation-mediated phase transition. *Phys. Rev. B*, 61:15011–15018, Jun 2000. doi: 10.1103/PhysRevB.61.15011. URL https://link.aps.org/doi/10.1103/PhysRevB.61.15011.

[242] O L Keller, Jr, J. L. Burnett, T. A. Carlson, and C W Nestor, Jr. Predicted properties of the super heavy elements. i. elements 113 and 114, eka-thallium and eka-lead. *J. Phys. Chem.*, 74:1127–1134, 1970.

[243] Kenneth S. Pitzer. Are elements 112, 114, and 118 relatively inert gases? *J. Chem. Phys.*, 63(2):1032–1033, 1975. doi: 10.1063/1.431398.

[244] I. P. Grant and N. C. Pyper. Theoretical chemistry of superheavy elements e116 amd e114. *Nature*, 265:715–717, 1977.

[245] P Pyykkö and J P Desclaux. Dirac-Fock one-centre calculations show $114(h)_4$ to resemble Pbh_4. *Nature*, 266:336–337, 1977.

[246] Michael Seth, Knut Faegri, and Peter Schwerdtfeger. The stability of the oxidation state +4 in group 14 compounds from carbon to element 114. *Angew. Chem. Int. Ed.*, 37(18):2493–2496, 1998. ISSN 1521-3773. doi: 10.1002/(SICI)1521-3773(19981002)37:18⟨2493::AID-ANIE2493⟩3.0.CO;2-F. URL http://dx.doi.org/10.1002/(SICI)1521-3773(19981002)37:18<2493::AID-ANIE2493>3.0.CO;2-F.

[247] Peter Schwedtfeger and Michael Seth. Relativistic quantum chemistry of the superheavy elements. Closed-shell element 114 as a case study. *J. Nucl. Radiochem. Sci*, 3:133–136, 2002.

[248] Clinton S. Nash. Atomic and molecular properties of elements 112, 114, and 118. *J. Phys. Chem. A*, 109(15):3493–3500, 2005.

[249] Y. J. Yu, C. Z. Dong, J. G. Li, and B. Fricke. The excitation energies, ionization potentials, and oscillator strengths of neutral and ionized species of uuq (z=114) and the homolog elements ge, sn, and pb. *J. Chem. Phys.*, 128(12):124316, 2008. doi: 10.1063/1.2838985. URL https://doi.org/10.1063/1.2838985.

[250] Tim Hangele, Michael Dolg, Michael Hanrath, Xiaoyan Cao, and Peter Schwerdtfeger. Accurate relativistic energy-consistent pseudopotentials for the superheavy elements 111 to 118 including quantum electrodynamic effects. *J. Chem. Phys.*, 136(21):214105, 2012. doi: http://dx.doi.org/10.1063/1.4723805. URL http://scitation.aip.org/content/aip/journal/jcp/136/21/10.1063/1.4723805.

[251] V. A. Dzuba and V. V. Flambaum. Electron structure of superheavy elements uut, fl and uup (z=113 to 115). *Hyperfine Int.*, 237(1):160, 2016. doi: 10.1007/s10751-016-1365-7. URL https://doi.org/10.1007/s10751-016-1365-7.

[252] M. Y. Kaygorodov, D. P. Usov, E. Eliav, Y. S. Kozhedub, A. V. Malyshev, A. V. Oleynichenko, V. M. Shabaev, L. V. Skripnikov, A. V. Titov, I. I. Tupitsyn, and A. V. Zaitsevskii. Ionization potentials and electron affinities of rg, cn, nh, and fl superheavy elements, 2022. URL https://arxiv.org/abs/2202.08304.

[253] C. E. Moore. Atomic energy levels. Technical report, Natl. Bur. Stand. Ref. Data Ser., Nat. Bur. Stand. (US) Circ. No. NSRDS-NBS 35, U.S. GPO, Washington D.C., 1971.

[254] W H E Schwarz, E M van Wezenbeek, E J Baerends, and J G Snijders. The origin of relativistic effects of atomic orbitals. *J. Phys. B: At. Mol. Phys.*, 22(10):1515–1530, 1989. URL http://stacks.iop.org/0953-4075/22/i=10/a=008.

[255] E J Baerends, W H E Schwarz, P Schwerdtfeger, and J G Snijders. Relativistic atomic orbital contractions and expansions: magnitudes and explanations. *J. Phys. B: At. Mol. Phys.*, 23(19):3225–3240, oct 1990. doi: 10.1088/0953-4075/23/19/010. URL https://doi.org/10.1088/0953-4075/23/19/010.

[256] Anastasia Borschevsky, Valeria Pershina, Ephraim Eliav, and Uzi Kaldor. Electron affinity of element 114, with comparison to sn and pb. *Chem. Phys. Lett.*, 480(1):49–51, 2009. ISSN 0009-2614. doi: https://doi.org/10.1016/j.cplett.2009.08.059. URL https://www.sciencedirect.com/science/article/pii/S0009261409010562.

[257] M. Y. Kaygorodov, L. V. Skripnikov, I. I. Tupitsyn, E. Eliav, Y. S. Kozhedub, A. V. Malyshev, A. V. Oleynichenko, V. M. Shabaev, A. V. Titov, and A. V. Zaitsevskii. Electron affinity of oganesson. *Phys. Rev. A*, 104:012819, Jul 2021. doi: 10.1103/PhysRevA.104.012819. URL https://link.aps.org/doi/10.1103/PhysRevA.104.012819.

[258] Knut Faegri Jr. Relativistic gaussian basis sets for the elements k –uuo. *Theoret. Chem. Acc.*, 105(3):252–258, 2001. doi: 10.1007/s002140000209. URL https://doi.org/10.1007/s002140000209.

[259] W. L. Bade. Drude-model calculation of dispersion forces. i. general theory. *J. Chem. Phys.*, 27(6):1280–1284, 1957. doi: 10.1063/1.1743991. URL https://doi.org/10.1063/1.1743991.

[260] Alexandre Tkatchenko and O. Anatole von Lilienfeld. Popular kohn-sham density functionals strongly overestimate many-body interactions in van der waals systems. *Phys. Rev. B*, 78: 045116, Jul 2008. doi: 10.1103/PhysRevB.78.045116. URL https://link.aps.org/doi/10.1103/PhysRevB.78.045116.

[261] Antony Burrows, Shaun Cooper, and Peter Schwerdtfeger. The lattice sum for a hexagonal close packed structure and its dependence on the c/a ratio of the hexagonal cell parameters, unpublished results, 2022.

[262] U. Häussermann and S. I. Simak. Origin of the c/a variation in hexagonal close-packed divalent metals. *Phys. Rev. B*, 64:245114, Dec 2001. doi: 10.1103/PhysRevB.64.245114. URL https://link.aps.org/doi/10.1103/PhysRevB.64.245114.

[263] S. Hofmann, S. Heinz, R. Mann, J. Maurer, G. Münzenberg, S. Antalic, W. Barth, H. G. Burkhard, L. Dahl, K. Eberhardt, R. Grzywacz, J. H. Hamilton, R. A. Henderson, J. M. Kenneally, B. Kindler, I. Kojouharov, R. Lang, B. Lommel, K. Miernik, D. Miller, K. J. Moody, K. Morita, K. Nishio, A. G. Popeko, J. B. Roberto, J. Runke, K. P. Rykaczewski, S. Saro, C. Scheidenberger, H. J. Schött, D. A. Shaughnessy, M. A. Stoyer, P. Thörle-Pospiech, K. Tinschert, N. Trautmann, J. Uusitalo, and A. V. Yeremin. Review of even element super-heavy nuclei and search for element 120. *Europ. Phys. J. A*, 52(6):180, 2016. doi: 10.1140/epja/i2016-16180-4. URL https://doi.org/10.1140/epja/i2016-16180-4.

[264] Robert Eichler. *Superheavy Element Chemistry*, pages 33–43. Springer International Publishing, Cham, 2015. ISBN 978-3-319-10199-6. doi: 10.1007/978-3-319-10199-6_4. URL https://doi.org/10.1007/978-3-319-10199-6_4.

[265] N. M. Chiera, N. V. Aksenov, Y. V. Albin, G. A. Bozhikov, V. I. Chepigin, S. N. Dmitriev, R. Dressler, R. Eichler, V. Ya. Lebedev, A. Madumarov, O. N. Malyshev, D. Piguet, Y. A. Popov, A. V. Sabelnikov, P. Steinegger, A. I. Svirikhin, A. Türler, G. K. Vostokin, A. Vögele, and A. V. Yeremin. Interaction of elemental mercury with selenium surfaces: model experiments for investigations of superheavy elements copernicium and flerovium. *J. Radioanalyt. Nucl. Chem.*, 311(1):99–108, 2017. doi: 10.1007/s10967-016-5018-8. URL https://doi.org/10.1007/s10967-016-5018-8.

[266] Robert Eichler. The periodic table – an experimenter's guide to transactinide chemistry. *Radiochim. Acta*, 107(9-11):865–877, 2019. doi: doi:10.1515/ract-2018-3080. URL https://doi.org/10.1515/ract-2018-3080.

[267] Dahvyd Wing, Guy Ohad, Jonah B. Haber, Marina R. Filip, Stephen E. Gant, Jeffrey B. Neaton, and Leeor Kronik. Band gaps of crystalline solids from wannier-localization–based optimal tuning of a screened range-separated hybrid functional. *Proceedings of the National Academy of Sciences*, 118(34):e2104556118, 2021. doi: 10.1073/pnas.2104556118. URL https://www.pnas.org/doi/abs/10.1073/pnas.2104556118.

[268] Ricardo Ramirez and L. M. Falicov. Band structure of cubic and hexagonal argon. *Phys. Rev. B*, 1:3464–3471, Apr 1970. doi: 10.1103/PhysRevB.1.3464. URL https://link.aps.org/doi/10.1103/PhysRevB.1.3464.

[269] Ethan A. Mastny and Juan J. de Pablo. Melting line of the lennard-jones system, infinite size, and full potential. *J. Chem. Phys.*, 127(10):104504, 2007. doi: 10.1063/1.2753149. URL https://doi.org/10.1063/1.2753149.

[270] Hermann Stoll, Beate Paulus, and Peter Fulde. On the accuracy of correlation-energy expansions in terms of local increments. *J. Chem. Phys.*, 123(14):144108, 2005. doi: 10.1063/1.2052708. URL https://doi.org/10.1063/1.2052708.

[271] Beate Paulus. The method of increments—a wavefunction-based ab initio correlation method for solids. *Phys. Rep.*, 428(1):1–52, 2006. ISSN 0370-1573. doi: https://doi.org/10.1016/j.physrep.2006.01.003. URL https://www.sciencedirect.com/science/article/pii/S0370157306000330.

[272] Hermann Stoll. Toward a wavefunction-based treatment of strong electron correlation in extended systems by means of incremental methods. *J. Chem. Phys.*, 151(4):044104, 2019. doi: 10.1063/1.5109860. URL https://doi.org/10.1063/1.5109860.

[273] Jan-Michael Mewes, Paul Jerabek, Odile R. Smits, and Peter Schwerdtfeger. Oganesson is a semiconductor: On the relativistic band-gap narrowing in the heaviest noble-gas solids. *Angew. Chem. Int. Ed.*, 58(40):14260–14264, 2019. doi: https://doi.org/10.1002/anie.201908327. URL https://onlinelibrary.wiley.com/doi/abs/10.1002/anie.201908327.

[274] Karl O. Christe. Bartlett's discovery of noble gas fluorides, a milestone in chemical history. *Chem. Commun.*, 49:4588–4590, 2013. doi: 10.1039/C3CC41387J. URL http://dx.doi.org/10.1039/C3CC41387J.

[275] Walther Kossel. Über Molekülbildung als Frage des Atombaus. *Annalen der Physik*, 354(3): 229–362, 1916.

[276] John H Holloway and Eric G Hope. Recent advances in noble-gas chemistry. *Advances in Inorganic Chemistry*, 46:51–100, 1998.

[277] Joel F. Liebman and Carol A. Deakyne. Noble gas compounds and chemistry: a brief review of interrelations and interactions with fluorine-containing species. *Journal of Fluorine Chemistry*, 121(1):1–8, 2003. ISSN 0022-1139. doi: https://doi.org/10.1016/S0022-1139(03)00009-5. URL https://www.sciencedirect.com/science/article/pii/S0022113903000095.

[278] Gary J. Schrobilgen and David S. Brock. Noble gases. *Annu. Rep. Prog. Chem., Sect. A: Inorg. Chem.*, 107:135–141, 2011. doi: 10.1039/C1IC90019F. URL http://dx.doi.org/10.1039/C1IC90019F.

[279] Richard Betz and Gary J. Schrobilgen. The synthesis of xef2; a predictable outcome with a significant chemistry. *Zeitschrift für anorganische und allgemeine Chemie*, 638(10):1385–1388, 2012. doi: https://doi.org/10.1002/zaac.201210012. URL https://onlinelibrary.wiley.com/doi/abs/10.1002/zaac.201210012.

[280] Jay A Labinger. Why isn't noble gas chemistry 30 years older? the failed (?) 1933 experiment of yost and kaye. *Bull Hist Chem*, 40:29–36, 2015.

[281] Ranajit Saha, Gourhari Jana, Sudip Pan, Gabriel Merino, and Pratim Kumar Chattaraj. How far can one push the noble gases towards bonding?: A personal account. *Molecules*, 24(16), 2019. ISSN 1420-3049. doi: 10.3390/molecules24162933. URL https://www.mdpi.com/1420-3049/24/16/2933.

[282] Neil Bartlett and DH Lohmann. 1005. fluorides of the noble metals. part ii. dioxygenyl hexafluoroplatinate (v), o 2+[ptf 6]–. *Journal of the Chemical Society (Resumed)*, pages 5253–5261, 1962.

[283] Lionell Graham, Oliver Graudejus, Narendra K. Jha, and Neil Bartlett. Concerning the nature of xeptf6. *Coordination Chemistry Reviews*, 197(1):321–334, 2000. ISSN 0010-8545. doi: https://doi.org/10.1016/S0010-8545(99)00190-3. URL https://www.sciencedirect.com/science/article/pii/S0010854599001903.

[284] Howard H. Claassen, Henry. Selig, and John G. Malm. Xenon tetrafluoride. *Journal of the American Chemical Society*, 84(18):3593–3593, 09 1962. doi: 10.1021/ja00877a042. URL https://doi.org/10.1021/ja00877a042.

[285] J Slivnik, B Brčić, B Volavšek, J Marsel, V Vrščaj, A Šmalc, B Frlec, and Z Zemljič. Uber die synthese von xef6. *Croatica Chemica Acta*, 34(4):253–253, 1962.

[286] D. R. MacKenzie. Krypton difluoride: Preparation and handling. *Science*, 141(3586):1171–1171, 1963. doi: 10.1126/science.141.3586.1171.a. URL https://www.science.org/doi/abs/10.1126/science.141.3586.1171.a.

[287] R. D. Peacock and J. H. Holloway. New noble gas compounds. *Science Progress (1933-)*, 52(205):42–49, 1964. ISSN 00368504, 20477163. URL http://www.jstor.org/stable/43418912.

[288] Neil Bartlett and FO Sladky. The relative fluoride ion donor abilities of xef2, xef4, and xef6 and a chemical purification of xef4. *Journal of the American Chemical Society*, 90(19):5316–5317, 1968.

[289] R. M. Gavin and L. S. Bartell. Molecular structure of xef6. i. analysis of electron-diffraction intensities. *The Journal of Chemical Physics*, 48(6):2460–2465, 1968. doi: 10.1063/1.1669470. URL https://doi.org/10.1063/1.1669470.

[290] N. Bartlett and M. Wechsberg. The xenon difluoride complexes xef2 · xeof4; xef2 · xef6 · asf5 and xef2 · 2 xef6 · 2 asf5 and their relevance to bond polarity and fluoride ion donor ability of xef2 and xef6. *Zeitschrift für anorganische und allgemeine Chemie*, 385(1-2):5–17, 1971. doi: https://doi.org/10.1002/zaac.19713850103. URL https://onlinelibrary.wiley.com/doi/abs/10.1002/zaac.19713850103.

[291] Karl O Christe and William W Wilson. Perfluoroammonium and alkali-metal salts of the heptafluoroxenon (vi) and octafluoroxenon (vi) anions. *Inorganic Chemistry*, 21(12):4113–4117, 1982.

[292] Jon B Nielsen, Scott A Kinkead, John D Purson, and P Gary Eller. New syntheses of xenon hexafluoride (xef6) and xenon tetrafluoride (xef4). *Inorganic Chemistry*, 29(9):1779–1780, 1990.

[293] Gang Wu, Xiaoli Huang, Yanping Huang, Lingyun Pan, Fangfei Li, Xin Li, Mingkun Liu, Bingbing Liu, and Tian Cui. Confirmation of the structural phase transitions in xef2 under high pressure. *The Journal of Physical Chemistry C*, 121(11):6264–6271, 03 2017. doi: 10.1021/acs.jpcc.6b11558. URL https://doi.org/10.1021/acs.jpcc.6b11558.

[294] JJ Turner and George C Pimentel. Krypton fluoride: preparation by the matrix isolation technique. *Science*, 140(3570):974–975, 1963.

[295] John F. Lehmann, Hélène P.A. Mercier, and Gary J. Schrobilgen. The chemistry of krypton. *Coordination Chemistry Reviews*, 233-234:1–39, 2002. ISSN 0010-8545. doi: https://doi.org/10.1016/S0010-8545(02)00202-3. URL https://www.sciencedirect.com/science/article/pii/S0010854502002023.

[296] Matic Lozinšek and Gary J. Schrobilgen. The world of krypton revisited. *Nature Chemistry*, 8 (7):732–732, 2016. doi: 10.1038/nchem.2538. URL https://doi.org/10.1038/nchem.2538.

[297] Mark R. Bortolus, Hélène P. A. Mercier, Brianna Nguyen, and Gary J. Schrobilgen. Syntheses and characterizations of the mixed noble-gas compounds, [fkriifxeiif][asf6]·0.5 kriif2·2hf, ([krii2f3][asf6])2·xeivf4, and xeivf4·kriif2. *Angewandte Chemie International Edition*, 60(44):23678–23686, 2021. doi: https://doi.org/10.1002/anie.202102205. URL https://onlinelibrary.wiley.com/doi/abs/10.1002/anie.202102205.

[298] Matic Lozinšek, Hélène P. A. Mercier, and Gary J. Schrobilgen. Mixed noble-gas compounds of krypton(ii) and xenon(vi); [f5xe(fkrf)asf6] and [f5xe(fkrf)2asf6]. *Angewandte Chemie International Edition*, 60(15):8149–8156, 2021. doi: https://doi.org/10.1002/anie.202014682. URL https://onlinelibrary.wiley.com/doi/abs/10.1002/anie.202014682.

[299] John F. Lehmann, Hélène P.A. Mercier, and Gary J. Schrobilgen. The chemistry of krypton. *Coordination Chemistry Reviews*, 233-234:1–39, 2002. ISSN 0010-8545. doi: https://doi.org/10.1016/S0010-8545(02)00202-3. URL https://www.sciencedirect.com/science/article/pii/S0010854502002023.

[300] Lawrence Stein. Ionic radon solutions. *Science*, 168(3929):362–364, 1970.

[301] D. C. Lorents, D. L. Huestis, M. V. McCusker, H. H. Nakano, and R. M. Hill. Optical emissions of triatomic rare gas halides. *The Journal of Chemical Physics*, 68(10):4657–4661, 1978. doi: 10.1063/1.435574. URL https://doi.org/10.1063/1.435574.

[302] Leonid Khriachtchev, Mika Pettersson, Nino Runeberg, Jan Lundell, and Markku Räsänen. A stable argon compound. *Nature*, 406(6798):874–876, 2000. doi: 10.1038/35022551. URL https://doi.org/10.1038/35022551.

[303] Gernot Frenking and Dieter Cremer. The chemistry of the noble gas elements helium, neon, and argon — experimental facts and theoretical predictions. In *Noble Gas and High Temperature Chemistry*, pages 17–95, Berlin, Heidelberg, 1990. Springer Berlin Heidelberg. ISBN 978-3-540-46880-6.

[304] Ming Wah Wong. Prediction of a metastable helium compound: Hhef. *Journal of the American Chemical Society*, 122(26):6289–6290, 07 2000. doi: 10.1021/ja9938175. URL https://doi.org/10.1021/ja9938175.

[305] Karl O Christe and William W Wilson. Convenient synthesis of xenon oxide tetrafluoride. *Inorganic Chemistry*, 27(7):1296–1297, 1988.

[306] Jon B Nielsen, Scott A Kinkead, and P Gary Eller. A new synthesis of xenon oxytetrafluoride (xeof4). *Inorganic Chemistry*, 29(18):3621–3622, 1990.

[307] Daniel J. Grant, Tsang-Hsiu Wang, David A. Dixon, and Karl O. Christe. Heats of formation of xef3+, xef3-, xef5+, xef7+, xef7-, and xef8 from high level electronic structure calculations. *Inorganic Chemistry*, 49(1):261–270, 01 2010. doi: 10.1021/ic901956g. URL https://doi.org/10.1021/ic901956g.

[308] Thomas Weiske, Diethard K. Böhme, Jan Hrušák, Wolfgang Krätschmer, and Helmut Schwarz. Endohedral cluster compounds: Inclusion of helium within c and c through collision experiments. *Angewandte Chemie International Edition in English*, 30(7):884–886, 1991. doi: https://doi.org/10.1002/anie.199108841. URL https://onlinelibrary.wiley.com/doi/abs/10.1002/anie.199108841.

[309] Martin Saunders, Hugo A Jimenez-Vázquez, R James Cross, Stanley Mroczkowski, Michael L Gross, Daryl E Giblin, and Robert J Poreda. Incorporation of helium, neon, argon, krypton,

and xenon into fullerenes using high pressure. *Journal of the American Chemical Society*, 116(5):2193–2194, 1994.

[310] Ralf Tonner, Gernot Frenking, Matthias Lein, and Peter Schwerdtfeger. Packed to the rafters: Filling up c60 with rare gas atoms. *ChemPhysChem*, 12(11):2081–2084, 2011. doi: https://doi.org/10.1002/cphc.201100360. URL https://chemistry-europe.onlinelibrary.wiley.com/doi/abs/10.1002/cphc.201100360.

[311] Andreas Krapp and Gernot Frenking. Is this a chemical bond? a theoretical study of ng2@c60 (ng=he, ne, ar, kr, xe). *Chemistry – A European Journal*, 13(29):8256–8270, 2007. doi: https://doi.org/10.1002/chem.200700467. URL https://chemistry-europe.onlinelibrary.wiley.com/doi/abs/10.1002/chem.200700467.

[312] Rosa M. Gomila and Antonio Frontera. Covalent and non-covalent noble gas bonding interactions in xefn derivatives (n = 2–6): A combined theoretical and icsd analysis. *Frontiers in Chemistry*, 8, 2020. ISSN 2296-2646. doi: 10.3389/fchem.2020.00395. URL https://www.frontiersin.org/articles/10.3389/fchem.2020.00395.

[313] Zoran Mazej. Noble-gas chemistry more than half a century after the first report of the noble-gas compound. *Molecules*, 25(13), 2020. ISSN 1420-3049. doi: 10.3390/molecules25133014. URL https://www.mdpi.com/1420-3049/25/13/3014.

[314] Stefan Seidel and Konrad Seppelt. Xenon as a complex ligand: the tetra xenono gold (ii) cation in auxe$_4^{2+}$ (sb$_2$f$_{11}^-$) 2. *Science*, 290(5489):117–118, 2000.

[315] Pekka Pyykkö. Noblesse oblige. *Science*, 290(5489):64–65, 2000. doi: 10.1126/science.290.5489.64. URL https://www.science.org/doi/abs/10.1126/science.290.5489.64.

[316] Gerald K. Johnson, John G. Malm, and Ward N. Hubbard. The enthalpies of formation of xef6(c), xef4(c), xef2(c), and pf3(g). *The Journal of Chemical Thermodynamics*, 4(6):879–891, 1972. ISSN 0021-9614. doi: https://doi.org/10.1016/0021-9614(72)90010-9. URL https://www.sciencedirect.com/science/article/pii/0021961472900109.

[317] Carol A Deakyne, Kathleen F Edwards, Maja Ponikvar-Svet, and Joel F Liebman. The existence of argon difluoride: Is there any reason for optimism? *International Journal of Chemical Modeling*, 8(3/4):257–264, 2016.

[318] Kenneth S. Pitzer. Bonding in xenon fluorides and halogen fluorides. *Science*, 139(3553):414–415, 1963. doi: 10.1126/science.139.3553.414. URL https://www.science.org/doi/abs/10.1126/science.139.3553.414.

[319] C.E. Moore. *Atomic Energy Levels*. Natl. Stand. Ref. Data Ser., Natl. Bur. Stand., USA, 1971.

[320] Yangyang Guo, Lukáš Félix Pašteka, Ephraim Eliav, and Anastasia Borschevsky. Ionization potentials and electron affinity of oganesson. *arXiv preprint arXiv:2107.02164*, 2021.

[321] Michael Filatov and Dieter Cremer. Bonding in radon hexafluoride: An unusual relativistic problem? *Phys. Chem. Chem. Phys.*, 5:1103–1105, 2003. doi: 10.1039/B212460M. URL http://dx.doi.org/10.1039/B212460M.

[322] Thom H. Dunning and P. Jeffrey Hay. The covalent and ionic states of the rare gas monofluorides. *The Journal of Chemical Physics*, 69(1):134–149, 1978. doi: 10.1063/1.436397. URL https://aip.scitation.org/doi/abs/10.1063/1.436397.

[323] Gulzari L. Malli, Jacek Styszynski, and Alberico B. F. Da Silva. Ab initio calculations of relativistic and electron correlation effects in polyatomics using the universal gaussian basis set: Xef2. *International Journal of Quantum Chemistry*, 55(3):213–225, 1995. doi: https://doi.org/10.1002/qua.560550302. URL https://onlinelibrary.wiley.com/doi/abs/10.1002/qua.560550302.

[324] Meng-Sheng Liao and Qian-Er Zhang. Chemical bonding in xef2, xef4, krf2, krf4, rnf2, xecl2, and xebr2: From the gas phase to the solid state. *The Journal of Physical Chemistry A*, 102(52):10647–10654, 12 1998. doi: 10.1021/jp9825516. URL https://doi.org/10.1021/jp9825516.

[325] Young-Kyu Han and Yoon Sup Lee. Structures of rgf_n (rg = xe, rn, and element 118. $n = 2$, 4.) calculated by two-component spin-orbit methods. a spin-orbit induced isomer of (118)f4. *The Journal of Physical Chemistry A*, 103(8):1104–1108, 02 1999. doi: 10.1021/jp983665k. URL https://doi.org/10.1021/jp983665k.

[326] G.L. Malli. Relativistic all-electron dirac–fock calculations on rnf6 and its ions. *Journal of Molecular Structure: THEOCHEM*, 537(1):71–77, 2001. ISSN 0166-1280. doi: https://doi.org/10.1016/S0166-1280(00)00663-1. URL https://www.sciencedirect.com/science/article/pii/S0166128000006631.

[327] Roberto Luiz Andrade Haiduke, Harley de Paiva Martins Filho, and Albérico Borges Ferreira da Silva. A theoretical study on the xef2 molecule. *Chemical Physics*, 348(1):89–96, 2008. ISSN 0301-0104. doi: https://doi.org/10.1016/j.chemphys.2008.02.031. URL https://www.sciencedirect.com/science/article/pii/S0301010408001365.

[328] Benoît Braïda and Philippe C. Hiberty. The essential role of charge-shift bonding in hypervalent prototype xef2. *Nature Chemistry*, 5(5):417–422, 2013. doi: 10.1038/nchem.1619. URL https://doi.org/10.1038/nchem.1619.

[329] Dominik Kurzydłowski, Magdalena Sołtysiak, Aleksandra Dżoleva, and Patryk Zaleski-Ejgierd. High-pressure reactivity of kr and f2-stabilization of krypton in the+ 4 oxidation state. *Crystals*, 7(11):329, 2017.

[330] Clinton S. Nash and Bruce E. Bursten. Spin-orbit coupling versus the vsepr method: On the possibility of a nonplanar structure for the super-heavy noble gas tetrafluoride (118)f4. *Angewandte Chemie International Edition*, 38(1-2):151–153, 1999. doi: https://doi.org/10.1002/(SICI)1521-3773(19990115)38:1/2⟨151::AID-ANIE151⟩3.0.CO;2-1.

[331] D. S. Urch. 1103. the stereochemically inert lone pair? a speculation on the bonding in sbcl63–, sebr62–, tebr62–, if6–, xef6, etc. *J. Chem. Soc.*, pages 5775–5781, 1964. doi: 10.1039/JR9640005775. URL http://dx.doi.org/10.1039/JR9640005775.

[332] L. S. Bartell. Evidence for pseudo jahn–teller effect in xef6. *The Journal of Chemical Physics*, 46(11):4530–4531, 1967. doi: 10.1063/1.1840580. URL https://doi.org/10.1063/1.1840580.

[333] JN Cutler, GM Bancroft, JD Bozek, KH Tan, and GJ Schrobilgen. Ligand field splitting on the xenon 4d core levels in xefx (x= 2, 4, 6) compounds from high-resolution gas-phase photoelectron spectra: the structure of xef6. *Journal of the American Chemical Society*, 113 (24):9125–9131, 1991.

[334] William J. Ehlhardt and Lawrence L. Lohr. A theoretical study of the optical absorption band shape for xenon hexafluoride. *The Journal of Chemical Physics*, 67(5):1935–1941, 1977. doi: 10.1063/1.435125. URL https://aip.scitation.org/doi/abs/10.1063/1.435125.

[335] Sh. Sh. Nabiev. Vibrational spectra and structural features of noble gas fluorides in cryogenic and nonaqueous solutions. *Russian Chemical Bulletin*, 47(4):535–559, 1998. doi: 10.1007/BF02495952. URL https://doi.org/10.1007/BF02495952.

[336] Konrad Seppelt. Molecular hexafluorides. *Chemical Reviews*, 115(2):1296–1306, 01 2015. doi: 10.1021/cr5001783. URL https://doi.org/10.1021/cr5001783.

[337] Maxim Gawrilow, Helmut Beckers, Sebastian Riedel, and Lan Cheng. Matrix-isolation and quantum-chemical analysis of the c3v conformer of xef_6, $xeof_4$, and their acetonitrile adducts. *The Journal of Physical Chemistry A*, 122(1):119–129, 01 2018. doi: 10.1021/acs.jpca.7b09902. URL https://doi.org/10.1021/acs.jpca.7b09902.

[338] Itzhak Sedgi and Sebastian Kozuch. Heavy atom tunnelling on xef6 pseudorotation. *Phys. Chem. Chem. Phys.*, 22:17725–17730, 2020. doi: 10.1039/D0CP03205K. URL http://dx.doi.org/10.1039/D0CP03205K.

[339] M. Kaupp, Ch. van Wüllen, R. Franke, F. Schmitz, and W. Kutzelnigg. The structure of xef6 and of compounds isoelectronic with it. a challenge to computational chemistry and to the qualitative theory of the chemical bond. *Journal of the American Chemical Society*, 118(47):11939–11950, 01 1996. doi: 10.1021/ja9621556. URL https://doi.org/10.1021/ja9621556.

[340] Lan Cheng, Jürgen Gauss, and John F. Stanton. Relativistic coupled-cluster calculations on xef6: Delicate interplay between electron-correlation and basis-set effects. *The Journal of Chemical Physics*, 142(22):224309, 2015. doi: 10.1063/1.4922112. URL https://doi.org/10.1063/1.4922112.

[341] Kirk A. Peterson, David A. Dixon, and Hermann Stoll. The use of explicitly correlated methods on xef6 predicts a c3v minimum with a sterically active, free valence electron pair on xe. *The Journal of Physical Chemistry A*, 116(39):9777–9782, 10 2012. doi: 10.1021/jp3084259. URL https://doi.org/10.1021/jp3084259.

[342] Christel M Marian. Spin–orbit coupling and intersystem crossing in molecules. *Wiley Interdisciplinary Reviews: Computational Molecular Science*, 2(2):187–203, 2012.

[343] Dmitri G Fedorov, Shiro Koseki, Michael W Schmidt, and Mark S Gordon. Spin-orbit coupling in molecules: Chemistry beyond the adiabatic approximation. *International Reviews in Physical Chemistry*, 22(3):551–592, 2003.

[344] Sam Schott, Erik R McNellis, Christian B Nielsen, Hung-Yang Chen, Shun Watanabe, Hisaaki Tanaka, Iain McCulloch, Kazuo Takimiya, Jairo Sinova, and Henning Sirringhaus. Tuning the effective spin-orbit coupling in molecular semiconductors. *Nature communications*, 8(1):15200, 2017.

[345] Mao Lin, Iñigo Robredo, Niels BM Schröter, Claudia Felser, Maia G Vergniory, and Barry Bradlyn. Spin-momentum locking from topological quantum chemistry: Applications to multifold fermions. *Physical Review B*, 106(24):245101, 2022.

[346] Frederik Thorning, Frank Jensen, and Peter R Ogilby. Geometry dependence of spin–orbit coupling in complexes of molecular oxygen with atoms, h2, or organic molecules. *The Journal of Physical Chemistry A*, 126(6):834–844, 2022.

[347] Jorge David, Doris Guerra, and Albeiro Restrepo. The jahn- teller effect: A case of incomplete theory for d 4 complexes? *Inorganic Chemistry*, 50(4):1480–1483, 2011.

[348] Dimitrije Stepanenko, Nicholas E Bonesteel, David P DiVincenzo, Guido Burkard, and Daniel Loss. Spin-orbit coupling and time-reversal symmetry in quantum gates. *Physical Review B*, 68(11):115306, 2003.

[349] AL Khosla, AC Jacko, J Merino, and BJ Powell. Spin-orbit coupling and strong electronic correlations in cyclic molecules. *Physical Review B*, 95(11):115109, 2017.

[350] George F Koster, John O Dimmock, Robert G Wheeler, and Hermann Statz. The properties of the thirty-two point groups (research monograph), 1963.

[351] J. Pérez and A. Restrepov. Ascec v03: Annealing simulado con energá cuántica, 2008. Property, development, and implementation: Grupo de Química-Física Teŕica,.

[352] Jhon F Pérez, Elizabeth Florez, Cacier Z Hadad, Patricio Fuentealba, and Albeiro Restrepo. Stochastic search of the quantum conformational space of small lithium and bimetallic lithium- sodium clusters. *The Journal of Physical Chemistry A*, 112(25):5749–5755, 2008.

[353] Jhon F Pérez, Elizabeth Florez, Cacier Z Hadad, Patricio Fuentealba, and Albeiro Restrepo. Stochastic search of the quantum conformational space of small lithium and bimetallic lithium- sodium clusters. *The Journal of Physical Chemistry A*, 112(25):5749–5755, 2008.

[354] Carlo Adamo and Vincenzo Barone. Toward reliable density functional methods without adjustable parameters: The pbe0 model. *The Journal of chemical physics*, 110(13):6158–6170, 1999.

[355] Detlev Figgen, Guntram Rauhut, Michael Dolg, and Hermann Stoll. Energy-consistent pseudopotentials for group 11 and 12 atoms: adjustment to multi-configuration dirac–hartree–fock data. *Chemical physics*, 311(1-2):227–244, 2005.

[356] Kirk A Peterson and Cristina Puzzarini. Systematically convergent basis sets for transition metals. ii. pseudopotential-based correlation consistent basis sets for the group 11 (cu, ag, au) and 12 (zn, cd, hg) elements. *Theoretical Chemistry Accounts*, 114(4):283–296, 2005.

[357] César Ibargüen, Marcela Manrique-Moreno, CZ Hadad, Jorge David, and Albeiro Restrepo. Microsolvation of dimethylphosphate: a molecular model for the interaction of cell membranes with water. *Physical Chemistry Chemical Physics*, 15(9):3203–3211, 2013.

[358] Andy Zapata-Escobar, Marcela Manrique-Moreno, Doris Guerra, CZ Hadad, and Albeiro Restrepo. A combined experimental and computational study of the molecular interactions between anionic ibuprofen and water. *The Journal of chemical physics*, 140(18):05B611_1, 2014.

[359] Natalia Rojas-Valencia, César Ibargüen, and Albeiro Restrepo. Molecular interactions in the microsolvation of dimethylphosphate. *Chemical Physics Letters*, 635:301–305, 2015.

[360] Alba Vargas-Caamal, Jose Luis Cabellos, Filiberto Ortiz-Chi, Henry S Rzepa, Albeiro Restrepo, and Gabriel Merino. How many water molecules does it take to dissociate hcl? *Chemistry–A European Journal*, 22(8):2812–2818, 2016.

[361] Juliana Murillo, Jorge David, and Albeiro Restrepo. Insights into the structure and stability of the carbonic acid dimer. *Physical Chemistry Chemical Physics*, 12(36):10963–10970, 2010.

[362] Jhon F Pérez, CZ Hadad, and Albeiro Restrepo. Structural studies of the water tetramer. *International Journal of Quantum Chemistry*, 108(10):1653–1659, 2008.

[363] Gina Hincapie, Nancy Acelas, Marcela Castano, Jorge David, and Albeiro Restrepo. Structural studies of the water hexamer. *The Journal of Physical Chemistry A*, 114(29):7809–7814, 2010.

[364] Jorge David, Doris Guerra, and Albeiro Restrepo. Structural characterization of the (methanol) 4 potential energy surface. *The Journal of Physical Chemistry A*, 113(38):10167–10173, 2009.

[365] Edison Flórez, Alejandro F Maldonado, Gustavo A Aucar, Jorge David, and Albeiro Restrepo. Microsolvation of methylmercury: structures, energies, bonding and nmr constants (199 hg, 13 c and 17 o). *Physical Chemistry Chemical Physics*, 18(3):1537–1550, 2016.

[366] Yuly Chamorro, Edison Flórez, Alejandro Maldonado, Gustavo Aucar, and Albeiro Restrepo. Microsolvation of heavy halides. *International Journal of Quantum Chemistry*, 121(7): e26571, 2021.

[367] Angie Velásquez, Yuly Chamorro, Alejandro Maldonado, Gustavo Aucar, and Albeiro Restrepo. Microsolvation of sr2+, ba2+: Structures, energies, bonding, and nuclear magnetic shieldings. *International Journal of Quantum Chemistry*, 121(18):e26753, 2021.

[368] Sara Gomez, Doris Guerra, Jose G Lopez, Alejandro Toro-Labbe, and Albeiro Restrepo. A detailed look at the reaction mechanisms of substituted carbenes with water. *The Journal of Physical Chemistry A*, 117(9):1991–1999, 2013.

[369] Jhon F Pérez, Elizabeth Florez, Cacier Z Hadad, Patricio Fuentealba, and Albeiro Restrepo. Stochastic search of the quantum conformational space of small lithium and bimetallic lithium- sodium clusters. *The Journal of Physical Chemistry A*, 112(25):5749–5755, 2008.

[370] Jonathan Romero, Andres Reyes, Jorge David, and Albeiro Restrepo. Understanding microsolvation of li+: structural and energetical analyses. *Physical Chemistry Chemical Physics*, 13(33):15264–15271, 2011.

[371] Norberto Moreno, Franklin Ferraro, Elizabeth Flórez, CZ Hadad, and Albeiro Restrepo. Spin–orbit coupling effects in au m pt n clusters (m+ n= 4). *The Journal of Physical Chemistry A*, 120(10):1698–1705, 2016.

[372] César Ibargüen, Doris Guerra, CZ Hadad, and Albeiro Restrepo. Very weak interactions: structures, energies and bonding in the tetramers and pentamers of hydrogen sulfide. *RSC Advances*, 4(102):58217–58225, 2014.

[373] Florian Weigend and Reinhart Ahlrichs. Balanced basis sets of split valence, triple zeta valence and quadruple zeta valence quality for h to rn: Design and assessment of accuracy. *Physical Chemistry Chemical Physics*, 7(18):3297–3305, 2005.

[374] Takeshi Yanai, David P Tew, and Nicholas C Handy. A new hybrid exchange–correlation functional using the coulomb-attenuating method (cam-b3lyp). *Chemical physics letters*, 393 (1-3):51–57, 2004.

[375] Jeng-Da Chai and Martin Head-Gordon. Long-range corrected hybrid density functionals with damped atom–atom dispersion corrections. *Physical Chemistry Chemical Physics*, 10 (44):6615–6620, 2008.

[376] Éric Brémond, Juan Carlos Sancho-García, Ángel José Pérez-Jiménez, and Carlo Adamo. Communication: Double-hybrid functionals from adiabatic-connection: The qidh model. *The Journal of Chemical Physics*, 141(3):031101, 2014.

[377] Martin Head-Gordon, John A Pople, and Michael J Frisch. Mp2 energy evaluation by direct methods. *Chemical physics letters*, 153(6):503–506, 1988.

[378] George D Purvis III and Rodney J Bartlett. A full coupled-cluster singles and doubles model: The inclusion of disconnected triples. *The Journal of Chemical Physics*, 76(4):1910–1918, 1982.

[379] Gustavo E Scuseria and Henry F Schaefer III. Is coupled cluster singles and doubles (ccsd) more computationally intensive than quadratic configuration interaction (qcisd)? *The Journal of Chemical Physics*, 90(7):3700–3703, 1989.

[380] MJ Frisch, GW Trucks, HB Schlegel, GE Scuseria, MA Robb, JR Cheeseman, G Scalmani, V Barone, GA Petersson, H Nakatsuji, et al. Gaussian 16 revision c. 01. 2016; gaussian inc. *Wallingford CT*, 421, 2016.

[381] Kenneth G Dyall. An exact separation of the spin-free and spin-dependent terms of the dirac–coulomb–breit hamiltonian. *The Journal of chemical physics*, 100(3):2118–2127, 1994.

[382] Miroslav Iliaš and Trond Saue. An infinite-order two-component relativistic hamiltonian by a simple one-step transformation. *The Journal of chemical physics*, 126(6):064102, 2007.

[383] Kenneth G Dyall. Relativistic quadruple-zeta and revised triple-zeta and double-zeta basis sets for the 4p, 5p, and 6p elements. *Theoretical Chemistry Accounts*, 115(5):441–447, 2006.

[384] Kenneth G Dyall. Relativistic double-zeta, triple-zeta, and quadruple-zeta basis sets for the 7p elements, with atomic and molecular applications. *Theoretical Chemistry Accounts*, 131 (3):1–20, 2012.

[385] L. Visscher and K.G. Dyall. Dirac–fock atomic electronic structure calculations using different nuclear charge distributions. *Atomic Data and Nuclear Data Tables*, 67(2):207–224, 1997. ISSN 0092-640X. doi: https://doi.org/10.1006/adnd.1997.0751. URL https://www.sciencedirect.com/science/article/pii/S0092640X97907518.

[386] Joost NP van Stralen, Lucas Visscher, Christoffer Vaaben Larsen, and Hans Jørgen Aa Jensen. First-order mp2 molecular properties in a relativistic framework. *Chemical physics*, 311(1-2):81–95, 2005.

[387] Avijit Shee, Lucas Visscher, and Trond Saue. Analytic one-electron properties at the 4-component relativistic coupled cluster level with inclusion of spin-orbit coupling. *The Journal of Chemical Physics*, 145(18):184107, 2016.

[388] T Takeda. The scalar relativistic approximation. *Zeitschrift für Physik B Condensed Matter*, 32(1):43–48, 1978.

[389] Kenneth G Dyall. An exact separation of the spin-free and spin-dependent terms of the dirac–coulomb–breit hamiltonian. *The Journal of chemical physics*, 100(3):2118–2127, 1994.

[390] Miroslav Iliaš and Trond Saue. An infinite-order two-component relativistic hamiltonian by a simple one-step transformation. *The Journal of chemical physics*, 126(6):064102, 2007.

[391] Joshua. Jortner, E. Guy. Wilson, and Stuart A. Rice. The heats of sublimation of xef_2 and xef_4 and a conjecture on bonding in the solids. *Journal of the American Chemical Society*, 85(6):814–815, 03 1963. doi: 10.1021/ja00889a034. URL https://doi.org/10.1021/ja00889a034.

[392] M Kaupp, Ch Van Wüllen, R Franke, F Schmitz, and W Kutzelnigg. The structure of xef6 and of compounds isoelectronic with it. a challenge to computational chemistry and to the qualitative theory of the chemical bond. *Journal of the American Chemical Society*, 118(47): 11939–11950, 1996.

[393] Lawrence Stein. Hydrolytic reactions of radon fluorides. *Inorganic Chemistry*, 23(22):3670–3671, 1984.

[394] Jaeeun Kang, Ina Park, Ji Hoon Shim, Duck Young Kim, and Wooyong Um. Prediction of stable radon fluoride molecules and geometry optimization using first-principles calculations. *Scientific Reports*, 13(1):1–9, 2023.

[395] Carlos Ariel Giménez, Alejandro Fabián Maldonado, and Gustavo Adolfo Aucar. Relativistic and electron correlation effects on nmr j-coupling of sn and pb containing molecules. *Theoretical Chemistry Accounts*, 135(8):1–11, 2016.

[396] Peter Schwerdtfeger. Relativistic and electron-correlation contributions in atomic and molecular properties: benchmark calculations on au and au2. *Chemical physics letters*, 183(5):457–463, 1991.

[397] Michael Seth and Peter Schwerdtfeger. A comparison of relativistic and electron correlation effects for (111) f,(111) h and (111) li. *Chemical Physics Letters*, 318(4-5):314–318, 2000.

[398] Vaida Arcisauskaite, Stefan Knecht, Stephan PA Sauer, and Lars Hemmingsen. Fully relativistic coupled cluster and dft study of electric field gradients at hg in 199 hg compounds. *Physical Chemistry Chemical Physics*, 14(8):2651–2657, 2012.

[399] Andrej Antušek, Miroslav Urban, and Andrzej J Sadlej. Lone pair interactions with coinage metal atoms: Weak van der waals complexes of the coinage metal atoms with water and ammonia. *The Journal of chemical physics*, 119(14):7247–7262, 2003.

[400] WA De Jong, J Styszynski, L Visscher, and WC Nieuwpoort. Relativistic and correlation effects on molecular properties: The interhalogens clf, brf, brcl, if, icl, and ibr. *The Journal of chemical physics*, 108(13):5177–5184, 1998.

[401] L Visscher and KG Dyall. Relativistic and correlation effects on molecular properties. i. the dihalogens f2, cl2, br2, i2, and at2. *The Journal of chemical physics*, 104(22):9040–9046, 1996.

[402] L Visscher, J Styszynski, and WC Nieuwpoort. Relativistic and correlation effects on molecular properties. ii. the hydrogen halides hf, hcl, hbr, hi, and hat. *The Journal of chemical physics*, 105(5):1987–1994, 1996.

[403] Christophe Gourlaouen, Jean-Philip Piquemal, Trond Saue, and Olivier Parisel. Revisiting the geometry of nd10 (n+ 1) s0 [m (h2o)] p+ complexes using four-component relativistic dft calculations and scalar relativistic correlated csov energy decompositions (mp+= cu+, zn2+, ag+, cd2+, au+, hg2+). *Journal of computational chemistry*, 27(2):142–156, 2006.

[404] Lan Cheng, Jürgen Gauss, and John F Stanton. Relativistic coupled-cluster calculations on xef6: Delicate interplay between electron-correlation and basis-set effects. *The Journal of Chemical Physics*, 142(22):224309, 2015.

[405] Konrad Seppelt. Molecular hexafluorides. *Chemical Reviews*, 115(2):1296–1306, 2015.

[406] David A Dixon, Daniel J Grant, Karl O Christe, and Kirk A Peterson. Structure and heats of formation of iodine fluorides and the respective closed-shell ions from ccsd (t) electronic structure calculations and reliable prediction of the steric activity of the free-valence electron pair in clf6-, brf6-, and if6-. *Inorganic chemistry*, 47(12):5485–5494, 2008.

[407] Y Simon-Manso and P Fuentealba. On the location of the electron lone pair of xef6 and related molecules. *Journal of Molecular Structure: THEOCHEM*, 634(1-3):89–94, 2003.

[408] Lina Chen, David E Woon, and Thom H Dunning Jr. High level ab initio calculations on clfn-(n= 1–6): Recoupled pair bonding involving a closed-shell central ion. *Computational and Theoretical Chemistry*, 1116:73–85, 2017.

[409] Karl O Christe, William W Wilson, Raman V Chirakal, Jeremy CP Sanders, and Gary J Schrobilgen. The hexafluorochlorate (v) anion, clf6. *Inorganic Chemistry*, 29(18):3506–3511, 1990.

[410] Julien Pilmé, Edward A Robinson, and Ronald J Gillespie. A topological study of the geometry of af6e molecules: weak and inactive lone pairs. *Inorganic chemistry*, 45(16): 6198–6204, 2006.

[411] Preston J MacDougall. Molecular geometry and fluxionality of the ax6e system clf6. *Inorganic Chemistry*, 25(24):4400–4404, 1986.

[412] JD Bernal and RH Fowler. A theory of water and ionic solution, with particular reference to hydrogen and hydroxyl ions. *The Journal of Chemical Physics*, 1(8):515–548, 1933.

[413] John F Ouyang and Ryan Bettens. Modelling water: a lifetime enigma. *CHIMIA International Journal for Chemistry*, 69(3):104–111, 2015.

[414] John L Finney. The water molecule and its interactions: the interaction between theory, modelling, and experiment. *Journal of Molecular Liquids*, 90(1-3):303–312, 2001.

[415] Bertrand Guillot. A reappraisal of what we have learnt during three decades of computer simulations on water. *Journal of Molecular Liquids*, 101(1-3):219–260, 2002.

[416] Krzysztof Szalewicz, Claude Leforestier, and Ad Van Der Avoird. Towards the complete understanding of water by a first-principles computational approach. *Chemical Physics Letters*, 482(1-3):1–14, 2009.

[417] William L Jorgensen. Quantum and statistical mechanical studies of liquids. 10. transferable intermolecular potential functions for water, alcohols, and ethers. application to liquid water. *Journal of the American Chemical Society*, 103(2):335–340, 1981.

[418] William L Jorgensen, Jayaraman Chandrasekhar, Jeffry D Madura, Roger W Impey, and Michael L Klein. Comparison of simple potential functions for simulating liquid water. *The Journal of chemical physics*, 79(2):926–935, 1983.

[419] Michael W Mahoney and William L Jorgensen. A five-site model for liquid water and the reproduction of the density anomaly by rigid, nonpolarizable potential functions. *The Journal of Chemical Physics*, 112(20):8910–8922, 2000.

[420] Hiroki Nada and Jan PJM van der Eerden. An intermolecular potential model for the simulation of ice and water near the melting point: A six-site model of h 2 o. *The Journal of chemical physics*, 118(16):7401–7413, 2003.

[421] JLF Abascal, E Sanz, R García Fernández, and C Vega. A potential model for the study of ices and amorphous water: Tip4p/ice. *The Journal of chemical physics*, 122(23):234511, 2005.

[422] C. Vega, J. L. F. Abascal, and I. Nezbeda. Vapor-liquid equilibria from the triple point up to the critical point for the new generation of tip4p-like models: Tip4p/ew, tip4p/2005, and tip4p/ice. *The Journal of Chemical Physics*, 125(3):034503, 2006. doi: 10.1063/1.2215612.

[423] Michael W. Mahoney and William L. Jorgensen. Quantum, intramolecular flexibility, and polarizability effects on the reproduction of the density anomaly of liquid water by simple potential functions. *The Journal of Chemical Physics*, 115(23):10758–10768, 2001. doi: 10.1063/1.1418243.

[424] Carlos Vega and Jose L. F. Abascal. Simulating water with rigid non-polarizable models: a general perspective. *Phys. Chem. Chem. Phys.*, 13:19663–19688, 2011. doi: 10.1039/C1CP22168J. URL http://dx.doi.org/10.1039/C1CP22168J.